MAX-PLANCK-INSTITUT
FÜR POLYMERFORSCHUNG

Enhancing Reactivity of Heterogeneous Photocatalysts by Tailored Substrate-Catalyst Interactions

Dissertation

zur Erlangung des Grades
Doktor der Naturwissenschaften
im Promotionsfach Chemie

JG|U

Fachbereich Chemie, Pharmazie und Geowissenschaften
Johannes Gutenberg-Universität Mainz
Deutschland

vorgelegt von
Julian Heuer
geboren in Osnabrück

Mainz, 11.11.2024

Dekan: Prof. Dr. Eva Rentschler
1. Gutachter: Prof. Dr. Katharina Landfester
2. Gutachter: Prof. Dr. Christoph Kerzig

Die vorliegende Arbeit wurde im Zeitraum von Dezember 2020 bis Mai 2024 am Max-Planck- Institut für Polymerforschung im Arbeitskreis von Prof. Dr. Katharina Landfester unter der Betreuung von Dr. Calum Ferguson angefertigt.

Hiermit erkläre ich,

dass ich die vorliegende Arbeit selbstständig verfasst und keine anderen als die angegebenen Quellen und Hilfsmittel benutzt habe. Ich erkläre ferner, dass ich keine generativen KI-basierten Anwendungen oder Werkzeuge genutzt habe. Sämtliche wörtlichen oder sinngemäßen Übernahmen und Zitate sind kenntlich gemacht und nachgewiesen. Ich versichere, dass ich keine Hilfsmittel verwendet habe, deren Nutzung die Prüferin oder der Prüfer explizit ausgeschlossen hat.

Mit Abgabe der vorliegenden Leistung übernehme ich die Verantwortung für das eingereichte Gesamtprodukt. Die Richtigkeit übernommener Aussagen und Inhalte habe ich nach bestem Wissen und Gewissen geprüft.

Ich habe die Arbeit nicht zum Erwerb eines anderen Leistungsnachweises in gleicher oder ähnlicher Form eingereicht.

Mir ist bekannt, dass ein Verstoß gegen die genannten Punkte prüfungsrechtliche Konsequenzen hat und insbesondere dazu führen kann, dass die Promotionsleistung als mit ”nicht bestanden” bewertet wird. Die Einschreibung kann für bis zu zwei Jahre widerrufen werden, wenn Studierende zweimal oder häufiger bei Prüfungsleistungen täuschen (§ 69 Abs. 4 und 5 HochSchG).

Julian Heuer
Mainz, November 2024 Prüfungsdatum 16.12.2024

Acknowledgment

This thesis would have never been possible without the elaborate help and effort of many people, to whom I am extremely grateful. First and foremost, I sincerely thank Prof. Dr. Katharina Landfester for her extensive support, invaluable knowledge, and general supervision over the course of my PhD. Thanks to her guidance and continuous efforts, this PhD thesis reached the quality and state it is in now.

Furthermore, my deepest appreciation goes to my co-supervisor Dr. Calum Ferguson. Your scientific support literally guided me through my PhD and had a great influence on shaping me as the scientist I am today. You have always been not only a mentor but also a good friend to me. Especially your optimistic, protective, and diplomatic supervision has made you an outstanding supervisor.

Another great and irreplaceable help was the support of the technical staff and the members of the expert committee. All the conducted experiments and intense thematic discussions you have done for/with me are of unparalleled importance to me and taught me more than many lectures I have attended before. I thank Dr. Robert Graf and Dr. Manfred Wagner for the experimental support of my NMR measurements. Further, I thank Christine Rosenauer, Sandra Seywald, Beate Müller, and Ute Heinz for the DLS, GPC and HPLC measurements. I am especially thankful to Gunnar Glaßer, Katrin Kirchhoff, and Christoph Sieber for the many conducted TEM and SEM experiments. I thank Walther Scholdei for his FTIR experience and Stefan Schuhmacher for his strong Blender support. And last but not least Angelika Manhart for her extensive synthetic support.

To me, the people I got to know here are of special importance. I have met many people, that I don't want to miss in my life anymore. You have made my stay here in Mainz worthwhile and I can honestly say, despite tough times, you made it the best time of my life. I seriously hope we can stay in contact. Especially Seunghyeon, Anton, Sharafu, and Thomas, without whom I would not have finished this thesis (or even a single project). But also everyone else, with whom I could have fun with and enjoy life: Rong, Yazhou, Shuai, Wenxin, Shoupeng, Yenal, Tsvetomir, Maria, and Francesca. Thank you all so much for your support and the great time spent.

And certainly, my most profound gratitude goes to my parents. The freedom and support you gave me continuously, without a single exception, enabled me to get to this point. My life would have been a different one and I could not have had all the great experiences I was allowed to. I will be forever grateful for that. Thank you. This thesis is equally your contribution and mine.

Abstract

Over the last decades, photocatalysis has established itself as an irreplaceable tool in the field of synthetic chemistry. The utilization of abundant solar energy for the synthesis of valuable compounds represents a promising approach to meet the increasing sustainability demands of the 21st century. However, despite its impressive evolution, photocatalysis remains in its infancy for industrial scales and complex synthesis. The main reasons for this are the long required reaction times and the poor stereoselective reaction control, respectively. To address these challenges, this thesis presents novel concepts and insights into the codependency of substrates and the photocatalytic microenvironment. The inspiration for this was drawn from nature's unparalleled catalysts, enzymes, which exploit macromolecular interactions for the implementation of orthogonal selectivity and the establishment of adjusted microenvironments to the targeted substrate.

As a first principle, macromolecular hydrophilicity-hydrophobicity gradients, typically employed in natural enzymes, were implemented into a heterogeneous polymeric photocatalyst. Amphiphilic polymer chains were synthesized and covalently functionalized with a diphenyl benzothiadiazole-based photocatalyst, yielding photocatalytic nanoparticles. To compare the effect of the local microenvironment around the photocatalytic center on the photocatalytic activity, two stoichiometrically identical systems were synthesized. Therefore, only the spatial location of the photocatalytic species was altered, incorporating the photocatalyst exclusively either into the hydrophilic domain or into the hydrophobic domain of the polymer chain. Localization-dependent effects on the conversion of different photocatalytic reactions were then evaluated, showing a significant dependency between accessibility of photocatalytically active site and substrate hydrophilicity. More hydrophilic substrates were converted faster with the hydrophilic located photocatalyst, while more hydrophobic substrates were converted faster with the hydrophobic located photocatalyst.

Next, the exploitation of non-covalent interactions between the substrate and the photocatalytically active site for photocatalytic rate acceleration was investigated. For natural enzymes, a defined binding environment in the enzymatic pocket yields the exceptional reaction selectivity. A major coordination site in these enzymatic pockets is the arginine end group, the guanidyl group, which is a strong binding group for carboxylate or phosphonate moieties. Therefore, the strongly coordinative guanidyl group was functionalized onto a photocatalytic conjugated microporous polymer (CMP). To investigate the effect of defined substrate coordination towards the photocatalytically active surface, identical guanidyl-functionalized and non-functionalized CMPs were investigated towards the photocatalytic reactivity in a set of reactions. Defined hydrogen-bonding and electrostatic interactions of a carboxylate substrate, a phosphonate substrate and a metal-oxo substrate towards the guanidyl groups close to the photocatalytic active sites showed strongly accelerated reaction rates for the guanidylated CMP.

Lastly, a possible application of a benzothiadiazole-based photocatalyst as heterogeneous, artificial organelles was analyzed. Two different approaches were evaluated, implementing a catalytic functionality into peptide-coacervates. Targeted sequestration of hydrophobic catalysts or dyes into the liquid-liquid-phase separated coacervate droplets was achieved, explained by the formation of hydrophobic microenvironments within the aqueous solution. Catalyst-loaded dipeptide coacervates were successfully employed as artificial organelles in artificial cell-like systems and natural HeLa cells. Further, single amino-acid-based compounds which were covalently linked to a photocatalytic species, were developed as stable coacervates with intrinsic photocatalytic function, allowing for precise control of the photocatalyst colocalization. The phenylalanine-photocatalyst coacervates demonstrated promising photocatalytic reactivity, outperforming the small-molecule photocatalyst in a homogeneous solution in a photocatalytic sulfide oxidation.

In conclusion, this thesis provides valuable insights into innovative selectivity concepts, aiming to enhance the reaction rates of heterogeneous photocatalysts. Furthermore, often overlooked substrate dependencies and interactions with the photocatalytic system were evaluated.

Zusammenfassung

In den letzten Jahrzehnten hat sich die Photokatalyse als ein unverzichtbares Werkzeug im Bereich der synthetischen Chemie etabliert. Die Nutzung des reichlich vorhandenen Sonnenlichts zur Synthese wertvoller Verbindungen stellt einen geeigneten Ansatz dar, um den steigenden Nachhaltigkeitsanforderungen des 21. Jahrhunderts gerecht zu werden. Trotz ihrer beeindruckenden Entwicklung steht die Photokatalyse jedoch noch am Anfang, wenn es um industrielle Maßstäbe und komplexe Synthesen geht. Die Hauptgründe hierfür sind die langen erforderlichen Reaktionszeiten und die unzureichende Kontrolle von stereoselektiven Reaktionen. Um diese Herausforderungen zu bewältigen, präsentiert diese Dissertation neuartige Konzepte und Einsichten in die wechselseitige Abhängigkeit von Substraten und der photokatalytischen Mikroumgebung. Dabei wurde Inspiration aus den unvergleichlichen Katalysatoren der Natur, den Enzymen, gezogen, die makromolekulare Eigenschaften nutzen, um orthogonale Selektivitätsprinzipien umzusetzen und angepasste Mikroumgebungen für das Zielsubstrat zu schaffen.

Als erstes Prinzip wurden hydrophile-hydrophobe Gradienten in Makromolekülen, die typischerweise in natürlichen Enzymen verwendet werden, in einen heterogenen polymeren Photokatalysator integriert. Amphiphile Polymerketten wurden synthetisiert und kovalent mit einem Diphenyl-Benzothiadiazol-basierten Photokatalysator funktionalisiert, wodurch photokatalytische Nanopartikel entstanden. Um den Effekt der lokalen Mikroumgebung um den Photokatalysator auf die photokatalytische Aktivität zu vergleichen, wurden zwei stöchiometrisch identische Systeme synthetisiert. Dabei wurde nur die Platzierung der photokatalytischen Spezies verändert, indem der Photokatalysator ausschließlich entweder in die hydrophile oder in die hydrophobe Domäne der Polymerkette eingebaut wurde. Die von der Lokalisierung abhängigen Effekte auf die Umwandlung verschiedener photokatalytischer Reaktionen wurden dann bewertet, wobei eine signifikante Abhängigkeit zwischen der Zugänglichkeit der photokatalytisch aktiven Spezies und der Hydrophilie des Substrats gezeigt wurde. Hydrophilere Substrate wurden schneller mit dem hydrophil lokalisierten Photokatalysator umgesetzt, während hydrophobere Substrate schneller mit dem hydrophob lokalisierten Photokatalysator umgesetzt wurden.

Anschließend wurde die Nutzung von nicht-kovalenten Wechselwirkungen zwischen den Substraten und den photokatalytisch aktiven Stellen zur Beschleunigung photokatalytischer Reaktionen untersucht. Bei natürlichen Enzymen führt eine definierte Bindungsumgebung in der enzymatischen Tasche zu einer außergewöhnlichen Reaktionsselektivität. Eine wesentliche Koordinationsspezies in diesen enzymatischen Taschen ist die Arginin-Endgruppe, die Guanidyl-Gruppe, die eine starke Bindungsgruppe für Carboxylat- oder Phosphonat-Gruppen darstellt. Daher wurde die stark koordinative Guanidyl-Gruppe auf ein photokatalytisches konjugiertes mikroporöses Polymer (CMP) funktionalisiert. Um den Effekt der definierten Substratkoordination an der photokatalytisch aktiven

Oberfläche zu untersuchen, wurden identische Guanidyl-funktionalisierte und nicht-funktionalisierte CMPs in einer Reihe von Reaktionen auf ihre photokatalytische Reaktivität untersucht. Definierte Substrat-Wasserstoffbrückenbindungen und elektrostatische Wechselwirkungen eines Carboxylat-Substrats, eines Phosphonat-Substrats und eines Metall-Oxo-Substrats mit den Guanidyl-Gruppen nahe den photokatalytisch aktiven Stellen zeigten stark beschleunigte Reaktionsraten für das guanidylierte CMP.

Abschließend wurde eine mögliche Anwendung eines Benzothiadiazol-basierten Photokatalysators als heterogene, künstliche Organellen analysiert. Zwei verschiedene Ansätze wurden evaluiert, die die Kombination von Peptid-Koazervaten mit katalytischer Funktionalität umfassen. Eine gezielte Akkumulation hydrophober Katalysatoren oder Farbstoffe in die flüssig-flüssig-phasengetrennten Koazervattropfen wurde erreicht, was mit der Bildung hydrophober Mikroumgebungen innerhalb der wässrigen Lösung erklärt wird. Mit Katalysator beladene Dipeptid-Koazervate wurden erfolgreich als künstliche Organellen in künstlichen Zell-ähnlichen Systemen und natürlichen HeLa-Zellen eingesetzt. Weiterhin wurden Mono-Aminosäure-basierte Verbindungen, die kovalent an eine photokatalytische Spezies gebunden sind, als stabile Koazervate mit intrinsischer photokatalytischer Funktion entwickelt, woduch eine präzise Kontrolle der Katalysator-Kolokalisation ermöglicht wurde. Die Phenylalanin-Photokatalysator-Koazervate zeigten vielversprechende photokatalytische Reaktivität und übertrafen den unfunktionalisierten Photokatalysator in homogener Lösung bei einer photokatalytischen Sulfid-Oxidation.

Zusammenfassend liefert diese Dissertation wertvolle Einblicke in innovative Selektivitätskonzepte, die darauf abzielen, die Reaktionsraten heterogener Photokatalysatoren zu erhöhen. Darüber hinaus wurden oft übersehene Substratabhängigkeiten und Wechselwirkungen mit dem photokatalytischen System evaluiert.

Table of Contents

Chapter 1

Theoretical Background

1.1 The Principle of Catalysis

Catalysis has played a central role in shaping modern society, driving the evolution of countless chemical processes from the fermentation of alcohol and cheese in ancient times to the sophisticated synthetic pathways in today's industries. While natural catalysts have been used for millennia, it wasn't until the 19th century that the scientific community began to unravel the principles underlying catalysis.[1] Wilhelm Ostwald's pioneering work defined a catalyst as a substance, that increases the rate of a chemical reaction without itself being consumed and without changing the final thermodynamic equilibrium of this reaction.[2]

Together with the understanding of the catalytic principle, the development of the first synthetic catalysts was demonstrated, resulting in important breakthroughs for the industrial production of hydrocarbon fuels, fertilizers, and much more. From then on, the field of catalyst development has undergone a series of transformative advancements. These advances made catalysis indispensable to modern society, integral to approximately 85% of all industrial chemical processes.[3]

Nowadays, the field of catalysis can be divided into homogenous and heterogenous catalysis, organic and inorganic catalysis, or even into thermal and photocatalysis. Distinguished catalyst systems were desired, to solve targeted problems in process scalability, feasibility and sustainability. However, ongoing challenges remain, including the need for even greater catalyst efficiency, selectivity, and sustainability in the face of increasing global demand and environmental concerns.

Figure 1.1 illustrates the kinetic reaction profile of an exothermic reaction involving starting materials X and Y, and resulting in product Z. The black reaction curve depicts the reaction without a catalyst, while the red curve represents the catalyzed reaction pathway. Notably, there is no alteration in the energy levels of the starting materials or the product between the two pathways, indicating that the catalyst does not influence the thermodynamics of the reaction. Both pathways exhibit an exothermic behavior; however, they differ significantly in reaction progression. To achieve the desired product

Z, a certain activation energy E_a is required to surmount the energy barrier. The peak of the energy curve represents the formation of favorable transition states or intermediates, leading to energy release and the formation of the final product Z. The energy gain from the starting materials to the product is referred to as ΔG. In the presence of a catalyst, multiple intermediates/transition states are formed depending on the catalytic mechanism. Overall, the required activation energy E_a is reduced, facilitating a more favorable reaction progression and accelerating the kinetic reaction rate.

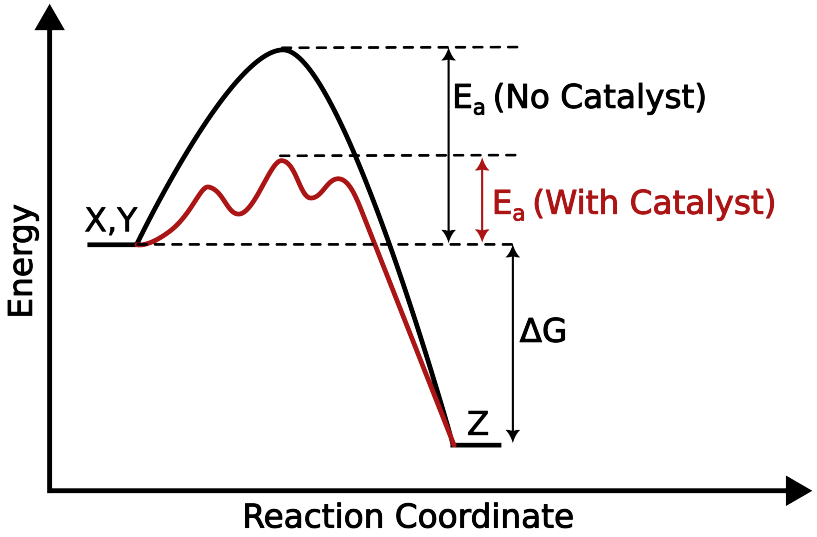

Figure 1.1: Energy diagram, illustrating the effect of a catalyst on the reaction progression. The starting materials X, Y undergo an exothermic reaction to yield product Z. The catalyst lowers the activation energy through the formation of transition states, thereby accelerating the reaction rate.

1.2 Photocatalysis

1.2.1 The Evolution of Photocatalysis

Shortly after the initial successes of catalytic processes in the early 20th century, such as the osmium-catalyzed NH_3 synthesis or vanadium pentoxide-catalyzed H_2SO_4, the concept of "photocatalysis" emerged. Inspired by nature's photosynthesis, scientists worldwide endeavored to harness and store energy from sunlight. A first approach was presented by Eibner, using ZnO to form reactive species after irradiation, bleaching the dye pigment Prussian blue.[4] However, photocatalysis faced serious challenges in its practical application and remained therefore in its infancy for several decades. It was not until the 1970s that photocatalytic processes began to be investigated as effective solutions to address environmental challenges. With the groundbreaking work of Fujishima and Honda, the powerful potential of photocatalysis was demonstrated: The efficient photo-assisted H_2O splitting into O_2 and H_2,[5] as well as the photoreduction of CO_2 into formic acid, formaldehyde, methanol and methane,[6] driven by irradiation of TiO_2 marked a significant milestone in the history of photocatalysis.

Extensive efforts have been dedicated to understand the fundamental principles of photocatalysis, facilitating the development of increasingly sophisticated systems. In consideration of the spectrum of sunlight, which can be divided into 3% highly energetic ultraviolet (UV, 100-380 nm), 44% visible (VIS, 380-780 nm), and 53% low energetic infrared radiation (IR, 780-1000 nm), particular attention has been given to the development of visible-light active photocatalysts. UV-light, with energies ranging from 3.3-12.4 eV (380-100 nm), is capable of the homolytic and heterolytic cleavage of virtually every chemical bond. Therefore, utilizing visible light results in significantly more controlled reactions, inhibiting potential side reactions and the formation of undesired radical species. A well-established system, developed in the 1980s, is the initiation of photochemical processes by conversion of solar energy using polypyridine ruthenium complexes. Irradiation of these complexes with visible light generates a photoexcited state, which has been exploited for the selective photoreduction of H_2O or CO_2.[7] Furthermore, harnessing visible light for photocatalysis significantly reduces the required energy input, showcasing its advantage over energy-intensive UV light.

In the 21st century, sustainability and environmental remediation moved into the focus of the scientific community. Motivated by concerns regarding resource scarcity and environmental pollution, a shift in photocatalysis from transition metal complexes to organic photocatalysts was initiated. Additionally, organic photocatalysts offer access to unique chemistries that are unreactive in most synthetic contexts. Particularly the structural tunability serves as a powerful base for tailor-made organophotocatalysts. Through powerful oxidation or reduction states, organic dyes e.g. methylene blue, eosin Y, acridinium, and pyrylium salts, form the core of modern organophotocatalysis. Combined with the ability to absorb light of the visible spectrum, these dyes offer mild conditions in a wide range of reactions.[8, 9]

Over time, photocatalysis has evolved into a cornerstone of synthetic chemistry, facilitating the efficient production of fine chemicals, pharmaceuticals, and natural products. However, achieving broad industrial applications for large-scale organic transformations or fuel generation remains a major challenge of the 21st century. Presently, photocatalysts complement traditional thermal catalysis rather than replacing it.[10] The significant capital costs associated with constructing complex industrial photoreactors, along with high energy costs and challenges in upscaling, limit the applicability of photocatalysts.[11] But with the rapid development of innovative photocatalytic systems, combined with a growing emphasis on economic feasibility and sustainability, the transition of photocatalysis into the industrial landscape seems inevitable.[12] As Giacomo Ciamician predicted in 1912, if chemists can successfully scale up and control the process of solar energy conversion, "life and civilization will continue as long as the sun shines".[13]

1.2.2 Photocatalysis - A Mechanistic Outline

Photocatalysis harnesses the generation of electron-hole pairs upon light absorption, to drive chemical reactions.[14] A key component in this process is the photon-absorbing

molecule, known as the photocatalyst, which facilitates the formation of excited states necessary for the subsequent chemical transformations. These photocatalysts share similar characteristics with catalysts, as they only influence the reaction kinetics while staying unconsumed over the reaction period. Photocatalysts can be divided into two classes: homogeneous and heterogeneous photocatalysts. However, this thesis will cover only heterogeneous photocatalysts. The photocatalysis of chemical reactions harnesses two major mechanisms: electron transfer (ET) and energy transfer (EnT) photocatalysis.[15] For ET photocatalysis, the excited state photocatalyst is exploited to drive reductive or oxidative processes, building the foundation for photoredox catalysis. Figure 1.2 illustrates the fundamentals of ET photoredox catalysis. After photoexcitation, and the formation of the excited state photocatalyst (PC*), either a reductive quenching cycle or an oxidative quenching cycle proceeds. During reductive quenching, an electron-donor substrate (S_D) encounters the PC*, forming a donor-acceptor complex ($[S_D \cdots PC^*]$) due to polarization effects. This transition state then propagates to the successor complex $[S_D^{\bullet+} \cdots PC^{\bullet-}]$ after a successful electron transfer from the donor to the acceptor species.

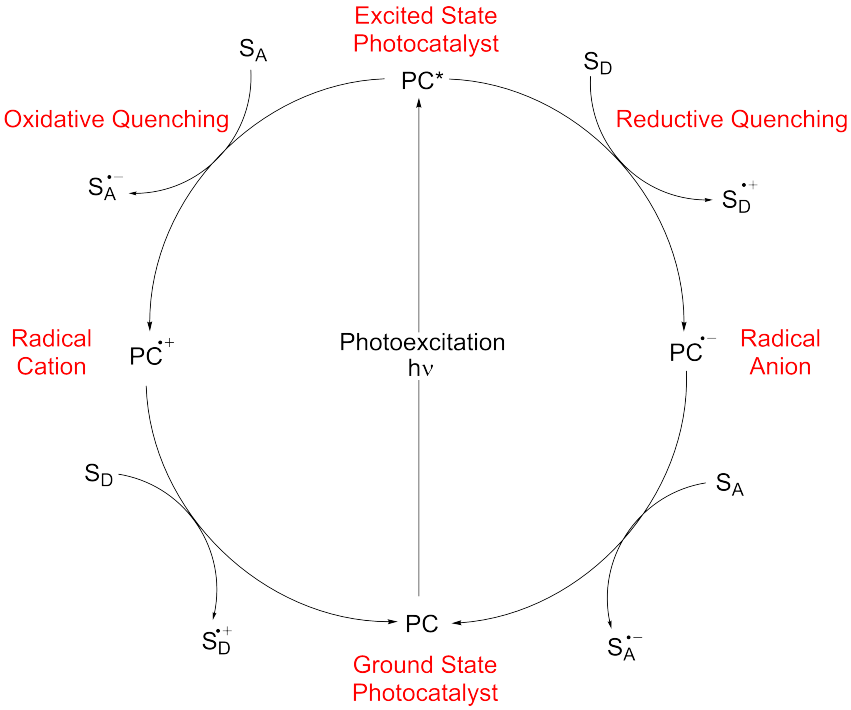

Figure 1.2: Schematic illustration of the possible photoredox pathways in a photocatalytic cycle.

After the ET, the encounter complex separates fast. As the participating species are not bridged, the reaction follows an outer-sphere electron transfer. The electron transfer rate depends strongly on the diffusion-controlled encounter complex formation, as electron transfers proceed significantly fast (actual ET rates depend strongly on the monitored species). The diffusion often represents the rate-limiting step, as each encounter complex typically leads to an efficient electron transfer, in accordance with the Rehm-Weller mechanism.[16] The probability of electron transfer is explained by the basic equation of Marcus theory:

$$k_{et} = \frac{2\pi}{\hbar}|H_{AB}|^2 \frac{1}{\sqrt{4\pi\lambda k_B T}} exp\left(-\frac{(\lambda + \Delta G^\circ)^2}{4\lambda k_B T}\right) \tag{1.1}$$

and depends strongly on the electronic coupling strength H_{AB}, the reorganization energy λ and the total Gibbs free energy ΔG°.[17] Using this equation, the electron transfer rate constant k_{et} can be calculated. As Marcus theory is built upon the traditional Arrhenius equation, the basic Marcus equation provides the necessary activation energy for an ET. Figure 1.3 illustrates the principles of Marcus theory. An exergonic process, characterized by a decrease in Gibbs free energy from the electron donor to the acceptor drives the electron transfer (ET) thermodynamically. This decrease in Gibbs free energy provides the necessary energetic favorability for the electron transfer to occur spontaneously. For an electron transfer to occur, according to Marcus theory, the system must absorb enough energy to overcome the desired reorganization energy (λ). This energy corresponds to the work needed to shift the system from the initial thermodynamically stable position of the donor (d_D) to the point where the donor and acceptor states' free energy curves intersect (d_c). The reorganization energy includes the energy required to bring the donor and acceptor to their transition state configurations and align their nuclear and electronic coordinates.[17]

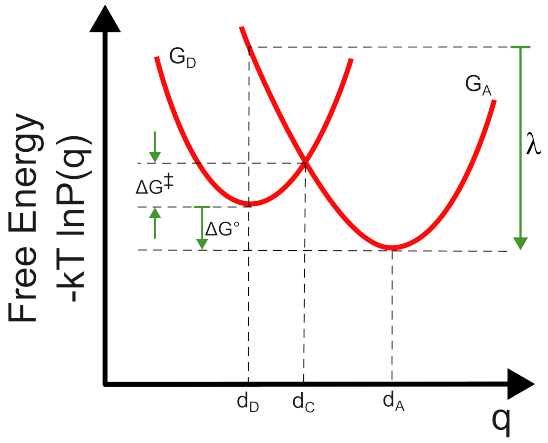

Figure 1.3: Illustration for the electron transfer based on the Marcus theory. The Gibbs free energy and coupling strength dependency are visualized.

As previously discussed, the h^+ is associated with the HOMO, which means for organic semiconductors the h^+ is mostly located in the valence band. For the case of the reductive quenching cycle, the transferred electron fills the previosuly generated h^+, forming the radical anion $PC^{\bullet -}$ and the corresponding substrate cation $S_D^{\bullet +}$. Afterwards, the corresponding $S_D^{\bullet +}$ reacts further to the desired product or induces a reaction cascade (Figure 1.2). The $PC^{\bullet -}$ closes the photocatalytic cycle by transferring the electron to the acceptor substrate S_A, forming another activated species $S_A^{\bullet -}$. The ET from the photocatalyst to the substrate S_A can occur from the singlet excited state or the triplet excited state. However,

due to symmetry reasons, the electron transfer from the singlet excited state is the predominant process for organic semiconductors.[18] Finally reaching the ground state of the photocatalyst PC, the cycle for a photoinduced electron transfer can be reiterated.

In addition to the previously discussed single electron transfer mechanism, two other electron transfer processes will be outlined, namely proton-coupled electron transfer (PCET) and hydrogen atom transfer (HAT). Both PCET and HAT are stoichiometrically similar, as they involve the simultaneous transfer of an electron and a H^+.[19, 20] However, both processes are distinct from each other. In PCET, the H^+ and the electron start from different orbitals and are transferred concertedly to different atomic orbitals (Figure 1.4a). In contrast, in the HAT process the electron and the H^+ start in the same orbital and move together to the final orbital.[21] Therefore, this process is considered a free radical reaction, commonly found in e.g. cytochrome P450 or hydrocarbon combustion (Figure 1.4b).[21, 22] For PCET/HAT to proceed, the activation energy of an ET or proton transfer has to be higher, than the concerted mechanism of PCET/HAT. These processes can be investigated via the kinetic isotope effect (tracking of deuterium).

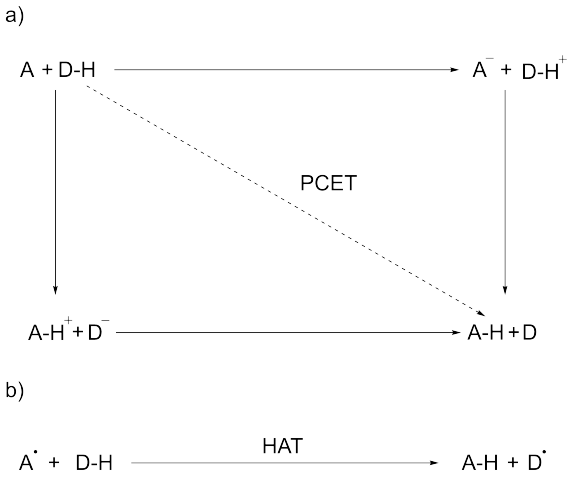

Figure 1.4: Illustration for the differentiation between PCET, HAT and ET.

For applied photocatalysis, the excited and ground states of the molecules are often referred to as the HOMOs and LUMOs (as discussed previously) and their redox potential is referenced against electrochemical reference electrodes. The employed reference electrode strongly influences the obtained potential of the obtained redox potentials.[23] In the literature, a variety of reference electrodes are established. The most commonly used electrodes are "normal hydrogen electrode" (NHE), "standard calomel electrode" (SCE) or "silver chloride electrode" (AgCl). In this thesis, all reported redox potentials of photocatalysts and substrates will be referenced against the SCE. To predict the reactivity of substrates and the photocatalyst, the redox potentials of all reaction partners have to be considered. To ensure the thermodynamic feasibility of a reduction reaction, the LUMO level of the photocatalyst, which is often expressed as a negative value versus the Saturated Calomel Electrode (SCE), must be more negative than the LUMO level of the substrate. If the opposite case would be present, the reaction would be thermodynamically unfavorable. For oxidative processes (electron transfer from the substrate S_D to the PC), the

HOMO values have to be considered. For a successful oxidation reaction, the HOMO level of the substrate, typically represented as a positive value versus SCE, must be less positive than the HOMO level of the photocatalyst. Only under these circumstances, the reaction is thermodynamically feasible and reasonable catalytic turnover numbers (TON) can be achieved. The TON indicates the amount of generated product per catalyst molecule. To illustrate the relevance of redox potentials for the reaction design, Figures 1.5 and 1.6 visualize the redox potentials of selected photocatalysts and substrates.[24,–26] The outlined principles for the photocatalytic reductive quenching cycle also apply to the photocatalytic oxidative quenching cycle (Figure 1.2).

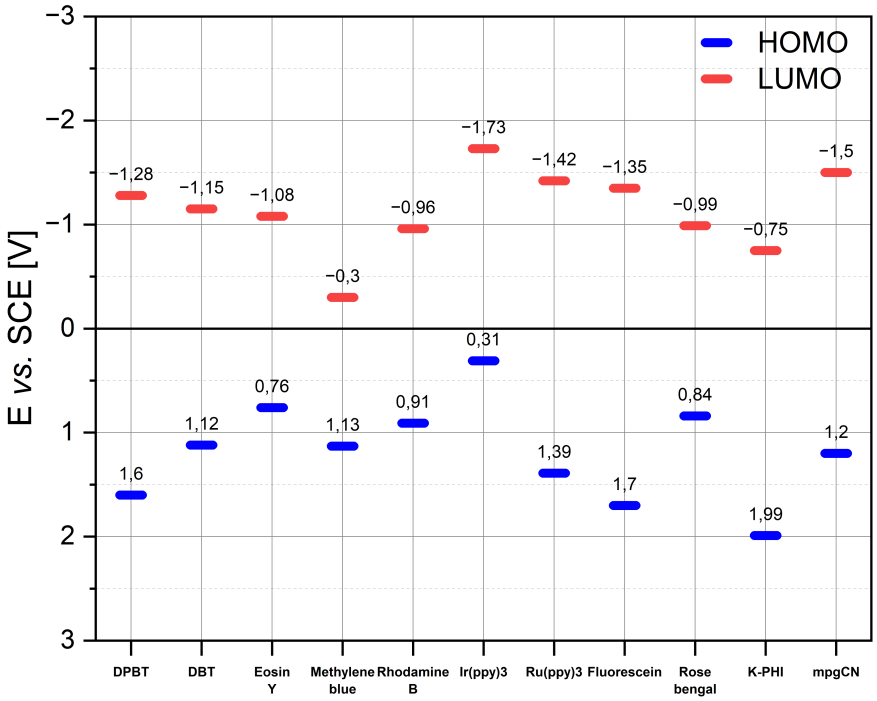

Figure 1.5: HOMO and LUMO values of selected, relevant organophotocatalysts. Values obtained from CV measurements (DPBT, DBT, mpgCN) and literature (others).[24,–26]

As mentioned earlier within this section, besides photoredox catalysis (ET-based), the other important photocatalytic reaction pathway is the energy transfer photocatalysis (EnT). Mechanistically, EnT differs greatly from ET photocatalysis, as no single electron transfer occurs. EnT can thereby be divided into two main mechanisms: Förster (dipole-dipole interactions and Coulombic interactions) and Dexter energy transfer (exchange or collisional interactions).[15] The Förster-type energy transfer describes the radiationless transfer of energy from the donor molecule to the acceptor molecule via electrical dipole-dipole interactions.[27] The excited state donor exhibits higher oscillator strength, which correlates with an increased transition dipole moment. When the donor and acceptor molecules are within a spatial proximity of 0.5-10 nm (the Förster radius), the excited state dipole of the donor (D*) can induce a dipole change in the acceptor molecule (A) through resonance energy transfer, leading to the deactivation of the donor (D) and excitation of the acceptor (A*). A key characteristic of Förster Energy Transfer (EnT) is the

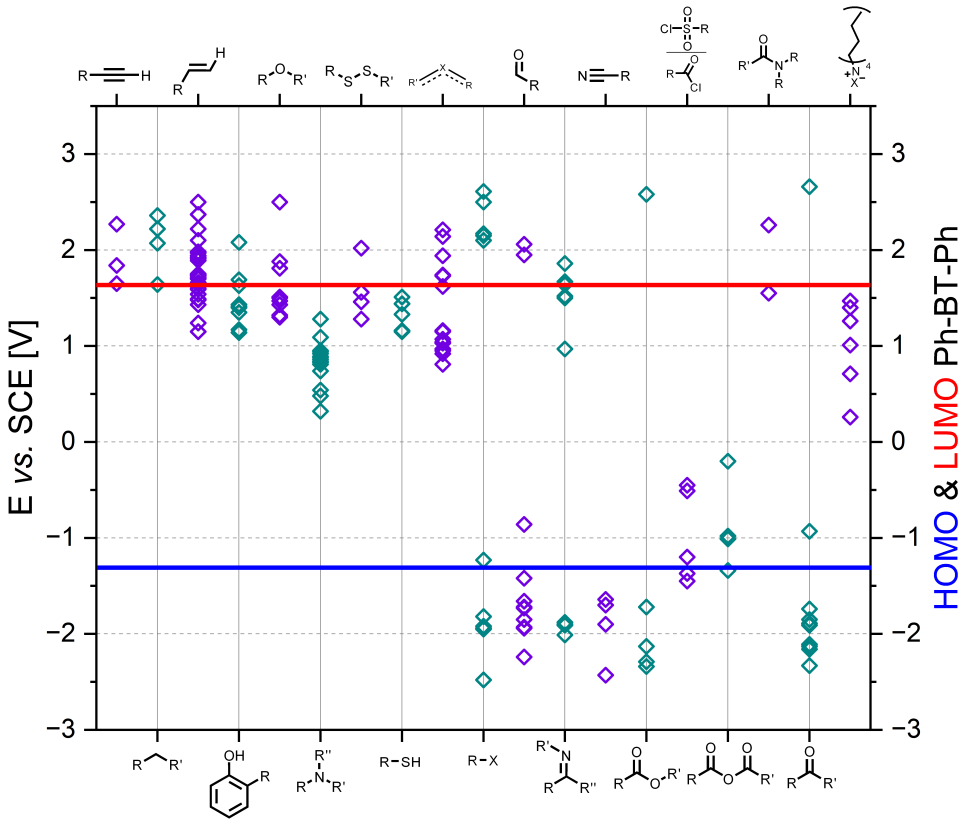

Figure 1.6: HOMO and LUMO values of selected functional groups. Values obtained from the literature.[24,–26]

conservation of total spin, which typically results in energy transfer occurring from the singlet excited state of the donor molecule to the singlet state of the acceptor molecule, known as singlet-singlet transfer.[28] Förster EnT from the triplet excited state may occur, but is less frequent due to ISC rates.[29] To predict the efficiency of Förster-type EnT, the absorption and emission spectra of the donor and acceptor molecule must be considered. If the emission spectrum of the donor species shows a strong overlap with the absorption spectrum of the acceptor species, a Förster-type resonance-based energy transfer has enhanced probability.[30] However, in the context of photocatalysis Dexter energy transfer (Dexter EnT) is predominantly relevant. Dexter EnT describes energy transfer as the simultaneous exchange of an electron from the excited state D* to the excited state of the acceptor molecule A and the transfer of an electron from the ground state A to the ground state of D, filling the photogenerated h^+ in D* or vice versa. This transfer can be considered as double electron transfer, which can be described via Marcus theory. Dexter EnT occurs mostly via a triplet-triplet energy transfer mechanism. So the triplet excited state donor molecule transfers the energy to the triplet excited state of the acceptor molecule. The Dexter EnT rate is strongly dependent on the orbital overlap (J) and the formation of a solvent-shared encounter complex $[D* \cdots A]$. As the spectral orbital overlap J represents one of the most decisive parameters for a high Dexter EnT rate, the spatial proximity of the D and A species has to be very close to ensure a sufficient orbital overlap

of the D and A (<0.5 nm). With increasing distance, the energy transfer rate decreases exponentially.[15] Therefore, the formation of the encounter complex represents the rate-limiting step, making this process a diffusion-mediated process.[31] To achieve high Dexter EnT rates, the photocatalyst needs to exhibit high ISC rates and a higher triplet state energy than the acceptor moiety (thermodynamic feasibility $\Delta E_{EnT}<0$).[32]

Among the discussed mechanisms, maintaining constant temperature and consistent photon exposure is crucial for achieving optimal photocatalytic performance, necessitating the use of standardized photoreactors. Increased temperatures can result in destabilization of the photogenerated excited states due to accelerated Brownian motion and vibrational decay. Additionally, raised temperatures increase the formation of side products or facilitate reactions, wherefore reaction control is decreased. Furthermore, the photon can be considered a traceless reagent within the reaction system.[33] For reaction design it is therefore essential to control the parameters of photon flux and wavelength/energy. The amount of photons (in mol) added into a system should be referenced to the amount of photoactive species (in mol) to ensure unrestricted photoexcitation. The energy of a photon can be calculated by equation:

$$E_P = hf = \frac{hc}{\lambda} \tag{1.2}$$

and is dependent on the wavelength λ. As discussed previously, the photon needs to exhibit the right amount of energy to induce the photoexcitation process. After choosing a suitable light source (by wavelength) for the desired photocatalyst system, the photon flux can be calculated by equation:

$$N_P = \frac{I}{E_P} = \frac{I \times \lambda \times 10^{-9}}{hc} [m^2 s] \tag{1.3}$$

yielding the number of photons per second and surface unit. Subsequent conversion of N_P with Avogadros constant N_A into a unit of molarity yields the final photon flux as $\mu E/m^2 s$ or W/m^2:

$$E_{QF} = \frac{N_P}{N_A \times 10^{-6}} [\mu mol/m^2 s = \mu E/m^2 s] \tag{1.4}$$

To ensure unrestricted photochemical processes, the number of photons should always exceed the quantity of photoactive species present.

1.3 Heterogeneous Organophotocatalysts

The following review of state-of-the-art heterogeneous organophotcatalysts is based on the article "Photocatalytic polymer nanomaterials for the production of high value compounds", published in *Nanoscale*, 2022, 14, 1646-1652.[191] The article was authored by me and Calum Ferguson. Paragraphs, sections and sentences that have been adopted from this article are indicated by quotation marks ("").

Organometallic photocatalytic complexes, primarily derived from iridium or ruthenium, have found widespread application within synthetic chemistry.[34, 35] Recently, a shift towards exclusively organic compounds has been observed, due to economic advantages over expensive transition-metal-based materials.[36] Furthermore, to enhance the recyclability of photocatalytic materials there has been a transition towards heterogeneous photocatalysts. These are often bulk materials that can be easily recycled through centrifugation, cleaned, and reused. Typically, conjugated donor-acceptor polymers are used as photocatalytic materials, due to their tunable optoelectronic and physical properties.[37, 38] Early approaches to creating bulk organic heterogeneous photocatalysts primarily focused on linear conjugated polymers. The first presented linear organic semiconductor for a hydrogen evolution reaction (HER) was a polyphenylene compound.[39] The implementation of a donor-acceptor structure, using dibenzo[b,d]thiophene, into the polyphenylene backbone resulted in a 7-fold increase of the HER rate.[40] After the initial success, a variety of D-A-conjugated linear polymer photocatalysts were developed. Popular examples include dioctylfluorene-co-benzothiadiazole[41] or indacenodithiophene-co-benzothiadiazole[42] based materials. Following their impressive demonstration of photocatalytic efficiency in HER (hydrogen evolution reaction), the development of heterogeneous photocatalysts progressed to include applications in organic transformations.[43] Specifically, mesoporous polymeric graphitic carbon nitride (mpg-CN) has proven to be a reliable photocatalyst with significant potential. The controlled framework design of mpg-CN pioneered an early approach, yielding nanostructured heterogeneous organophotocatalysts. Due to its ease of synthesis and the tunability of the optical band gap, mpg-CN demonstrated its versatility in a diverse range of reactions, such as decarboxylation, halogenation, or C-O reactions.[44, 45] These systems paved the way for the development of other microporous/mesoporous organic polymer photocatalysts, enhancing the total photoactive surface.

Throughout this section, promising, recently emerged heterogeneous, polymer photocatalyst systems will be described in more detail. "Photocatalytic systems use visible light to enable a broad range of chemical reactions to proceed including water splitting,[41, 46,–48] CO_2 reduction,[49,–52] C-C coupling reactions,[53, 54] C=C bond cleavage,[55, 56] pericyclic reactions,[57, 58] metal reduction,[59, 60] enzyme co-factor activation,[61, 62] trifluoromethylation of arenes,[63] oxidation of sulfides,[64, 65] dehalogenation of haloketones,[66] heterocycle formation[67] and enantioselective alpha-alkylation.[68] These reactions proceed through the formation of photogenerated radical species within the photocatalytic material. The lifetime of these active species varies depending on the photocatalytic materials and reaction

conditions. However, the highest concentration of these active agents is typically localized at the photocatalytically active sites. Therefore, efficient photocatalytic conversions require reagents to be in close proximity to the photocatalytic material."

"Multiple strategies have been implemented to maximize reagent and photocatalytic proximity, most notably by increasing the surface area of photocatalytic materials. The emergence of porous organic polymers (POP)[69] and the subsequent utilization of this material class for photocatalysis has yielded high surface area photocatalysts. Conjugated mesoporous polymers (CMPs)[38] and subsequently covalent triazine frameworks (CTF)[70] have been widely reported for visible light-mediated photocatalysis." These systems consist of large conjugated networks with defined nanostructures, maximizing surface area and facilitating diffusion into the network. "However, due to their size often ranging from hundreds of micrometers to millimeters, mass transport across the entire photocatalytic material can be challenging."

"Nanomaterials have been used to maximize the surface area of photocatalytic materials. Further enhancement of total surface area has also been achieved by the utilization of porous structures. Initially, bulk porous photocatalysts were produced, comprised of a highly cross-linked aromatic 3D network.[37, 38] These porous polymeric nanomaterials offer several advantages over their bulk analogues including higher surface-to-volume ratio, easy synthesis, high tunability of the donor-acceptor structure, recyclability, and increased turnover rate for catalytic reactions.[37, 70, 72, 73]"

"A prominent class of porous nanomaterials are CMPs. These CMPs comprise a π-conjugated backbone, featuring donor- and acceptor-type monomers.[74] CMPs are synthesized in a one-pot procedure, where the composition of the CMP is controlled by the monomer types and their molar ratios. This flexibility in synthesis has enabled the generation of a wide range of CMPs over the last decade, targeting various applications. CMPs represent well-established materials in the fields of organic synthesis,[55] CO_2[75] reduction, and H_2O splitting.[76]"

"Recently, nano-based CMP systems have been reported to further enhance the photocatalysts' surface area.[77] Moreover, due to the nanosize of these materials, the diffusion length of substrates into photocatalytic material is reduced, creating higher-performing systems. Nano-CMPs are typically formed using a mini-emulsion strategy where the conjugated polymers are formed within droplets that are dispersed in water. This dispersibility in water has enabled the shift to undertaking photocatalytic reactions in water. Ma et al. produced a series of nanomaterials by either Suzuki–Miyaura or Sonogashira–Hagihara cross-coupling polycondensation reactions in an oil-in-water mini-emulsion, followed by solvent evaporation.[78] Spherical, rod, and ring-shaped nanomaterials were produced depending on the monomers selected. Here, nano-CMPs could be used for rapid photocatalytic degradation of rhodamine B, with ring-shaped nano-CMPs being the most efficient. It was recently shown, that the morphology of the CMPs and the polymer composition plays an important role in photocatalytic efficiency.[79]"

"Ma et al. also investigated the use of CMP nanoparticles for the regeneration of the cofactor NAD^+.[80] Using oil-in-water mini-emulsion polymerization, triethynylbenzene, and oxadiazole components were polymerized, resulting in the formation of spherical, microporous CMP nanoparticles with sizes ranging from 50 to 80 nm. These nanoparticles were encapsulated into giant polymer vesicles, creating an effective nanoreactor, which could be used in combination with modified enzymes for photobiocatalysis. Finally, Ma et al. investigated the use of CMP nanoparticles for use in photodynamic therapy (PDT).[71] Here, the aqueous compatibility of the nanomaterials enabled the eradication of bacteria using non-toxic, purely organic systems. Both Escherichia coli K-12 and Bacillus subtilis were inactivated by photogenerated singlet oxygen (Figure 1.7)."

"In addition to CMPs, covalent triazine frameworks (CTFs) are an interesting class of porous polymers. Similarly to CMPs, CTFs are porous networks formed from an aromatic backbone, but here, triazine donor units are used.[81] Typically, cyanide-containing monomers undergo a one-pot trimerization reaction to form triazine groups, allowing for tunability via monomer selection and ratios.[82,–84]"

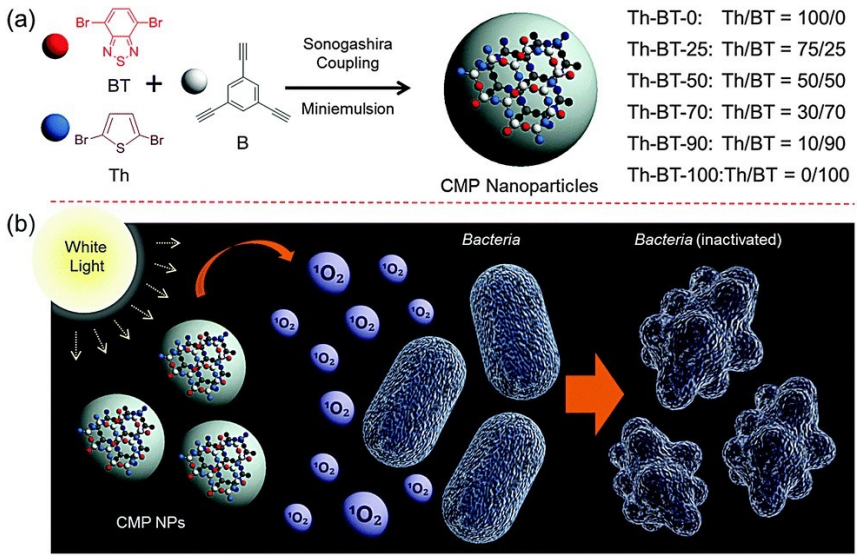

Figure 1.7: (a) Synthesis route for the production of photocatalytic CMP nanoparticles by Sonogashira–Hagihara cross-couplings. (b) Bacterial deactivation by active oxygen. Reproduced with permission from ref[71].

"The production of CTF materials was initially undertaken using conventional liquid-phase approaches in molten $ZnCl_2$[69, 85] or trifluoromethanesulfonic acid (TfOH).[86] Unfortunately, these methods do not produce materials with regular morphologies and defined optical properties. Huang et. al. recently reported a size-controllable confinement synthesis of CTF nanoparticles. Since the synthesis of covalent triazine frameworks (CTFs) typically involves ionothermal procedures under harsh reaction conditions, producing controlled CTF nanoparticles with defined morphologies has been challenging. In a combined sol-gel emulsion, assisted by TfOH vapour, confined silica templates were used to encapsulate a thiophene -derived dinitrile monomer (Figure 1.8). After polymerization of these monomers, the silica template was removed using an etching procedure, giving

CTF-NP with a discrete particle size, confirmed by BET, TEM, and EDX measurements. The incorporation of an additional electron-withdrawing benzothiadiazole group into the polymer induced an increased charge-transfer. This modification altered the energetic levels of the system, enabling control over the morphology of the polymer. Therefore the photogenerated charge separation was boosted, resulting in very high conversion rates and selectivity for a [3+2] cycloaddition. By comparison with the bulk polymer, an 18-fold increase in conversion rate was observed.[70]"

"Lastly, a new type of porous polymer nanoparticles was presented by Ferguson et al.[87] Here, hyper crosslinked porous nanoparticles were synthesized containing a benzothiadiazole based vinyl-monomer, using RAFT-PISA. PEG-based polymeric stabilizing units were used, allowing the polymer particles to be dispersed in different continuous phases. This allows for widespread application since an optimal solvent selection for the photocatalytic reaction can be provided. Ferguson et al. demonstrated that this new porous material could be used in water, acetonitrile, or toluene, while the hydrophobic small molecule photocatalyst shows no solubility in water."

In addition to conjugated porous polymers, cross-linked polymer gel networks containing photoactive species have recently gained significant interest."Both organo and hydrogel-based systems have been implemented for the production of high value compounds. Similarly to porous polymers, polymer gel networks enable enhanced reagent and catalyst contact. Here, photocatalytic gels have been produced to allow easy partitioning of reagents into the gel network, where they can be readily transformed. To date conjugated,[88] polymer/inorganic,[89] polymer/metal,[90] and classical polymer[57] gel networks have been investigated."

"Similar to the previously discussed porous polymeric nanomaterials, photocatalytically modified gels exhibit significant advances over linear, bulk polymers. Besides an enlargement of the photocatalytically available surface, an enhancement of compatible solvents can be achieved. Moreover, the implementation of photocatalysts onto highly crosslinked gels allows for the introduction of new functionality. Bulk gels have shown promising catalytic efficacy. However, most of the catalytic centers are often not available due to spatial hindrances inside the polymer gel. Similarly to CMPs and CTFs, recently nano-based gel systems have been reported to tackle spatial hindrance. Reagents in the nano/microgel systems are required to diffuse much shorter distances compared to bulk systems. As the diffusion of reagents to the catalyst is often the rate-limiting step in photocatalytic systems, significantly reducing the length scales required, vastly increases the photocatalytic performance of these materials."

"Petrizza et al. prepared one of the first examples of photocatalytic polymer microgels.[91] Here, a cross-linked block-copolymer was synthesized by free radical mini-emulsion polymerization of vinyl acetate and vinyl caprolactam (Figure 1.9). Into this hydrogel network, a vinyl benzyl derivative of rose bengal (RB) was copolymerised, resulting in covalently bound, swellable microgel particles. Polymer microgels around 200 nm in size were produced, which under irradiation of light could generate reactive oxygen species.

These microgels were used to synthesize compounds such as 6-hydroxy-(2H)-pyran-3-one and 1,2-dibenzoylbenzene."

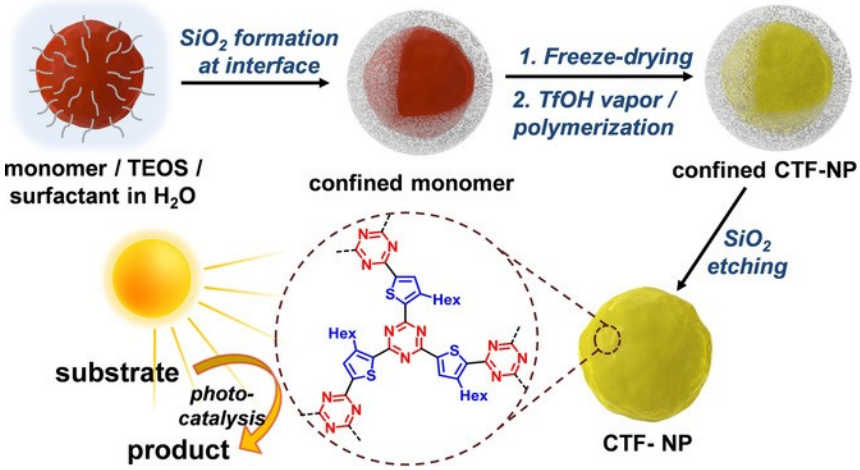

Figure 1.8: Synthesis route for nanoparticle CTFs using a silica shell to confine the monomers and allow polymerisation in TfOH vapour. Reproduced with permission from ref[70].

"Radjagobalou et. al. further expanded the use of photocatalytic microgels, showing their use in flow chemistry.[92] Poly(N-vinylcaprolactam-covinyl acetate-co-vinylbenzyl rose bengal) microgels were used for the photooxygenation of α-terpinene. The microporous structural properties of the photoactive microgels allowed not only for the diffusion of the reagent to the catalytic centers but also for the application into a spiral flow chemistry setup. A similar product conversion to free RB was observed, moreover, advantages in a decrease of photobleaching as well as a fixed microgel for continuous usage was observed."

"Further to the synthesis of polymer nanogels, that can be swollen to allow photocatalysis, Ferguson et al. produced a responsive system that could be turned on or off (Figure 1.10).[93] Photocatalytic nano/microgels were synthesized by copolymerising diphenylbenzothiadiazoleacrylamide together with N-isopropylacrylamide (NIPAM) and poly(ethylene glycol) dimethacrylate as cross-linker. The gels produced had an average diameter of around 190 nm at ambient temperature. NIPAM groups display lower critical solution temperature (LCST) behavior, therefore, a thermoresponsiveness was established in the polymer network. Upon heating to 40 °C, a shrinkage of the nanogel to 70 nm was observed, giving a compressed and non-photocatalytically active material. When cooled down to 25 °C, swelling of the particles back to 190 nm was observed, demonstrating the reversibility of the system. Reaction control by light and temperature was extensively investigated for NAD^+ regeneration in water, as well as an oxidation, reduction, and redox catalytic conversion. Reaction control by temperature and light was achieved, with additional high conversion rates of at least 87% presented."

"Classical polymer photocatalysts have recently emerged as an alternative to conjugated photocatalytic systems.[94] Here, a small molecular photocatalyst is modified so that it can be incorporated into a classical polymer. This incorporation can be during the polymerization of the polymer, or as a post-functionalization. This methodology enables a broad range of

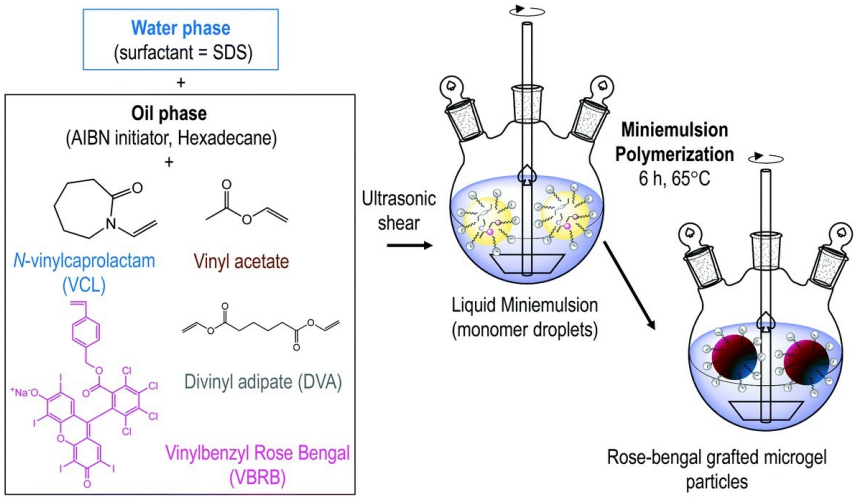

Figure 1.9: Synthesis of photoactive microgels by mini-emulsion polymerisation. A dispersed phase of N-vinylcaprolactam, vinyl acetate, divinyl adipate, vinyl benzene rose bengal, AIBN and hexadecane was polymerised to produce rose bengal grafted microgels. Reproduced with permission from ref[91].

photocatalytic materials to be synthesized, where the physical properties of the polymer can be easily varied while maintaining photocatalytic activity."

"Controlled radical polymerization techniques, such as reversible addition-fragmentation chain-transfer (RAFT) and atom transfer radical polymerization (ATRP), allow more complex polymer architectures to be synthesized. Here, well-defined block copolymers can be synthesized, where the location of any given monomer on the polymer chain is known. This spatial control of monomers has been utilized when forming classical polymer photocatalysts. The photocatalytic moiety can easily be incorporated within a desired polymeric block."

"Furthermore, polymerization-induced self-assembly (PISA) enables superstructures (including nanoparticles) to be formed in solution. Typically, reactions are undertaken in aqueous or alcoholic conditions, where initially a hydrophilic macro chain transfer agent (mCTA) is chain extended by a more hydrophobic monomer. As the polymer chain extends the second block becomes insoluble in the continuous phase, driving self-assembly."

"Recently, RAFT-mediated PISA has been used by multiple research groups to form photocatalytic classical polymer nanoparticles. Here, organic dyes have been modified to include a vinyl functionality enabling their copolymerization within RAFT polymerization. Interestingly, the inclusion of the photoactive monomer into both the hydrophobic particle core and hydrophilic corona has been investigated. Lessard et al. chain extended a PEG mCTA with a methacrylate functionalized Eosin Y and benzyl methacrylate.[95] The synthesis was undertaken in the absence of any initiator where the photocatalytic monomer was able to self-initiate the polymerization through photo-induced electron/energy transfer-RAFT (PET-RAFT) (Figure 1.11). Further to the self-synthesizing polymer nanoparticles Lessard et al. used a PMMA Eosin Y for the successful photo-mediated oxidation of 4-methoxyphenyl boronic acid to 4-methoxyphenol.[95]"

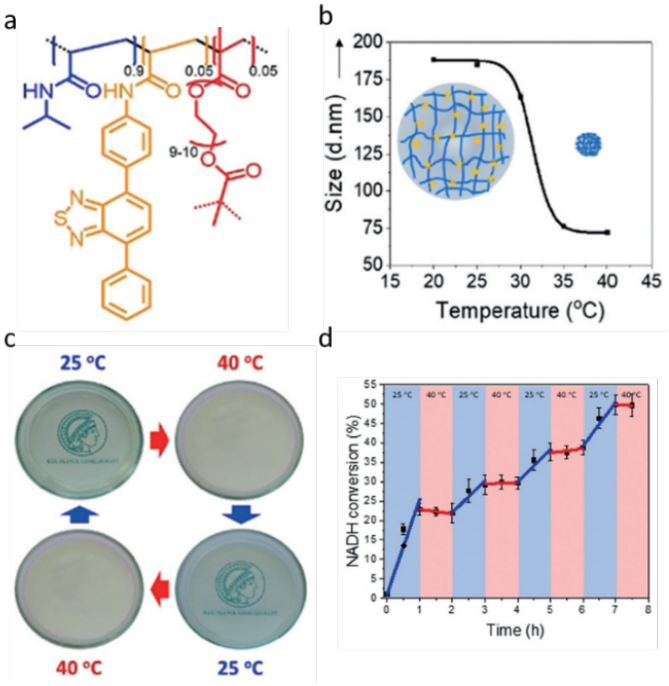

Figure 1.10: (a) Photocatalytic temperature-responsive nanogels structure. (b) Temperature-dependent size of nanogels. (c) Reversible phase changes by changing temperature. (d) Temperature-dependent photocatalytic conversion of the enzyme cofactor NADH to NAD^+. Reproduced with permission from ref[93].

"Recently Korpusik et al. incorporated a methacrylate functionalized RB derivative into a diblock copolymer, using PISA-RAFT. An azide-modified mCTA enabled modification of the polymer nanoparticles to be achieved by a subsequent Huisgen-cyclization reaction of DNA aptamers.[96] This conjugation of aptamers onto the surface resulted in enhanced cellular uptake of the nanoparticles. Decreased aggregation of photocatalyst (compared to free RB) was observed due to the equal distribution of the active molecule across the hydrophobic portion of the polymer chains. The enhanced distribution led to increased singlet oxygen production, creating a promising material for use in photodynamic therapy."

"Boussiron et al. also utilized RAFT-mediated PISA to form photocatalytic classical polymer nanoparticles.[97] Here, RB was selected as the photocatalytic unit, which was again modified to contain a polymerizable group, an acrylate or styrene derivative. Early work by Boussiron et al. produced photoactive latex particles, where RB was incorporated into an acrylic acid macroCTA and then chain extended with n-butyl acrylate.[97] These self-assembled photoactive particles showed low polydispersities and sub-100 nm diameters, typical for the polymerization technique used and suggesting the inclusion of the bulk photocatalyst did not significantly impede the polymerization or self-assembly process. Furthermore, the photoactive nanoparticles produced readily produced reactive oxygen species upon irradiation with visible light. Boussiron et al. further investigated the inclusion of RB into self-assembled nanoparticles to determine the optimum position of the photocatalytic material within the self-assembled nanoparticle.[98] They demonstrated

the easy incorporation of the photoactive material into both environments, combining different monomers. Independent on the location of the photoactive monomer sub-100 nm particles were again formed. No particular difference in the photooxidation reaction of furfuryl alcohol was observed when RB was found in the core, corona, or as a free molecule. Conversely, Ibrahimova et al. found significant differences in the performance of a BODIPY-based photoactive monomer when it was incorporated into the hydrophilic or hydrophobic portion of a self-assembled polymersome.[99] Here, significantly higher performance was observed for the photoperoxidation of anthracene 9, 10-divinylsulfonate by singlet oxygen when the BODIPY was located in the corona compared to the core. It is currently unclear what causes the differences in performance between these systems, it may be due to the differences in monomers, photoactive molecules, catalyzed reactions, or polymeric structures."

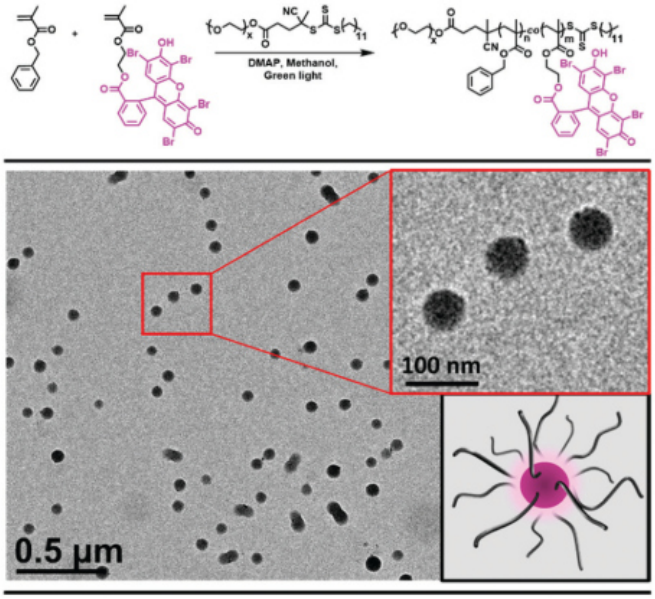

Figure 1.11: Eosin Y containing polymer nanoparticles produced by PET RAFT-PISA. Synthesized in the absence of initiator sub 100 nm photoactive polymer nanoparticles are formed. Reproduced with permission from ref[95].

1.4 Design Principles of Organic Semiconductors

As mentioned in the previous section, heterogeneous photocatalysts (HPs) offer high tunability. In this section, established tuning approaches of HPs are outlined. The most important design principle within HPs is the design of optoelectronic properties. Through the design of defined molecular structures, the HOMO-LUMO energy levels and the band gap of the HP can be precisely engineered. This tuning facilitates the optimization of the material for specific targeted reactions. The donor-acceptor structure of HPs enables electron migration from the donor to the acceptor moiety. Important aspects for this migration are the systems' planarity and orbital alignment. A high planarity and perpendicular orbital alignment result in an extension of the π-conjugation, delocalizing the π-electrons

and therefore narrowing the optical band gap.[38] The used orbital transition defines the potential of the frontier molecular orbital band gap. For example, band gap narrowing can be achieved by the substitution of oxygen with nitrogen within a heterogeneous system. Oxygen mostly uses a $\pi \rightarrow \pi^*$ transition, while nitrogen usually employs a $n \rightarrow \pi^*$ transition. The $n \rightarrow \pi^*$ requires smaller energies for the excitation process by lifting the HOMO.[100] Another popular approach to exploit the structure-property relationship is the halogenation of the HPs. Substitution of hydrogen with chlorines, bromines, or fluorines simultaneously shifts the LUMO and HOMO. Due to higher electronegativity, a stronger bond polarization is observed, changing the π-electron distribution within the system and accelerating electron mobility. This leads to a stabilization of the frontier molecular orbitals, the stabilization of the radical anion, and reduces the barrier for electron injections. The effect of increasing halogenation degree on an organic semiconductor system is shown in Figure 1.12 for pentacene and tetracene derivatives.[101] A similar effect is observed for increasing amounts of acceptor moieties, such as benzothiadiazole or perylene diimide, within the polymer backbone, resulting in a LUMO lowering due to higher electronegativity and π-extensions (Figure 1.13).[102] Substitution of C-H bonds with sp^2 nitrogen not only lowers the HOMO and LUMO simultaneously but also promotes the planarity of the system, reducing steric hindrance and increasing the packing order. Higher packing orders of the HPs can result in higher $\pi - \pi$ stacking and reduce the probability of vibrational relaxation, often reducing the hole reorganization energies, thus yielding faster hole transfers (p-type organic semiconductor).[102] However, the actual effect of a defined functionalization is hard to predict, as the resulting change is strongly dependent on the polymer backbone and has to be reevaluated for each system. Over the past decade, computational predictions have become a powerful tool for the design of HPs. Especially density functional theory (DFT) is indispensable for modern molecular design. Through molecular modeling of the electron density of a molecular structure by Kohn-Sham orbitals, it allows the estimation of a wide array of parameters like the ionization potential, the electron affinity, the polarization, and the planarity of a system.[103]

Besides adjusting the HPs redox potentials for the targeted reactions, the band gap defines the necessary energy of light for photoexcitation. Particularly band gaps below 3.18 eV, for the absorption of visible light, are desired. In recent years, there has been a growing interest in evermore red-shifted absorption of HPs. Red light-activated photocatalysts require less energy for photoexcitation, utilize the natural abundance of red-light within the solar light spectrum, reduce the amount of occurring side reactions and show a higher penetration depth for turbid media or biological applications. An interesting demonstration of red-light-based photocatalysis using HPs is presented by Niu et al., irradiating a covalent organic framework at 660 nm for the generation of $^1O_2$, utilizing the ROS for a defined olefin cleavage.[104] However, despite its impressive progress over the recent years, the field of red-light-based photocatalysts remains in its infancy due to the limitations of inducing chemical reactions with low amounts of energy.

The molecular modifications discussed, primarily aim to alter key properties such as ionization potential, electron affinity, and absorbance. These properties are essential for

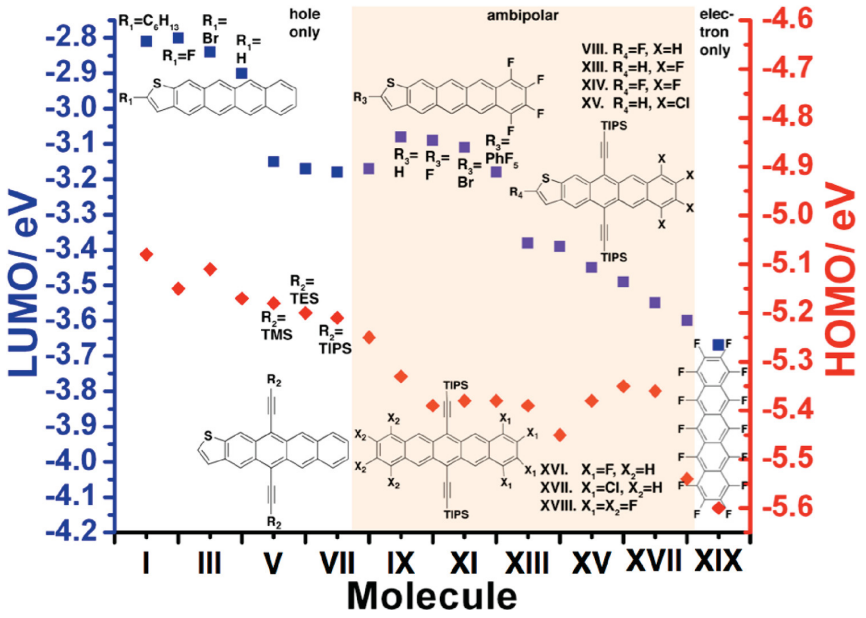

Figure 1.12: Effect of the stepwise halogenation of organic semiconductors on the band gap. Increased halogenation results in a lowered band gap. Reproduced with permission from ref[105].

optimizing electron mobility. However, in the context of designing photocatalysts based on energy transfer (EnT) mechanisms, enhancing the population of the triplet state is desired. The population of the triplet state is governed by the quantum yield of the intersystem crossing (ISC). As stated by El-Sayed, there are two popular approaches to design increased ISC rates within a specific system.[106] A well-established strategy to enhance the ISC is the exploitation of the heavy atom effect. The heavy atom effect can be divided into the internal and the external heavy atom effect. As the ISC transition strongly depends on the spin-orbit coupling, which is highly dependent on the atomic number of atoms in the vicinity of the excited electron, the incorporation of halogens or the substitution with high mass atoms results in an increased ISC and an increased phosphorescence quantum yield.[107] This is called the internal heavy atom effect. The external heavy atom effect describes the intermolecular interaction between heavy mass atoms and the corresponding chromophore. Dissolving chromophores in halogenated solvents or with additional heavy-atom-rich chemical species also strongly increases the ISC.[108] The triplet spin-state of the solute mixes with the spin-state of the solvent/chemical species, wherefore the transition from one species to another is not strongly forbidden by spin selection rules.[109] The other approach for increasing ISC rates is more abstract and harder to design practically. As mentioned, the ISC rate strongly depends on spin-orbit coupling, which correlates to the orbital symmetry and electronic integral of a system, due to necessary spin-orbit perturbation. When a change in spin occurs, it needs to be accompanied by a change in angular momentum, so the total angular momentum is conserved.[110] Therefore, a promotion of ISC rate can be achieved by utilization of $n - \pi^* \rightarrow \pi - \pi^*$ ISC transitions, instead of $\pi - \pi^* \rightarrow \pi - \pi^*$ ISC transitions. This reduces the electron exchange energy, thus reducing the S_1-T_1 energy gap and accelerating

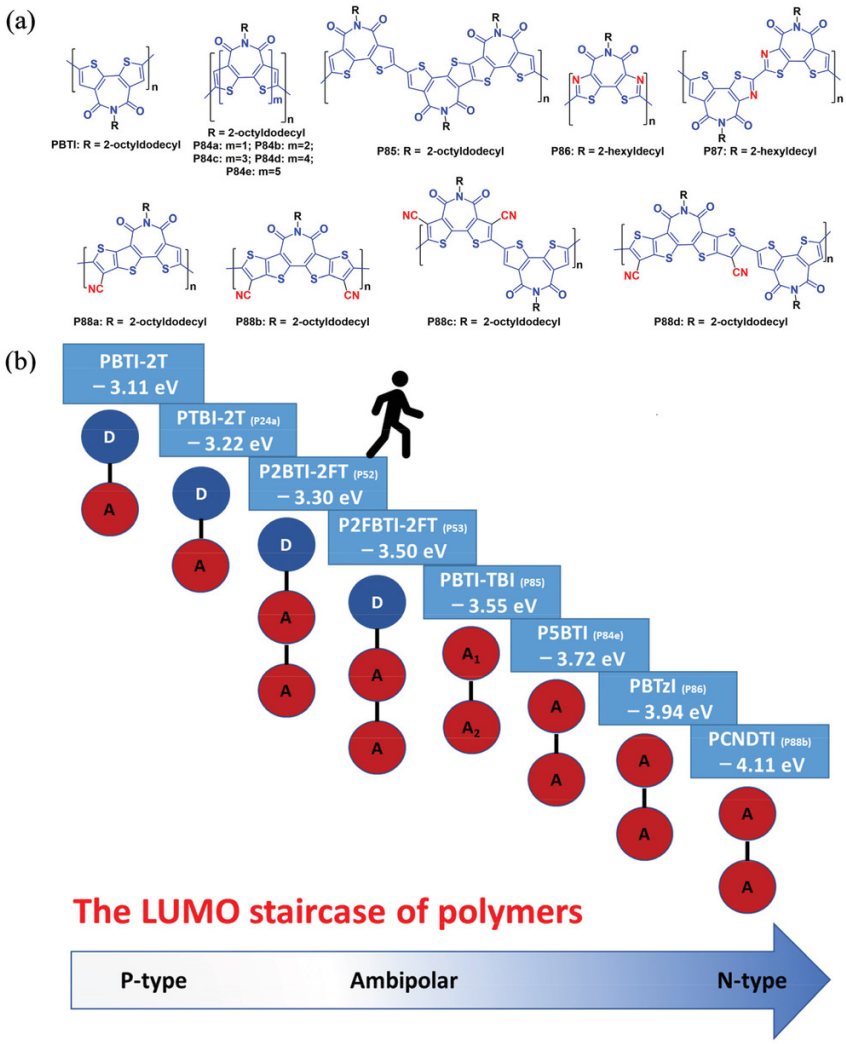

Figure 1.13: Effect of increased amounts of acceptor moieties on the band gap of an organic semiconductor. Synthesized organic semiconductors (a) and the corresponding LUMO values (b), showcasing the impact of increasing acceptor moieties on LUMO values. a) Reproduced with permission from ref[102], b) Reproduced with permission from ref[112].

the ISC rate.[111] The spin-orbit coupling is purely dependent on the electronics of the systems. Spin-vibronic coupling can have a significant impact on the ISC rate while being additionally dependent on the nuclear coordinates (Franck-Condon weighted density of states).

While these considerations focused on the molecular structure and the relevant design of optoelectronic properties, HPs offer high tunability also on a macromolecular level. An often-claimed advantage of heterogeneous photocatalytic systems over homogeneous photocatalytic systems is their recyclability/reusability. However, the heterogeneity of the system brings severe problems with it. Processability and solubilization of existing HPs often limit their widespread application. A simple strategy to reduce the aggregation and subsequent precipitation of HPs out of the dispersion is the implementation of alkyl side chains.[113] The incorporation of aliphatic alkyl chains into the polymeric, conjugated backbone strongly reduces $\pi - \pi$ stacking within the system, which can significantly

enhance the low-temperature processability and solubility.[114] These, linear, typically 5-12 carbon long, alkyl-spacers reduce the intermolecular interactions within the HPs, while leaving its FMOs unchanged. However, due to the modified stacking behavior, side chains have been found to influence the charge mobility and conjugation length of the polymeric backbone.[115, 116]

A popular approach to tuning the HP performance is the defined formation of nanostructures. This strategy gained ever-increasing attention over the last decades, due to its impact on catalytic performance, combined with accessible synthetic pathways. The controlled formation of nanoparticles, nanosheets, nanoclusters, nanocrystals, or hollow microspheres was achieved, yielding high surface-to-volume ratios and increased dispersibility/processability.[117] Significantly increased photoactive sites and the corresponding substrate accessibility to these are expressed in a strong size- and morphology dependency of the photocatalytic performance. As demonstrated by quantum dots, the nanostructure and morphology of a system significantly impact its optical and electronic properties. These nanoscale materials exhibit unique light absorption characteristics and defined changes in their electronic band gap due to quantum confinement effects.[118] The morphology and size control can be induced inherently, by the molecular structure, or by processing techniques such as emulsion polymerizations and precipitation polymerizations. The formation of 1, 2, or 3-dimensional structures was vastly explored, underlining the potential of different morphologies on HPs and its effect on the electronic properties of HPs.[117] While nanoparticulate HPs exhibit strongly enhanced dispersibility due to reduced sizes and the corresponding increased colloidal stability, they often suffer from high electron-hole recombination rates because of their comparatively low degree of conjugation. 1D and 2D nanomaterials, like nanosheets, show increased π-conjugation and provide shorter carrier migration distances, stabilizing the generated exciton.[119] Combing these 2D materials with high porosity (like in CMPs or CTFs), yields high photocatalytic activities due to the high photoactive surface-to-volume area combined with an extended carrier stabilization.[117] As discussed throughout this section, the aggregation and nucleation of these 2D materials often lead to their precipitation from the dispersion. This aggregation also induces stacking-related changes in optical properties and increases morphology defect-based recombinations of charge carriers.[120]

To address these challenges, Kim et al. presented an interesting approach.[79] The defined formation of CMP-based nanoparticles using a mini-emulsion polymerization gave a HP system with high photoactive surface-to-volume ratio. However, the colloidal stability of this system remained low, so that a low solvent compatibility was observed. Grafting polymer chains from the surface of these CMP nanoparticles greatly enhanced the dispersibility, due to increased solvent interactions. Combining morphology, size, and side chain effects, a strong amplification in photocatalytic activity was achieved, while concurrently increasing processability (Figure 1.14).[79] Especially the increased solvent compatibility should be emphasized here, as the liquid-solid interface of heterogeneous photocatalysts plays a defining role in the photocatalytic activity. The mass transfer of substrates to the corresponding photocatalytically active sites and the stabilization of

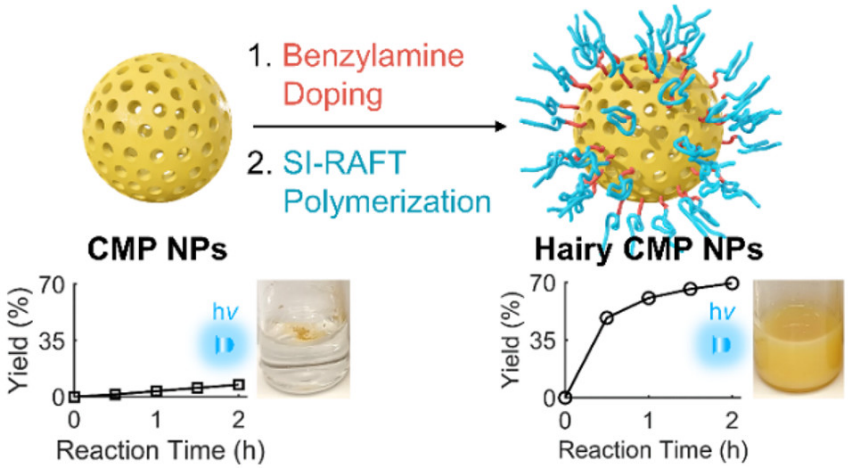

Figure 1.14: Increasing processability and photocatalytically-active surface-to-volume ratio by morphology control. Reproduced with permission from ref[79].

the generated reactive intermediates show a strong solvent dependency.[121] As the mass transfer represents the governing driving force, enhanced adsorption of the substrate to the photocatalyst surface, fast desorption of the generated product or intermediate, and suppression of readsorption of the formed product strongly enhance the photocatalytic activity and determines the TON. In addition to stabilizing generated intermediates, solvents interact with the HP itself, influencing the favorability of specific reaction pathways depending on the solvent's polarity and hydrogen-bonding strength. Selective solvent-induced quenching of h^+, e^-, or •OH can be observed.[122] The solvent can even participate within the photocatalytic reaction cycle, by e.g. proton donation, basic proton abstraction, or as a sacrificial oxidant/reductant. Therefore, solvent effects can be a relevant driving factor for the reaction's selectivity and product formation.[123]

1.5 Selectivity Concepts in Heterogeneous Photocatalysis

Controlling the selectivity of a reaction has been a perpetual challenge in the synthesis of high value compounds. Especially the field of photocatalysis suffers from a shortage in substrate selectivity concepts. As described in section 1.4, the tuning of optoelectronic properties has been a well-established method, defining the potential reaction parters for the catalytic system. However, most of the designed reactions occur in an uncontrolled fashion, as the selectivity is solely determined by the inherent reactivity of the reaction partners. If designed carefully, substrate diffusion and steric hindrance can yield a preferential formation of the targeted product (often the kinetic product). As this approach requires extensive reaction design, the reports on selective photocatalytic processes remain low.

Comparing the fields of homogeneous, thermal catalysis to photocatalysis, substantial differences in the design strategies are obvious. The creation of defined microenvironments represents a staple in the reaction design of homogeneous, thermal catalysis.[124] While the implementation of similar microenvironments into photocatalytic mechanisms remains

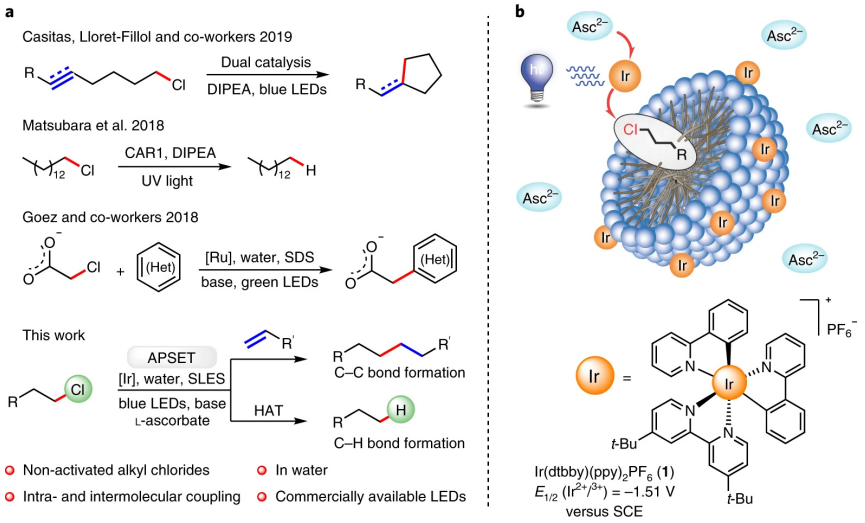

Figure 1.15: a) Previously reported approaches on the light-driven activation of C-Cl bonds. b) Schematic representation of the assembly-promoted single electron transfer (APSET); Asc, L-ascorbate. Reproduced with permission from ref[126].

challenging due to their inherent mechanism, first approaches on innovative selectivity concepts were presented in recent years.

A promising strategy to influence the selectivity of a photocatalytic reaction is the implementation of differing microenvironments into the photocatalytic system.[125] The incorporation of molecular photocatalysts into multiphase systems has demonstrated its enormous potential. Here, emulsion or dispersion-based approaches are used to enable the utilization of several microenvironments within a single reaction mixture, offering enhanced solvent compatibility and reaction control. Giedyk et al. demonstrated the adsorption of a positively charged metal complex as a photocatalyst onto the negatively charged surface of sodium lauryl oligoethylene glycol sulfate (SLES) micelles.[126] This supramolecular photocatalytic system was then used for a selective reductive dehalogenation of alkyl chlorides (1.15). The photocatalytic activation of alkyl chlorides remained challenging, due to generally high reduction potentials of around -2.8 V vs. SCE. However, an assembly-promoted single electron transfer mechanism was observed, stabilizing the generated radical anion of the photocatalyst via non-covalent interactions, allowing a second excitation, yielding the excited state radical anion of the photocatalyst. This consecutive photoinduced electron transfer enabled the reduction of alkyl chlorides. An additional benefit of the micellar reaction system was the existence of a hydrophobic (inside micelle) and a hydrophilic (aqueous solvent) microenvironment. The accumulation of hydrophobic alkyl chlorides within the micelle membrane decreased the spatial distance between the photocatalyst and substrate, thereby increasing the reaction rate. It was proposed, that the more polarized end of the alkyl chlorides (C-Cl bond) is facing towards the hydrophilic environment, further accelerating the photoreduction of the substrate. The exploitation of adsorption processes for an enhancement of photocatalytic selectivity was also demonstrated for liposomes, polymeric nanoparticles, lipid membranes, and hydrogels.[126]

Besides the adsorption-driven facilitation and acceleration of photocatalytic reactions, the photocatalytic moiety can be covalently linked to the supramolecular assemblies. An approach was presented by Eisenreich et al., utilizing polymeric single chain nanoparticles, which were post-functionalized with 10-phenylphenothiazine as photocatalytic species.[127] These photocatalytic nanoreactors were subsequently employed for a C-C crosscoupling of N-methylpyrrole and 2-iodobenzonitrile, yielding 99% conversion within ^{1}H reaction time. Hereby, the defined confinement for the photocatalyst and the generation of a hydrophobicity gradient within the system resulted in a solvophobic substrate aggregation, allowing fast reaction rates with low photocatalyst loadings. The reaction conditions should be highlighted, as the C-C cross-coupling was carried out under ambient conditions and in the presence of oxygen. Under usual circumstances, the oxygen within the reaction mixture quenches the excited photocatalyst. However, the densely packed nanoparticle inhibited the quenching process, facilitating the reaction. Furthermore, the covalent linkage enabled the successful recycling of the photocatalytic material, demonstrating constant conversion rates for up to five reaction cycles.[127]

Hydrophilic-hydrophobic gradients are also widely employed within natures catalysts, enzymes. Enzymes are considered the role model in catalysis, exhibiting unparalleled substrate specificity and selectivity. Naturally localized in a highly complex medium, surrounded by a wide range of compounds, enzymes exploit several selectivity concepts, to achieve the enantioselective product conversion. The catalytically active site is typically located in an enzymatic pocket, which shows an increased hydrophobic microenvironment, resulting in the establishment of a hydrophobicity gradient, leading to defined substrate diffusion to the active site.[128] In some cases, the enzymatic pocket can be so hydrophobic, so that no aqueous medium can be found within. Besides increased hydrophobicity, the enzymatic pocket utilizes defined interactions, fixing the substrate to a specific position by hydrophilic (e.g. hydrogen-bonding) and hydrophobic (e.g. $\pi - \pi$ stacking) interactions of the protruding amino acids, enabling the precise conversion of the targeted functionality.[129] Kuckhoff et al. exploited the intrinsic selectivity of a protein for photocatalysis.[130] Therefore, the steroid carrier protein SCP-2L, possessing a hydrophobic tunnel, was modified by site-selective mutagenesis to introduce non-native cysteine residues. After the investigation of a suitable cysteine location, the protein was post-functionalized with the small molecule organic semiconductor diphenylbenzothiadiazole, exhibiting an iodo-acetamide group for coupling. The obtained photoenzyme was then investigated for its photocatalytic activity in the oxidation of a hydrophobic sulfide. A strong location dependency of the photocatalyst was found, showing the highest reaction rate for the photocatalyst located within the hydrophobic tunnel. This finding underlines the importance of substrate diffusion to the photocatalytically active site, which can be accelerated by exploitation of the defined microenvironment of enzymes.[130]

Inspired by the selective substrate binding of enzymes, Breslow et al. pioneered the field of artificial enzymes, utilizing the defined binding affinity of substrates towards the hydrophobic cavity of cyclodextrins.[131] Therefore they functionalized β-cyclodextrins with catalytic moieties, proving their potential for amino acid synthesis and selective

bond cleavages. The coordination affinity of adamantane or phenyl groups was shown to alter the stereospecificity of the reaction.[132] This approach was later expanded to the field of heterogeneous photocatalysis. Initially presented in the work of Gosh-Mukerji et al., thiolated cyclodextrins were combined with an inert gold surface, assembling into self-assembled monolayers (SAM) with broad cavity opening facing towards the solution phase.[133] Photocatalytically active titanium dioxide was placed in close proximity to the cyclodextrin SAM, which led to a shuttling of the substrate to the active site. The cyclodextrins served as molecular recognition sites, facilitating the preferential conversion of a mixture of two substrates by selectively binding the substrate with higher affinity to the cyclodextrin.

Taking the concept of molecular recognition sites for photocatalytic selectivity enhancement further, Shen et al. used a substrate templating technique on a heterogeneous titanium dioxide photocatalyst.[134] Herein, titanium dioxide nanoparticles were prepared and dispersed in a solution of substrates (chlorophenol) and monomers (o-phenylenediamine). Through careful design, a tridentate binding interaction between the chlorophenol and the phenylenediamine was established. Afterwards, the phenylenediamine was polymerized on top of the titanium dioxide nanoparticles and the non-covalently bound chlorophenol was removed. Therefore, a molecularly imprinted polymer was obtained on the nanoparticle surface. Comparison of a non-imprinted nanoparticle and the molecular imprinted nanoparticle towards the photocatalytic degradation of chlorophenols revealed an acceleration of reaction rate of 143% for the imprinted nanoparticle.[134]

Besides substrate binding and diffusion acceleration, the utilization of confined space within photocatalysis showed remarkable effects on the reactivity.[135] Cyclodextrins, cucurbiturils, coordination cages, frameworks, and micelles exhibit additional confinement effects, fundamentally changing the chemical and physical properties. A wide range of properties was modulated using metal-organic coordination cages (MOCs) as confinement space. These MOCs represent a highly tunable and straightforward approach on mimicking and exploring artificial confinement effects.[136] The chemical environment of these systems can be tailor-made for the targeted substrate by precise adjustment of the metal charge, the ligand binding angle, and introduced molecular functionalities.[137] Within confined spaces, an enhanced stabilization of unstable intermediates was observed, explained by substrate preorganization, hence thermodynamic restriction of an undesired conformation. Other confinement effects include defined charge separation or targeted modulation of optical and electrochemical properties. Extensive research on this complex topic has been carried out so that the reader is referred to recent reviews for further information.[135, 138] Underlining the potential of nanoconfinement spaces, Kumar et al. presented a prismatic platinum-based cage with a tetraphenylethylene-based linker and varying pillar linking groups, like 1,4-diethynylbenzene (Figure 1.16). The prismatic alignment of the defined MOC allowed for a stacking of several MOCs, showing aggregation-induced emission at 540 nm. Afterwards, the defined encapsulation of rhodamine B, showing strong absorption at 540 nm, resulted in a Förster resonance energy transfer from the MOC

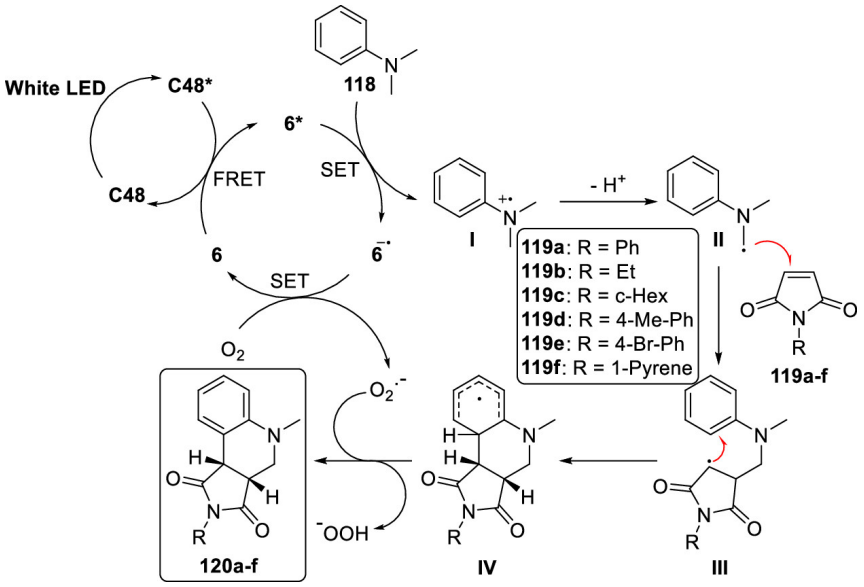

Figure 1.16: Proposed reaction mechanism for the light-harvesting antenna complex C48:RhB for the photoinduced oxidative cyclization of a maleimide with an aniline derivative. Reproduced with permission from ref[136].

to rhodamine B. The excited state rhodamine B was then exploited for a confinement-enhanced stereoselective cyclization reaction of n N,N-dimethylaniline and N-phenyl maleimide. Comparison of the MOC-RhB and sole rhodamine B at the same conditions showed a significant increase to 97% from 5%, highlighting the utilization of the MOC as a light-harvesting antenna.[139]

So far, the reviewed photocatalytic systems mostly relied on polarity or confinement effects. Another important concept is the implementation of electrostatic interactions between substrate and catalytically active sites/surface.[140] These coordination sites represent a major selectivity driving force in enzymatic biocatalysis. Utilizing the electrostatic interaction between a substrate and the heterogeneous support material or photocatalyst can greatly alter the photocatalytic reactivity. For example, the formed Stern layer of a negatively charged micelle can be exploited to accumulate positively charged substrates in higher concentrations, accelerating the photocatalytic reaction rates by decreasing the spatial distance between the micellar photocatalyst and the solvated substrate.[125] Additionally, altered steric substrate orientations are expected, due to the polarization of the substrate coordination side, causing an orientation to the charged photocatalyst moiety.[126] A popular biocatalytic example of electrostatic interaction, is the establishment of a potential gradient by the positively charged guanidyl group of arginine, driving the selective coordination of carboxylates,[141] phosphates[142] or anionic metal ions[143] towards the catalytically active sites. An interesting projection of this coordination concept was the implementation of guanidyl groups onto β-cyclodextrins, initiating a selective coordination of a carboxylated anthracene substrate.[144] This anthracene substrate undergoes a dimerization upon irradiation. Comparing the dimerization reaction under coordination with a guanidylated cyclodextrin and a non-guanidylated cyclodextrin, revealed a solvent-dependent inversion of the photochirogenesis. The hydrophobic preorganization

of the negatively charged anthracenecarboxylate within the cyclodextrin cavity and the attractive electrostatic interaction with the cationic guanidine on the cyclodextrin yielded a strong change in enantiomer formation. A strong enrichment of head-to-head enantiomer was observed, showing a ratio of up to 1.3 head-to-head/head-to-tail for the guanidylated cyclodextrin, compared to the non-guanidylated system which only yielded a ratio of 0.2. Thus, the significant influence of the electrostatic guanidine-carboxylate binding interaction on the confinement-driven photodimerization of anthracene carboxylate was demonstrated.[144]

To date, the targeted formation of desired enantiomers is predominantly achieved through homogeneous catalysis.[145] Considering the selectivity concepts of transition metal complexes for thermal catalysis, the utilization of defined hydrogen bonding interactions is found to be the predominant design concept. The coordination of chiral ligands to a metal center creates a precise steric environment, constraining the substrate into a preferential conformation or enabling further reaction from a specific site (quadrant model).[146] This steric hindrance facilitates the favorable formation of the targeted enantiomer. One of the first examples in synthetic chemistry for the accumulation of a targeted enantiomer was the asymmetric hydrogenation of olefins via rhodium/ruthenium complexes and organophosphorus ligands like 2,2'-bis(diphenylphosphino)-1,1'-binaphthyl (BINAP).[147] This approach on three-dimensional spatial selectivity yielded Noyori, Sharpless, and Knowles the Nobel Prize 2001.[148] Thereby, the selectivity is defined by the reagents and catalyst, and not from the target molecule itself, which leads to the transfer of spatial information from one molecular to another. A methodologically similar information transfer represents the major strength of enzymes. Creating a confinement space with precise hydrogen bonding interactions, transfers the stereochemical information from the microenvironment to the targeted molecular and selectively yields the desired enantiomer. However, due to the mechanistic constraints of photocatalysis, the photocatalytic transfer of spatial information from the microenvironment remained challenging. A first successful approach to a stereocontrolled, photocatalytic reaction was presented by Bach et al.[149] Herein, a benzophenone-based photocatalyst was functionalized with 1,5,7-trimethyl-3-azabicyclo[3.3.1]nonan-2-one via an oxazole. The structural rigidity of this functionalization, caused by the oxazole and the methyl groups, fixed the benzophenone into a plane. This structural rigidity was exploited for enantiomer enrichment within a photoinduced electron transfer-based cyclization reaction. The prochiral precursor exhibited a quinolone moiety, which selectively binds to the amide functionality of the chiral photocatalyst (Figure 1.17). Due to the steric constraints after the electron abstraction, the cyclization to the pyrrolizidine yielded an enantiomeric ratio of 85/15. By switching the chirality of the photocatalyst, the enantiomeric ratio of the formed product was inverted to 31/69. This represents a first proof-of-concept, demonstrating favored enantiomer formation due to steric environmental constraints.[149] Since then, several approaches have been investigated for stereoselective photocatalysis.

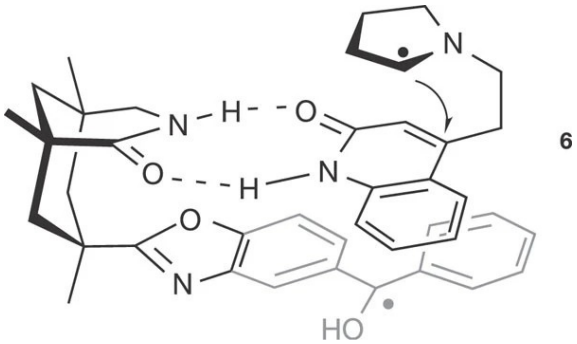

Figure 1.17: A sterically controlled binding mechanism for the photocatalytic cyclization of quinolone. The preferential formation of a targeted enantiomer was observed. Reproduced with permission from ref[149].

Bach et al. presented another bifunctional catalyst system by combining a thioxanthone photocatalyst with a chiral phosphoric acid derivative.[150] The photocatalyst was covalently bound to the chiral directing group by a phenylene linker. Afterwards, this complex photocatalyst was evaluated for its stereocontrol during a [2+2] photocycloaddition reaction, achieving an enantiomeric ratio of up to 93/7 for the final product formation. Previously, a racemic product formation was reported. This strong enantiomer enrichment was explained by the selective binding interaction between the phosphoric acid and the carboxylic acid within the reacted substrate, whereby the binding interaction was confirmed by ^{1}H-NMR spectroscopy. Additionally, the spatial constraint of the binaphthyl group sterically induced a conformation bias of the substrate, finally yielding the targeted enantiomer.[150]

Further exploiting defined hydrogen bonding interactions for selective photocatalysis, Sivaguru et al. presented the enantioselective cyclization of coumarin derivatives.[151, 152] An organophotocatalyst was designed, exhibiting a chiral binaphthyl and a bis(trifluoromethyl)benzene group for steric induction. The two functionalities were linked via a thiourea bridge. The complex design of this dedicated system led to the defined hydrogen bonding of thiourea's N-H to the coumarin ester functionality. The increased spatial proximity of the substrate to the binaphthyl and bis(trifluoromethyl)benzene resulted in steric control via stereoelectronic effects, enriching the desired orientation. This coordination of the substrate additionally led to the formation of static and dynamic $[3 \cdots 1]$ exciplexes with the photocatalyst, quenching the excited state via a photocatalytic energy-sharing mechanism. The exciplex formation was thoroughly investigated via absorption and emission spectroscopy. Lastly, the stereocontrolled coumarin cyclization was conducted for six different substrates, yielding up to 100% conversion with 96% enantiomeric excess. This system impressively demonstrated the powerful potential of defined non-covalent bonding interactions for stereocontrol in photocatalytic reactions.[151, 152]

Over the last 20 years, the field of photocatalysis, specifically selective photocatalysis has made enormous progress.[153, 154] And there are many more interesting and novel design approaches to photocatalytic selectivity, like dual catalysis approaches,[155] responsivenesses,[93, 156] chromoselectivity[157] or element doping into heterogeneous systems[158]

(and so on). The targeted functionalization of photocatalysts offers endless opportunities and will remain one of the most investigated research fields. However, since selective photocatalysis represents the 21st century like no other field, in terms of sustainability and scientific dedication, more selectivity concepts and higher degrees of substrate specificity are necessary, to unlock the next level of photocatalysis.

Chapter 2

Motivation

As shown in the previous chapter, the field of photocatalysis became one of the most discussed and researched topics in chemistry. The possibility of replacing fossil fuels with photochemical energy conversion methods has significantly boosted interest in the field of photocatalysis, as evidenced by the annual publication of over 8,000 research articles.[159] Recently, the photocatalytic formation of fine chemicals and valuable compounds gained increasing attention. In there, traditional thermal catalysis methods currently dominate the field, accounting for nearly 85% of all commercially produced chemical products.[3] Most thermally activated catalyst systems involve the utilization of high temperatures, high pressures, and expensive transition metals. However, the field of photocatalysis, especially visible-light organophotocatalysis, demonstrates promising progress in enabling selective transformations, therefore addressing relevant sustainability challenges.[160] Especially in terms of milder conditions, reduced waste, and use of renewable resources, photocatalysis clearly outperforms traditional catalysis.[161] So far, photocatalytic systems successfully proved their potential, tackling problems in natural product synthesis[162] and general drug discovery.[163] Until now, organophotocatalysts primarily served to complement traditional catalysts rather than replace them. However, recent advancements in selectivity have enhanced the competitiveness of organophotocatalysts, leading to the development of the first stereoselective photocatalysts. However, these steps represent just the beginning of the development of stereoselective and controlled photocatalytic reactions.[149, 164] Ongoing limitations like long reaction times and limited scalability still inhibit their broad industrial applicability.[161]

To address these challenges, the development of novel selectivity concepts for photocatalysis is essential. Therein, heterogeneous, visible-light, polymeric organophotocatalysts represent a particularly promising framework, providing several advantages, like catalyst recyclability and tunability. The adjustment of optical and electronic properties to the targeted reaction enable tailor-made photocatalysts with enhanced photocatalytic reactivity. Furthermore, polymeric organophotocatalysts facilitate the implementation of orthogonal selectivity approaches, making them versatile tools to advance the field of photocatalytic selective reactions.[154] In there, the utilization of macromolecular features, such as specific hydrophilic or electrostatic interactions at the solid-liquid interface between the substrate

and the photocatalyst, emerged as a possible orthogonal selectivity concept to increase the photocatalytic reaction control. However, to properly exploit these surface interactions, the photocatalysts' solvent compatibility and the substrate accessibility to the catalytically active site have to be considered, as they represent major limitations in achieving optimal catalytic rates. The substrate accessability to the photocatalytically active surface can be increased for example by controlling the catalyst morphology. Down-scaling of heterogeneous photocatalysts to nanometer-sized structures resulted in increased photocatalytic activity due to enhanced substrate accessibility and light penetration.[79, 165] However, diffusion limitations and mass transfer effects remain problematic, limiting the widespread applicability of heterogeneous photocatalysts. Further enhancement of the photocatalytically active surface and substrate accessibility could therefore be an important approach to improve the applicability of heterogeneous photocatalysts.

The employment of macromolecular, organic structures for high substrate selectivity/accessibility is also used in nature's most powerful and unparalleled catalyst systems, enzymes.[166] Even though the enzymatic reaction mechanism differs greatly from polymeric photocatalysts, their utilization of a wide range of orthogonal selectivity concepts represents an inspiring example to achieve outstanding selectivity control. The exploitation of hydrophilicity-hydrophobicity gradients across the enzyme results in a strong acceleration and control of substrate diffusion towards the catalytically active sites. The substrate diffuses into the enzymatic pocket through a substrate-adjusted confined cavity. Within the enzymatic pocket, defined binding interactions like hydrogen-bonding, electrostatic interactions, or coordinative bondings achieve a spatial fixation of the substrate, sterically restricting the reactive groups and thereby creating their unparalleled stereoselective catalysis. The confinement space within the enzymatic pocket exhibits a unique reactivity through differing microenvironments, enabling typically inaccessible reactivity profiles. Taking inspiration from the natural approach on combining selectivity concepts and substrate-binding interactions could drastically improve the substrate specificity and reaction selectivity of heterogeneous photocatalysts.

This thesis aims to improve the photocatalytic reactivity of heterogeneous organophotocatalysts by implementing biomimetic selectivity concepts. Inspired by enzymatic selectivity mechanisms, this work elucidates the effect of employing orthogonal selectivity concepts to enhance substrate diffusion to the photocatalytically active sites, therefore reducing the required reaction times. Conventional selectivity methods, like optoelectronic tuning of polymeric photocatalysts, were combined with defined hydrophilicity gradients or electrostatic substrate attraction to evaluate their effects on the photocatalytic reaction rates. The change in substrate diffusion to the photocatalytically active sites was assessed by photocatalytic pollutant degradations and the formation of valuable products. Additionally, the applicability of these materials as microreactors in artificial cell-like systems will be discussed.

In Chapter 4, the effect of defined hydrophilic and hydrophobic microenvironments on the photocatalytic reactivity will be covered. The establishment of microenvironments with different hydrophilicities around the photocatalytically active sites and their impact

on the photocatalytic reaction rates will be elucidated. The possible correlation between photocatalyst microenvironment and substrate hydrophilicity/polarity concerning the change in reaction rate will be discussed. Reviewing the observed results will help to further understand the reaction mechanisms of heterogeneous organophotocatalysts and enhance the reaction control for improved product formation.

In Chapter 5, the use of substrate-adjusted binding groups to accelerate photocatalytic reaction rates will be covered. The placement of defined substrate binding groups in proximity to the photocatalytically active surface of heterogeneous organophotocatalysts will be investigated towards an increase in reaction rate. Employment of guanidyl groups for specific substrate attraction of phosphonates, chromates, or carboxylates via attractive hydrogen-bonding and electrostatic interactions will be analyzed for the acceleration of mass transfer and enhanced substrate accessibility to the photocatalytically active sites. The impact of the established guanidyl binding groups on substrate attraction and a corresponding acceleration of substrate mass transfer to the active sites will be evaluated by comparison with a non-functionalized system. The presented results will supplement the understanding for the construction of defined binding environments for specific substrates in heterogeneous organophotocatalysis.

The final Chapter 6 will discuss the application of organophotocatalysts as microreactors in artificial cell-like systems. Using the framework of phase-separated coacervate-based systems, the targeted sequestration of photocatalysts into stable microreactors will be investigated. Additionally, the controlled photocatalyst localization and formation of stable and independent microreactors will be elucidated. Their utility as functional synthetic cell organelles will be tested by the execution of several photocatalytic reactions under physiological conditions. The obtained insights will give valuable information into the utilization of photocatalytic microreactors as orthogonal synthetic organelles.

Chapter 3

Characterization Methods

In this chapter, an overview of the most relevant characterization techniques, that were used in this work, is presented. However, for in-depth information on the theoretical background of the techniques and principles, the reader is referred to the literature. Herein, a practical outline will be focused.

3.1 Fourier-Transform Infrared Spectroscopy

Fourier-transform infrared (FTIR) spectroscopy uses light in the infrared range (4000 to 700 cm^{-1}) to characterize chemical bonds within the analyzed sample. As chemical bonds absorb light, discrete bond rotations and vibrations are induced, resulting in a characteristic absorption band within the spectrum for a specific bond type. A defined fingerprint for each molecule can be obtained, identifying the chemical composition of a material. Usually, in FTIR spectra the wavenumber (in cm^{-1}) is plotted against the relative transmittance. It is important to note, that FTIR measurements are sensitive to humidity and residual solvents, as these can shift the observed absorption band. Thorough analysis of the spectra can provide conclusions on the molecular structure and possible impurities. To measure a transmission FTIR, a small sample amount was mixed with potassium bromide (KBr) and then pressed into a transparent disk (detailed information can be found within the corresponding experimental section of each chapter).

3.2 UV/Vis Absorption and Fluorescence Emission Spectroscopy

With UV/Vis absorption spectroscopy, the light absorption behavior of a sample is analyzed within the ultraviolet and visible range (200-800 nm). For characterization, the sample is dissolved in a solvent (which does not absorb light in the desired region). The solution is then typically transferred into a quartz cuvette and irradiated with monochromatic light of the corresponding wavelength. In an absorption spectrum, the wavelength is plotted against the absorption intensity. The obtained absorption intensity is highly dependent on the absorption coefficient of the analyzed compound and its interaction with the solvent. The change in polarity of the solvent can result in bathochromic (red-shifted)

or hypsochromic (blue-shifted) shifts, which is described by the effect of solvatochromism. Additionally, the absorption intensity is strongly dependent on the concentration (usually in the µm to nM range) of the analyzed photoactive compound, as described by the Beer-Lambert-law (Eq. 3.1):

$$A = log_{10}\left(\frac{I_0}{I_1}\right) = \epsilon_\lambda \cdot c \cdot d \tag{3.1}$$

Herein, the product of the concentration c, the optical path length "d" and the molar absorptivity ϵ_λ describe the attenuation of light during the measurement, finally yielding the absorbance A of the compound. The characteristic absorption of a compound is related to the photon-compound interaction and can yield valuable information on the optical properties of the analyzed compound. To distinguish the photon-material interaction from the solvent-photon interaction, a blank measurement has to be conducted for baseline subtraction. In the case of heterogeneous materials, the absorption behavior of dispersions can be analyzed as well. However, the results should be interpreted carefully, as scattering phenomena can greatly alter the obtained spectra. For these materials diffuse reflectance UV/Vis spectroscopy is recommended.

A similar setup is used for fluorescence emission spectroscopy. However, here the emission behavior of the compound is analyzed. The sample is irradiated with monochromatic light at the excitation wavelength, and the photon emission behavior is monitored by plotting the wavelength against the emission intensity. The observed emission peak is typically red-shifted compared to the absorption peak, primarily due to energy loss from vibrational relaxation of the excited state compound and solvent reorganization effects. The shift is described as the Stokes shift. If the emitted photon exhibits more energy than the absorbed one, a blue shift is observed which is called anti-Stokes shift. Analyzing the absorption and the emission spectra together can give information on important optical parameters, such as the optical band gap. Performing the fluorescence spectroscopy with time-dependency gives the quantum yield and fluorescence lifetime.

3.3 Nuclear Magnetic Resonance Spectroscopy

Nuclear magnetic resonance (NMR) spectroscopy represents one of the most powerful tools to characterize chemical structures. A general overview of the working principle of NMR spectroscopy is shown in Figure 3.1. Herein, an external strong magnetic field is applied to the sample, resulting in the alignment (polarization) of the magnetic nuclear spins of the compounds' nuclei. After polarization, electromagnetic radiation in the radio frequency range (4-900 MHz) is pulsed on the sample, perturbing the alignment of the spins by exciting some nuclei spins from the lower energy spin state to the higher energy spin state. During the relaxation process back to the ground state, the relaxation time T_1 and the transversal relaxation time T_2 can be obtained from the free induction decay (FID)

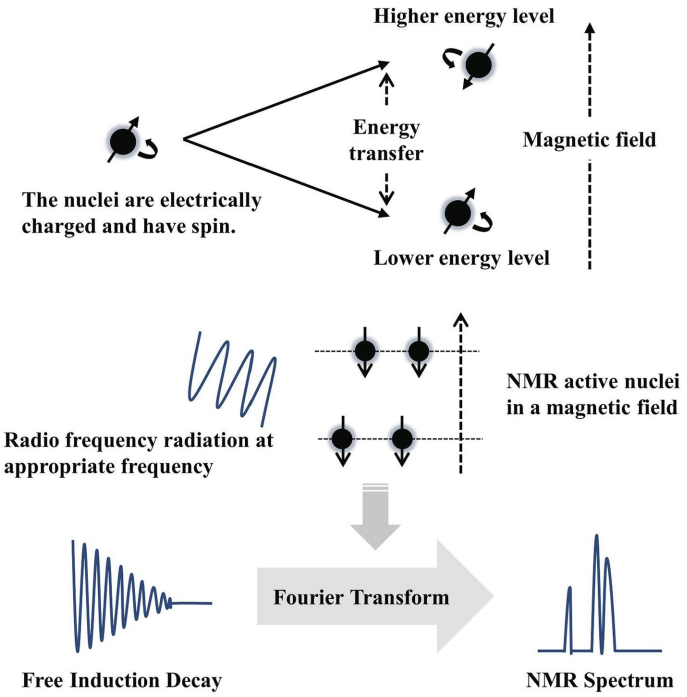

Figure 3.1: Illustration of the general work principle of a NMR experiment. Reproduced with permission from ref[167].

spectrum. This FID visualizes the nuclear magnetic resonance response, which is monitored by a radio receiver. The continuing Larmor precession causes the nuclear spins to realign with the external magnetic field. This precession generates an oscillating magnetic field that induces an electrical current in the receiver coil surrounding the sample, producing the FID signal. Fourier-transformation of the FID yields a spectrum and characteristic peaks are observed for nuclei in defined environments. For NMR spectroscopy, atomic nuclei with non-zero spins are required, with the highest sensitivity for spin 1/2 nuclei. The choice of radiofrequency (RF) pulse used to perturb the nuclear spins is specific to the type of nucleus being analyzed. This selection is based on the unique Larmor frequency of each type of nucleus in a given magnetic field. Common examples include nuclei like ^{1}H, ^{13}C, ^{19}F, or ^{31}P. The magnetic response of nuclei is significantly influenced by their chemical environment, as surrounding atoms strongly influence the electronic environment. This dependence allows for a detailed analysis of the nucleus environment. The characteristic peaks enable the identification of functional groups, the molecular structure, molecular diffusion, and spatial interactions. Since the chemical environment has a strong influence on the nucleus' shift, a strong solvent dependency has to be considered.

A special case of NMR spectroscopy, specifically designed for solid materials (crystals, powders, gels) and insoluble compounds is the solid-state NMR (ssNMR) spectroscopy. Comparing the obtainable resolution of ssNMR spectroscopy to liquid-phase NMR spectroscopy reveals a significant broadening of the peaks. The effects of dipolar coupling and chemical shift anisotropy (CSA) become much more pronounced, compared to liquid-state NMR spectroscopy, leading to complications in obtaining high-resolution spectra, particularly ^{1}H NMR spectroscopy. To reduce the effect of anisotropic nuclear magnetic

interactions, fast spinning (in kHz) of the sample at the magic angle (54.7°) is applied, simulating increased molecular mobility. For ^{13}C measurements, a technique called cross-polarization is used. Here, the sensitive nuclear polarization of an abundant spin (often ^{1}H) is used to amplify the polarization of another spin (^{13}C). Irradiation of the sample with radio frequencies first for the abundant spin, then with another pulse for cross-polarization contact with a frequency at the Hartmann-Hahn condition allows the magnetization transfer from the abundant spin to the other spin, dramatically increasing the nucleus sensitivity for ssNMR spectroscopy.

3.4 Electron Paramagnetic Resonance Spectroscopy

Electron paramagnetic resonance (EPR) spectroscopy is conceptually similar to NMR spectroscopy. Herein, the analysis of unpaired electrons within a compound is conducted. An external magnetic field is applied to a sample, aligning the electron spins along the direction of the magnetic field (both up and down spins). However, most spins are found in the thermodynamically favorable state, usually the spin $+\frac{1}{2}$ state. Using microwave frequency pulses of distinct energies, some electrons are excited into the higher energy spin state. The required energy of that pulse is characteristic for each radical species. The relaxation time back into the lower energy state is described as the T_1 time. After obtaining the FID and the Fourier-transformation of it into a spectrum, characteristic signals for specific radical species can be obtained. Showing a similar hyperfine splitting as NMR spectroscopy, dependent on the surrounding chemical environment, for the signal multiplicity. EPR spectroscopy is especially useful to determine generated reactive oxygen species within a sample. To analyze these species, trapping into long-lived radical species is required.

3.5 Cyclic Voltammetry

Cyclic voltammetry (CV) represents a fundamental technique to investigate redox reactions, electron transfer reactions, and electrochemical electrode processes. It is referred to as a potentiodynamic measurement. For characterization, linearly increasing and decreasing voltages are applied on the working electrode and plotted against the current or current density (Figure 3.2). Changes in current indicate an occurrence of a reduction or oxidation process. Typically, CV is measured in a three-electrode setup, consisting of a working electrode, a counter electrode, and a reference electrode. These three electrodes are submerged into an electrolyte solution, a conductance salt dissolved in a solvent (organic or aqueous). In this work, mostly tetrabutylammonium hexafluorophosphate dissolved in acetonitrile (0.1 M) is used. A compound can be analyzed by dissolving it in the electrolyte or by forming a thin film on the working electrode. Then, the voltage change is measured between the working electrode and the reference electrode (strongly altering the observed voltages), while the current is measured between the working electrode and the counter electrode. In this work, a comprehensive electrochemical analysis was performed using a standard three-electrode setup. The setup consisted of a glassy carbon electrode as the

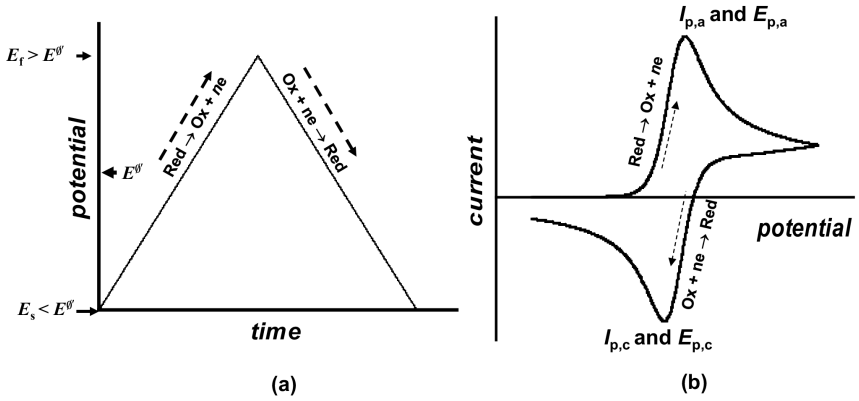

Figure 3.2: a) Time-dependent potential variation for a CV measurement and b) shape of the resulting current-potential diagram for a reversible system. Reproduced with permission from ref[168].

working electrode, platinum as the counter electrode, and a standard calomel electrode (SCE) as the reference electrode. Afterwards, the compound can be analyzed for its redox stability, the corresponding electron affinity/ionization potentials, and the reversibility of its redox processes. The utilized solvent has to be considered, as it limits the analyzable potential window, due to the solvent instability. Reversible redox reactions show a point symmetric curve progression. Oxidative processes are typically observed during voltage increases, while reductive processes are typically observed at decreasing voltages. In this work, the electron affinity/ionization potentials of the photocatalyst were investigated. It is important to note, that residual oxygen and water within the electrode setup show a strong sensitivity, resulting in strong peak formations.

3.6 Gas Chromatography with Mass Spectrometry Detection

Gas chromatography-mass spectrometry (GC-MS) is a powerful analytical technique that combines the features of gas chromatography (GC) and mass spectrometry (MS) to identify different substances within a test sample. This method is particularly important in the investigation of photocatalytic reactions and the identification of formed products. The fundamental structure of a GC-MS is illustrated in Figure 3.3. GC-MS analyses the molecular composition of a crude sample. Therefore, a solution of a crude sample dissolved in a volatile solvent (e.g. dichloromethane or acetonitrile), is submitted into an injector. The injector has a high temperature (200-300 °C), vaporizing the analyte. Utilizing a carrier gas (He, N_2, H_2) as a mobile phase, the vaporized analyte is introduced into a glass capillary column, which is coated with a thin film in the inside. This thin film acts as a stationary phase and often consists of polysiloxanes. While the helium carrier gas flows with a certain pressure, it carries the vaporized analyte along the stationary phase. The analyte interacts with the stationary phase based on its polarity, volatility, and molecular size, leading to varying retention times for the different compounds within the crude sample and ultimately achieving their separation. The column capillary is placed in a temperature-controlled oven and a temperature gradient is applied during the

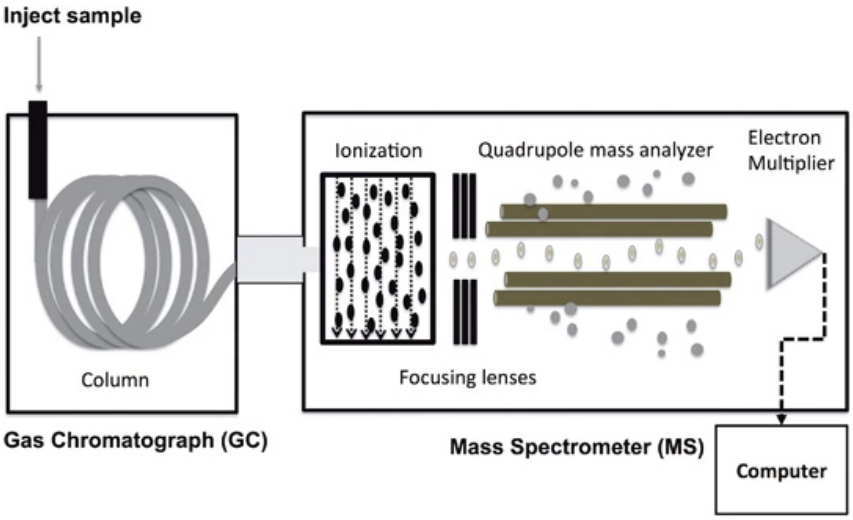

Figure 3.3: Schematic illustration of gas chromatography coupled with a mass spectrometer. Reproduced with permission from ref[169].

measurement, enhancing the separation. The separated molecules give a chromatogram, allowing for quantitative analysis of each compound. For qualitative analysis, a detector is required, here, a mass spectrometer. Each vaporized and separated molecule is trapped in an ionization chamber and ionized subsequently (using electron ionization). The resulting ionized molecules or molecular fragments are then separated by a quadrupole and the corresponding mass-to-charge ratios are obtained. These finally yield the mass spectrum of the analyzed compound. GC-MS enables precise determination of molecular species within crude samples, making it a powerful tool for evaluating kinetic reaction performance or analyzing challenging products.

3.7 Gel Permeation Chromatography

Gel permeation chromatography (GPC) is a well-established characterization technique for the determination of the molecular weight, size distribution, and dispersity of macromolecules or colloidal systems. It is a liquid size-exclusion chromatography technique, separating the analyte by size or hydrodynamic radius. An analyte solution is prepared and submitted onto a column. The column employs a solvent such as DMF or THF as the mobile phase and porous gel beads as the stationary phase, exhibiting defined pore sizes. The analyte is carried by the mobile phase along the stationary phase. Through exclusion or inclusion of the analyte in the pores, a size/molecular weight-based separation is achieved. Large molecules show exclusion of the pores and therefore elute earlier. Small molecules can enter the pores more easily, showing inclusion behavior, which leads to increased retention times. In GPC measurements, the separation solely relies on the pore inclusion/exclusion, as no stationary phase surface interactions are involved. Since GPC is not an absolute measurement, reliable results are obtained by referencing against a defined standard sample with known molecular weight and dispersity. The elugram and

molecular weight distributions obtained enable the analysis of dispersity, number-average molecular weight, weight-average molecular weight, and size-average molecular weight.

3.8 Electron Microscopy

In electron microscopy (EM), accelerated electron beams serve as the illumination source and are controlled similarly to optical light microscopes. Due to their significantly smaller wavelength compared to photons of visible light, electrons enable much higher resolutions, as governed by the Abbe diffraction limit. It allows the imaging of morphologies at dimensions down to several angstroms. The formation of supramolecular structures such as nanoparticles, nanocarriers, and fibers can thus be analyzed. Two popular types of electron microscopy are transmission electron microscopy (TEM) and scanning electron microscopy (SEM). For TEM, a high-voltage electron beam (40-400 keV) is focused by electromagnetic lenses and then transmitted through a thin sample (less than 100 nm thick). The sample is typically suspended on a copper grid, coated with a thin carbon film. The electron-matter interaction results in the scattering of electrons, while other electrons are transmitted through the sample. Therefore an inverted contrast image (dark field) is generated, as the transmitted electrons carry information about the characterized morphology, magnifying the structure on a detector. On the other hand, SEM utilizes electron scattering during electron-matter interactions. It employs a focused electron beam (0.2-40 keV) that raster scans across a sample. During the electron-matter interaction, secondary electrons are attracted to a positively charged detector and carry topographic information about the analyzed structure. Several other electronic signals, such as backscattered electrons or Auger electrons are observed, giving additional information about the sample. For SEM measurements, a thin film of the sample is deposited onto a small silicon wafer. The electrical conductivity and stability of the sample are of crucial importance. Overall, the SEM enables resolution from 1-20 nm. In this work, SEM and TEM were used to characterize the morphology of polymeric samples.

3.9 Gas Sorption

In gas sorption measurements, the porosity of solids and powders can be analyzed. By exploiting changes in adsorbed gas volume as a function of partial pressure, information about the material's porosity and pore size can be obtained. Building upon the Langmuir theory, the Brunauer, Emmett, and Teller (BET) model is employed to characterize the specific surface area of materials. This model describes interactions at the solid-gas interface using a multilayer adsorption model of the solid adsorption sites. The BET model posits that the gas (adsorbate) can physically adsorb in multiple layers on a solid surface and interact with adjacent adsorbate layers. It applies a monolayer adsorption theory to each layer, resulting in a pressure-dependent equation for surface coverage. The specific surface area is often described in cm^2/g. To perform the measurement, the prepared solid sample is dried thoroughly, to remove residual gases and liquids. Afterwards, the sample is placed under vacuum and cooled to -196 °C (for N_2 gas as adsorbate). Then the physisorption

of the adsorbate is measured and its corresponding volume change is plotted against the partial pressure. The resulting adsorption isotherm contains valuable information about the pore size distribution, the BET surface area, and the materials' adsorption behavior. It allows the determination if the material is microporous (<2 nm), mesoporous (2-50 nm), or macroporous (>50 nm). In photocatalytic material design, the accessible photocatalytically active surface strongly influences the catalytic efficiency, wherefore gas sorption measurements represent an important characterization technique. However, it has to be stated, that gas sorption measurements are valuable for qualitative analysis but may be insufficient for quantitative purposes.

Chapter 4

Microenvironment Effects on the Photocatalytic Activity of Polymeric Photocatalysts

Photocatalysis has attracted significant attention over the past few decades. However, its widespread application faces challenges due to the high costs associated with the necessary irradiation techniques. These techniques often require long reaction times and substantial energy input, limiting their feasibility for industrial use. To overcome these barriers, there is a pressing need for novel strategies that can boost the activity and efficiency of photocatalysts. One promising approach is to take inspiration from natural catalysts, such as enzymes. Specifically, the integration of a hydrophilicity gradient within a macromolecular system can potentially improve substrate specificity and catalytic reactivity. This hydrophilicity gradient should be tailored to match the hydrophilicity of the substrate, which facilitates effective mass transport to the catalytically active sites. Moreover, this custom-designed gradient can help suppress the formation of by-products and minimize side reactions, further enhancing the efficiency and selectivity of the photocatalytic process.

When applied to synthetic photocatalysts, this design strategy is expected to significantly enhance photocatalytic activity while incorporating substrate specificity. As discussed in Section 1.5, the effects of confinement space and modified microenvironments profoundly influence catalytic activity and reactivity. To explore the potential for controlling photocatalytic selectivity, we synthesized and tested macromolecular photocatalysts with varying microenvironments, assessing their dependency on different substrates for photocatalytic performance.

The following Chapter 4 is based on two articles and discusses the effect of changes in the microenvironment on the conversion rate of photocatalytic reactions. Two different approaches will be evaluated. In the first article, presented in section 4.2, the effect of differently hydrophilic macromolecular microenvironments around the photocatalytic center will be discussed. The second article, presented in section 4.3, will elaborate on mimicking different macromolecular solvent microenvironments around the photocatalytic center.

The first sections (section 4.1 and 4.2) are based on the manuscript "Tunable Photocatalytic Selectivity by Altering the Active Center Microenvironment of an Organic Polymer Photocatalyst" published in *ACS Appl. Mater. Interfaces* 2023, 15, 2, 2891–2900.[165] This work represents a collaborative project in which I was responsible for the synthesis, characterization, and photocatalytic performance studies of the photocatalytic nanoparticles. Thomas Kuckhoff performed the synthesis of the photocatalytic monomer and Rong Li provided strong support in the synthesis and purification of the polymeric nanoparticles. Paragraphs, sections and sentences that have been adopted from this article are indicated by quotation marks ("").

In this work the creation of a differently hydrophilic/ hydrophobic macromolecular microenvironment around the photocatalytic center and the corresponding effect on the photocatalytic activity is discussed. Therefore, the copolymerization of a small molecule photocatalyst into amphiphilic polymer chains was conducted. A defined localization of the photocatalytic unit in the polymer chains was targeted. Polymerization-induced self-assembly (PISA) reversible addition-fragmentation chain-transfer (RAFT) polymerization was utilized for the polymerization process, resulting in the formation of defined polymeric nanoparticles. Depending on the photocatalyst copolymerization, the photocatalyst is either located in the hydrophilic domain of the amphiphilic polymer chain (nanoparticle shell) or in the hydrophobic domain (nanoparticle core) of the amphiphilic polymer. Therefore, solely spatial microenvironment effects were expected, when comparing the photocatalytic reactivity of the two systems. For polar substrates, enhanced reaction rates were expected for the hydrophilic photocatalytic microenvironment. Conversely, hydrophobic substrates were assumed to show faster conversion rates in the hydrophobic microenvironment.

Furthermore, the second article (section 4.3) covers the work of the collaborative project "Comonomer effects in vinyl based photocatalytic polymers", published in *RSC Appl. Polym.*, 2024, 2, 155-162.[170] In this work, Thomas Kuckhoff was responsible for the design, synthesis, and characterization of the photocatalytic polymers. He also investigated their variations in photocatalytic reactivity. My role involved resynthesizing these photocatalytic polymers, performing Density Functional Theory (DFT) calculations, and assessing their photocatalytic reactivity in the C-C coupling reaction between 3-methyl indole and diethyl bromomalonate.

The objective of this study was to examine the influence of the microenvironment generated by the copolymerized comonomers. This study specifically aimed to investigate the impact of adjacent copolymer units within the polymer chain on the performance of the photocatalyst. A comprehensive understanding of this relationship is essential for the rational design of polymers with optimized photocatalytic properties. In this study, a series of vinyl-based polymers, copolymerized with a vinyl-based diphenylbenzothiadiazole photocatalyst, were synthesized. The photocatalyst-functionalized homopolymers were subjected to a thorough analysis to elucidate the copolymer-induced effects on the photophysical properties and photocatalytic activity.

4.1 Motivation

"Catalysis has become one of the central anchors of organic chemistry, with evermore sophisticated catalytic systems reported every year.[171, 172] Much of this progress has been in the pursuit of selective catalysis. For the preferential generation of a specific stereoisomer at increased reaction rates, enantioselective catalysts are targeted.[173,–176] However, many of these synthetic catalysts still produce undesired side products, due to impure starting materials, functional group interference, or insufficient substrate selectivity.[177, 178] The broad variety of products leads to increased separation and purification costs, as well as poor selectivity and therefore reduced sustainability.[179]"

"Enzymes are nature's catalysts, exhibiting inherent selectivity for a specific substrate and the formation of its desired corresponding product. From a pool of substrates, a single species is converted into a specific product with maximum selectivity.[180, 181] This selectivity stems from the variation of two key components within these biomaterials, the active center and the macromolecular structure. The three-dimensional macromolecular structure selects the substrate based on its polarity and electronic configuration, while the active center within the enzyme determines the spatial conformation of the substrate through interaction with protruding local amino acid residues. To date, much of the selective catalysis research has aimed to miniaturize and reproduce a synthetic enzymatic active center.[182,–184] However, the macromolecular nature of enzymes plays an essential role in substrate specificity by retaining different functionalities or shielding the active site from water.[134, 182,–186] Recent advances in macromolecular chemistry have enabled intricate catalytic sites to be produced, showing increased substrate selectivity. Yet, the scalability of macromolecular catalytic systems can often be a major challenge, due to the complexity of the catalyst and challenging recovery processes.[182, 186]"

"To mimic enzymatic substrate specificity and selectivity, the development of synthetic macromolecular catalytic systems should be targeted, where the macromolecular structure induces a particular reaction selectivity. This polymeric material should contain catalytic centers comparable to enzymatic active sites, where transformations take place. The selected reactive sites should enable the catalysis for a broad range of reactions to create a versatile catalytic center. By controlling the microenvironment around the catalytic centers, the spatial proximity of the substrate to the catalyst could be controlled, potentially reducing side reactions and therefore inducing selectivity. Additionally, the heterogeneous catalytic system should be readily dispersible or soluble in green solvents such as water, whilst being capable of processing a broad range of reagents with varying polarities. Finally, the catalytic material should be reusable and have the potential for future scalability."

"Over the past decade, photocatalysis has proven to be a reliable and valuable synthetic tool, with numerous reported examples of photocatalytic variants for classical catalytic reactions.[35, 187,–190] Through harnessing of visible light, photocatalysis facilitates a large array of different chemical reactions.[187] Additionally, changes within the photocatalysts' molecular structure allow enhanced control over the desired reaction through adjustable physicochemical properties, such as redox potential and lifetime.[35, 188,–190] Embedding

photocatalysts into macro- or supramolecular structures offers additional opportunities for tunability through morphological control, therefore enabling photocatalyst compartmentalization and enhanced substrate accessibility.[80, 94, 126, 191] A homogeneous, nanoscale distribution of photocatalysts within polymersomes,[80] micelles,[126] nanoparticles,[192] and on surfaces[193] has been reported, but the desired implementation of selectivity concepts into these structures is still a subject of on-going research.[38, 94, 191]"

"The versatility of photocatalysis has already been demonstrated in a variety of chemical reactions such as water splitting,[46, 194] CO_2 reduction,[52, 195] organic pollutant degradation,[196] C-C coupling reactions,[53, 197, 198] C=C bond cleavage,[57, 58, 70] metal reduction,[199] oxidative coupling of amines,[93] trifluoromethylation of arenes,[63] oxidation of sulfides,[93] free radical polymerizations,[200,–202] dehalogenation of halo ketones,[66] photodynamic therapy,[71, 203, 204] heterocycle formation,[67] bacterial treatment[205] and enantioselective alpha-alkylation.[68] However, the scope in selectivity has been limited to date with restricted control given by the structural properties of the photocatalyst. Some selectivity has been achieved due to the inherent selectivity within the photocatalytic mechanism.[154, 206]"

To investigate the effect of different macromolecular microenvironments on the photocatalytic activity of heterogeneous photocatalysts, two different studies are presented in this thesis. The following section, 4.2, examines the impact of varying hydrophilic and hydrophobic microenvironments around the photocatalytic center. The conversion rate disparity of photocatalytic reactions will be investigated in relation to the hydrophilic or hydrophobic microenvironment and correlated with substrate hydrophilicity. Moreover, section 4.3 discusses the effect of varying copolymers around the photocatalytic center, mimicking different solvent microenvironments. The corresponding effect of different copolymers on the conversion rate of photocatalytic reactions and their influence on the optoelectronic properties of the copolymerized photocatalyst will be elaborated.

4.2 Tunable Photocatalytic Selectivity by Altering the Active Center Microenvironment of an Organic Polymer Photocatalyst

"Here, we report photocatalyst-embedded polymeric nanoparticles, where the location of the photocatalytic center can be tuned (Figure 4.1). The variation from a hydrophilic to a hydrophobic microenvironment of the photocatalytic center induces an increase in selectivity and differing reaction rates depending on the polarity of the substrate. This macromolecular photocatalytic system was synthesized using RAFT-PISA, where a photocatalytic monomer could be readily polymerized into the polymer at a specified location.[95, 98] Previously, photocatalytic self-assembled particles have been reported where the inclusion of the photocatalytic moiety has been concentrated in either the hydrophilic or hydrophobic portion. Conflicting reports and confusion seem to have arisen over whether inclusion into either phase is preferential.[91, 92, 95, 98, 99] Here, we elucidate some of the dynamics within the photocatalytic material by investigating three model reactions and aim to use these dynamics to invoke preferential reactivity in these reactions. Lastly, the microenvironment of the photocatalyst was further modified through the introduction

of a secondary solvent that preferentially swells the self-assembled material, enhancing reagent exchange and reaction conversion."

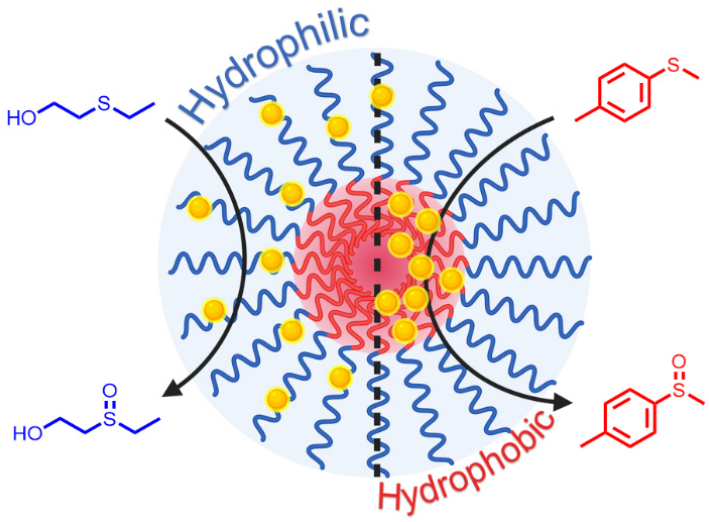

Figure 4.1: Polymeric nanoparticles modified with covalently bound photocatalysts at different chain positions (yellow dots), showing higher substrate conversions aligning with respective substrate hydrophilicity (blue=hydrophilic, red=hydrophobic). Reproduced with permission from ref[165].

"Polymer-based, photocatalytic nanoparticles were synthesized by RAFT-PISA (Figure 4.2). First, a macromolecular chain transfer agent (mCTA) was prepared by reacting the water-soluble trithiocarbonate 4-((((2-carboxyethyl)thio)carbonothioyl)thio)-4-cyanopentanoic acid (CCCP) with 100 equivalents of the hydrophilic monomer glyceryl monomethacrylate (GMA). The required amphiphilicity of the polymer was achieved by blocking off with 200 equivalents of the hydrophobic monomer benzyl methacrylate (BzMA), which resulted in dispersion-based polymerization-induced self-assembly (PISA) into homogeneous nanoparticles. Depending on the addition of the photocatalyst 4-(7-phenylbenzo-[1,2,5]thiadiazol-4-yl)benzyl methacrylate (BTPMA) during either the hydrophilic mCTA synthesis or during the hydrophobic blocking off, its position within the polymer chain was controlled. For the incorporation of the photocatalyst in both positions, colloidally stable homogeneous, spherical, polymeric nanoparticles of discrete size and solid content were formed (Figure 4.5).[207,–209]"

"Characterization by ^{1}H-NMR spectroscopy of the amphiphilic block copolymer systems revealed similar conversion rates and photocatalyst incorporation for the hydrophilic and hydrophobic located photocatalyst polymer (Figure 4.2). Using ^{1}H-NMR spectroscopy, a precise determination and characterization of the GMA and BzMA blocks of the polymeric nanoparticles was possible. However, due to the low targeted loading of photocatalyst into the polymer chain of 2 equivalents, the determination of photocatalyst incorporation, solely by NMR spectroscopy was not possible. As shown in Figure 4.2, the ^{1}H-NMR signal for H_6 corresponds to the aromatic groups of the photocatalyst, but this signal gets lost in the background noise due to the presence of the strong polymer peaks. A minimal

difference in photocatalyst incorporation between the hydrophilic and the hydrophobic-located photocatalyst was visible. The small differences in conversion rate may be due to the prior copolymerization of the hydrophobic photocatalyst into the hydrophilic block, disfavoring the hydrophilic steric stabilization."

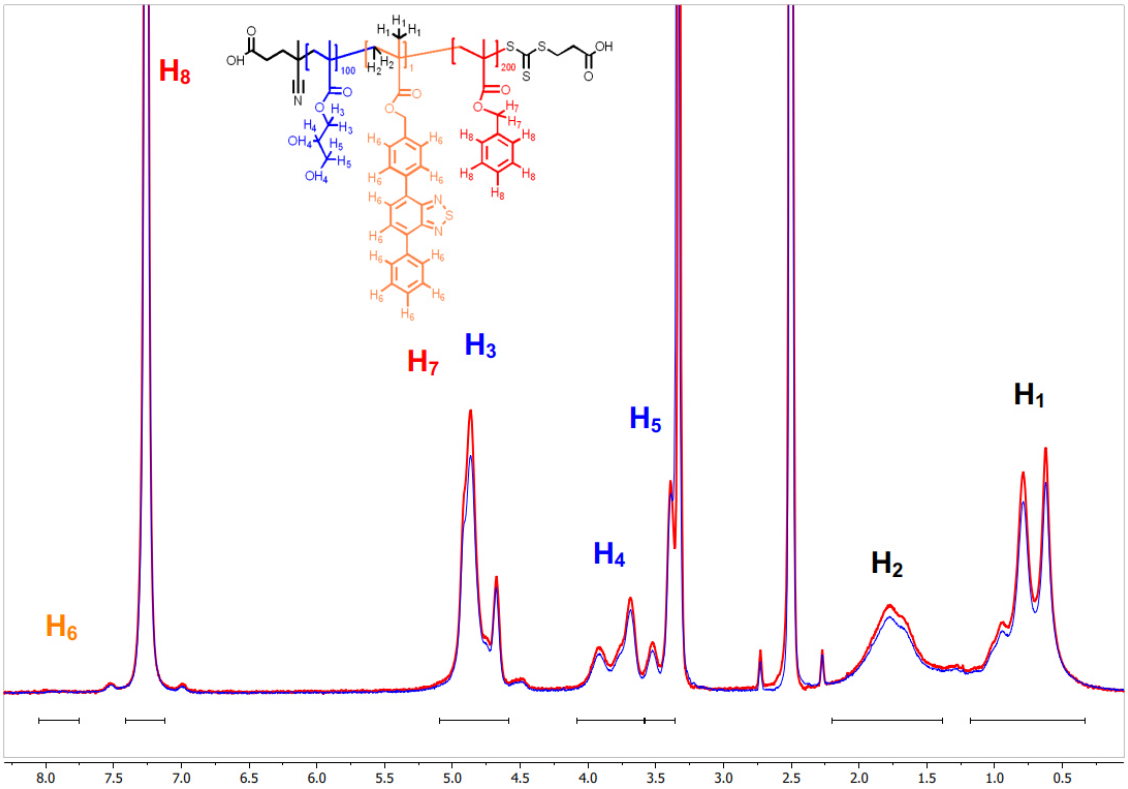

Figure 4.2: Superimposed ^{1}H-NMR spectra of the amphiphilic block-copolymer with the hydrophobic located photocatalyst (red line) and the hydrophilic located photocatalyst (blue line). The respective ^{1}H-signals are assigned to their structural position. Reproduced with permission from ref[165].

"Gel permeation chromatography (GPC) analysis gave identical elution times and a polydispersity of 1.5 for both photocatalytic systems, which is higher than typically achieved for RAFT-mediated PISA, but probably arises from the inclusion of the photocatalytic monomer (Figure 4.3, right). Consulting the results of the NMR studies and correlating these with the obtained GPC results, the determination of monomer ratios within the polymers was achieved. The ratios were found to be: $P(GMA)_{96}$–*b*–$P(BzMA)_{210}$–$BTPMA_{1.08}$ for the hydrophilic located photocatalyst and $P(GMA)_{99}$–*b*–$P(BzMA)_{217}$–$BTPMA_{1.07}$ for the hydrophobic located photocatalyst."

Additionally, the prepared photocatalytic systems were characterized by FTIR spectroscopy. Herein, the broad absorption bands at 3436 and 2946 cm^{-1} correspond to aliphatic C-H and secondary amine stretches. The strong absorption band at 1730 cm^{-1} is associated with the C=O stretch and at 1158 cm^{-1} with the C-O stretch of the methacrylate esters. Furthermore, the methyl group of the methacrylate units was confirmed with the 1448 cm^{-1} absorption band. Several broad peaks below 1000 cm^{-1} were observed, indicating the occurrence of aromatic C-H groups, but could not be quantified precisely, due to the

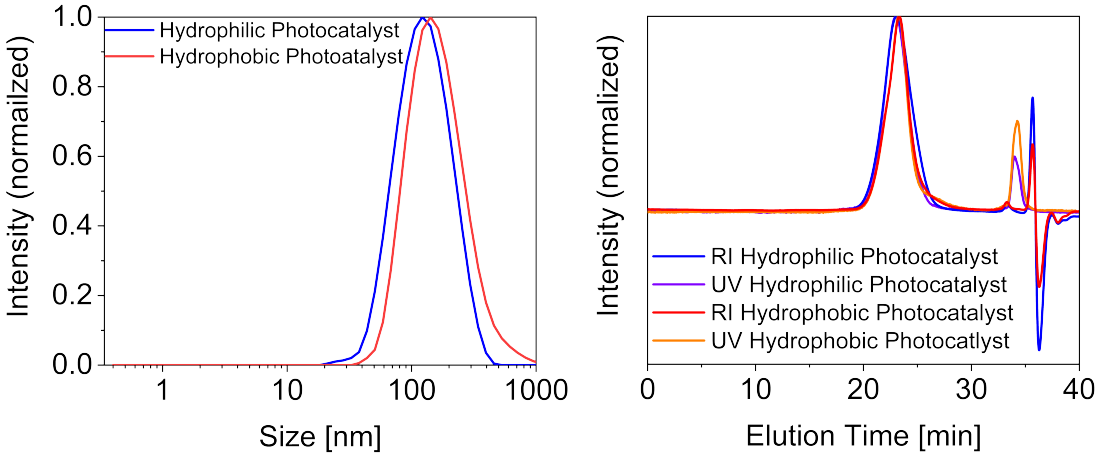

Figure 4.3: Left: Dynamic light scattering measurements of the hydrophilic and the hydrophobic located photocatalytic nanoparticles in H_2O. The comparison of both systems shows minimal differences in size. Particle distribution (PD) is 1.5 for hydrophilic and hydrophobic photocatalyst. Right: Comparison of the GPC elution diagram of both photocatalytic polymers. Using DMF as eluent with PMMA standard. Reproduced with permission from ref[165].

presence of varying aromatics within the systems. In total, negligible differences were observed between the two species within FTIR spectroscopy (Figure 4.4).

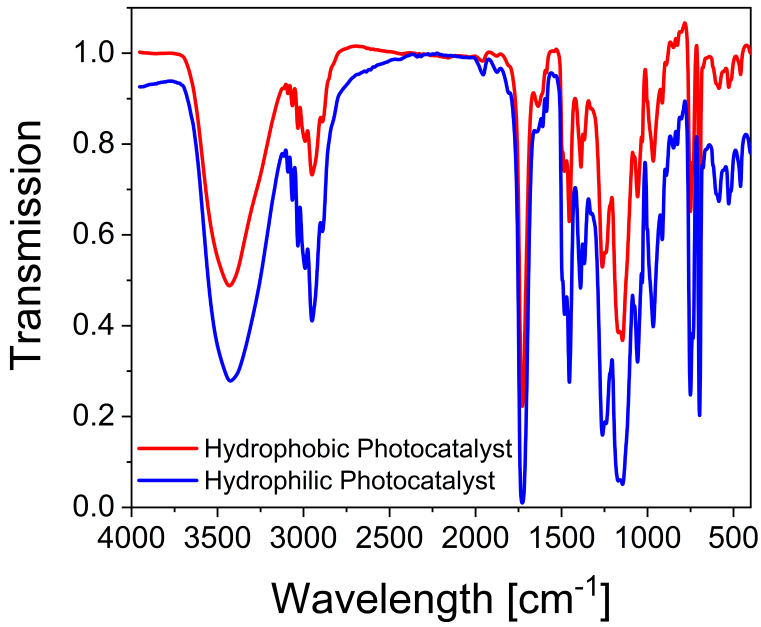

Figure 4.4: FTIR spectra and comparison of the hydrophilic and hydrophobic located photocatalytic polymer. Reproduced with permission from ref[165].

"The structural morphology and size of the self-assembled polymers were analyzed by transmission electron microscopy (TEM) and dynamic light scattering (DLS) measurements, indicating homogeneous nanoparticle formation with monomodal size distributions. The average size diameters obtained by TEM showed 40±5 nm spherical nanoparticles for both species (Figure 4.5). DLS analysis gave an average hydrodynamic radius of 140±10 nm (Figure 4.3 left). The DLS measurement revealed a marginally higher hydrodynamic diameter for the hydrophobic-located photocatalyst, attributed to the slightly higher BzMA conversion within the nanoparticle formation process. The size difference between TEM and DLS may be due to morphological changes upon drying of the nanoparticles for TEM analysis."

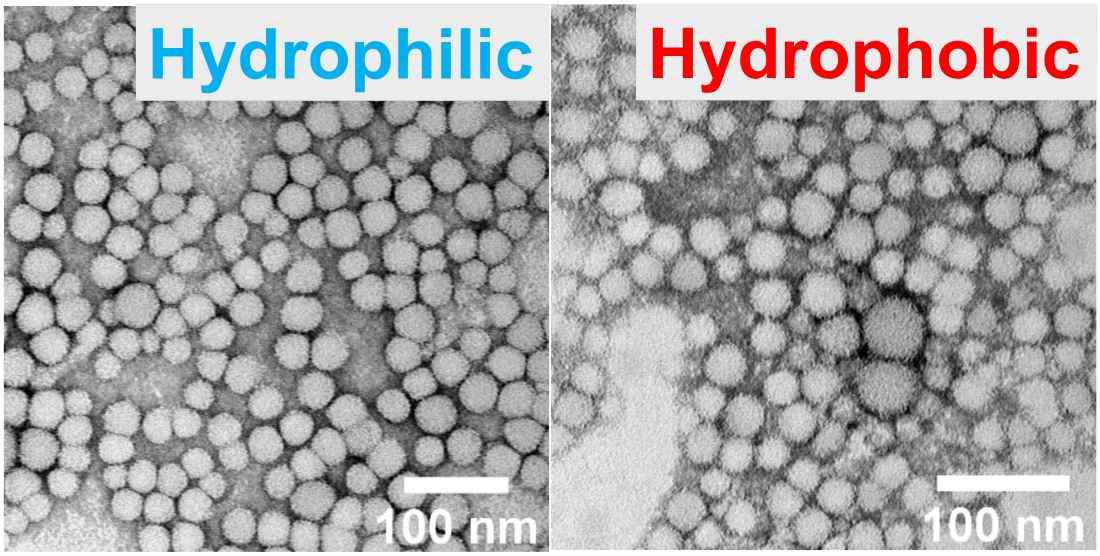

Figure 4.5: TEM images of the hydrophilic (left) and hydrophobic (right) located photocatalyst nanoparticles. Reproduced with permission from ref[165].

"UV-Vis absorption spectroscopy of both polymeric nanoparticles was conducted. Both samples were dissolved in dimethyl sulfoxide (DMSO) to guarantee full disassembly of the nanoparticles. Between the two samples only a small difference of 3% in absorption at the characteristic maximum absorption wavelength (373 nm) of the photocatalyst within the UV-A region was observed (Figure 4.6). A slightly higher difference of 7% was observed at the overlapping absorption wavelength of the polymer backbone and the energetically higher UV-B absorption peak of the photocatalyst at around 307 nm. These modest differences suggest a minimal deviation in the incorporation of the BTPMA and BzMA, which supports the structural characterization with NMR analysis (Figure 4.2). These findings strongly suggest, that differences in photocatalytic reactivity between the two systems are exclusively reliant on the spatial location of the photocatalytically active site, as both systems exhibit a comparable loading of photocatalyst."

Further characterizing the photophysical properties of the synthesized photocatalysts, the emission behavior was investigated with an excitation at 373 nm. Both systems were again dissolved in DMSO and an intense emission peak at around 500 nm was observed for

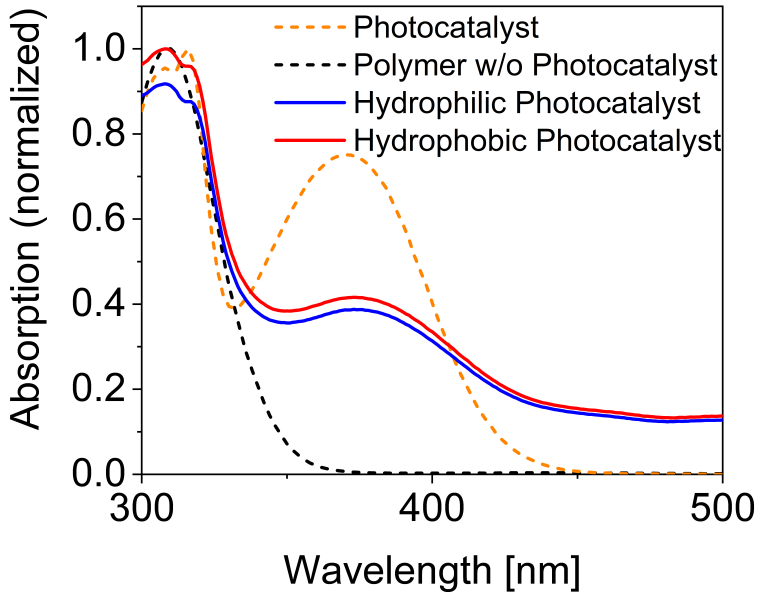

Figure 4.6: UV/VIS-absorption spectra, comparing the photophysical activity of both nanoparticle systems. Showing minimal differences of 3% between the systems at 373 nm. Reproduced with permission from ref[165].

both polymers, which is attributed to the characteristic emission behavior of the BTPMA photocatalyst (Figure 4.7). Comparing the observed emission behavior to the identical systems dispersed in water, severe differences in the emission spectra were found. The strong increase in emission at around 400 nm and the parallel decrease at 500 nm indicates the occurrence of scattering phenomena, therefore inhibiting the proper excitation of the photocatalytic unit. The observation was made for both systems.

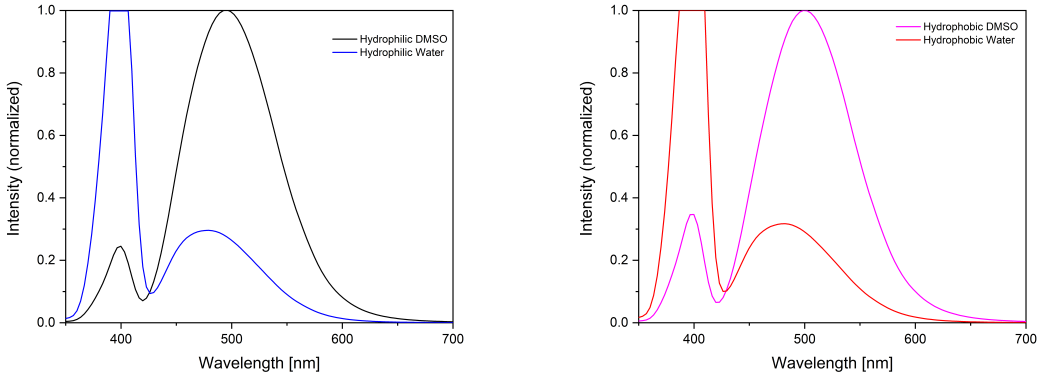

Figure 4.7: Emission spectra for the hydrophilic (left) and the hydrophobic (right) localized photocatalyst nanoparticle. Comparison between water and DMSO as solvent reveals high scattering peak at 400 nm in water and higher photocatalyst emission in DMSO at 501 nm. Reproduced with permission from ref[165].

As the synthesized polymeric nanoparticles are supposed to be utilized as photocatalyst in a variety of reactions, the photocatalytic activity should be analyzed. In literature,

diphenylbenzothiadiazole-based photocatalysts are well-established for the ROS-mediated oxidation of compounds. These photocatalysts are reportedly strong ROS generators, primarily generating singlet oxygen."The generation of singlet oxygen for both systems was monitored by electron paramagnetic resonance (EPR) spectroscopy. Therefore, the photocatalytic nanoparticles were dispersed in an aqueous solution and irradiated for 10 min at 465 nm. Afterwards, the trapping agent (2,2,6,6-tetramethylpiperidin-1-yl)oxyl (TEMPO) was added to the reaction mixture and the trapped oxygen radical was used to analyze the singlet oxygen generation (Figure 4.8). For both samples the generation of singlet oxygen was detected, however, the hydrophobic-located photocatalyst showed a slightly higher signal. Considering the lipophilicity of the trapping agent and oxygen, a possible higher concentration of trapping agent and oxygen around the hydrophobic-located photocatalyst may explain an increased formation of TEMPO compared to the hydrophilic-located photocatalyst."

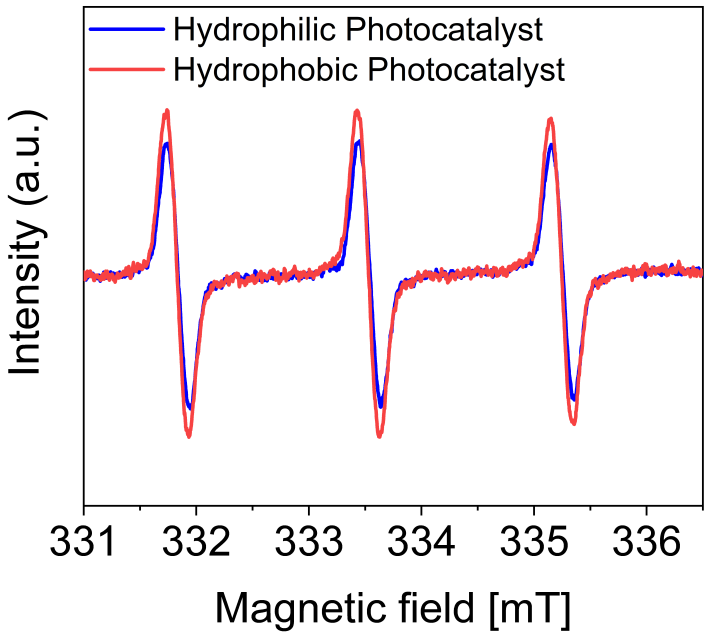

Figure 4.8: Electron paramagnetic resonance spectra comparing the singlet oxygen generation of both nanoparticle systems after 10 min of 465 nm LED irradiation in H_2O with TEMPO trapping. Reproduced with permission from ref[165].

"To investigate the impact of the microenvironment on photocatalytic activity, we evaluated the nanoparticles' reactivity in a sulfide oxidation reaction. A series of substrates with varying functional groups were selected, taking into account their structural and electronic properties. These substrates were characterized by their Log P value, which provides an approximation of membrane permeability and solvation of a compound. The Log P values allowed an estimation of the substrate location within the nanoparticle system (Figure 4.10 right).[210] Figure 4.9 shows the kinetic profiles of the sulfide oxidation reaction for three thioethers (increasing in hydrophobicity from left to right) into sulfoxides under identical reaction conditions. A clear difference in the conversion of 2-(ethylthio)ethan-1-ol (Log

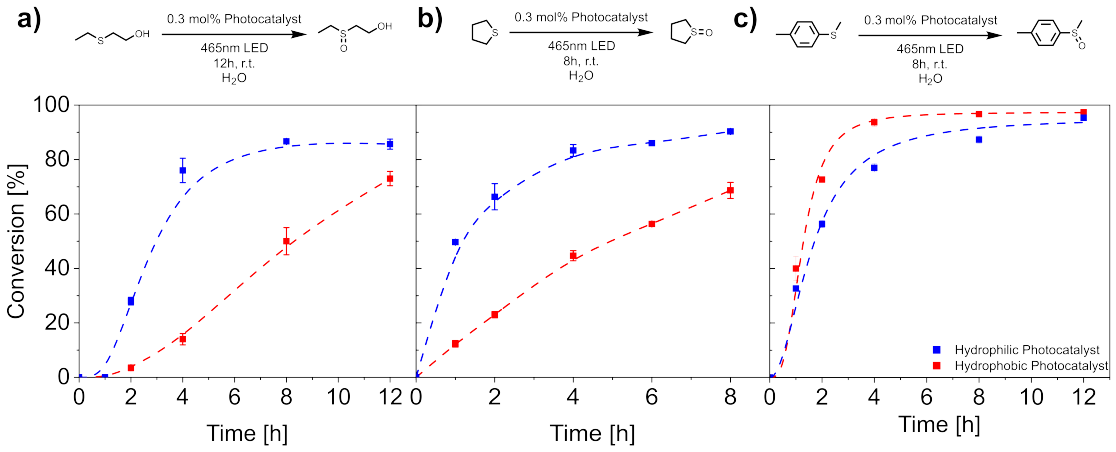

Figure 4.9: Kinetic profiles of the sulfide oxidation reaction performed by both polymeric, photocatalytic nanoparticles. Ranked from left to right from the most hydrophilic to the most hydrophobic substrates, underlining the dependence on substrate hydrophilicity. a) Oxidation of 2-(ethylsulfanyl)ethanol. b) Oxidation of tetrahydrothiophene. c) Oxidation of methyl p-tolyl sulfide. Conditions: Sulfide species (19.96 µmol), photocatalyst polymer (0.096 µmol, 0.3 mol% photocatalyst), dispersed in H_2O (2 mL, sonicated 20 min), 15 °C, 7.14 W, 465 nm, 16 h. The conversion was calculated from GC measurements by comparison of peak area intensity. Reproduced with permission from ref[165].

P=0.63), the most hydrophilic substrate, between the hydrophilic and hydrophobic located photocatalyst was observed (Figure 4.9a). Specifically, a faster rate of conversion with a maximum difference of 62% after 4 h was observed for the hydrophilic-based photocatalyst compared to the hydrophobic one, plateauing at 80% for both photocatalytic systems (product Log P=-1.32). Conversely, the hydrophobic-based catalyst had only converted around 70% of the hydrophobic substrate after 12 h. A similar trend was observed for tetrahydrothiophene (Log P=1.13) (Figure 4.9b), where the conversion was again faster in the hydrophilic system than in the hydrophobic one (product Log P=-0.83). Interestingly, in the case of the most hydrophobic substrate methyl p-tolyl sulfide (Log P=2.96) (Figure 4.9c), the photocatalyst in the hydrophobic microenvironment outperformed the hydrophilic equivalent. Here, the hydrophobic-located photocatalyst showed a faster conversion with a maximum difference of 16% after 4 h compared to the hydrophilic-located photocatalyst (product Log P=1.18). Interestingly, a linear relationship is observed between the substrate lipophilicity (Log P) and the substrate conversion difference after 4 h reaction time (Figure 4.10 right). Lastly, a recyclability screening of the polymeric, photocatalytic nanoparticles was demonstrated for the oxidation of 4-(methylthio)toluene. It was found, that the photocatalyst showed high performance of the recycled material, showing a conversion of 95% for up to 4 cycles (Figure 4.10 left)."

"The sulfide oxidation reaction mechanism is initiated by a nucleophilic attack of thioether by the reactive oxygen species, such as singlet oxygen, and is therefore highly dependent on local oxygen concentration.[211] Oxygen accessibility may be higher in the aqueous environment compared to the packed particle core, even though oxygen has a more hydrophobic character. The reactivity of hydrophilic, photocatalytic mCTA was

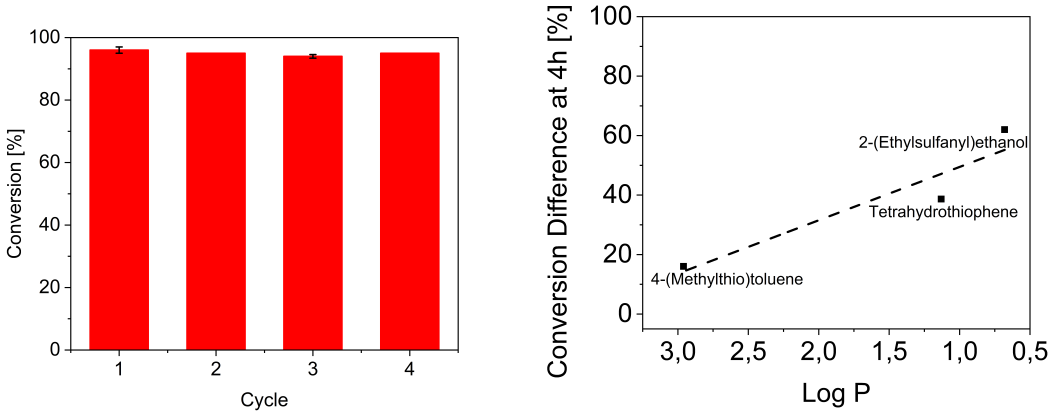

Figure 4.10: Left: Recyclability investigation for the photooxidation of 4-(methylthio)toluene to the corresponding sulfoxide. The reaction was performed under standard conditions in triplicates. Right: Log P-values of sulfide oxidation starting materials against conversion rate after 4 h reaction time. (Log P-values obtained by ChemDraw 20.1, using the methodology of a literature reference.[210]) Reproduced with permission from ref[165].

compared to hydrophilic-located photocatalytic nanoparticles towards the sulfide oxidation of 4-(methylthio)toluene, showing higher conversion for the mCTA, due to increased oxygen accessibility (Figure 4.12 right). When using a hydrophilic substrate, the product formation is favored within the hydrophilic microenvironment, due to enhanced spatial proximity of the substrate to the active site and higher oxygen concentration compared to the hydrophobic system. When a more hydrophobic substrate is selected, it will preferentially partition into the hydrophobic phase of the self-assembled particle, increasing the spatial proximity to the hydrophobic active site. This increase in local concentration of the substrate around the hydrophobic active center might surpass the impact of slow oxygen diffusion into the hydrophobic portion of the nanoparticle and the inherently increased reaction rate by strongly electron donating functional groups, resulting in a slightly higher conversion within the hydrophobic microenvironment. Ideally, the reactivity of 4,7-diphenyl-2,1,3-benzothiadiazole (the small molecule photocatalyst) should be compared to the polymeric photocatalyst under identical reaction conditions, but due to the photocatalysts' insolubility in water, this was not possible."

"To investigate the microenvironment impact on aromatic compounds, three substrates of varying Log P values were investigated towards an oxidative imine formation (Figure 4.11). The imine formation of 3,4-dimethoxybenzylamine (Log P=0.83) was selected as the most hydrophilic substrate. Initially, a similar reaction rate was observed for both photocatalytic microenvironments. However, after 4 h, the reaction rate diverges, with the hydrophilic photocatalyst outperforming the hydrophobic one (product Log P=3.47) (Figure 4.11a). Due to increased substrate hydrophilicity compared to the other substrates, a higher substrate and oxygen accessibility for the photocatalyst is expected. Together with the decreased reactivity of the electron-withdrawing functional groups, a slower reaction rate is assumed, which is reflected in the slowly diverging kinetic profile.[212] A similar but less

prominent trend was also observed for the coupling of benzylamine (Log P=1.08), where the hydrophilic microenvironment slightly outperformed the hydrophobic one (product Log P=3.97) (Figure 4.11b). Due to its strong electron-donating character, which increases the oxidation reaction rate, the coupling of strongly hydrophobic 4-tert-butylbenzylamine (Log P=2.78) showed no differences between the kinetic profiles (product Log P=7.38) (Figure 4.11c)."

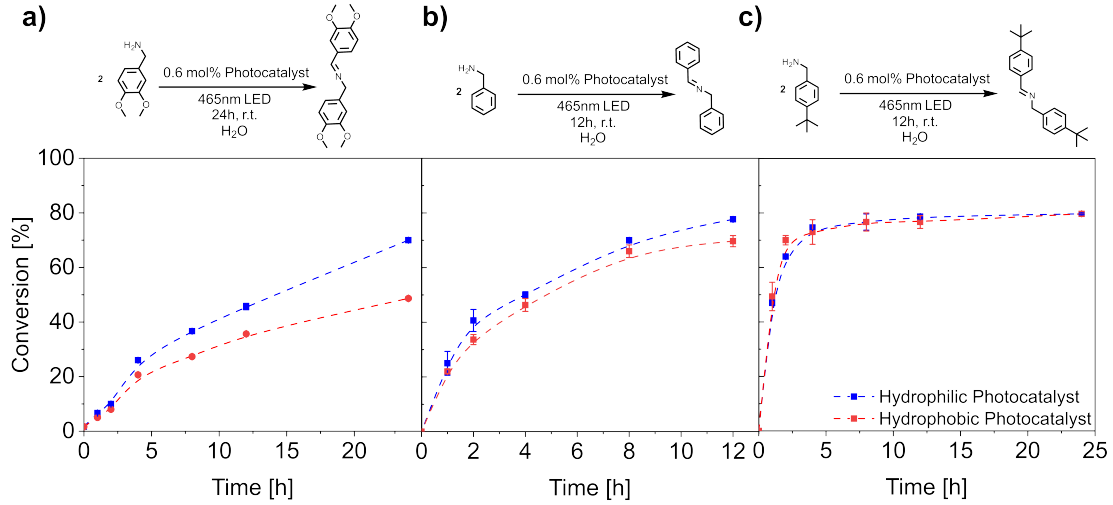

Figure 4.11: Kinetic profiles of the imine formation reaction performed by both polymeric, photocatalytic nanoparticles. Ranked from left to right from the most hydrophilic to the most hydrophobic substrates, underlining the dependence on substrate hydrophilicity. (a) Reaction of 3,4-dimethoxybenzylamine. (b) Reaction of benzylamine. (c) Reaction of 4-tert-butylbenzylamine. Conditions: Benzylic amine species (13.5 µmol), photocatalyst polymer (0.192 µmol, 0.6 mol% photocatalyst), dispersed in H_2O (2 mL, sonicated 20 min), 15 °C, 7.14 W, 465 nm, 16 h. The conversion was calculated from GC measurements by comparison of peak area intensity. Reproduced with permission from ref[165].

"It was expected that, by investigation of hydrophobic functional groups such as tert-butyl groups, the hydrophobic based photocatalyst would outperform its hydrophilic analog. The constant differences in reactivity suggest a limitation of the reaction rate within the hydrophobic microenvironment by hindered substrate diffusion. The self-assembled photocatalytic particles have a fully solvated hydrophilic shell and a precipitated hydrophobic core. Mass transfer into the core is therefore slower than to the corona, affecting reaction kinetics. This appears to be more prevalent for reactions that proceed through reactive oxygen species, where diffusion of the substrate and oxygen are required. Also, the lifetime of these ROS is variable, depending on the microenvironment, which may also play an important role. With careful consideration of the reaction mechanism, the increased reaction rate of more hydrophobic substrates can be explained by electron donating character of the substituents, therefore increasing the electron density of the sulfide, accelerating the formation of the reactive peroxysulfoxide species.[213] These factors may account for the marginal observed differences within the discussed imine formation (Figure 4.11). Since the reaction conditions require singlet oxygen and benzylic amines, which are

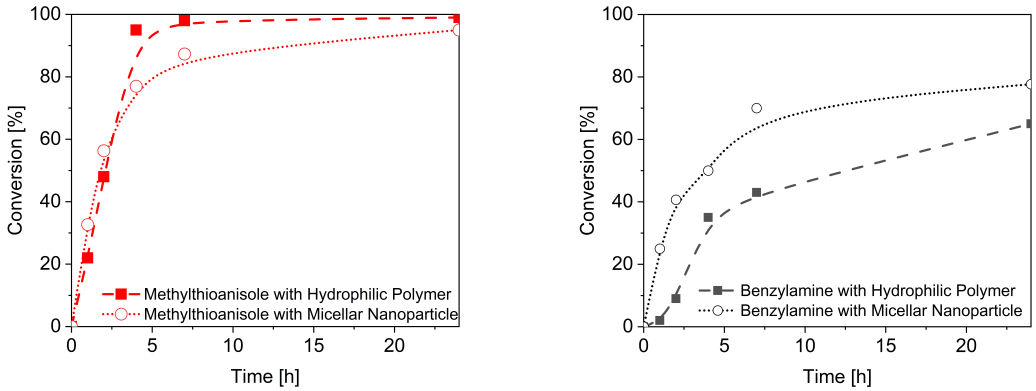

Figure 4.12: Left: Comparison of reactivity towards the sulfide oxidation of 4-(methylthio)toluene of photocatalytic, hydrophilic polymer (mCTA) and photocatalytic, amphiphilic polymeric nanoparticles. Right: Comparison of reactivity towards the imine formation of benzylamine of photocatalytic, hydrophilic polymer (mCTA) and photocatalytic, amphiphilic polymeric nanoparticles. Reproduced with permission from ref[165].

generally more hydrophobic than the investigated sulfide oxidation substrates, the diffusional exchange between the continuous phase and the hydrophobic core could represent a rate-limiting transfer process.[212] To further investigate the effect of the nanoparticle core, the hydrophilic, photocatalytic mCTA was compared against the hydrophilic-located photocatalyst nanoparticles. A higher conversion for the nanoparticle was observed, possibly explained by an increased substrate accessibility and accumulation of benzylic amines within the core (Figure 4.12 right)."

"Lastly, a reductive dehalogenation of 2-bromobenzaldehyde (Log P=2.61) with a subsequent radical-radical coupling (product Log P=3.2) was performed in an aqueous dispersion of the photocatalytic nanoparticles, using additional 0.75 vol% of triethylamine as a sacrificial agent.[214, 215] Initially, a low total conversion was observed for both the hydrophilic and the hydrophobic photocatalyst, which may be due to the induced spatial division of 2-bromobenzaldehyde, accumulating inside the dense particle core due to its hydrophobic character, while the relatively hydrophilic triethylamine is located within the aqueous solution (Figure 4.13 left). To enhance the core accessibility and improve phase exchange, 0.75 vol% of additional swelling solvents with varying hydrophilicity and singlet oxygen stabilizations were investigated regarding their influence on reactivity (Figure 4.13 left)."

"The addition of hydrophobic toluene showed a small improvement in conversion for both photocatalytic systems by swelling the particle core and increasing interphasic reagent exchange. Hexafluorobenzene (HFB) additionally stabilizes singlet oxygen, resulting in a 2-fold increase for the hydrophilic photocatalyst compared to the additive-free reaction (Figure 4.13 left).[216, 217] The hydrophobic photocatalyst showed an identical conversion improvement after the addition of HFB compared to the addition of toluene, possibly reasoned by diffusional limitations of substrate and oxygen into the hydrophobic particle core.

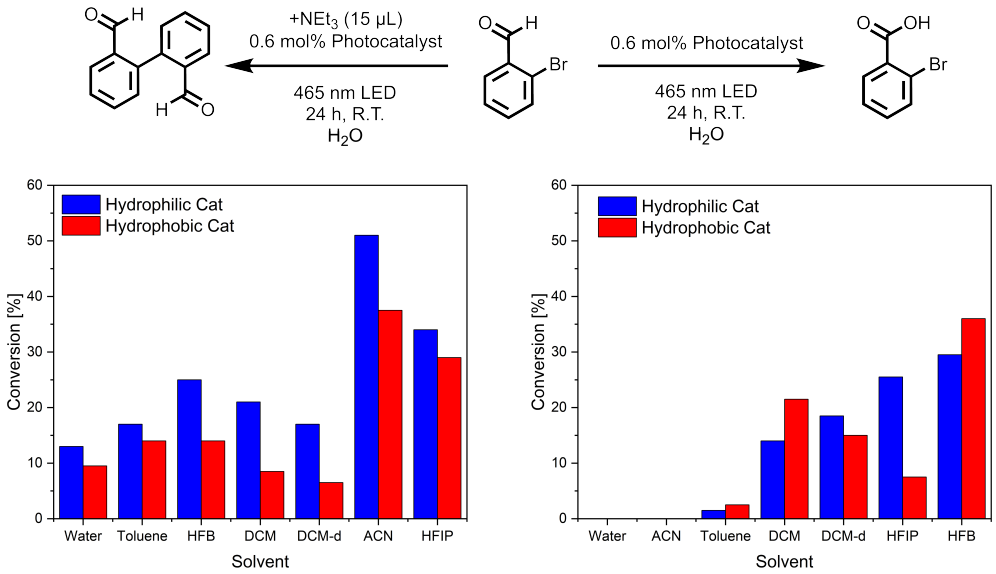

Figure 4.13: Investigation into the influences of different swelling additives on the photocatalytic reactivity of 2-bromobenzaldehyde. Left: Observation of a C-C coupling and the corresponding influences of different swelling solvents. The reaction occurs under addition of triethylamine. Right: Oxidation to bromobenzoic acid and the corresponding influences of different swelling solvents. 0.75 vol% solvent additive was added into the reaction system for all conducted reactions. Reproduced with permission from ref[165].

To combine water miscibility with singlet oxygen stabilization, the effect of hexafluoroisopropanol (HFIP) was investigated. HFIP gives increased total conversions compared to all hydrophobic additives and exhibits a lower divergence between the hydrophilic and the hydrophobic photocatalyst. However, the addition of water-miscible acetonitrile (ACN) resulted in the highest increase in reactivity for both catalytic systems. Yielding a 5.4-fold and 3.6-fold increase for the hydrophilic and hydrophobic photocatalysts, respectively, when compared to additive-free conditions (Figure 4.13 left). Within the presented reaction, the solubility-limited exchange of reagents between the nanoparticle core and the continuous phase appears to be the rate-limiting step. Depending on their polarity, partitioning of additives between particle core and continuous phase occurs, allowing for increased substrate exchange and acting as a phase-transfer agent. This is reflected by the conversion increase with water-miscible solvents, compared to hydrophobic solvents. Providing the opportunity of a biphasic reaction environment within a single photocatalytic system represents a powerful tool, regarding reaction control and substrate accessibility, yielding a reaction optimization of a maximal 5.4-fold increase in conversion. The observed results were confirmed by time-dependent conversion rate investigations (Figure 4.14). Herein, the C-C coupling formation was monitored for the blank photocatalytic nanoparticles, the best-performing hydrophilic swelling solvent (ACN) and the best-performing hydrophobic swelling solvent (HFB). It was observed, that both blank nanoparticles showed a plateau formation after only 4 h reaction time. After the addition of HFB into the reaction mixture, the observed conversion behavior showed no plateau formation anymore.

However, only minimal changes in total conversion can be observed. Comparing these results to the reaction mixture including ACN as a swelling solvent, strong changes in conversion behavior were observed. The maximum conversion was found to be a 5.4-fold increase compared to the blank samples, with a slow divergence of the hydrophilic and the hydrophobic located photocatalyst. It is assumed, that the increased interphasic mass transfer accelerates the diffusion, reducing the diffusion-limited reaction behavior of the blank photocatalytic nanoparticle."

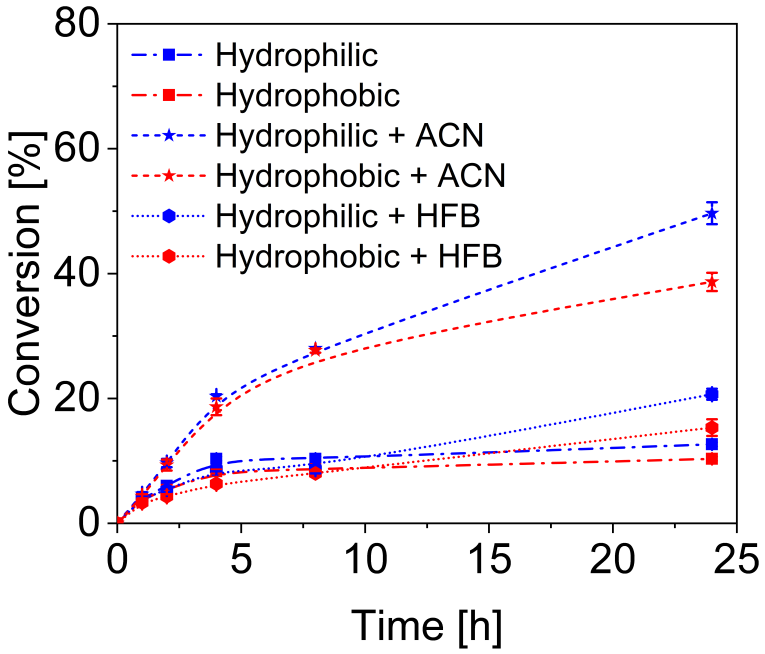

Figure 4.14: Kinetic profile of polymeric nanoparticles without additive, with the best performing hydrophilic additive (ACN) and the best performing lipophilic additive (HFB), each performing the reductive dehalogenation. Conditions: 2-bromobenzaldeyhde (12.2 µmol), NEt_3 (15 µL), hydrophilic photocatalyst polymer (0.192 µmol, 0.6 mol% photocatalyst), dispersed in H_2O (2 mL, sonicated 20 min), 15 °C, 7.14 W, 465 nm, 16 h. The conversion was calculated from GC measurements by comparison of peak area intensity. Reproduced with permission from ref[165].

During the optimization studies an interesting change was observed (section 4.5). Removing the sacrificial agent (NEt_3) from the reaction mixture resulted in the absence of any product formation. However, performing the reaction with different solvent additives resulted in a strong change in reactivity (Figure 4.13 right). While the blank photocatalyst and the ACN-swollen photocatalyst remained to show no reactivity, the addition of HFIP and hydrophobic swelling solvents resulted in a reversed reaction behavior. No C-C coupling was observed, but the defined oxidation of bromobenzaldehyde to bromobenzoic acid. Therein, toluene showed a minimal product formation while HFB achieved the highest conversion of 37%. In this case, the hydrophobic-located photocatalyst outperformed the hydrophilic-located one. A similar behavior was observed for dichloromethane, yielding up to 21% conversion for the hydrophobic-located photocatalyst and 15% for the hydrophilic-located one. The most drastic discrepancy was found for HFIP, showing 25%

conversion for the hydrophilic photocatalyst and only 8% for the hydrophobic photocatalyst. The change in product formation from the C-C coupling to the oxidation might be explained by inhibition of the fast electron transfer for the reductive dehalogenation, as no sacrificial agent is present to refill the HOMO, restricting the kinetics of the reduction process. Therefore, the formation of stable ROS is favored, resulting in the oxygenation reaction. However, further investigation of the reaction mechanism has to be conducted, especially focusing on the solvent-dependency of the reaction, to fully understand the reaction behavior.

4.3 Comonomer Effects in Vinyl-Based Photocatalytic Polymers

In addition to the investigation of hydrophilicity gradients and their substrate-dependent photocatalytic activity, the influence of defined microenvironments on the photoactivity of a polymeric photocatalyst was tested. In a collaborative project, different vinyl-based homopolymers were prepared with identical photocatalyst loading and compared towards their difference in photocatalytic reactivity. In here, Thomas Kuckhoff was responsible for the design, synthesis, and characterization of the photocatalytic polymers. He also investigated their variations in photocatalytic reactivity. My role involved resynthesizing these photocatalytic polymers, performing DFT calculations, and assessing their photocatalytic reactivity in the C-C coupling reaction between 3-methyl indole and diethyl bromomalonate. In this section, only my contribution to the collaborative project is presented. For a comprehensive discussion, additional results, and experimental details, readers are referred to the corresponding article published in RSC Applied Polymers.[170]

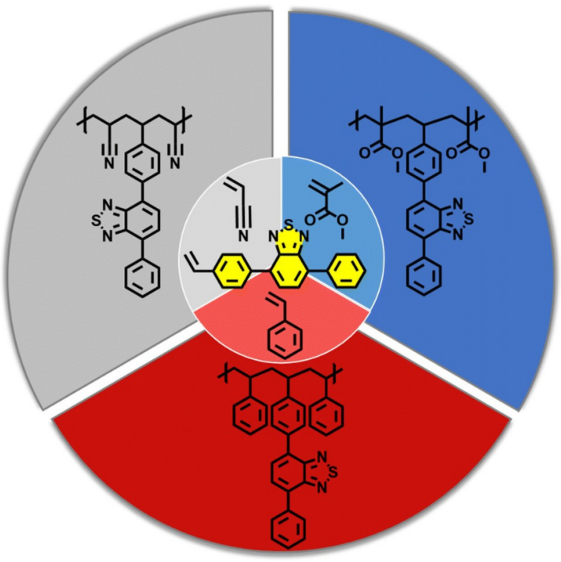

Figure 4.15: A photocatalytic moiety is copolymerized with three distinct monomers, styrene, methyl methacrylate and acrylonitrile, to investigate the effect of the comonomer on the photocatalytic efficiency and photophysical properties. Reproduced with permission from ref[170].

A vinyl-functionalized diphenylbenzothiadiazole was copolymerized with styrene, methyl methacrylate and acrylonitril using a radical polymerization (Figure 4.15).[170] After confirmation of comparable photocatalyst incorporation into the polymers, the influence of the polymeric microenvironment on the photophysical properties was analyzed. Non-covalent interactions between the photocatalytic moiety and neighboring groups of the polymer chain were expected to influence the photophysical properties in terms of excitation lifetimes, electronic band gap and redox potentials, similar to the corresponding solvent functionalities.

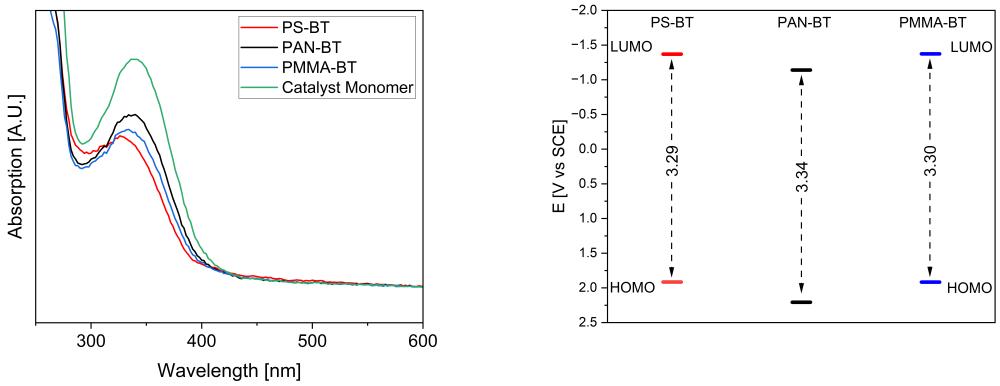

Figure 4.16: Left: UV/Vis absorption spectra for the synthesized polymeric photocatalysts and the corresponding photocatalytic monomer. Right: Density Functional Theory (DFT) calculations at the B3LYP/6-31+g(d) level for the repetition units of the polymeric photocatalysts. Reproduced with permission from ref[170].

A thorough analysis of the photophysical properties of the compounds was conducted. The photocatalytic monomer was characterized towards its solvatochromism and was found to exhibit a blue-shifted absorption maximum in acetonitrile (ACN), compared to the toleuene and dimethylformamide (DMF) absorption. Comparing these results with polymeric photocatalysts, a similar trend was observed for the corresponding polymeric environment. Therefore, photocatalytic polyacrylonitrile showed a minimally blue shifted absorption maximum (Figure 4.16 left). However, solvent influences during the absorption spectroscopy might inhibit significantly pronounced environment effects. Furthermore, differences in optical band gap and fluorescence lifetimes were observed for all compounds. The observed differences were supported by DFT calculations for the HOMO-LUMO values of the isolated repetition units (Figure 4.16 right). Herein, only minimal shifts in optical band gap were observed, showing 3.29 eV for the polystyrene (PS), 3.34 eV for the polyacrylonitrile (PAN) and 3.30 eV for the polymethylmethacrylic acid (PMMA). The HOMO-LUMO values for the PAN photocatalyst showed a shift towards more positive FMO energy values. The increased band gap for PAN indicates a higher required energy for the excitation process, therefore aligning with the experimental results, showing a blue shift for PAN. This phenomenon might be explained by the electron-donating character of the acrylonitrile group, decreasing hydrophobic interactions of the spatially neighboring diphenylbenzothiadiazole and therefore destabilizing the excited state.

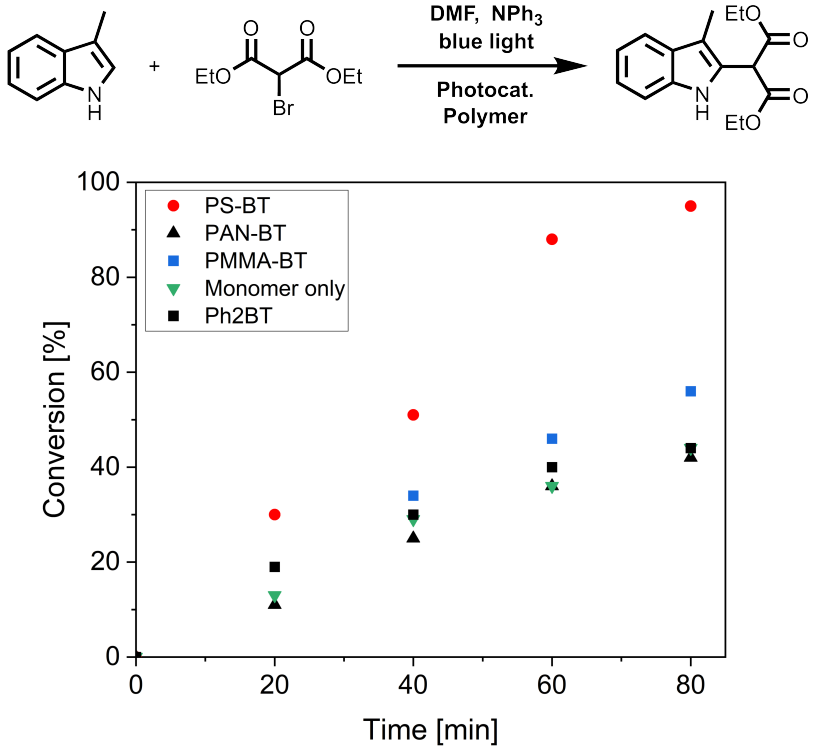

Figure 4.17: Reactivity comparison of the photocatalytic polymers, the photocatalytic monomer and a reference photocatalyst in the reductive dehalogenation with subsequent C-C coupling with 3-methyl indole. The kinetic investigation was conducted using a 1% photocatalyst containing polymer or small molecule. Measurements were carried out over 80 minutes showing full conversion for PS-BT. 3-Methyl indole (19.7 mg, 150 µmol), diethyl bromomalonate (71.7 mg, 300 µmol), triphenylamine (73.6 mg, 300 µmol) and photocatalytic polymer (5% polymer, 250 nmol photoactive unit) in DMF (2 mL) under an Ar atmosphere with blue light irradiation were used. Reproduced with permission from ref[170].

To further evaluate the influence of the polymeric microenvironment on the photoactivity of the photocatalyst, the photocatalytic reactivity of the polymeric photocatalysts was investigated. Therefore, a range of reactions was analyzed by the time-dependent conversion rate of each material. The exemplary reaction of the dehalogenative coupling of 3-methyl indole with bromomalonate is discussed (Figure 4.17). Performing the reaction under identical conditions for all polymeric materials, as well as the photocatalytic monomer and a reference photocatalyst, with an identical catalyst loading. For equal solubility, DMF was used as the reaction solvent. Additionally, triphenylamine was utilized as sacrificial base. Interestingly, under blue light irradiation, the reaction showed stark differences between all investigated systems. The PS-photocatalyst showed the fastest conversion rate, reaching around 95% of the coupled indole after 80 min. In contrast, no other material, neither polymeric or small molecule, was able to achieve more than 55% conversion within the same time frame. The PMMA compound showed the second-highest conversion rate. The PAN material and the small molecule photocatalysts were found to exhibit nearly identical conversion behaviors,showing the lowest conversions in this reaction series. It should

be highlighted, that both small molecule photocatalysts were strongly outperformed by the PS-photocatalyst. This interesting finding underlines the relevance of the polymeric microenvironment towards the photoactivity of the utilized photoactive species. Possible explanations for the observed conversion improvement could include the stabilization of photoexcited intermediates through non-covalent interactions within the hydrophobic microenvironment or the accelerated mass transfer of hydrophobic compounds (sacrificial base and indole) to the photocatalytically active sites. However, a more in-depth study is necessary to evaluate the observed phenomena.

4.4 Conclusion

"In conclusion, careful consideration of the microenvironment of photocatalytic active centers can be used to tune the reactivity of polymer photocatalysts. The incorporation of photocatalytic active centers into either hydrophilic or hydrophobic compartments of polymeric micelles results in significantly different reaction rates depending on the substrate. More hydrophilic substrates, which preferentially partition in the continuous phase, were converted significantly faster with the active center in the hydrophilic section. Change of the photocatalyst localization within the nanoparticle microenvironments showed drastically different performance with up to 62% conversion difference observed. More hydrophobic substrates showed no to little conversion differences, possibly reasoned by limited mass transfer between the microenvironments combined with the inherent mechanism of the chosen reactions. Additionally, the reaction performance of these photocatalytic particles within a reductive dehalogenation was improved through addition of 0.75 vol% of a secondary swelling solvent, resulting in an up to 5.4-fold increase in reaction conversion. This swelling solvent enhances the accessibility of the core, while also increasing the lifetime of photocatalytically generated reactive oxygen species." Moreover, the establishment of this biphasic photocatalytic system enabled the precise tuning for an orthogonal reaction mechanism, which would remain unavailable to a single solvent reaction mixture. Lastly, we copolymerized three common monomers with a donor–acceptor-based photocatalyst and investigated the impact of the comonomer on the photocatalytic activity. The microenvironment influence on the photophysical properties of these heterogeneous photocatalyst systems was investigated. Herein, a solvatochromism-like influence was found, showing correlations in lifetime and absorbance with the corresponding solvent moiety and therefore a strong dependency on the chosen comonomer. It was successfully confirmed by an indole coupling reaction that this effect even expresses its influence in the photocatalytic activity. Comparing this reactivity to the photocatalytic monomers or small-molecule photocatalysts, the heterogeneous photocatalyst constantly outperformed the small-molecule analogues, showing the potential advantage of heterogeneous, polymeric photocatalysts over small-molecule systems." We suggest careful consideration of the photocatalysts' microenvironment as it may strongly influence the photocatalytic activity."

4.5 Experimental Details for Both Projects

1. General Experimental Information

"All organic synthesis for the photocatalysts were performed in oven-dried glassware under argon, unless otherwise stated. Polymerization reactions were conducted in 20 mL screw-top vials with a PTFE-membrane cap. Reactions investigating the catalytic activity of the substrates were performed in 4 mL screw-top vials. Reaction temperatures are referred to the ones of the heating/cooling media (aluminum heating block, water cooling), unless otherwise stated. Reagents were purchased from Sigma-Aldrich, Merck, ACROS Organics, Alfa Aesar, TCI and used without further purification. Reactions were conducted, using a PTFE-coated, egg-shaped stir bar at around 1900 rpm. Solvents were removed by rotary evaporation under reduced pressure, heating the solution with a water bath at 40-60 °C. Residual high boiling solvents were removed in vacuo (<1 mbar) at room temperature. Formed compounds were characterized by ^{1}H-NMR spectroscopy, ^{13}C-NMR spectroscopy, APCI-MS and GC-MS. Throughout all experiments Millipore quality water (Milli-Q-Synthesis 230 V/50 Hz, Milli-Q Q-Gard 2, 18.2 MΩ cm^{-1}) was used, unless stated otherwise."

2. General Analytical Techniques

"^{1}H- and ^{13}C-NMR spectra were recorded at room temperature on a Bruker AVIII 300 spectrometer (^{1}H: 400.13 MHz; ^{13}C: S 4 100.62 MHz), in deuterated solvents (>99.5 Deuteration) purchased from Sigma-Aldrich, stored at 4 °C (CD_2Cl_3,CD_2Cl_2, DMSO-d_6, D_2O). Chemical shifts (δ) for ^{1}H and ^{13}C NMR spectra were referenced against TMS (tetramethylsilane) and are given in parts per million (ppm). First order multiplicities in ^{1}H NMR signals were reported using the following abbreviations : s = singlet, d = doublet, t = triplet, q = quartet, p = quintet, h =sextet; m = multiplet, br = broad signal. Data processing of NMR spectra was done with MestReNova 14.2.3."

"APCI-MS were recorded on an Advion ASAP (Advion Inc., Ithaca) with DART injection. Considering $[M+H]^+$, $[M+NH_4]^+$, $[M+Na]^+$ or $[M+K]^+$ for positive Ionization methods."

"Fourier-transform infrared spectroscopy measurements were conducted using a Bruker Vertex 70 (Bruker Inc. , Billerica), using a well dispersed, homogenous mixture of 2 mg sample together with 200 mg of KBr (dried and spectroscopic grade) to from stable KBr discs with a Perkin Elmer hydraulic press(15 tons pressure, 4 min), aided by a high vacuum pump. Data processing of obtained FTIR spectra was done with Bruker OPUS 7.8 software."

3. Photophysical Analytical Techniques

"Absorption spectra were recorded with an Agilent Cary 60 UV/Vis spectrometer with xenon light source, using response time 0.04 s, 1.5 nm spectral bandwidth in 0.5 nm intervals and baseline correction. All measurements were conducted in 10x10 mm VWR ES-quartz cuvettes (dimensions: 12.5×12.5×45 mm) fitted with PTFE caps."

"Emission spectra were recorded with on a J&M Tidas FL3005SL fluorescence spectrometer with a Perkin Elmer diode array (300-1100 nm). Data analysis was conducted by fitting with a Gaussian function and normalization using Origin 2019b (V. 9.65)."

"EPR (Electron Paramagnetic Resonance) was measured on a Magnettech Miniscope MS200 spectrometer at room temperature, microwave frequency: 9.391 GHz, microwave power: 10 mW, modulation amplitude: 9.8 G, field modulation: 0.2 mT at 100 kHz, scan time: 60 s."

4. Macromolecular Analytical Techniques

"GPC experiments were performed using an PSS SECcurity2 instrument consisting of a pump, autosampler and column oven .A column set consisting of 3 columns: GRAM 1000 Å , GRAM 1000Å and GRAM 100Å (PSS Standards Service GmbH, Mainz, Germany), all of 300 x 8 mm and 10 µm average particle size were used at a flow rate of 1.0 mL min^{-1} and a column temperature of 60 °C. As eluent DMF with 1 g/L LiBr was used. The samples having 1 mg ml^{-1} concentration were filtererd prior to measurement through 0.45 µm PTFE filter. The injection volume was 100 µL. Detection was accomplished with a RI detector and UV detector at 270 nm wavelength."

"Data acquisition and evaluation was performed using PSS WINGPC UniChrom (PSS Polymer Standards Service GmbH, Mainz, Germany). Calibration was carried out by using poly(methyl methacrylate) provided by PSS Polymer Standards Service GmbH (Mainz, Germany)."

"Particle size distributions were analysed by 90° dynamic light scattering (DLS) measurements, which were performed using a Zetasizer Nano S500 and Nano S90(Malvern Pananalytical Mdt., Worcestershire). Therefore, aqueous particle dispersions were measured in 10x10 mm disposable, semi-micro polystyrene cuvettes (1.5-3 mL volume). Data acquisition was performed by Zetasizer Software (Version: 7.2, Malvern)."

"Transmission electron microscopy measurements were conducted using a JEM 1400 (JEOL, Tokyo), equipped with a 120 kV tungsten emitter, Fishione high angle annular darkfield detector combined with an on axis Gatan US1000 2k CCD camera. Data acquisition was conducted using Gatan Microscopy Suite (Version: 2.11.1404, DigitalMicrograph, Gatan). Sample preparation was performed by drop-casting on carbonized copper grids (300 mesh, C-layer 10 20 nm), followed by staining with uranyl acetate (30 s, 4% aqueous solution) and solvent deduction with filter paper."

5. Purification Techniques

"Flash column chromatography was performed on Machery-Nagel 60 M silica gel (40-63 microns) under pressure gradients using the Biotage Isolera One Purification system, within Biotage KP-Sil cartridges of differing size. Product elution was analysed by the internal UV-detector (200-800 nm). Thin layer chromatography was conducted using Machery-Nagel Alugram SIL G/UV254, pre-coated aluminium sheets and was visualized by UV light (254 nm or 366 nm), Iodine chamber or stained with basic potassium permanganate solution (1.5 g $KMnO_4$, 10 g K_2CO_3, 1.25 mL 10% NaOH in 200 mL of distilled

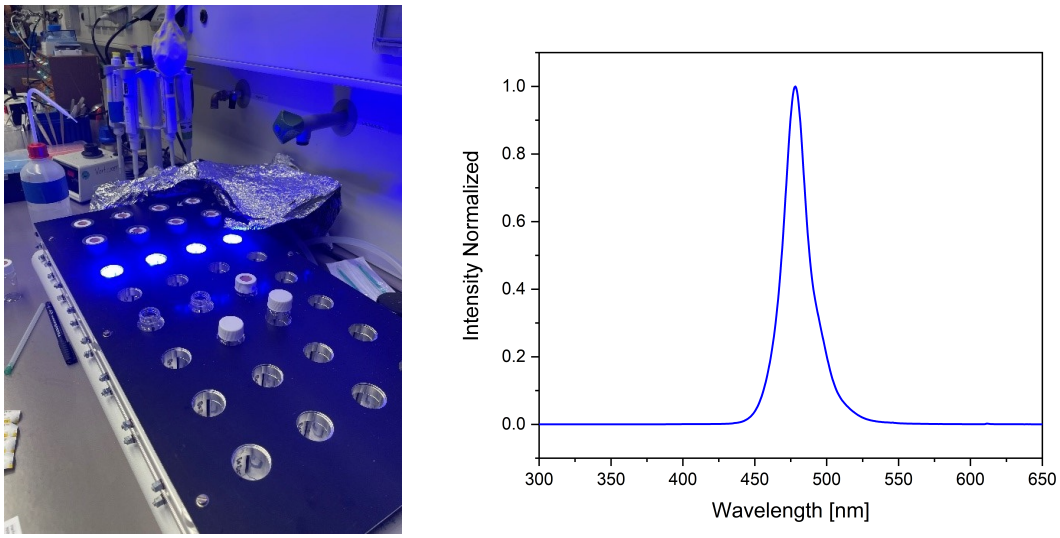

Figure 4.18: Left: Photo of the utilized photoreactor with build-in water cooling, turned on. Right: Emission spectra of the used Tru Components HighPower-LEDs. Reproduced with Permission from[165].

water). All dialysis purifications were performed using Spectra/Por 1 to 4 Spectra/Por 3 - MWCO 3500, 18 mm, regenerated cellulose (Carl Roth, Germany), hydrating membranes for 15 min in Milli-Q water (200 mL), closing the membranes with knots."

6. Solvents

"Dry solvents DMSO, DMF and toluene were bought from ACROS Organics, containing H_2O <50 ppm, stored under activated molecular sieves of 3 Å pore diameter and transferred within an argon counter stream. P.a. grade triethylamine was purchased from Sigma-Aldrich, with a purity of $\geq$ 99.5%, stored under identical conditions to dry solvents. Solvents for flash column chromatography (EtOAc, chloroform, n-hexane, CH_2Cl_2 and MeOH) were purchased in technical grade and used without further purification."

7. Photoreactor Setup

"All photochemical reactions were performed within the customized photoreactor depicted in Figure 4.18. Bearing reaction vial slots, each provided with 6 blue light LEDs (Tru Components HighPower, 1.4 W per LED, λ = 460-470 nm, see Figure 4.18). LEDs and reaction vials were constantly kept at 15 °C using the built-in water cooling system. Additionally, constant stirring at 450 rpm with PTFE-coated stir bars was ensured."

8. GC-MS Analysis

"Gas chromatographic analysis was conducted via on an Shimadzu GC-2010 plus GC-system equipped with a 7HG-G010-11 Phenomenex column (0.25 mm x 30 m (diameter:length), film thickness: 0.25 µm) and analysed using QP2010 ultra mass spectrometer. For peak separation two methods were used: 1) for small molecules with difficult separation (tetrahydrothiophene , 2-(ethylsulfanyl)ethanol and methyl p-tolyl sulfide) and 2) for larger molecules with longer retention time (3,4-dimethoxybenzylamine, benzylamine

and 4-tert-butylbenzylamine). 1) Splitless injection, injection temperature 250 °C, column oven 50 °C. Temperature gradient: 50 °C hold 2 min to 160 °C with a rate of 15 °C min^{-1} hold for 2 min to 280° C with a rate of 20 °C min^{-1} hold for 8 min. Total flow at 23.1 mL min^{-1}, 42.0 kPa Pressure, 0.86 mL min^{-1} column flow. 2) Splitless injection, injection temperature 280 °C, column oven 100 °C. Temperature gradient: 100 °C to 280 °C with a rate of 10 °C min^{-1} hold for 5 min Total flow at 19.6 mL min^{-1}, 43.6 kPa Pressure, 0.70 mL min^{-1} column flow. Preparation of GC-MS samples were performed by addition of 200 µL of crude solution mixture into 2 mL acetonitrile, followed by drying with $MgSO_4$ and then transferred into 2 mL GC vials, washing $MgSO_4$ with 1 mL acetonitrile. GC-MS spectra were analysed with GCMSolution Postrun Analysis (Version: 4.45 SP1).”

9. General Synthetic Procedures

"Photocatalytic polymer stock solution was prepared freshly before every reaction. Therefore, the polymer was dissolved in Milli-Q water (10 mg polymer/300 µL water, 75.3 µg photocatalyst) and sonicated for 20 min. After cooling down, the solution was used straight away."

9.1 Photocatalytic Sulfide Oxidation

"For each reaction, polymer stock solution (300 µL, 10 mg polymer, 75.3 µg photocatalyst) was given into a 4 mL screw-cap vial, equipped with a stir bar. Followed by addition of water (Milli-Q, 1.7 mL) and the sulfide substrate to give a 10 mM solution (0.3 mol% photocatalyst). Under constant stirring at 450 rpm, and cooling to 15 °C, the vials were placed into a photoreactor slot and irradiated with blue light for 24 h. Afterwards, each sample was analysed according to the GC-MS procedure."

9.2 Photocatalytic Imine Formation

"For each reaction, polymer stock solution (300 µL, 10 mg polymer, 75.3 µg photocatalyst) was given into a 4 mL screw-cap vial, equipped with a stir bar. Followed by addition of water (Milli-Q, 1.7 mL) and the amine substrate to give a 5 mM solution (0.6 mol% photocatalyst). Under constant stirring at 450 rpm, and cooling to 15 °C, the vials were placed into a photoreactor slot and irradiated with blue light for 24 h. Afterwards, each sample was analysed according to the GC-MS procedure."

9.3 Photocatalytic C-C Bond Coupling

"For each reaction, polymer stock solution (300 µL, 10 mg polymer, 75.3 µg photocatalyst) was given into a 4 mL screw-cap vial, equipped with a stir bar. Followed by addition of water (Milli-Q, 1.7 mL), triethylamine (10 eq., 15 µL), solvent additive (15 µL) and the halogen substrate to give a 5 mM solution (0.6 mol% photocatalyst). Under constant stirring at 450 rpm, and cooling to 15 °C, the vials were placed into a photoreactor slot and irradiated with blue light for 24 h. Afterwards, each sample was analysed according to the GC-MS procedure."

10. Materials

"4,7-Dibromobenzo[1,2,5]thiadiazole (>98%), (4-(4,4,5,5-tetramethyl-1,3,2-dioxaborolan-2-yl)phenyl)methanol (>98%), dimethylformamide (>99.5%), 1,4-dioxane (stab. with BHT, >99%), glycidyl methacrylate (stab. with MEHQ, >99.5%), tetrahydrothiophene (>99%), 2-(ethylthio)ethanol (>98%), 4,4,5,5-tetramethyl-2-phenyl-1,3,2-dioxaborolane (>98%) and 3,4-dimethoxybenzylamine (>97%) were purchased from Tokyo Chemical Industry (TCI). Methacryloyl chloride (stab. with MEHQ, >97%), dimethyl sulfoxide (>99.5%, anhydrous), 2-bromobenzaldehyde (98%), 4-((((2-carboxyethyl)thio)carbonothioyl)thio)-4-cyanopentanoic acid (95%), hexafluorobenzene (99%), hexafluoro-2-propanol (>99%) and 4-tert-butylbenzylamine (97%) were purchased from Sigma Aldrich. Tetrakis(triphenylphosphane)palladium (99%) and benzyl amine (99%) were pruchsed from ACROS Organics. Methyl p-tolyl sulfide (97%), benzyl methacrylate (stab. with 4-methoxy phenol, 98%)

and 4,4'-azobis(4-cyanopentanoic acid) (98%) were purchased from Alfa Aesar. Acetonitrile (>99.9%) was purchased from Honeywell. Toluene (>99.8%), ethanol (absolute) and dichloromethane (>99%) were purchased from Fisher Scientific. Na_2CO_3 (>99.5%) was purchased from Carl Roth. Deuterated dichloromethane (99.6%) was purcahsed from Deutero GmbH. Regenerated cellulose dialysis tubings (Sevapor 3, MWCO 3500, 16 mm diameter) were purchased from Serva."

11. Synthesis of Photocatalyst BTPMA

11.1 4-Bromo-7-phenylbenzo[1,2,5]thiadiazole

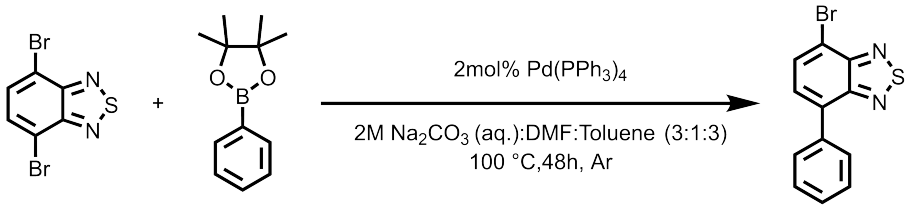

"Into a 150 mL schlenk tube with a stir bar, 25 mL of a 2 M Na_2CO_3 (aq.) solution, 25 mL of toluene and 9 mL of DMF were added inside. Subsequently, the solution was degassed with an argon stream for 15min, before adding 4,7-dibromobenzo[1,2,5]thiadiazole (1.5 eq., 2.16 g, 7.35 mmol) and 4,4,5,5-tetramethyl-2-phenyl-1,3,2-dioxaborolane (1 eq., 1 g, 4.90 mmol) and tetrakis(triphenylphosphane)palladium (0.02 eq., 113.25 mg, 98.00 µmol) in an argon counter stream. The reaction mixture was heated to 100 °C for 48 h with an attached reflux condenser under heavy stirring. After cooling down to room temperature, 30 mL of Milli-Q water were added, followed by dichloromethane extraction (4x 25 ml), washing by brine and drying over Na_2SO_4. After evaporation of all volatiles with the rotary evaporator, the crude mixture was purified using SiO_2 column chromatography (gradient from 10% DCM: 90% petrolether to 70% DCM: 30% petrolether). A mixture of the product and biphenylbenzothiadiazole was obtained and used without further purification (960 mg)."

^{1}H NMR (300 MHz, CD_2Cl_3, δ): 7.80 (m, 2H, Ar H), 7.60 (s, 2H; Ar H), 7.44 (m, 3H; Ar H);

11.2 (4-(7-Phenylbenzo[1,2,5]thiadiazol-4-yl)phenyl)methanol

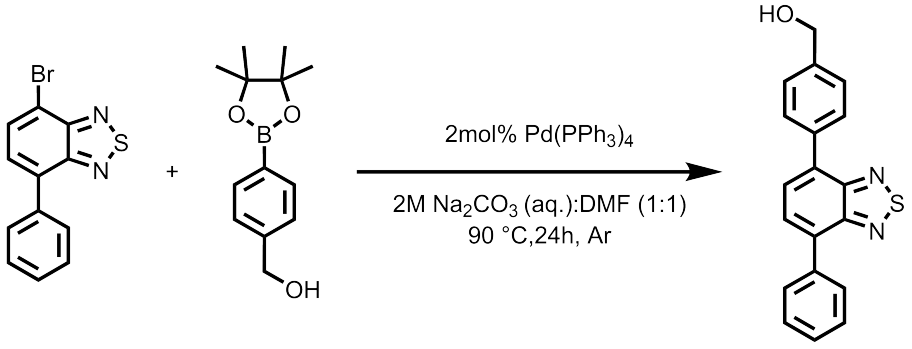

"Into a 150 mL schlenk tube with a stir bar, 10 mL of a 2 M Na_2CO_3 (aq.) solution and 10 mL of DMF were added inside. Subsequently, the solution was degassed with an argon stream for 15min, before adding 4-bromo-7-phenylbenzo[1,2,5]thiadiazole (1.0 eq., 550 mg, 1.89 mmol) and (4-(4,4,5,5-tetramethyl-1,3,2-dioxaborolan-2-yl)phenyl)methanol (1.5

eq., 663.31 mg, 2.83 mmol) and Tetrakis(triphenylphosphane)palladium (0.02 eq., 43.66 mg, 37.78 µmol) in an argon counter stream. The reaction mixture was heated to 90 °C for 24 h with an attached reflux condenser under heavy stirring. After cooling down to room temperature, 20 mL of Milli-Q water were added, followed by dichloromethane extraction (3x 25 ml), washing by brine and drying over Na_2SO_4. After evaporation of all volatiles with the rotary evaporator, the crude mixture was purified using SiO_2 column chromatography (Column deprotonated with 10% NEt_3: 90%EtOAc,;gradient from 10% EtOAc: 90% petrolether to 70% EtOAc: 30% petrolether). The product was obtained as yellow crystals (253 mg, 42% yield)."

^{1}H NMR (300 MHz, CD_2Cl_3, δ): 8.01 (m, 4H, Ar H), 7.85 (s, 2H; Ar H), 7.59 (m, 4H; Ar H), 7.49 (m, 1H; Ar H) , 4.81 (d, 2H; CH_2);

^{13}C NMR (300 MHz, CD_2Cl_3, δ): 132.3 (2C; Ar C=N), 129.4 (Ar C), 129.3 (5C; Ar C), 128.1 (4C; Ar C), 126.9 (6C; Ar C), 64.7 (1C, C-OH);

11.3 4-(7-Phenylbenzo[1,2,5]thiadiazol-4-yl)benzylmethacrylate

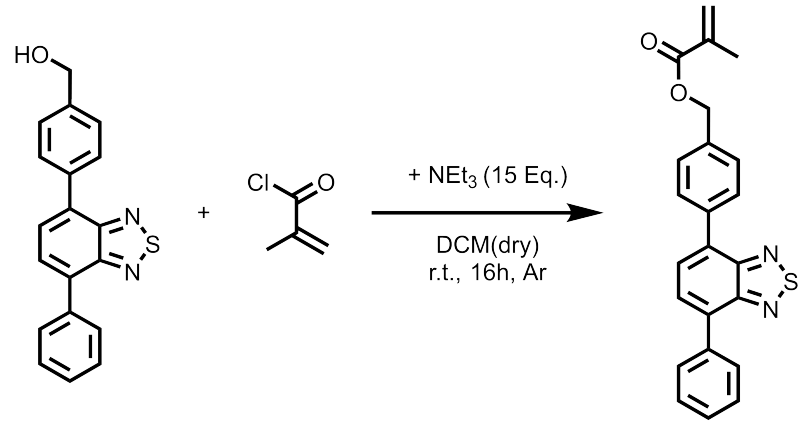

"Into an evacuated 50 mL schlenk tube with a stir bar, 25 mL DCM (dry) were added inside. Subsequently, (4-(7-phenylbenzo[1,2,5]thiadiazol-4-yl)phenyl)methanol (1.0 eq., 150 mg, 1.89 mmol) and Triethylamine (15 eq., 984.99 µL, 28.35 mmol) were added in an argon counter stream. The reaction mixture was stirred for 30 min, before slowly adding methacryloyl chloride (1.2 eq., 55 µL, 565.34 µmol) over 20 min. Afterwards, the mixture was kept under argon and stirring for 16 h. After that, 20 mL of Milli-Q water were added, followed by dichloromethane extraction (3x 25 ml), washing by brine and drying over Na_2SO_4. After evaporation of all volatiles with the rotary evaporator, the crude mixture was purified using SiO_2 column chromatography (column deprotonated with 10%NEt_3: 90%EtOAc, gradient from 10% EtOAc: 90% petrolether to 70% EtOAc: 30% petrolether). The product was obtained as bright yellow powder (134 mg, 73% yield)."

^{1}H NMR (300 MHz, CD_2Cl_3, δ): 7.98 (m, 4H, Ar H), 7.82 (s, 2H; Ar H), 7.61 (m, 4H; Ar H), 7.48 (m, 1H; Ar H), 4.81 (m, 2H; CH_2), 6.23 (s, 1H; CH_2), 5.64 (s, 1H; CH_2), 5.32 (s, 2H; CH_2), 2.03 (s, 3H; CH_3);

^{13}C NMR (300 MHz, CD_2Cl_3, δ): 144.7 (1C; C=O), 136.5 (2C; Ar C=N), 129.4 (2C; Ar C), 129.3 (3C; Ar C), 128.5 (3C; Ar C), 128.1 (6C; Ar C), 125.5 (2C; Ar C), 115.1 (1C; C4), 113.8 (1C; C2), 65.9 (1C, C2), 18.1 (1C; C1);

12. Synthesis of Photocatalytic Nanoparticles

12.1 2,3-Dihydroxypropylmethacrylate

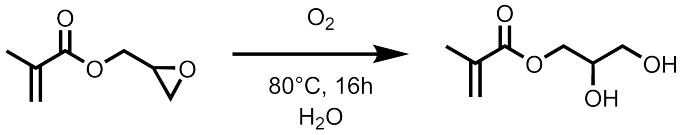

"In a 50 mL roundbottom flask equipped with a stir bar, a 20 wt% solution of glycidyl methacrylate (5g) in Milli-Q water(20 ml) were gassed with oxygen for 30 min. Afterwards the biphasic solution was reacted for 16 h at 80 °C under heavy stirring. This crude aqueous solution was used without further purification for the following macro-CTA generation."

12.2 Hydrophilic Macro-Chain Transfer Agent (mCTA)

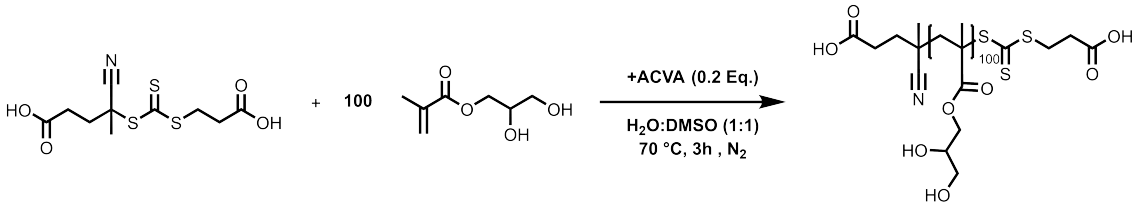

"Into a 20 mL screw-cap vial equipped with a stir bar, freshly synthesized 2,3-dihydroxypropyl methacrylate solution (2.5 mL, 20 wt/vol%, aqueous) was transferred. After addition of DMSO (2.5 mL), 4,4'-azobis(4-cyanopentanoic acid) (0.2 eq., 1.75 mg, 6.24 µmol) and 4-((((2-carboxyethyl)thio)carbonothioyl)thio)-4-cyanopentanoic acid (1 eq., 9.6 mg, 31.22 µmol), the crude mixture was degassed with N_2 for 20 min with a light pressure. Afterwards, the solution was reacted under heavy stirring for 3 h at 70 °C. After cooling down to room temperature, the solution was dialyzed (3x EtOH:H_2O, 1:1, exchange after 6 h, 12 h and 24 h, followed by 3x water, 100%, exchanged every day), followed by lyophilization until dry. The product was obtained as a colorless, loose solid."

^{1}H NMR (300 MHz, DMSO-d_6, δ): 4.91 (br, 1H, OH), 4.67 (br, 1H; OH), 3.90 (br, 1H), 3.68 (br, 2H; CH), 3.52 (br, 1H; CH_2), 3.38 (br, 2H; CH_2), 1.78 (br, 2H; CH_2), 0.85 (m, 3H; CH_3);

12.3 Copolymerized, Hydrophilic-located Photocatalyst Macro-Chain Transfer Agent (mCTA)

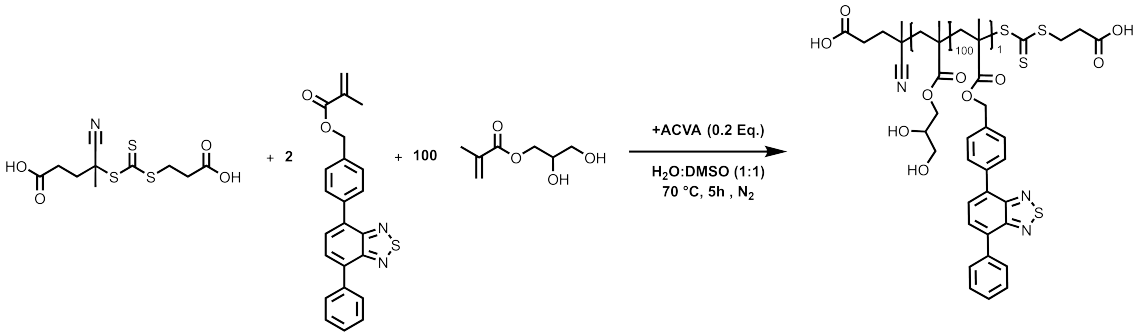

"Into a 20 mL screw-cap vial equipped with a stir bar, freshly synthesized 2,3-dihydroxypropyl methacrylate solution (2.5 mL, 20 wt/vol%, aqueous) was transferred. After addition of DMSO (2.5 mL), 4,4'-azobis(4-cyanopentanoic acid) (0.2 eq., 1.75 mg, 6.24 µmol), 4-(7-phenylbenzo[1,2,5]thiadiazol-4-yl)benzyl methacrylate (2 eq., 24.13 mg, 62.43 µmol) and 4-((((2-carboxyethyl)thio)carbonothioyl)thio)-4-cyanopentanoic acid (1 eq., 9.6 mg, 31.22 µmol), the crude mixture was degassed with N_2 for 20 min with a light pressure. Afterwards, the solution was reacted under heavy stirring for 5 h at 70 °C. After cooling down to room temperature, the solution was dialyzed (3x EtOH:H_2O, 1:1, exchange after 6 h, 12 h and 24 h, followed by 3x water, 100%, exchanged every day) followed by lyophilization until dry. The product was obtained as a slightly yellow, loose solid."

^{1}H NMR (300 MHz, DMSO-d_6, δ): 8.00 (m, 5H; Ar H), 7.41 (m, 6H; Ar H), 4.91 (br, 1H, OH), 4.67 (br, 1H; OH), 3.90 (br, 1H), 3.68 (br, 2H; CH), 3.52 (br, 1H; CH_2), 3.38 (br, 2H; CH_2), 1.78 (br, 2H; CH_2), 0.85 (m, 3H; CH_3);

12.4 Copolymerization of Photocatalyst and Hydrophobic Block with Hydrophilic mCTA

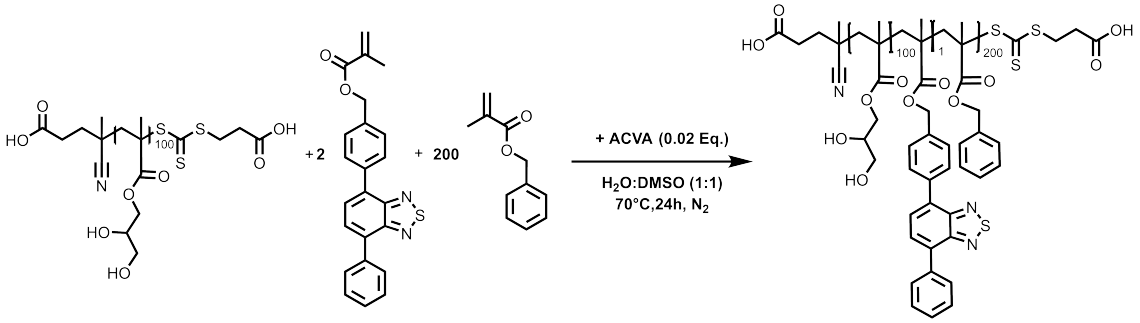

"Into a 20 mL screw-cap vial equipped with a stir bar, hydrophilic mCTA P(GMA)100 (1 eq., 300 mg, 18.38 µmol) was transferred. After addition of H_2O (3 mL) and DMSO (3 mL), 4,4′-azobis(4-cyanopentanoic acid) (0.2 eq., 1.03 mg, 3.68 µmol), 4-(7-phenylbenzo[1,2,5]-thiadiazol-4-yl)benzyl methacrylate (2 eq., 14.20 mg, 36.76 µmol) and Benzyl methacrylate (200 eq., 647.68 mg, 3.68 mmol) the crude mixture was degassed with N_2 for 20 min with a light pressure. Afterwards, the solution was reacted under heavy stirring for 24 h at 70 °C, forming an opaque dispersion. After cooling down to room temperature, the solution was dialyzed (3x EtOH:H_2O, 1:1, exchange after 6 h, 12 h and 24 h, followed by 3x Water, 100%,

exchanged every day), followed by lyophilization until dry. The product was obtained as a slightly yellow, loose solid."

^{1}H NMR (300 MHz, DMSO-d_6, δ): 7.52 (m, 11H; Ar H), 7.25 (br, 5H; Ar H), 4.86 (br,1H, OH), 4.67 (br, 1H; OH), 3.93 (br, 1H;), 3.68 (br, 2H; CH), 3.52 (br, 1H; CH_2), 3.38 (br, 2H; CH_2), 1.78 (br, 2H; CH_2), 0.80 (m, 3H; CH_3);

12.5 Copolymerization of the Hydrophobic Block with Hydrophilic, Photoctalytic mCTA

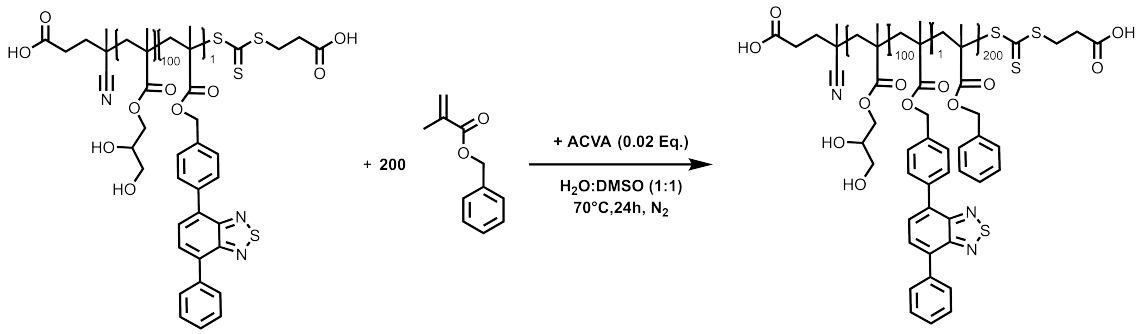

"Into a 20 mL screw-cap vial equipped with a stir bar, hydrophilic mCTA P(GMA)100 (MaBTPh)1(1 eq., 300 mg, 17.95 µmol) was transferred. After addition of H_2O (3 mL) and DMSO (3 mL), 4,4'-azobis(4-cyanopentanoic acid) (0.2 eq., 1.01 mg, 3.59 µmol) and Benzyl methacrylate (200 eq., 632.70 mg, 3.59 mmol) the crude mixture was degassed with N_2 for 20 min with a light pressure. Afterwards, the solution was reacted under heavy stirring for 24 h at 70 °C, forming an opaque dispersion. After cooling down to room temperature, the solution was dialyzed (3x EtOH:H_2O, 1:1, exchange after 6 h, 12 h and 24 h, followed by 3x Water, 100%, exchanged every day), followed by lyophilization until dry. The product was obtained as a slightly yellow, loose solid."

^{1}H NMR (300 MHz, DMSO-d_6, δ): 7.52 (m, 11H; Ar H), 7.25 (br, 5H; Ar H), 4.86 (br, 1H, OH), 4.67 (br, 1H; OH), 3.93 (br, 1H;), 3.68 (br, 2H; CH), 3.52 (br, 1H; CH_2), 3.38 (br, 2H; CH_2), 1.78 (br, 2H; CH_2), 0.80 (m, 3H; CH_3);

12.6 Synthesis of Photocatalytic Polymers for Comonomer Effect Investigation

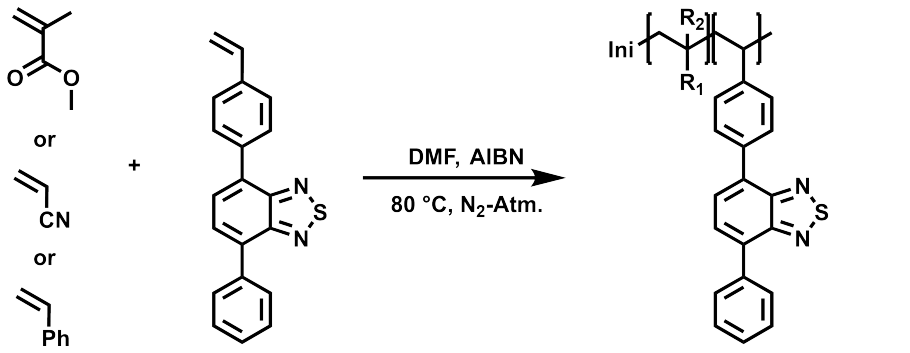

"The monomer was first purified by basic aluminum oxide. In a dry flask methyl methacrylate or acrylonitrile (500 mg) was combined with 4-phenyl-7-(4-vinylphenyl)benzo[c]-[1,2,5]thiadiazole (5 wt%. 25 mg) and dissolved in dry DMF (1.5 mL). The solution was degassed by N_2 bubbling for 10 min. AIBN (1 wt.%) was dissolved in DMF (0.5 mL) and

degassed by N_2 bubbling. The solutions were combined and heated under stirring at 80 °C overnight. The polymers were precipitated in diethyl ether and centrifuged for 10 min. (4000 rpm. 5 °C). The supernatant was discarded and the polymer taken up in DMF. The precipitation and centrifugation was repeated and the polymer purified via Soxhlet in diethyl ether for two days. The polymer was dried under vacuum and the concentration of incorporated photocatalyst is determined via a UV/Vis-calibration."

"The monomer was first purified by basic aluminum oxide. In a dry flask methyl styrene (500 mg) was combined with 4-phenyl-7-(4-vinylphenyl)benzo[c][1,2,5]thiadiazole (5 wt%. 25 mg) and dissolved in dry DMF (1.0 mL). The solution was degassed by N_2 bubbling for 10 min. AIBN (2 wt.%) was dissolved in DMF (0.5 mL) and degassed by N_2 bubbling. The solutions were combined and heated under stirring at 80 °C overnight. The polymers were precipitated in methanol and centrifuged for 10 min. (4000 rpm. 5°C). The supernatant was discarded and the polymer taken up in DMF. The precipitation and centrifugation was repeated and the polymer purified via Soxhlet in methanol for two days, yielding a yellow powder for all samples. The polymer was dried under vacuum and the concentration of incorporated photocatalyst was determined via a UV/Vis-calibration."

13. Photocatalytic Reactions

13.1 Sulfide Oxidation

13.1.1 Tetrahydrothiophene-1-oxide

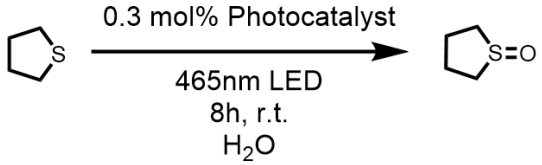

"The synthesis of tetrahydrothiophene 1-oxide was performed according to the general procedure for photocatalytic sulfide oxidations, explained in SI section 9.1. The purification of the compound was performed by flash column chromatography (hexane: EtOAc, 9:1) with potassium permanganate staining."

^{1}H NMR (300 MHz, $CDCl_3$, δ): 2.96 (m, 2H, CH_2), 2.15 (m, 2H; CH_2);

^{13}C NMR (101 MHz, $CDCl_3$, δ): 51.2 (2C; C2), 22.8 (2C; C2);

13.1.2 1-Methyl-4-(methylsulfinyl)benzene

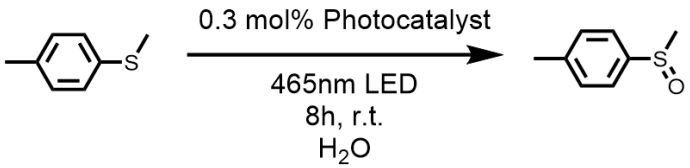

"The synthesis of 1-methyl-4-(methylsulfinyl)benzene was performed according to the general procedure for photocatalytic sulfide oxidations, explained in SI section 9.1. The purification of the compound was performed by flash column chromatography (hexane: EtOAc, 8:2)."

^{1}H NMR (300 MHz, $CDCl_3$, δ): 7.46 (m, 2H, Ar H), 7.28 (m, 2H, Ar H), 2.65 (s, 3H; CH_3), 2.35 (s, 3H; CH_3);

^{13}C NMR (101 MHz, $CDCl_3$, δ): 130.1 (2C; Ar C), 123.7 (2C; Ar C), 118.2 (2C; Ar C), 43.9 (1C; C1), 23.4 (1C; C1);

13.1.3 2-(Ethylsulfinyl)ethan-1-ol

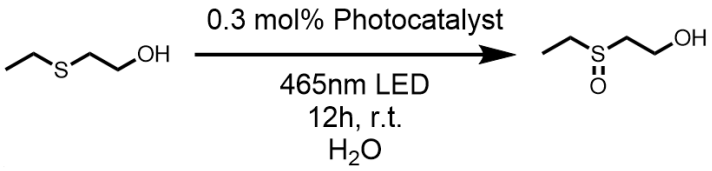

"The synthesis of 2-(ethylsulfinyl)ethan 1-ol was performed according to the general procedure for photocatalytic sulfide oxidations, explained in SI section 9.1. The purification of the compound was performed by flash column chromatography (hexane: EtOAc, 8:2)."

^{1}H NMR (300 MHz, $CDCl_3$, δ): 4.04 (t, 2H, CH_2), 3.13 (t, 2H, CH_2), 3.04 (m, 2H, CH_2), 2.44 (s, 1H; OH), 1.35 (m, 3H, CH_3);

^{13}C NMR (101 MHz, $CDCl_3$, δ): 56.4 (1C; C2), 54.1 (1C; C2), 48.9 (1C; C2), 6.5 (1C; C1);

13.2 Imine Formation

13.2.1 N-(3,4-Dimethoxybenzyl)-1-(3,4-dimethoxyphenyl)methanimine

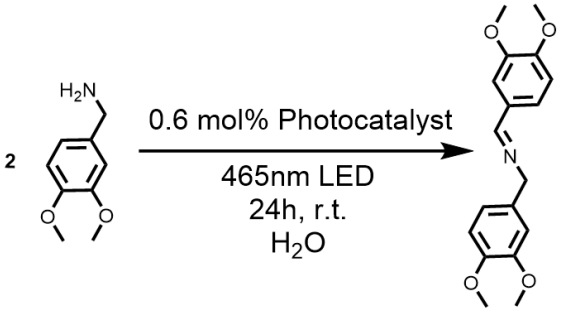

"The synthesis of N-(3,4-dimethoxybenzyl)-1-(3,4-dimethoxyphenyl)methanimine was performed according to the general procedure for photocatalytic imine formation, explained in SI section 9.2. The purification of the compound was performed by flash column chromatography (hexane: EtOAc, 6:4)."

^{1}H NMR (300 MHz, $CDCl_3$, δ): 8.27 (s, 1H, N=CH), 7.47 (m, 1H, Ar H), 7.19 (m, 1H, Ar H), 6.85 (m, 4H; Ar H), 4.73 (s, 2H, CH_2), 4387 (dd, 12H, CH_3) ;

^{13}C NMR (101 MHz, $CDCl_3$, δ): 161.3 (1C; C=N), 151.4 (1C; Ar H), 149.3 (1C; Ar H), 149.0 (1C; Ar H), 148.2 (1C; Ar H), 132.1 (1C; Ar H), 129.46 (1C; Ar H), 123.3 (1C; Ar H), 120.2 (1C; Ar H), 111.5 (1C; Ar H), 111.3 (1C; Ar H), 110.4 (1C; Ar H), 108.9 (1C; Ar H), 64.7 (1C; CH_2) , 55.9 (4C; CH_3);

13.2.2 N-Benzyl-1-phenylmethanimine

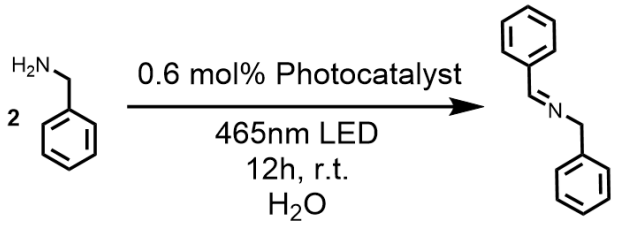

"The synthesis of N-benzyl-1-phenylmethanimine was performed according to the general procedure for photocatalytic imine formation, explained in SI section 9.2. The purification of the compound was performed by flash column chromatography (hexane: EtOAc, 6:4)."

^{1}H NMR (300 MHz, $CDCl_3$, δ): 8.26 (s, 1H, N=CH), 7.67 (m, 2H, Ar H), 7.29 (m, 2H, Ar H), 7.22 (m, 4H; Ar H), 7.16 (m, 2H, Ar H), 4.70 (s, 2H, CH_2);

^{13}C NMR (101 MHz, $CDCl_3$, δ): 162.0 (1C; C=N), 139.4 (1C; Ar H), 136.3 (1C; Ar H), 130.8 (1C; Ar H), 128.7 (2C; Ar H),128.5 (2C; Ar H), 128.35 (2C; Ar H), 128.1 (2C; Ar H), 127.1 (1C; Ar H), 65.1 (1C; CH_2);

13.2.3 N-(4-(Tert-butyl)benzyl)-1-(4-(tert-butyl)phenyl)methanimine

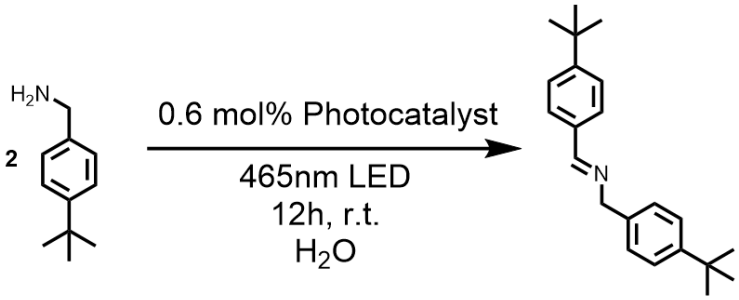

"The synthesis of N-(4-(tert-butyl)benzyl)-1-(4-(tert-butyl)phenyl)methanimine was performed according to the general procedure for photocatalytic imine formation, explained in SI section 9.2. The purification of the compound was performed by flash column chromatography (hexane: EtOAc, 6:4)."

^{1}H NMR (300 MHz, $CDCl_3$, δ): 8.26 (s, 1H, N=CH), 7.62 (m, 2H, Ar H), 7.36 (m, 2H, Ar H), 7.27 (m, 2H; Ar H), 7.19 (m, 2H, Ar H), 4.70 (s, 2H, CH_2), 1.23 (m, 18H, CH_3);

^{13}C NMR (101 MHz, $CDCl_3$, δ): 161.7 (1C; C=N), 154.1 (1C; Ar H), 149.8 (1C; Ar H), 136.4 (1C; Ar H), 133.7 (1C; Ar H), 128.1 (1C; Ar H), 127.7 (3C; Ar H), 125.5 (4C; Ar H), 64.8 (1C; CH_2), 34.9 (1C; C4), 34.4 (1C; C4), 31.2 (6C; C1);

13.3 [1,1′-Biphenyl]-2,2′-dicarbaldehyde

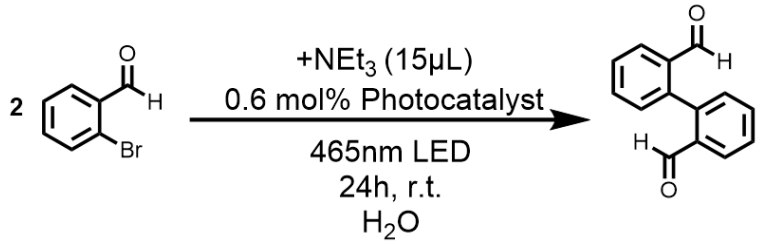

"The synthesis of [1,1′-biphenyl]-2,2′-dicarbaldehyde was performed according to the general procedure for photocatalytic radical C-C coupling, explained in SI section 9.3. The purification of the compound was performed by flash column chromatography (hexane: EtOAc, 6:4)."

^{1}H NMR (300 MHz, $CDCl_3$, δ): 9.76 (s, 2H; COH), 7.97 (m, 2H; Ar H), 7.55 (m, 4H; Ar H), 7.29 (m, 2H; Ar H);

^{13}C NMR (101 MHz, $CDCl_3$, δ): 191.0 (2C; C=O), 141.2 (2C; Ar), 134.6 (2C; Ar), 133.4 (2C; Ar), 131.7 (2C; Ar), 128.8 (2C; Ar), 128.5 (2C; Ar);

13.4 C-C Coupling of 3-Methylindol

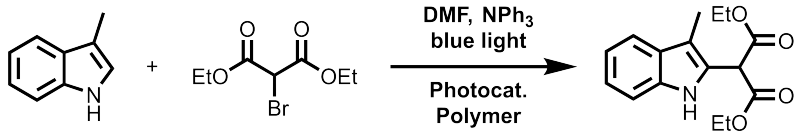

"In a 2 mL flask equipped with a stir bar, 3-methyl indole (19.7 mg, 150 µmol), diethyl bromomalonate (71.7 mg, 300 µmol) and triphenylamine (73.6 mg, 300 µmol) and photocatalytic polymer (250 nmol photoactive unit, from collaboration project) were dissolved in DMF (2 mL). The solution was degassed with argon for 10 min and irradiated under blue light (λ = 460-470 nm). Samples (100 µL) were taken, diluted with DCM and directly measured via GC-MS."

The reaction was purified via silica column chromatography DCM: PE 1:9 to EtAc: PE 8:2.

^{1}H NMR (400 MHz, CD_2Cl_2, δ): 8.93 (s, 1H), 7.54 (ddt, J = 7.9, 1.4, 0.8 Hz, 1H), 7.36 (dt, J = 8.1, 0.9 Hz, 1H), 7.18 (ddd, J = 8.2, 7.0, 1.2 Hz, 1H), 7.09 (ddd, J = 8.0, 7.1, 1.1 Hz, 1H), 5.00 (s, 1H), 4.35-4.10 (m, 4H), 2.30 (s, 3H), 1.29 (t, J = 7.1 Hz, 6H);

^{13}C NMR (101 MHz, CD_2Cl_2, δ): 167.75, 136.19, 128.66, 125.22, 122.65, 119.55, 119.06, 111.34, 110.84, 62.71, 49.79, 14.21, 8.59;

14. Optimization Studies

14.1 Sulfide Oxidation

Table 4.1 shows the optimization of the reaction conditions for the photocatalytic sulfide oxidation, presented in section 4.2.

Table 4.1: Investigation of the photocatalytic behaviour according to reaction condition variation by means of sulfide oxidation reaction.[a]

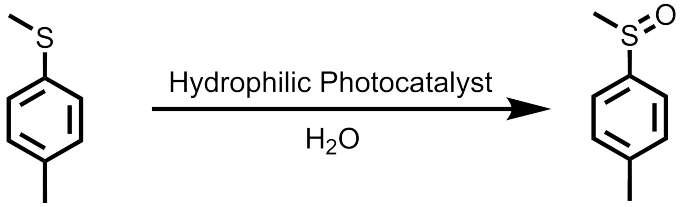

No	Reaction Condition Variation	Conversion [%][b]
1	-	91
2	Degassed by N_2	28
3	No light	0
4	No photocatalyst	0
5	Non-photocatalytic polymer	0
6	0.6 mol% photocatalyst + 10 mM substrate	89
7	0.3 mol% photocatalyst + 50 mM substrate	83
8	Reaction time 8 h	89
9	Additional acetonitrile (15 µL)	89
10	Additional acetonitrile (20 µL)	89
11	Additional NEt_3 (15 µL)	78
12	Additional NEt_3 + acetonitrile (each 15 µL)	51
13	Additional hexafluoroisopropanol (15 µL)	90
14	Additional hexafluorobenzene (15 µL)	90
15	Additional deuterated-dichloromethane (15 µL)	89
16	Additional toluene (15 µL)	89
17	Reduced light source (4.08 W total, 0.68 W per LED)	89

[a] Conditions: Methyl p-tolyl sulfane (20 µmol), hydrophilic photocatalyst polymer (0.096 µmol, 0.3 mol% photocatalyst), dispersed in H_2O (2 mL, sonicated 20 min), 15 °C, 7.14 W, 465 nm, 16 h.[b] Calculated from GC measurements by comparison of peak intensity.

14.2 Imine Formation

Table 4.2 shows the optimization of the reaction conditions for the photocatalytic imine formation, presented in section 4.2.

Table 4.2: Investigation of the photocatalytic behaviour according to reaction condition variation by means of imine formation reaction.[a]

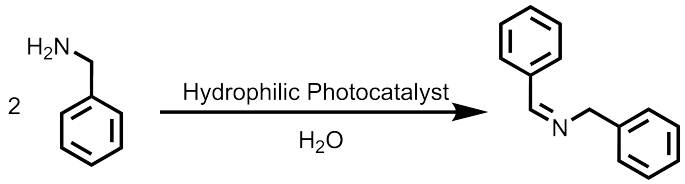

No	Reaction Condition Variation	Conversion [%][b]
1	-	79
2	Degassed by N_2	78
3	No light	<1
4	No photocatalyst	6
5	Non-photocatalytic polymer	1
6	0.3 mol% photocatalyst + 10 mM substrate	35
7	0.3 mol% photocatalyst + 50 mM substrate	29
8	Reaction time 8 h	71
9	Additional acetonitrile (15 µL)	76
10	Additional acetonitrile (20 µL)	69
11	Additional NEt_3 (15 µL)	10
12	Additional NEt_3 + acetonitrile (each 15 µL)	16
13	Additional hexafluoroisopropanol (15 µL)	11
14	Additional hexafluorobenzene (15 µL)	62
15	Additional deuterated-dichloromethane (15 µL)	63
16	Additional toluene (15 µL)	41
17	Reduced light source (4.08 W total, 0.68 W per LED)	56

[a] Conditions: Benzyl amine (13.5 µmol), hydrophilic photocatalyst polymer (0.192 µmol, 0.6 mol% photocatalyst), dispersed in H_2O (2 mL, sonicated 20 min), 15 °C, 7.14 W, 465 nm, 16 h.[b] Calculated from GC measurements by comparison of peak intensity.

14.3 C-C Coupling

Table 4.3 shows the optimization of the reaction conditions for the photocatalytic C-C coupling, presented in section 4.2.

Table 4.3: Investigation of the photocatalytic behaviour according to reaction condition variation by means of aromatic, radical C-C coupling reaction.[a]

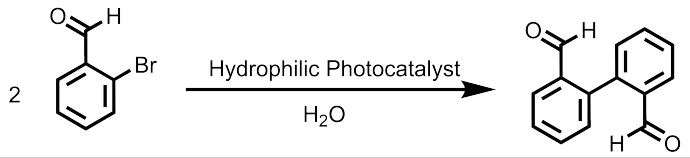

No	Reaction Condition Variation	Conversion [%]b
1	-	0
0	Degassed by N_2	0
3	No light	0
4	No photocatalyst	0
5	Non-photocatalytic polymer + NEt_3 (15 µL)	0
6	0.6 mol% photocatalyst + 10 mM substrate	0
7	0.3 mol% photocatalyst + 50 mM substrate	0
8	Reaction time 8 h	0
9	Additional acetonitrile (15 µL)	4
10	Additional acetonitrile (20 µL)	5
11	Additional NEt_3 (15 µL)	13
12	Additional NEt_3 + acetonitrile (each 15 µL)	51
13	Additional NEt_3 + hexafluoroisopropanol (15 µL)	34
14	Additional NEt_3 + hexafluorobenzene (15 µL)	25
15	Additional NEt_3 + deuterated-dichloromethane (15 µL)	18
16	Additional NEt_3 + toluene (15 µL)	16
17	Reduced light source (4.08 W total, 0.68 W per LED)	0

[a] Conditions: 2-Bromobenzaldehyde (20 µmol), hydrophilic photocatalyst polymer (0.096 µmol, 0.3 mol% photocatalyst), dispersed in H_2O (2 mL, sonicated 20 min), 15 °C, 7.14 W, 465 nm, 16 h.[b] Calculated from GC measurements by comparison of peak intensity.

15. Appendix

For all compound NMR spectra, the reader is reffered to the supporting information in section 8.1.1.

Chapter 5

Exploiting Binding Interactions to Enhance the Photocatalytic Reactivity

The previously discussed Chapter explored the effect of controlled hydrophilicity gradients on the photocatalytic reactivity in correspondence with the substrate hydrophilicity. The inspiration for that approach came from the selectivity concepts utilized in natural enzymes. However, as mentioned before in Chapter 4, enzymes exploit a wide range of selectivity concepts to sustain their selectivity and substrate specificity. Besides the catalytically active sites, enzymes are typically constructed from amino acid building blocks, leading to the formation of defined macromolecular structures. Through tightly knit hydrogen-bonding interactions and disulfide bridges, enzymes form precise tertiary and secondary structures, shaping the enzymatic pocket which is responsible for the substrate coordination and fixation. Defined binding interactions within the enzymatic pocket allow a targeted substrate fixation around the active site, enabling the precise conversion of the substrate to the desired enantiomer/product. Enzymes utilize thereby hydrophilic and hydrophobic interactions from the protruding amino acid residues and the peptide backbone, to transfer sterical information from the environment onto the substrate molecule. The establishment of a chemical gradient, resulting from strong Coulombic interactions and hydrogen-bonding towards the binding of the substrate, strongly accelerates substrate diffusion and mass transfer properties, enhancing the diffusion-limited reaction rate. Each substrate requires an adjusted coordination environment. However, specific amino acid residues are strategically used to coordinate certain molecular functionalities or to impart desired properties, such as hydrophilicity, within the enzymatic pocket.

Arginine, with its guanidyl group, serves as one of the strongest sites for Coulombic interactions and defined hydrogen bonding. Arginine's highly polar guanidyl headgroup, which is strongly basic and protonated under physiological conditions, serves versatile roles in enzyme structure and function. On the enzyme surface, it interacts with the polar environment, while within the enzymatic pocket, it forms specific hydrogen bonds with carboxylates, phosphates, nitrates, and other polar or negatively charged groups. A further advantage is its high stability, due to the conjugation between the three nitrogens, forming

the so-called Y-aromaticity. These properties make guanidyl-groups widely employed and a highly promising candidate for substrate coordination.

It was assumed that the projection of a substrate coordination moiety onto an artificial photocatalytic system could greatly enhance the substrate diffusion towards the photocatalytically active sites, therefore accelerating catalytic turnover by reducing the diffusion-limitation of the targeted reactions. Additionally, the coordination of specific molecular functionalities on the substrate could enable a substrate selectivity mechanism, orthogonal to traditional selectivity of photocatalysts (intrinsic mechanistic selectivity). Within a complex mixture of reagents, a defined substrate differentiation could be implemented.

To investigate the effect of defined substrate coordination on the respective photocatalytic conversion rate, an artificial, photocatalytic model system was designed. The following section 5.2 is based on the submitted manuscript "Controlling Photocatalytic Rates by Binding Group Functionalization of Conjugated Microporous Polymers". The article is authored by Julian Heuer, and co-authored by Seunghyeon Kim, Jeehye Byun, Robert Graf, Katharina Landfester and Calum Ferguson.

A precise implementation of the guanidyl-functionality into a heterogeneous photocatalytic system was targeted. Recently, conjugated microporous polymers (CMPs) have emerged as a highly tunable class of heterogeneous photocatalysts, which suffer from limited substrate accessibility to the photoactive surface due to mass transport constraints. Therefore, we decided to functionalize a CMP system with guanidyl groups for selective substrate interaction. By leveraging non-covalent binding interactions between the substrate and the guanidylated CMP, we achieved photocatalytic rate accelerations for different binding partners. Comparison of the photocatalytic activity of a non-functionalized CMP and the guanidylated CMP revealed an increase in conversion of up to 75% for the functionalized CMP. The investigated binding partners include carboxylates, phosphonates, nitrates, and metal-oxo complexes, successfully demonstrating the incorporation of an orthogonal selectivity concept and proving the reaction acceleration through guanidyl-based molecular recognition sites within photocatalysis.

5.1 Motivation

Pursuing selective and sustainable photocatalysts continues to drive innovation in catalytic systems.[206, 218] Photocatalysis has emerged as a sustainable method to catalyse reactions using visible light, but the output of photocatalytic reactions is often uncontrolled due to its inherent mechanism. Photogenerated electrons and holes are highly active species that react indiscriminately, often with the nearest suitable functional group. Additionally, photocatalytic reactions often use reactive oxygen species that are generated by either electron or energy transfer mechanisms. These are also highly active radical species, which are indiscrete and react with a broad range of functionalities. Therefore, it is often difficult to control the selectivity of photocatalytic reactions.

Recently, conjugated microporous polymers (CMPs) have received increasing attention due to their tunability.[219,–221] These fully organic, conjugated polymers have been used as photocatalysts for CO_2 reduction and H_2O splitting.[48, 195, 222,–224] Moreover, photocatalytic conjugated polymers have been used for a range of organic transformations including cycloadditions[79], halogenations[225] and alkylation reactions[226]. The success of this material class stems from its inherent modularity, allowing tailor-made systems to be developed with almost limitless control of the optoelectronic properties. This versatility has been vastly explored, using band gap tailoring and morphology control, to elevate the catalytic performance.[38, 227,–230]

However, controlling mass transfer of substrates to the reactive materials remains a critical challenge in heterogeneous photocatalysts. Restricted substrate diffusion to the photocatalytic-active sites dramatically reduces photocatalytic performance, often resulting in diffusion-limited reaction rates.[79, 191, 231, 232] Several approaches have been investigated to address these challenges, including varying pore structure, size distribution or morphology.[154, 165, 233,–236] Previously, we have shown that in vinyl-based polymer photocatalytic materials, mass transfer may be controlled using preferential partitioning.[87, 170] Surprisingly, the acceleration of external mass transfer by selective microenvironment modifications at the solid-liquid interface of a photocatalytic particle remains underexplored, despite its potential to improve performance and selectivity.

Molecular recognition sites (MRS) in proximity to the catalytically active sites could be implemented as a promising strategy to accelerate external mass transfer.[133, 154, 237] Previously, the affinity between a substrate and its corresponding MRS has been used to amplify catalytic efficacy or selectivity.[154] These supramolecular host-guest complexes or molecular template techniques, yielded the selective binding of a targeted substrate.[134, 184, 238,–240] However, the complexity of these systems limits their broad-scale application, and more versatile approaches are needed.

This work discusses the projection of guanidyl-functionalities onto a heterogeneous photocatalyst system, targeting the acceleration of photocatalytic conversions through the exploitation of defined coordination sites. Due to their high stability and tunability, recently emerging CMPs were chosen as a framework for functionalization. Guanidine-functionalized CMPs were synthesized and compared against the photocatalytic activity of a non-functionalized CMP. Guided by chemoselective binding interactions between the substrate and the binding groups, a photocatalytic rate acceleration for 3 different binding partners is demonstrated. Therefore, an emulsion-free precipitation synthesis of CMP nanoparticles via Suzuki-Miyaura couplings was developed. Defined photocatalytic nanoparticles were obtained and subsequently decorated with guanidine groups for selective interaction with the desired substrates. The photocatalytic reactivity of functionalized and non-functionalized CMP nanoparticles were compared in a range of photocatalytic reactions. Significant rate differences were observed for the photooxidation of a phosphonate, the photooxidation of tryptophane and the photoreduction of a dichromate ion. The specific interaction between the substrate and guanidyl binding group showed a strong improvement in reaction rate for all monitored reactions.

5.2 Results and Discussion

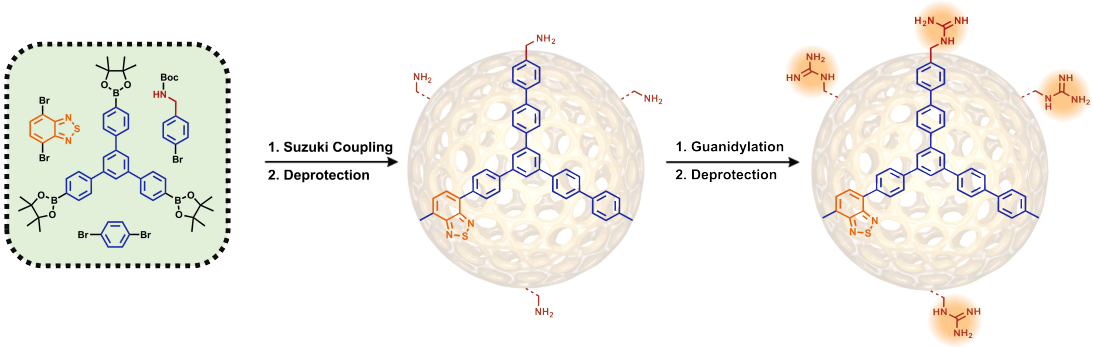

Figure 5.1: Schematic illustration of the CMP synthesis and post-guanidylation.

For synthesis of the CMP system, the boronic ester-based crosslinker 1,3,5-tri(4-pinacholatoborolanephenyl)benzene was polymerized with arylbromides 4,7-dibromo-2,1,3-benzothiadiazole, 1,4-dibromobenzene and N-Boc-4-bromobenzylamine via Suzuki-Miyaura couplings. The subsequent deprotection of the resulting conjugated polymer nanoparticles (Figure 5.1) yielded amine functionalized CMP (CMP-NH_2). These primary amines were then subsequently post-functionalized using 2-methyl-2-thiopseudourea to give guanidine functionalized CMP (CMP-Guanidine). To quantify the effect of the guanidine groups on the surface, we used the amine-functionalized CMP as a reference in all photocatalytic reactions.

The prepared CMPs were characterized using solid-state ^{1}H magic angle spinning (MAS) NMR spectroscopy. After Boc-deprotection, CMP-NH_2 and CMP Guanidine showed broad ^{1}H signals at 7 and 1.5 ppm. (Figure 8.31 & 8.32). The strong peak at 7 ppm indicated strongly deshielded aromatic protons, which can be assigned to the conjugated system. CMP-Guanidine showed a signal at 3 ppm, which was assigned to the benzylic CH_2 group. The broad signal at 1.5 ppm indicates residual amounts of Boc-protection groups, presumably trapped within the core of the formed CMP nanoparticles. However, no distinct guanidine ^{1}H peaks were observed in the deprotected state of CMP-Guanidine. To verify the successful guanidylation of CMP-NH_2, additional ^{1}H-MAS NMR measurements were conducted of the Boc-protected state. Interestingly, strong doublet signals were obtained at 17.8 and 14.6 ppm (Figure 5.2). These extremely deshielded protons are from the guanidine's N-H, due to its highly electronegative structure. The formation of doublets is due to the existence of conformation isomers. Through the mesomeric effect, two stable canonical resonance structures are formed between the ketimine functionality and the C-NH-Boc functionality.[241] This assumption is also supported by the pair-wise correlation of the guanidine N-H signals observed in the ^{1}H-^{1}H double quantum correlation spectrum shown in Figure 8.36.

The analysis of the solid-state ^{13}C cross polarization MAS NMR spectroscopy (Figure 8.31b & 8.32b) for the deprotected CMP NH_2 and CMP-Guanidine revealed a similar composition, exhibiting strong signals at 154, 141 and 128 ppm. Small signals were found at 84, 25 and 19 ppm. The peak at 154 ppm can be assigned to the C=N carbons of the

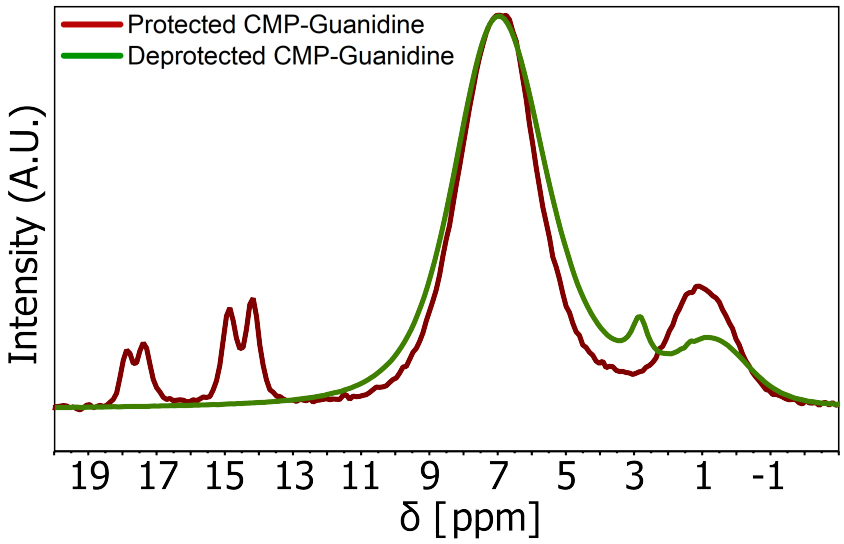

Figure 5.2: ^{1}H MAS NMR spectra of CMP-Guanidine before and after Boc-deprotection.

benzothiadiazole groups and the sp^2-hybridized guanidyl carbon. The peak at 141 ppm is from the quaternary carbons within the aromatic conjugated system. The intense peak at 128 ppm from the aromatic C-H carbons within the aromatic conjugated system. The small signals at 84 and 25 ppm correspond to the quaternary carbon and methyl groups of residual Boc-protection groups, respectively. Lastly, the small signal at 19 ppm is assigned to the benzylic CH_2 carbon. Furthermore, since no strong distinction between the CMP-NH_2 and CMP-Guanidine could be made, the Boc-protected compounds were analyzed (Figure 8.31b & 8.32b). Besides more pronounced peaks at 84, 25 and 19 ppm for the Boc-protection groups and benzylic CH_2 functionalities, two defined peaks emerged at 168 and 164 ppm for CMP-Guanidine, which are from the sp^2-hybridized carbamate carbons of the Boc-protection groups. The correlation between these carbons and the N-H protons of the guanidyl groups was confirmed by a ^{1}H-^{13}C cross-correlation NMR experiment (Figure 8.34). To further validate the proposed guanidylation of CMP-NH_2 by the discussed presented procedure, the guanidylation of a model compound was investigated. Here, 4-bromobenzylamine was guanidylated, using the identical reaction protocol of the CMP synthesis. Liquid state ^{1}H and ^{13}C-NMR experiments were used to verify the guanidylation of 4-bromobenzylamine (Figure 8.39-8.42). These results confirm the successful guanidylation of CMP-NH_2 to obtain CMP-Guanidine.

The CMP composition was investigated via infrared spectroscopy (Figure 5.3 & 5.17), where the characteristic absorption bands for aromatic (3440, 3014, 1400–1450, 1195, 889 cm^{-1}) and benzothiadiazole (2918, 2854, 1595, 1483, 819 cm^{-1}) units were confirmed in both CMP systems. Of particular interest was the characterization of the guanidyl functionalization. For CMP-Guanidine, distinct guanidine bands were observed for N-H stretches (3373, 3207 cm^{-1}), N-H bends (1643, 1485 cm^{-1}) and C-N stretch (1100 cm^{-1}). These results underline the guanidylation of the CMP-Guanidine and complement the

NMR studies. The distinction between residual primary amine and guanidyl groups on the CMP was not possible due to overlapping absorption bands.

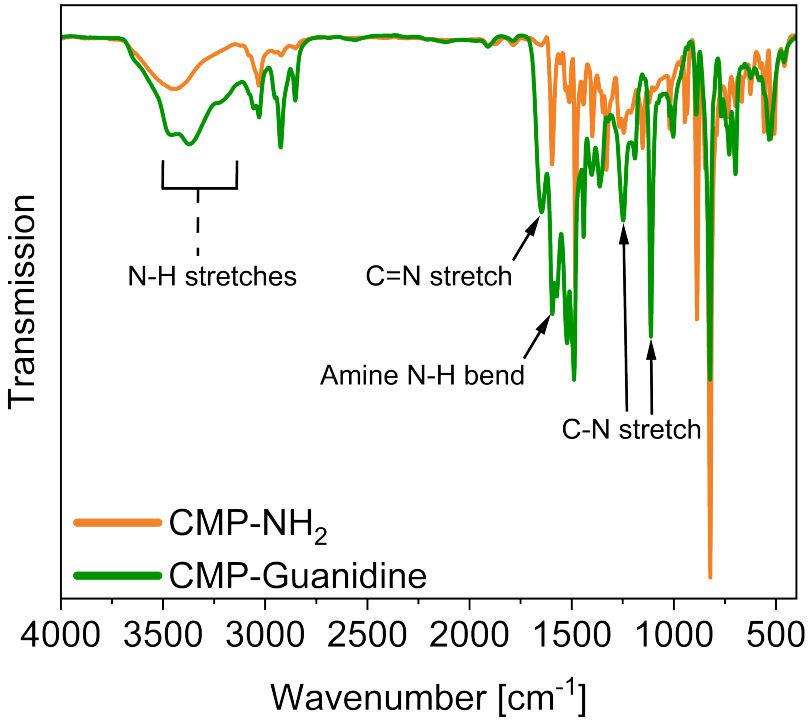

Figure 5.3: FTIR transmission spectra of CMP-NH_2 and CMP-Guanidine.

As the prepared CMPs were employed as photocatalysts, relevant optoelectronic properties were characterized by cyclic voltammetry (Figure 5.18 & 5.19). Comparing the obtained oxidation potentials (vs. Standard Calomel Electrode (SCE) in acetonitrile) of 1.44 V for CMP-NH_2 and 1.39 V for CMP-Guanidine, a difference of 0.05 V was observed for the HOMO. The minimal upshift of the HOMO may be due to the introduction of the more electron-withdrawing guanidyl group.[79] However, since the conjugated system is bridged by a methylene spacer group from the amine/guanidine functionality, only a minimal impact of the functionalization on the HOMO was observed. The analyzed LUMO values of -0.65 V for CMP-NH_2 and -0.77 V for CMP-Guanidine gave a LUMO upshift of 0.12 V for CMP-Guanidine. A LUMO lowering was expected for the CMP-Guanidine, due to the higher electronegativity of the guanidyl groups. The observed LUMO upshift may be due to the higher degree of π-conjugation of CMP-Guanidine, therefore improving the resonance-based stabilization of the excited electron. Considering the obtained frontier molecular orbital values, the electronic band gap can be calculated, giving 2.09 V for CMP-NH_2 and 2.16 V for CMP-Guanidine. It can be stated, that the incorporation of guanidine into the CMP system had no significant influence on the optoelectronic behavior of the CMPs. This means that any difference in photocatalytic activity between the systems is unlikely to be due to the performance of the photocatalyst.

Further characterization of the optical properties of both systems was conducted by UV/Vis absorption spectroscopy (Figure 5.4). Both CMP systems showed two absorption maxima at 328 nm and 428 nm. The absorption behavior aligns with comparable donor-acceptor CMPs in the literature.[78] The strong peak overlap and absorption decay until 700 nm can be explained by scattering phenomena. Investigation of the emission behavior resulted in identical fluorescence emission spectra for both samples, exhibiting a single emission maximum at 530 nm after excitation at 428 nm. These results support the assumption that post-guanidylation does not affect the optical properties of the CMP.

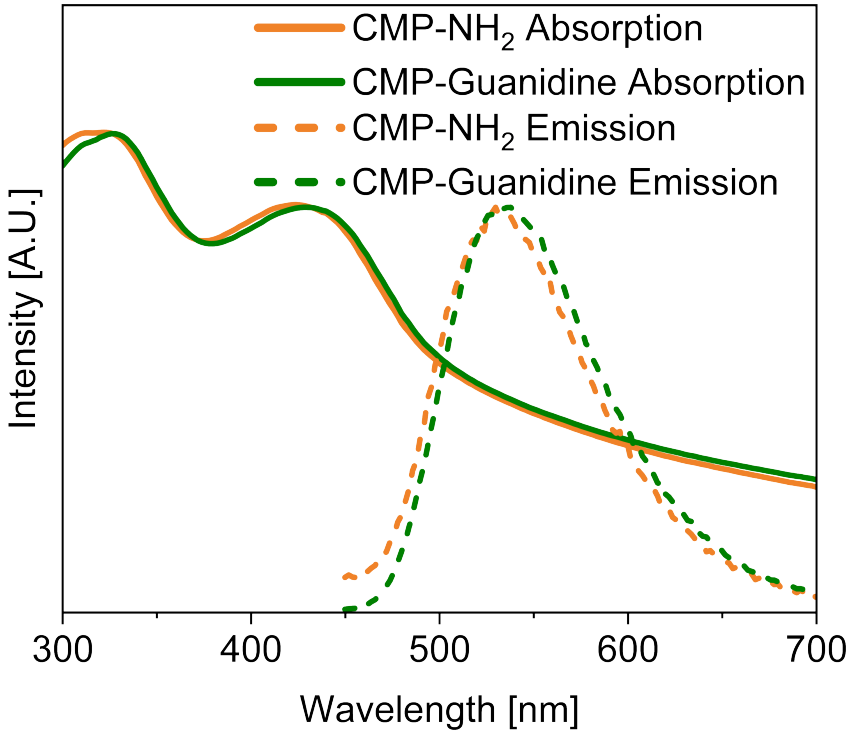

Figure 5.4: UV/Vis absorption and fluorescence emission spectra of CMP-NH_2 and CMP-Guanidine in acetonitrile.

The structure of the synthesized CMPs was investigated by multi-angle dynamic light scattering (MADLS) (Figure 5.5 & 5.20). MADLS showed comparable hydrodynamic radii for the CMP-NH_2 and CMP-Guanidine of around 200 nm. A single, monomodal peak was observed for both samples, indicating a homogeneous structure formation. Furthermore, both samples were investigated via scanning electron microscopy (SEM) (Figure 5.6) and transmission electron microscopy (TEM) (Figure 5.7). Interestingly, SEM and TEM revealed nanoparticle formation for both CMP systems. Qualitative SEM particle analysis gave an average size of 88 and 75 nm for CMP-NH_2 and CMP-Guanidine, respectively (Figure 5.6e and f). These results align with the MADLS measurements, comparing the hydrodynamic radius against the solvent-free collapsed particle under SEM conditions. The characterized CMP systems exhibit therefore similar morphological properties. However, the presence of polymeric nanoparticles was unexpected, due to the absence of an emulsion template or surfactant. The polymerization was carried out in a homogeneous solvent mixture of dimethylformamide (DMF) and 7 vol% 1M NaOH (aq.). The nanoparticle formation

is likely to be driven by increasing hydrophobicity of the growing polymer network and subsequent precipitation after reaching colloidal instability.[242] However, this would require a stabilizer to maintain the nanometer size of the particles. The addition of the Boc-protected amine may induce this stabilization but further investigation is required to explain the controlled formation of spherical nanoparticles.

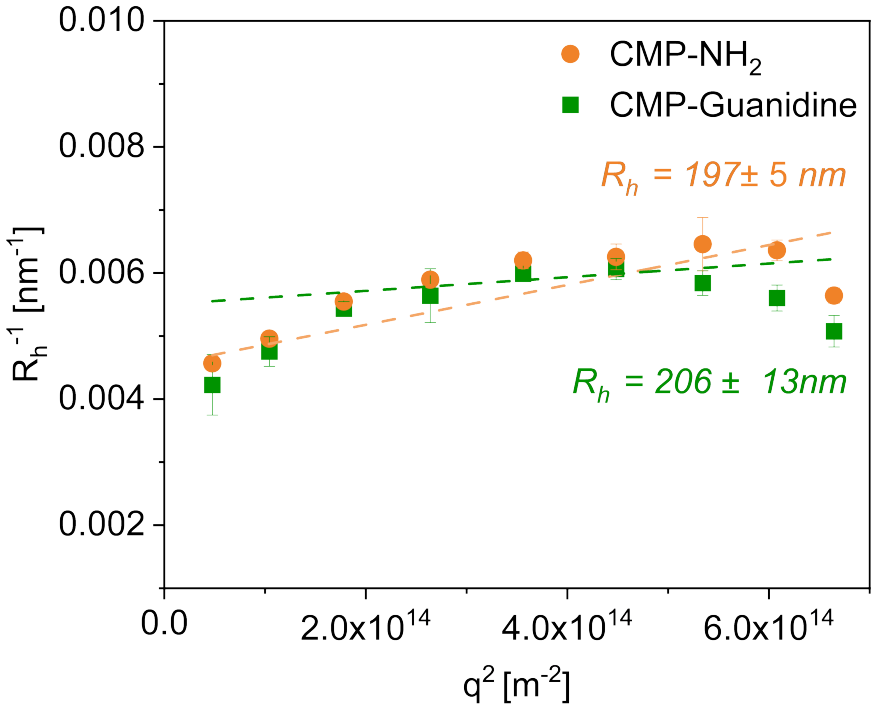

Figure 5.5: MADLS in acetonitrile for CMP-NH_2 and CMP-Guanidine.

Furthermore, Figure 5.8 shows the energy-dispersive X-ray (EDX) spectroscopy of the nanoparticles during the high-angle annular dark-field (HAADF) imaging TEM analysis. Comparable cluster sizes were analyzed for both systems, CMP-NH_2 and CMP-Guanidine. Herein, the palladium content of the particles was of interest. A prominent claim in photocatalysis is the involvement of palladium residues within the photocatalytic reaction (especially for coupling reactions). Comparing the obtained time-dependent EDX results, minimal palladium quantities were found in both samples. CMP-NH_2 shows a slightly higher content of palladium, however, both systems exhibit a comparable amount of palladium. Additionally, for CMP-NH_2 slightly higher bromine signals were observed, indicating an incomplete conversion during the Suzuki-Miyaura coupling. The observed copper signal in both samples is reasoned by copper residues in the carbon-coating of the utilized gold grids (found by comparison with a blank grid). In total it can be stated, that both particle systems exhibit comparable amounts of palladium. However, as CMP-NH_2 was used as a base for further guanidylation, and the systems were subsequently compared in reactivity, the palladium content can be disregarded as a cause for enhanced reactivity of one system over the other.

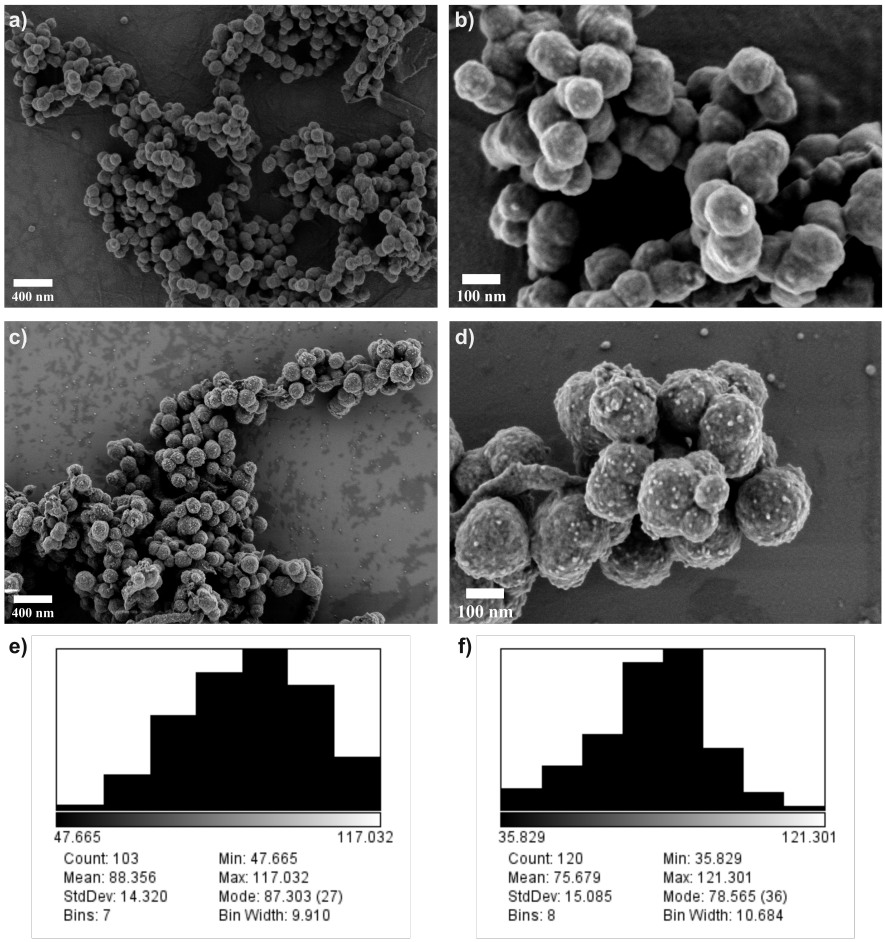

Figure 5.6: SEM images of (a-b) CMP-NH_2 and (c-d) CMP-Guanidine. Corresponding average size distribution particle analysis of (e) CMP-NH_2 and (f) CMP-Guanidine.

The defined particle formation of the designed systems without an emulsion/dispersion-based polymerization approach was highly unexpected. As mentioned above, a hydrophilcity -based influence of the N-Boc-bromobenzylamine during the polymerization process was assumed to induce the controlled formation of nanoparticles. To investigate the corresponding influence, another CMP system was synthesized under identical conditions. For this system however, the equivalent dibromobenzene (from CMP-NH_2) was substituted with an additional equivalent of N-Boc-bromobenzylamine, utilizing two equivalents in total. The further utilization of dibromobenzothiadiazole ensured the network formation. The morphological characterization via SEM of this system is depicted in Figure 5.9. Interestingly, using this synthetic protocol a strong morphology change of the CMP was observed. Instead of the previously obtained nanoparticles, hollow, long and short segmented nanorods were obtained. This finding clearly indicates the influence and relevance of N-Boc-bromobenzylamine within morphology control of CMP systems. However, an in-depth investigation of the monomer dependencies and morphology control is necessary, to unravel the mechanism of the observed nanostructure formation.

The surface area of the prepared CMPs was investigated using Brunauer-Emmett-Teller (BET) nitrogen sorption (Figure 5.10). Both CMP-NH_2 and CMP-Guanidine exhibited a BET

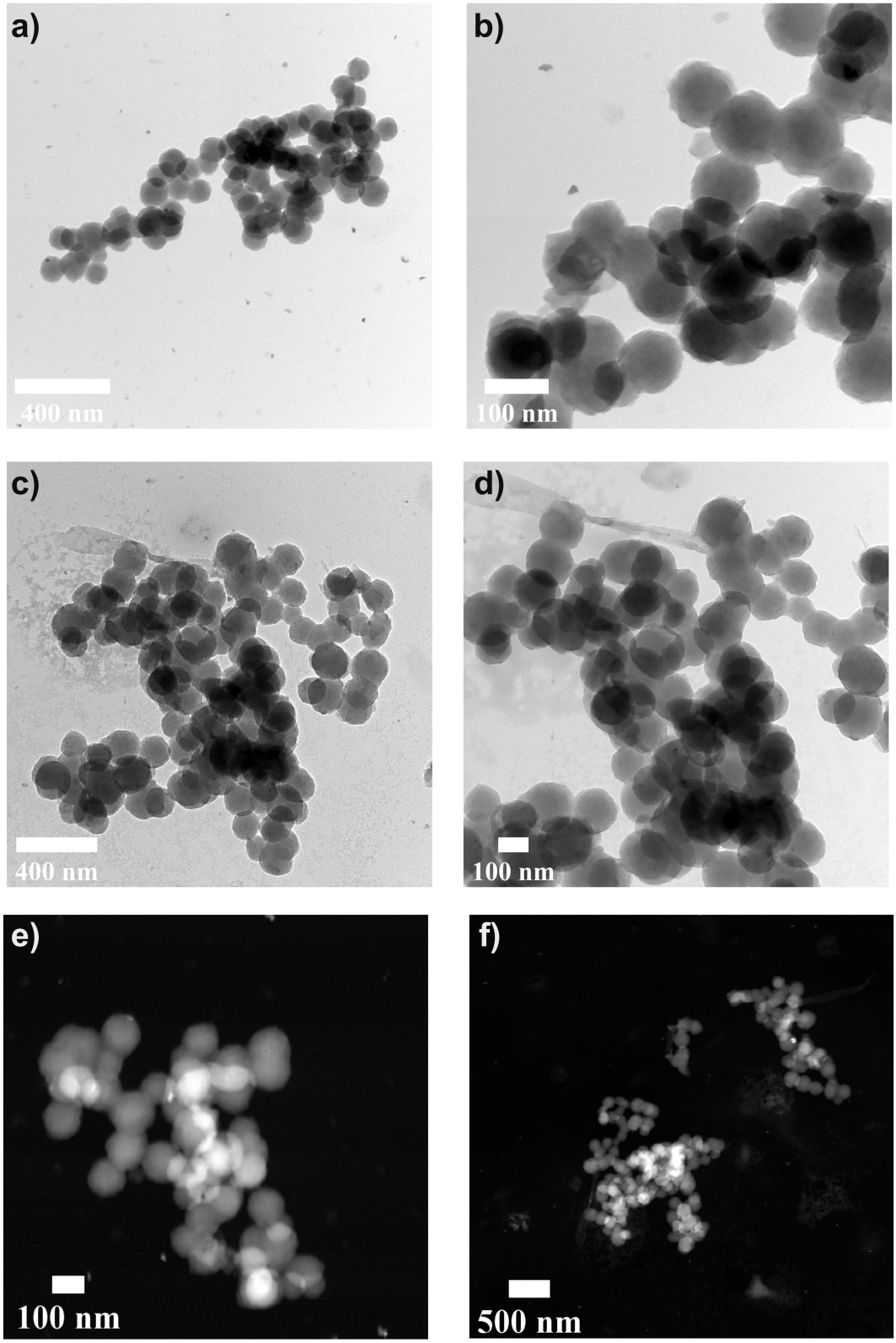

Figure 5.7: TEM images of (a-b) CMP-NH_2 and (c-d) CMP-Guanidine. HAADF image of (e) CMP-NH_2 and (f) CMP-Guanidine.

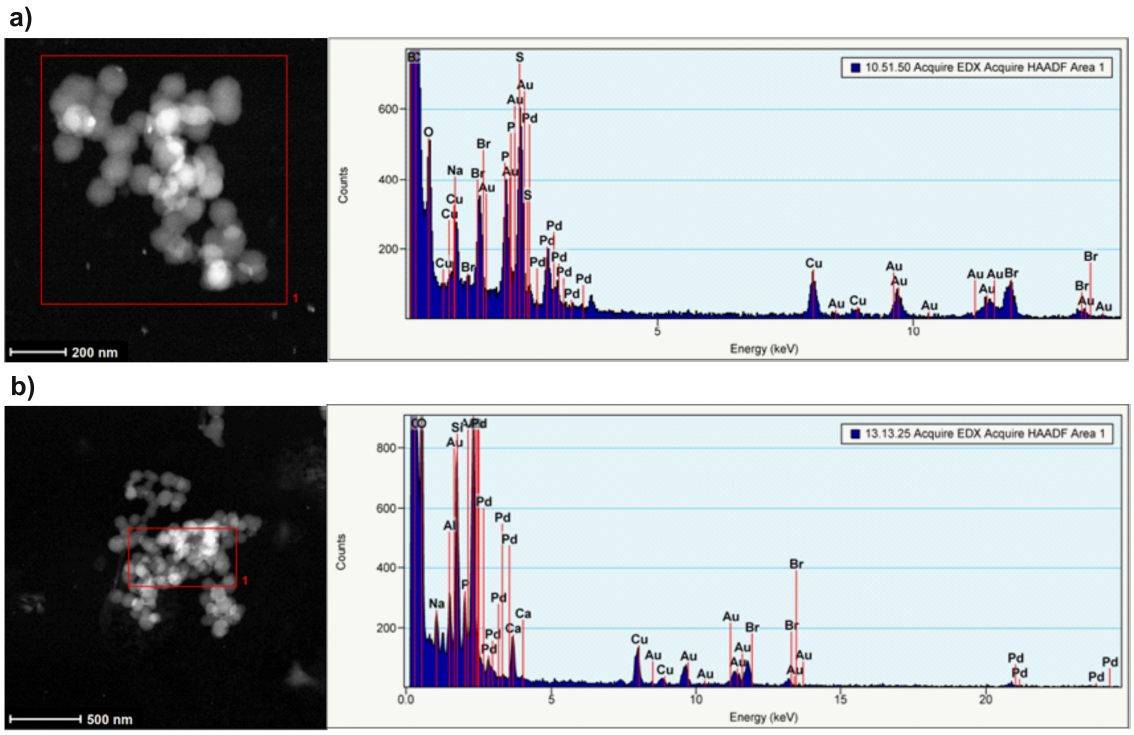

Figure 5.8: Energy-dispersive X-ray spectroscopy for both synthesized CMP nanoparticle systems. Showing similar quantities of palladium. a) CMP-NH_2 and b) CMP-Guanidine.

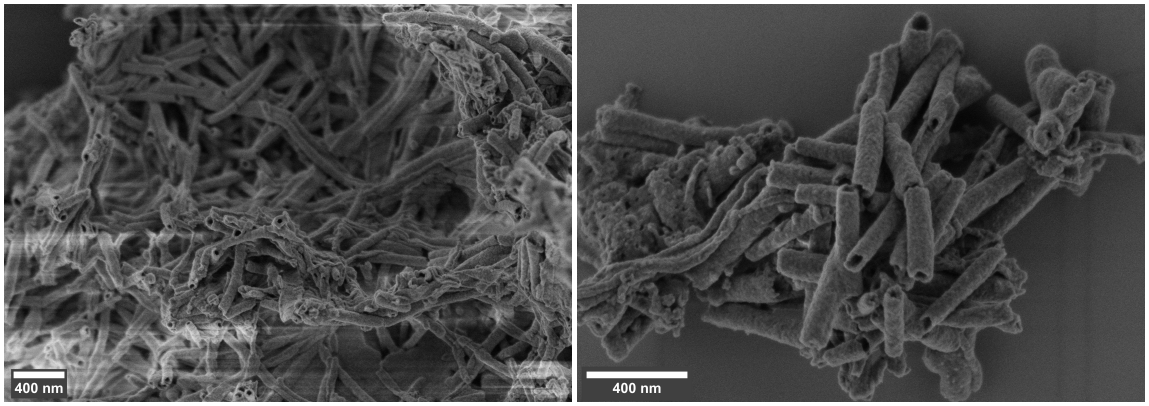

Figure 5.9: SEM image of formed CMP nanostructures after change in monomer equivalents. Dibromobenzene was substituted with an additional equivalent of N-Boc-4-bromobenzylamine.

surface area of 145 m^2g^{-1}. The pore size analysis showed an identical distribution for both systems, which is centered around 1-11 nm. The majority of the pores are between 1-3 nm in diameter. Microporosity is therefore present in both CMP systems. This microporosity is explained by the structurally restricted and sterically challenging monomer units used for the highly conjugated system.[243]

To evaluate the effect of the guanidyl directing groups on the catalytic performance, the photocatalytic activity of CMP-NH_2 and CMP-Guanidine were compared. Photocatalytic reactions where the substrate would interact favorably with the functionalized guanidine groups were targeted. A well-documented interaction is the phosphonate-guanidine

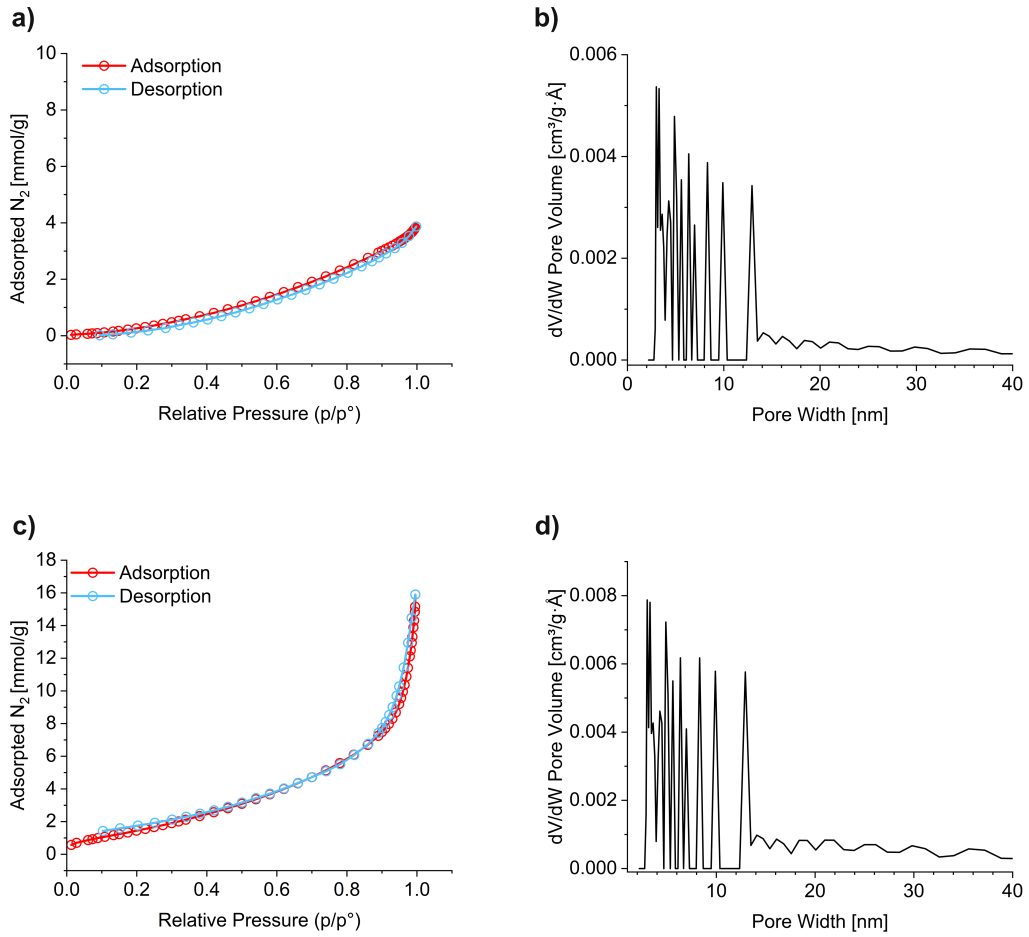

Figure 5.10: N_2 sorption-desorption isotherms for (a) CMP-NH_2 and (c) CMP-Guanidine. Pore size distributions of (b) CMP-NH_2 and (d) CMP-Guanidine.

binding through bidentate hydrogen bonding between the phosphonate oxygen and the guanidine hydrogens.[244] We investigated the phosphonate-guanidine binding in the degradation of the environmental pollutant glyphosate. To ensure complete dispersibility of CMP-NH_2 and CMP-Guanidine, 0.5 mg CMP of each sample was first dispersed in DMF before addition to the aqueous reaction mixture. The reaction was conducted under an O_2 atmosphere and was irradiated with blue LEDs (460 nm). The reaction kinetics were monitored by ^{31}P-NMR (Figure 5.11). Initially, the phosphonate signal of glyphosate was detected at 17 ppm. After 2 h irradiation, the targeted phosphate product was detected at 2.5 ppm. Furthermore, a range of intermediates were detected between 13-14 ppm and 7.3 ppm. According to literature reports, ROS-based glyphosate oxidation is often accompanied by the formation of aminomethylphosphonic acid and acetyl glyphosate.[196, 245, 246]

Further irradiation of the reaction mixture led to an increase in conversion of the corresponding phosphate until a plateau was observed after 3 h reaction time for CMP-Guanidine. This plateau formation was attributed to a potential accumulation of generated phosphate on the surface of CMP-Guanidine, thereby hindering further substrate

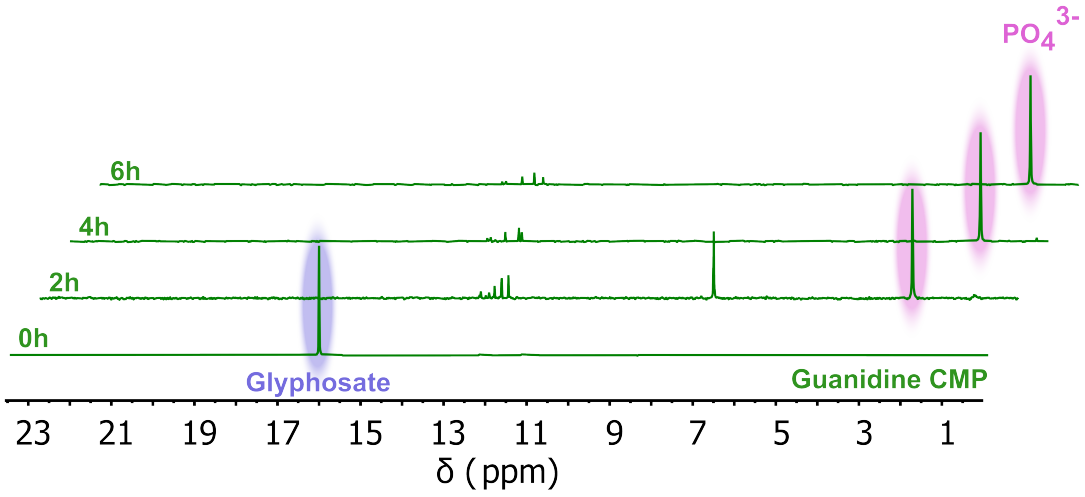

Figure 5.11: Time-dependent ^{31}P-NMR spectra for the glyphosate oxidation via CMP-Guanidine.

accessibility. As the reaction time increased, a slight shielding of the phosphate signal was noted, indicating an increasing acidity within the reaction system due to phosphate formation. CMP-Guanidine showed a final yield of 92% after 6 h, while CMP-NH_2 only reached 17%. Therefore, a total yield increase of 75% for CMP-Guanidine was achieved. This strongly divergent trend between the two CMP systems can be attributed to the directing phosphonate-guanidine affinity, accelerating external mass transfer of the substrate to the CMP surface. Here, a locally elevated concentration of ROS around the photocatalytic active surface strongly enhances the photooxidation rate of glyphosate.[122]

Carboxylate groups have preferential binding with the guanidine functionality. Coulombic attraction between the oppositely charged moieties, coupled with defined intermolecular hydrogen bonding, is reported to create a strong interionic binding interaction between guanidines and carboxylates.[141] Therefore, an investigation of the ROS-based photooxidation of tryptophan was conducted, which is an important step within tryptophan metabolism.[247] The reaction was conducted under atmospheric conditions and the reaction rate was monitored by ^{1}H-NMR. Initially, the reaction showed only slight differences, however, a stark diverging trend emerged as the reaction progressed (Figure 5.13). CMP-Guanidine significantly outperformed CMP-NH_2 after 8 h reaction time. A maximum conversion of 45% was achieved by CMP-Guanidine, whereas CMP-NH_2 only converted 15% within the same timeframe. The expected main product for the photooxidation of L-tryptophan was N-formylkynurenine.[248] However, in addition to N-formylkynurenine, a range of unidentified intermediates were observed. The literature reports known side products for this reaction, such as kynurenic acid, oxindolealanine and hydroxytryptophanes.[249, 250] Consequently, the photooxidation conversion rate was determined by monitoring the indolic C_2-H signal against the internal standard. Thus, it can be concluded that the carboxylate binding affinity for the guanidine groups strongly accelerates the

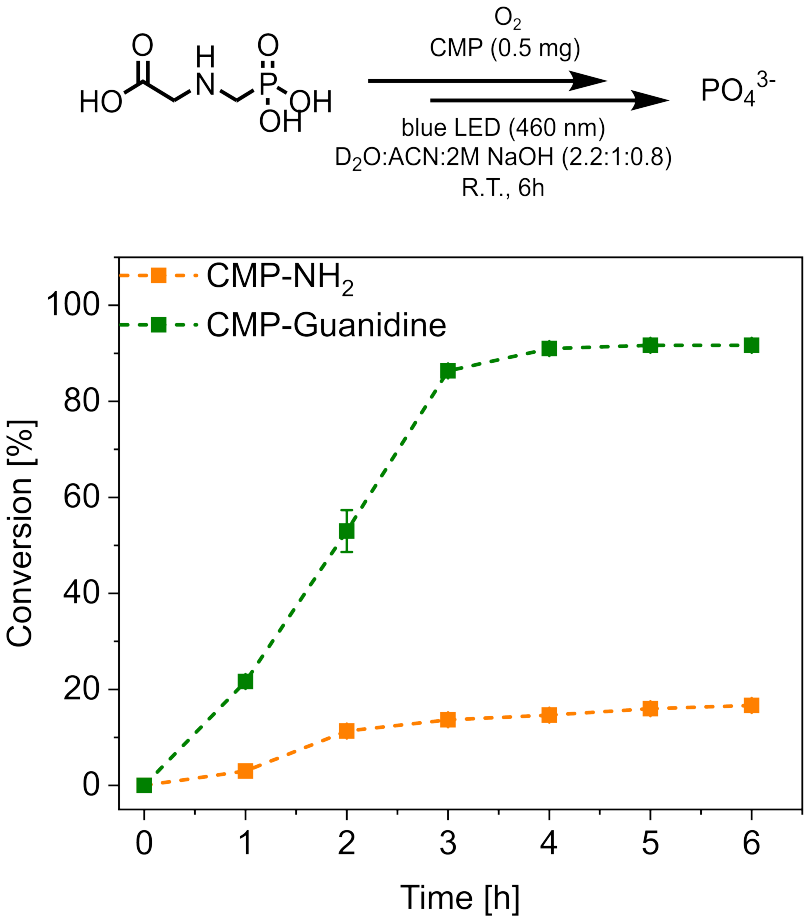

Figure 5.12: Kinetic profile of the glyphosate oxidation for both CMP systems, obtained via ^{31}P-NMR spectroscopy with triphenylphosphate as internal standard.

conversion in the photooxidation of L-tryptophan, resulting in a fourfold increase in conversion.

Recently, our group presented the enhancement of photocatalytic activity driven by Coulombic interaction.[251] To further evaluate the effect of Coulombic interaction on the CMP system, positively charged guanidyl groups were used to attract negatively charged dichromate ions to the photoactive surface.[252] The enhanced mass transfer to the photoactive surface was expected to improve the reaction rate for the photoreduction of dichromate ions. The residual chromium(VI) ions were complexed and then monitored via UV/VIS spectroscopy (Figure 5.14). After 10 min, CMP-Guanidine already showed a reduction of 38% of dichromate ions, while CMP-NH_2 only achieved 10%. This initial jump in conversion can be explained by the pre-coordination of the dichromate ions to the guanidyl-groups before the start of the reaction. Afterwards, the lower substrate concentration resulted in a slow equilibration of coordination and therefore a less pronounced reaction acceleration. CMP-NH_2 showed an entirely linear reaction progression, reaching a maximum conversion of 30% after 60 min. CMP-Guanidine showed a linear progression

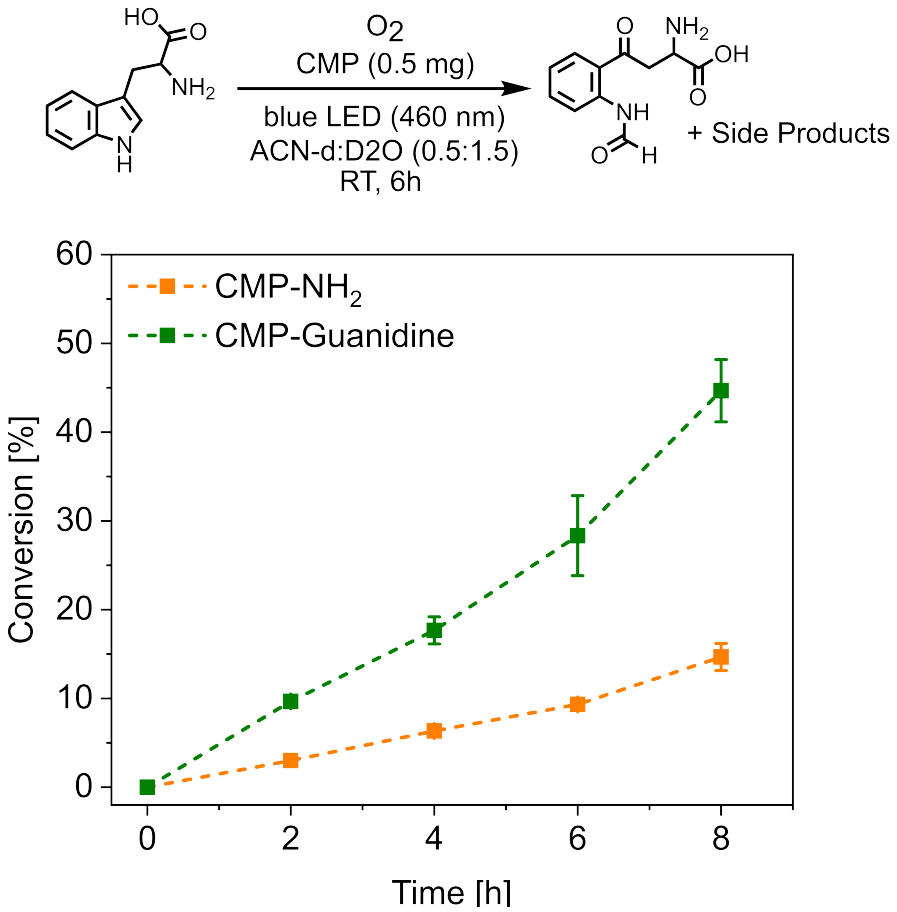

Figure 5.13: Kinetic reaction profile for the photocatalytic L-tryptophan oxidation for both CMP systems. Values obtained via ^{1}H-NMR spectroscopy with dimethylsulfone as internal standard.

from 10 min on as well, with a maximum conversion of 77%. However, the linear progression proceeds faster for CMP-Guanidine. The presented dichromate photoreduction demonstrates that the Coulumbic interaction can be used to accelerate the photocatalytic reaction rate.

Besides the discussed coordination effects of the guanidyl-group, guanidines exhibit additional promising characteristics. As mentioned earlier, guanidines have a strong basic character with a pK_b-value of 0.4, which led to a widespread application of guanidines as organocatalysts.[253] To investigate the utilization of the incorporated guanidine-groups on the CMP-Guanidine as organocatalyst, the organocatalytic bromolactonization of 5-hexenoic acid with N-bromosuccinimid was conducted (Figure 5.15). The reaction was carried out under dark conditions, ensuring the exclusion of photocatalytic effects. The comparison of a blank sample, CMP-NH_2 and CMP-Guanidine showed a clear difference in conversion. CMP-Guanidine showed the strongest conversion, yielding up to 50% conversion after 3 h reaction time. The reference system CMP-NH_2 yielded 40% conversion into the desired product. During the reaction progression, a diverging trend between CMP-NH_2 and CMP-Guanidine was observed. A maximum difference of 13% was already found after 45 min reaction time. The accelerated reaction rate is reasoned

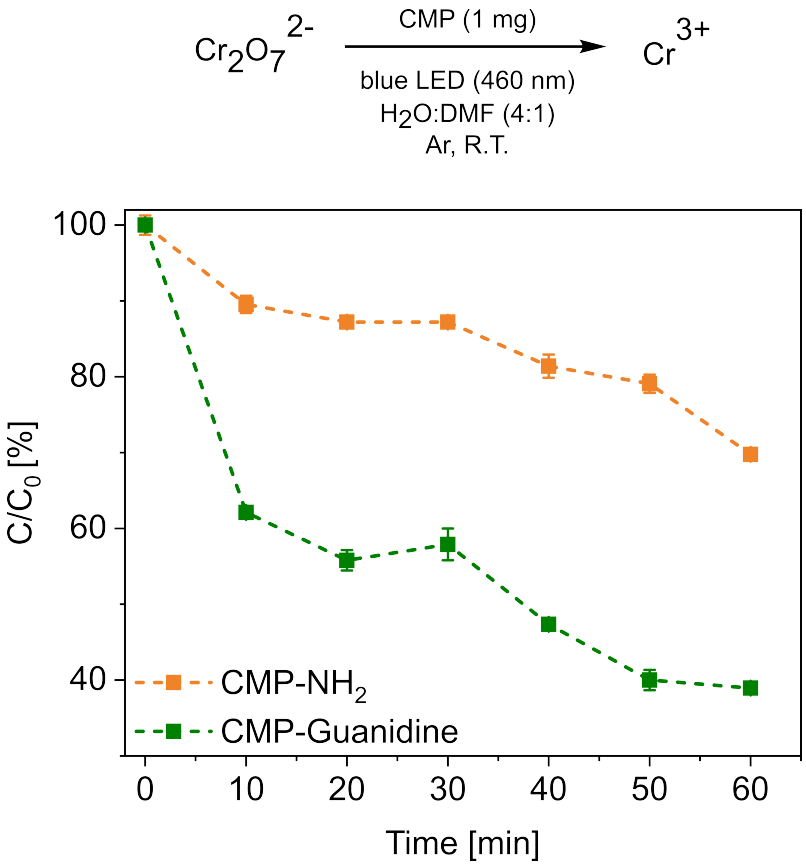

Figure 5.14: Kinetic reaction profile for the photoreduction of dichromate ions for both CMP systems. Values were obtained after the complexation of Cr(VI) and characterization via UV/Vis spectroscopy. C_0= initial Cr(VI) concentration under dark conditions; C= Cr(VI) concentration after irradiation.

by the coordination of the carboxylate-groupand the NBS towards the guanidine, which results in an accelerated activation of the compound. However, even the blank sample showed the formation of up to 20% product. Due to these findings, the organocatalytic acceleration of the bromolactonization was considered unreliable in terms of the investigation of the organocatalytic character of the guanidine-group. Therefore, this reaction was not investigated further.

In another approach to evaluate the organocatalytic character of guanidyl-groups, the organocatalytic reduction of nitro-phenol to the corresponding amino-phenol was investigated (Figure 5.16). The photoreduction of nitro-phenols represents an established reaction for benzothiadiazole-based photocatalysts, and is usually conducted under irradiation, showing nearly full conversion after 15-60 min. However, the presented reaction was conducted for 3 days at room temperature under dark conditions and with the addition of sodium borohydride as a reducing agent. Over the 3 days of reaction time, significant differences between CMP-NH_2 and CMP-Guanidine were observed. While CMP-NH_2 shows nearly no conversion (steadily below 5%), CMP-Guanidine showed ever-increasing product conversion over the reaction progression. After 3 days reaction time, CMP-Guanidine showed a maximal conversion of 87%. This behavior was repeatedly observed. It is assumed, that the coordination of the nitro-group towards the guanidyl-group weakens the

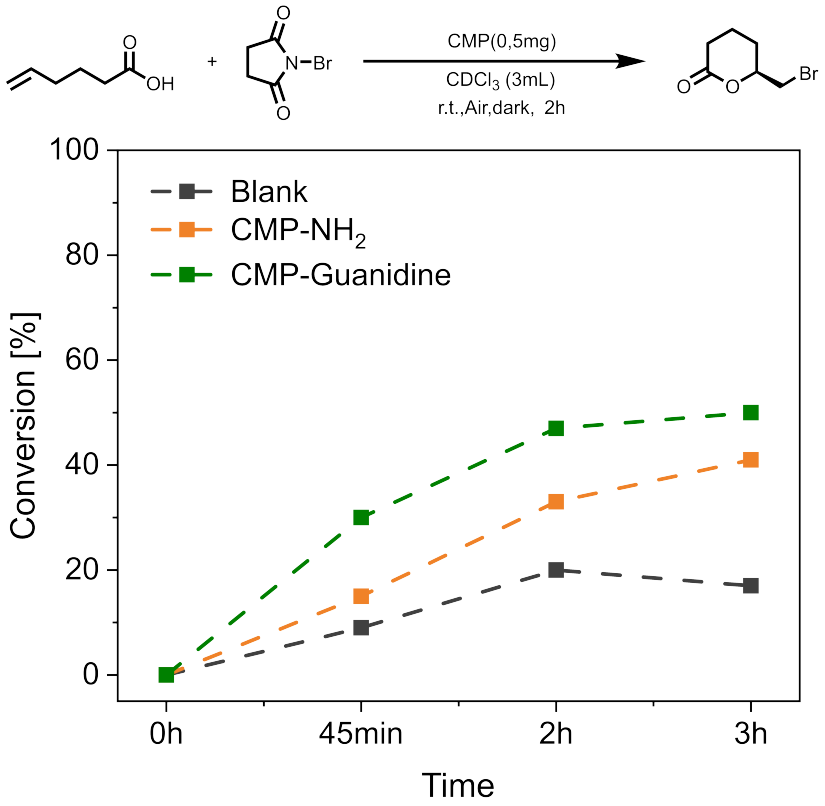

Figure 5.15: Kinetic profile of the investigated organocatalytic bromolactonization under dark conditions. The values were obtained by ^{1}H-NMR spectroscopy.

nitrogen-oxygen bond, which facilitates then the subsequent reduction of nitro-phenol by the hydride ions. The absence of product formation with CMP-NH_2 was puzzling, as the amino-group was expected to show coordinative behavior towards the nitro-group as well. Apparently, the binding interaction of nitro-amine is insufficient to activate the nitro-group for reduction.

To gain insights into the reaction mechanism, an optimization study for the reaction was conducted. In table 5.1, the reaction conditions and utilized catalyst systems are shown for each iteration. It is shown, that only the combination of CMP-Guanidine, NaOH and $NaBH_4$ yielded the desired product. The reaction was independent of light, as irradiated and dark reaction conditions gave the same yield. Surprisingly, even the utilization of guanidine hydrochloride as organocatalyst did not yield any product. This finding indicates a complex reaction mechanism for the utilization of CMP-Guanidine. The slight product formation observed with CMP-NH_2 might hint towards an involvement of the CMP framework, as CMP-free conditions did not yield any product. These results underline the utilization of the guanidyl-functionality within CMP-Guanidine for an organocatalytic reactivity, paving the way for the design of orthogonal catalyst designs. However, for the organocatalytic nitro-reduction, further investigation of the reaction mechanism has to be conducted.

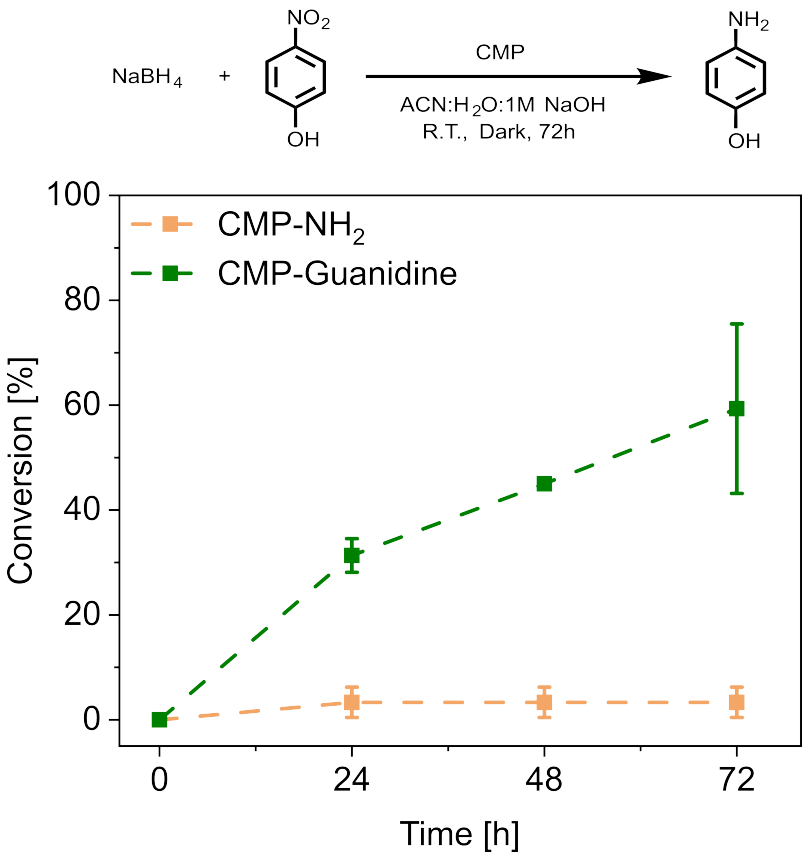

Figure 5.16: Kinetic profile of the investigated organocatalytic nitro-reduction under dark conditions. Values were obtained by ^{1}H-NMR spectroscopy.

Table 5.1: Optimization reactions for the organocatalytic nitro-reduction.

Entry	Catalyst	Solvent	Light	$NaBH_4$	Yield
1	None	ACN:H_2O:NaOH	-	+	0%
2	Guanidine HCl	ACN:H_2O:NaOH	-	+	0%
3	CMP-NH_2	ACN:H_2O:NaOH	-	+	5%
4	CMP Guanidine	ACN:H_2O:NaOH	-	+	87%
5	CMP Guanidine	ACN:H_2O	-	+	0%
6	CMP Guanidine	ACN:H_2O:NaOH	+	+	87%
7	CMP Guanidine	ACN:H_2O:NaOH	-	-	0%

5.3 Conclusion

In this chapter, a broad investigation of guanidyl-groups for catalytic rate acceleration is presented. Different small-molecule photocatalyst were functionalized with guanidyl-groups and thoroughly characterized towards their optoelectronic properties. The incorporated guanidyl-groups were employed for defined binding interactions with specific functional groups of the substrates, investigating their application in challenging organic transformations and depolymerizations. However, the limited solubility of the synthesized catalysts, due to their strong dipole moment and hydrophilicity gradient, and their low photostability during the reaction, led to a pivoting from homogeneous to heterogeneous catalyst systems. We were able to successfully demonstrate the implementation

of substrate-binding interactions into a CMP photocatalyst. To achieve this, conjugated microporous polymer photocatalysts were post-functionalized with guanidyl groups. The developed CMP synthesis protocol yielded thereby defined nanostructures for the CMP systems, using an emulsion-free approach. The prepared CMP systems were extensively characterized for their structural, optical, and electronic properties. Minimal differences between CMP-NH_2 and CMP-Guanidine were targeted, besides the implementation of guanidyl-groups, to ensure the exclusive analysis of coordinative reactivity influences by the guanidyl-moiety. The defined binding affinities between guanidines and phosphonates, carboxylates, or dichromate ions were leveraged to enhance the external mass transfer of substrates towards the photocatalytic active surface when compared to a non-functionalized CMP system. This improvement in mass transfer led to an increase in conversion of up to 75%. Besides the acceleration of photocatalytic reaction rates due to the implementation of defined binding interactions, the utilization of guanidyl-functionalized CMP as organocatalyst was additionally investigated. Therefore, the organocatalytic influence of CMP-Guanidine on a nitro-phenol reduction to the corresponding amino-phenol was analyzed. It was found, that CMP-Guanidine exhibited unique properties, facilitating the reaction with up to 87% product yield under dark conditions, while CMP-NH_2 achieved only 5%. The presented study thus highlights the integration of innovative selectivity concepts into heterogeneous photocatalysts and offers fundamental insights into orthogonal catalyst designs and selectivity concepts. However, for the successful application of these orthogonal photocatalytic systems, further investigation of binding-interactions for reaction acceleration and facilitation is desired.

5.4 Experimental Details

The materials and methods detailed in the previous section 4.5, were employed similarly for the work presented in this Chapter 5, unless stated otherwise. The following characterization and analysis techniques were additionally utilized.

2. General Analytical Techniques

Solid-state ^{1}H MAS and ^{13}C CP-MAS NMR measurements were performed using a Bruker Avance III solid-state NMR spectrometer operating at 500 MHz ^{1}H Larmor frequency with 25 kHz MAS. Broadband 1H decoupling was used during the ^{13}C NMR measurements.

3. Photophysical Analytical Techniques

Absorption and emission spectroscopy was conducted on a Horiba Duetta Fluorescence and Absorbance spectrometer with xenon light source, using response time 0.04 s, 1 nm spectral bandwidth in 2 nm intervals and baseline correction. All measurements were conducted in 10x10 mm VWR ES-quartz cuvettes (dimensions: 12.5×12.5×45 mm) fitted with PTFE caps. Data analysis was done via EzSpec software and data plotting via Origin 2019b (V. 9.65).

The photoreduction of potassium dichromate was evaluated using a TECAN infinite M1000 microplate reader in the range from 300-700 nm in 2 nm intervals and a bandwidth

of 5 nm. All measurements were conducted in black, µclear 96-well plates with transparent bottom.

Cyclic voltammetry was conducted on an Autolab PGSTAT204 (Metrohm, Switzerland) potentiostat/galvanostat in a three-electrode-cell system under inert atmosphere. A glassy carbon electrode was used as the working electrode, a saturated calomel electrode as the reference electrode, and platinum wire as the counter electrode. For sample preparation, a thin film of the CMP was prepared on the working electrode. Therefore, 1 mg CMP, 2 mL of ethanol absolute and 5 µL of Nafion® perfluorinated resin solution (5 wt%) were added into a mortar. Using a pestle, a homogenous dispersion was formed. This dispersion was drop-casted on the polished working electrode and the solvent was left to evaporate at room temperature. This procedure was repeated, until the electrode surface was fully covered with the yellow film. As electrolyte, 0.1 M NBu_4PF_6 in acetonitrile was used and prior to measurement purged with argon for 15 min. The measurement was conducted using a scan rate of 100 mV s^{-1} within the range of -2.0 V to 2.0 V vs. SCE.

4. Macromolecular Analytical Techniques

Light scattering measurements were performed on an ALV spectrometer consisting of a goniometer and an ALV-5004 multiple-tau full-digital correlator (320 channels) which allows measurements over an angular range from 30° to 150°. A He-Ne laser (wavelength of 632.8 nm) is used as light source. For temperature controlled measurements the light scattering instrument is equipped with a thermostat from Julabo. Diluted dispersions were filtered through PTFE membrane filters with a pore size of 5 µm (LS Millipore). Measurements were performed at 22 °C at 9 ranging from 30° to 150°.

Brunauer-Emmett-Teller surface areas were measured with nitrogen sorption at 77 K using a Tristar II Plus (Micromeritics, U.S.) with samples degassed for 12 h at 120 °C under vacuum prior to analysis. Pore size distributions were estimated using the Non-Local Density Functional Theory (NLDFT) model for carbon slit pore geometry built in Tristar II Plus.

Scanning electron microscopy measurements were conducted using a GeminiSEM 560 (Zeiss, Germany). The sample was dispersed in acetonitrile and then drop-casted on a 10x10 mm silicon wafer. After solvent evaporation, a yellow film was observed. This film was analyzed with an extractor target voltage of 3.33 kV and an EHT of 0.287 kV. Image processing was performed via ImageJ 1.53e.

Qualitative particle size analysis was conducted using the obtained SEM images of identical resolution. A manual particle analysis of at least 100 particles was conducted via the built-in Multi-point Tool in ImageJ 1.54 to obtain the mean average diameter of the characterized nanoparticles.

Transmission electron microscopy measurements were conducted using a FEI Tecnai F20 (Thermo Fisher, U.S.), equipped with a 200 kV tungsten emitter, Fishione® high angle annular darkfield detector combined with an on axis Gatan® US1000 2k CCD camera. Data

acquisition was conducted using Gatan® Microscopy Suite (Version: 2.11.1404, DigitalMicrograph, Gatan®). Sample preparation was performed by drop-casting on carbonized gold grids (300 mesh, C-layer 10-20 nm) and solvent deduction with filter paper.

8. Synthetic Protocols

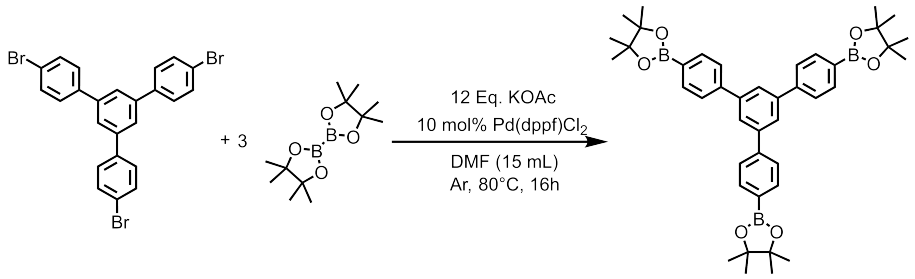

The compound was prepared according to the literature procedure.[254] Therefore, 1,3,5-tris(4-bromophenyl)benzene (1 eq., 680 mg, 1.25 mmol), Pd(dppf)Cl_2 (0.1 eq., 91.62 mg, 125 µmol), KOAc (12 eq., 1.47 g, 15.02 mmol) and bis(pinacolato)diboron (3.15 eq., 1g, 3.94 mmol) were added into an evacuated schlenk tube, equipped with a stir bar, under argon counter stream. Afterwards, to the reaction mixture anhydrous DMF (15 mL) was added. The heterogeneous mixture was vigorously stirred at 80 °C for 16 h. After reaction completion, the dark brown/black slurry was allowed to cool to room temperature. The solvent was removed under reduced pressure with a rotary evaporator. The residue was taken up into DCM (50 mL) and the organic phase washed with sat. $NH_4Cl_{(aq.)}$ and brine. Drying the reaction mixture over $MgSO_4$ and concentration of the mixture under reduced pressure, gave a dark black, oily residue. This was subjected to silica column chromatography (100% DCM) to give the product as white, fluffy solid (550 mg, 64% yield).

^{1}H NMR (400 MHz, DMSO-d_6, δ): 7.96 (s, 3 H, C-H Ar), 7.89 (d, 6 H, C-H Ar), 7.82 (d, 6 H, C-H Ar), 1.33 (s, 36 H, CH_3) ppm.

^{13}C NMR (101 MHz, DMSO-d_6, δ): 143 (4 C, C_q Ar), 141 (5 C, C_q Ar), 135 (6 C, C-H Ar), 127 (6 C, C-H Ar) 125 (3 C, C-H Ar), 84 (6 C, C_q), 25 (12 C, CH_3) ppm.

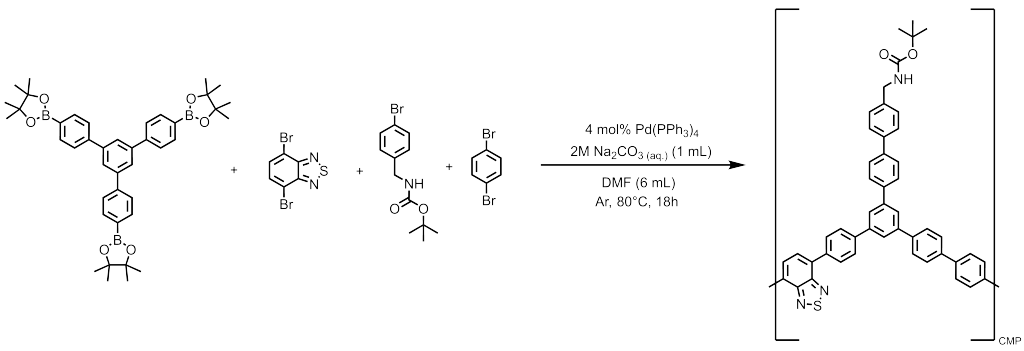

To synthesize Boc-protected CMP-NH_2, compound 1 (1 eq., 80 mg, 117 µmol), 4,7-dibromobenzo[1,2,5]thiadiazole (1 eq., 34.37 mg, 117 µmol), tert-butyl (4-bromobenzyl)carbamate (1 eq., 33.46 mg, 117 µmol) and 1,4-dibromobenzene (1 eq., 27.58 mg, 117 µmol) were added

into an evacuated schlenk tube, equipped with a stir bar. Afterwards, anhydrous DMF (6 mL) and 2 M Na_2CO_3(aq.) (1 mL) were added into the tube. The mixture was stirred under argon until all solids were dissolved. Under argon counterstream $Pd(PPh_3)_4$ (0.04 eq., 5.4 mg, 4.7 µmol) was added to the reaction mixture. The resulting heterogeneous mixture was heated to 80 °C and vigorously stirred for 18 h. A bright yellow precipitate was observed. After the mixture cooled down to room temperature, 40 mL methanol were added and the mixture was transferred to centrifugation tubes. The resulting CMP was purified via precipitation and centrifugation (3x 40 mL methanol, 2x 40 mL toluene, 1x 40 mL methanol; 4400 rpm, 15 min) until the supernatant was colorless. The obtained CMP was dried under vacuum at 40 °C (51 mg, 58% yield).

^{1}H NMR (500 MHz, solid state, δ): 6.96 (br, C-H Ar), 3.70 (br, CH_2), 1.34 (br, CH_3) ppm.

^{13}C NMR (125 MHz, solid state, δ): 154 (br, C=X), 142 (br, C-H Ar), 136 (br, C-H Ar), 128 (br, C-H Ar), 83 (br, C_q Boc), 25 (br, CH_3), 21(br, CH_2) ppm.

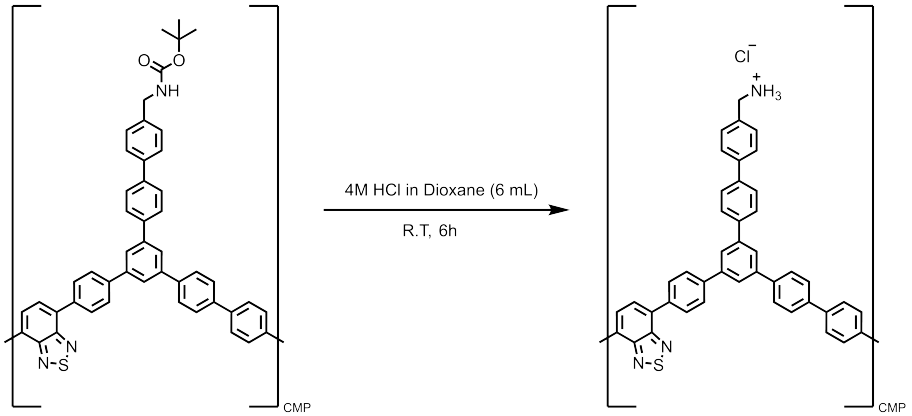

For the deprotection of the synthesized Boc-protected CMP-NH_2, the corresponding CMP (25 mg) was added into a 25 mL round-bottom flask equipped with a stir bar. Afterwards, 4 M HCl in Dioxane (6 mL) was added to the CMP. The mixture was stirred for 6 h at room temperature. A slight browning of the solution was observed. 30 mL methanol were added and the mixture was transferred into centrifugation tubes. The resulting CMP was purified via precipitation and centrifugation (3x 40 mL methanol; 4400 rpm, 15 min) until the supernatant was colorless. The obtained CMP was dried under vacuum at 40 °C (18 mg, 79% yield).

^{1}H NMR (500 MHz, solid state, δ): 6.96 (br, C-H Ar), 1.26 (br, CH_3) ppm.

^{13}C NMR (125 MHz, solid state, δ): 154 (br, C=X), 142 (br, C-H Ar), 136 (br, C-H Ar), 128 (br, C-H Ar), 83 (br, C_q Boc), 25 (br, CH_3), 21(br, CH_2) ppm.

^{1}H peaks at 1.26 ppm and ^{13}C peaks at 83, 25 and 21 ppm were associated to residual Boc-protection groups.

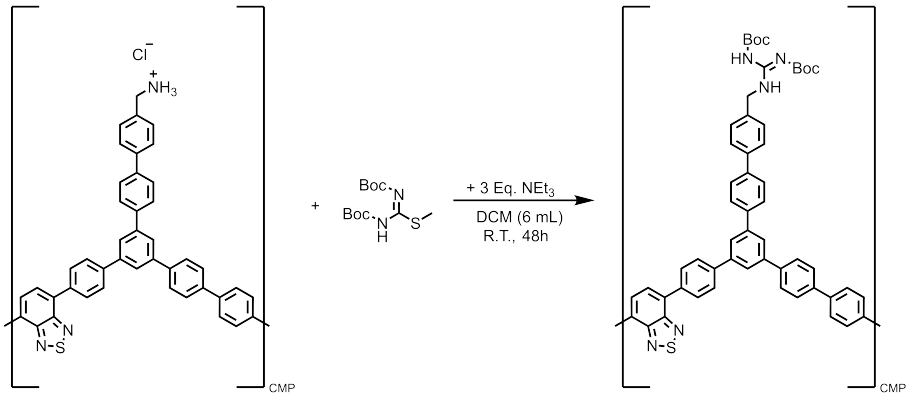

For the post-guanidylation of CMP-NH_2, CMP-NH_2 (1 eq., 18 mg) was dispersed in dichloromethane (6 mL) in a 25 mL round bottom flask, equipped with a stir bar. NEt_3 (3 eq., 11.9 µL) was added and the heterogeneous mixture was stirred for 15 min. Afterwards, 1,3-bis(tert-butoxycarbonyl)-2-methyl-2-thiopseudourea (1.7 eq., 13.5 mg, 47 µmol) was added to the reaction mixture. The reaction mixture was stirred vigorously for 48 h at room temperature. A color change from orange to yellow was observed. 30 mL methanol were added and the mixture was transferred into centrifugation tubes. The resulting CMP was purified via precipitation and centrifugation (3x 40 mL methanol; 4400 rpm, 15 min). The obtained CMP was dried under vacuum at 40 °C (14 mg, 59% yield).

^{1}H NMR (500 MHz, solid state, δ): 17.57 (br d, N-H), 14.3 (br d, N-H), 6.89 (br, C-H Ar), 1.26 (br, CH_3) ppm.

^{13}C NMR (125 MHz, solid state, δ): 167 (s, C_q-Guanidine), 162 (s, C_q-Guanidine), 154 (br, C=X), 142 (br, C-H Ar), 136 (br, C-H Ar), 128 (br, C-H Ar), 83 (br, C_q Boc), 25 (br, CH_3), 21(br, CH_2) ppm.

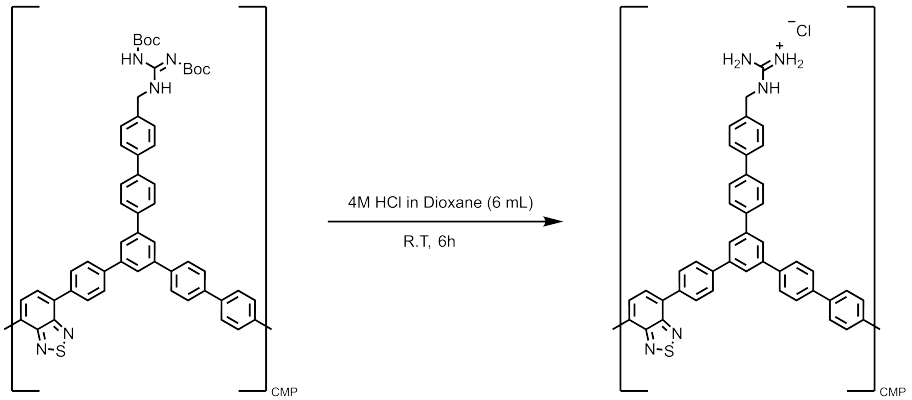

For the deprotection of the synthesized Boc-protected CMP-Guanidine, the corresponding CMP (18 mg) was added into a 25 mL round-bottom flask equipped with a stir bar. Afterwards, 4 M HCl in Dioxane (6 mL) was added to the CMP. The mixture was stirred for 6 h at room temperature. 30 mL methanol were added and the mixture was transferred into centrifugation tubes. The resulting CMP was purified via precipitation and centrifugation (2x 40 mL methanol; 4400 rpm, 15 min) until the supernatant was colorless. The obtained CMP was dried under vacuum at 40 °C (11 mg, 79% yield).

^{1}H NMR (500 MHz, solid state, δ): 6.96 (br, C-H Ar), 1.26 (br, CH_3) ppm.

^{13}C NMR (125 MHz, solid state, δ): 154 (br, C=X), 142 (br, C-H Ar), 136 (br, C-H Ar), 128 (br, C-H Ar), 83 (br, C_q Boc), 25 (br, CH_3), 21(br, CH_2) ppm.

^{1}H peaks at 1.26 ppm and ^{13}C peaks at 83, 25 and 21 ppm were associated to residual Boc-protection groups. Guanidyl peaks disappeared, due to strong rotation of the guanidyl group.

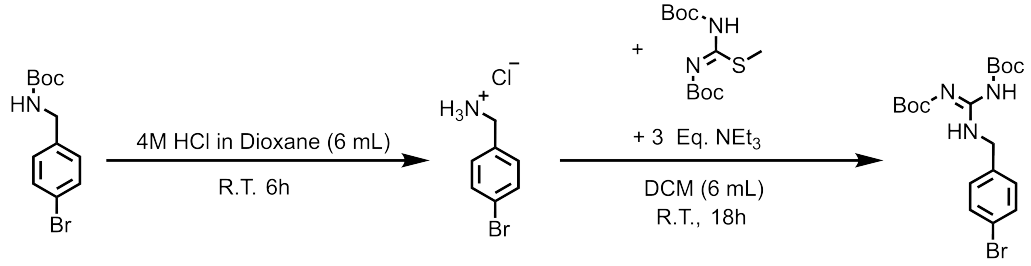

To validate the synthetic route, Boc-protected 4-bromobenzylamine (250 mg, 874 µmol) were added into a 25 mL round bottom flask, equipped with a stir bar. 4 M HCl in dioxane (6 mL) was added and the mixture was vigorously stirred for 6 h at room temperature. The formation of white precipitate was observed. The precipitate was filtered off, washed with dioxane (2x 15 mL) and dried under vacuum for 24 h. The obtained precipitate (150 mg) was transferred into a 25 mL round bottom flask, equipped with a stir bar. Dichloromethane (6 mL) was added into the flask and a dispersion was obtained. To this dispersion, NEt_3 (3 eq., 312 µL, 2.41 mmol) was added and the mixture was stirred for 15 min. Afterwards, 1,3-bis(tert-butoxycarbonyl)-2-methyl-2-thiopseudourea (1.7 eq., 233 mg, 802 µmol) was added to the reaction mixture. The reaction mixture was stirred vigorously for 18 h at room temperature. After reaction completion (monitored via TLC), the reaction mixture was washed with water (2x 20 mL) and brine. The obtained solution was dried over $MgSO_4$ and concentrated in vacuo. The obtained residue was subjected to silica column chromatography (EtOAc : petrolether; 6:4) to give the compound as white/greenish powder (158 mg, 78%).

^{1}H NMR (400 MHz, DCM-d_2, δ): 11.53 (s, 1 H, N-H), 8.58 (br, 1 H, N-H), 7.47 (d, 2 H, C-H Ar), 7.2 (d, 2 H, C-H Ar), 4.52 (d, 2H, CH_2), 1.45 (s, 18 H, CH_3) ppm.

^{13}C NMR (101 MHz, DCM-d_2, δ): 163 (1 C, C_q-Boc), 156 (1 C, C_q-Boc), 152 (1 C, C_q-Guanidine), 137 (1 C, C_q Ar), 132 (2 C, C-H Ar), 129 (2 C, C-H Ar), 120 (1 C, C-Br), 83 (1 C, C_q-Boc), 79 (1 C, C_q-Boc), 43 (1 C, CH_2), 28 (6 C, CH_3) ppm.

9. Photocatalytic Reaction Procedures

Photodegradation of N-(Phosphonomethyl)glycine

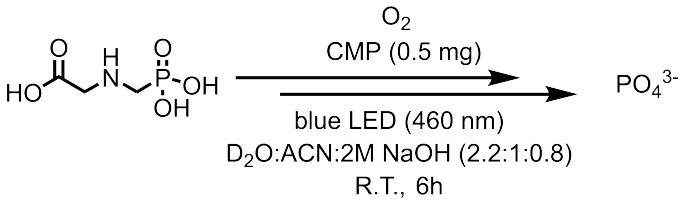

A 4 mL screw cap vial with septum was charged with 0.5 mg of the corresponding CMP (CMP-NH_2, CMP-Guanidine). The CMP was dispersed in acetonitrile (0.5 mL) by sonication in a bath sonicator for 15 min. To this dispersion a solution of N-(phosphonomethyl)-glycine (12 mg, 71 µmol) in D_2O: 2 M $NaOH_{(aq.)}$ (1100 µL:400 µL; 1:0.4) was added. After addition of a stir bar to the reaction mixture, the dispersion was gassed with oxygen for 15 min under stirring. The reaction mixture was then placed into the photoreactor and irradiated with blue light (11.9 mW cm^{-2}, 460 nm) under stirring while water-cooled to 18 °C. The reaction was conducted in triplicates for each CMP systems. Samples were taken every hour in a range from 0-6 h. Therefore, 250 µL of the crude reaction mixture were taken, added into an NMR tube, diluted with 250 µL D_2O and mixed with 50 µL of internal standard (triphenylphosphate in DMSO-d_6). After homogenization of the sample, the NMR tube was submitted to ^{31}P-NMR spectroscopy and the conversion was obtained by referencing to the internal standard.

^{31}P-NMR (160 MHz, D_2O, δ): 18.3 (glyphosate), 2 (phosphate), -8.7 (triphenylphosphate) ppm.

Several unidentified intermediates were observed during the reaction. With increasing acidification of the reaction due to phosphate ion generation, peak shifts for all monitored peaks were observed.

Photooxidation of L-Tryptophane

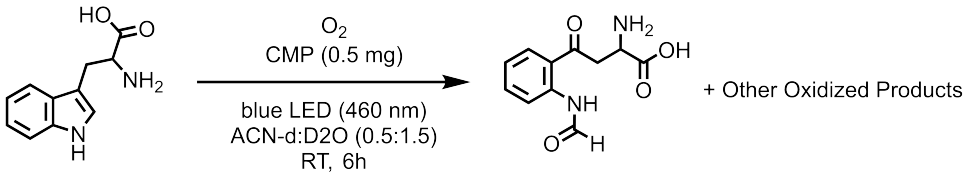

A 4 mL screw cap vial with septum was charged with 0.5 mg of the corresponding CMP (CMP-NH_2, CMP-Guanidine). The CMP was dispersed in deuterated acetonitrile (0.5 mL) by sonication in a bath sonicator for 15 min. To this dispersion a solution of L-tryptophane (20 mg, 98 µmol) in D_2O (1500 µL) was added. After addition of a stir bar to the reaction mixture, the reaction mixture was placed into the photoreactor and irradiated with blue light (11.9 mW cm^{-2}, 460 nm) under stirring while water-cooled to 18 °C. The reaction was conducted in triplicates for each CMP systems. Samples were taken every hour in a range from 0-6 h. Therefore, 250 µL of the crude reaction mixture were taken, added into an NMR tube, diluted with 250 µL D_2O and mixed with 50 µL of internal standard (dimethylsulfone). After homogenization of the sample, the NMR tube was submitted to

^{1}H NMR spectroscopy and the conversion was obtained by referencing to the internal standard.

For investigation of the kinetic profile, the internal standard dimethylsulfone was referenced against the observed formation of the aldehyde peak of N-formylkinurenine and the depletion of the C2 hydrogen of L-tryptophane.

Photoreduction of Potassium Dichromate

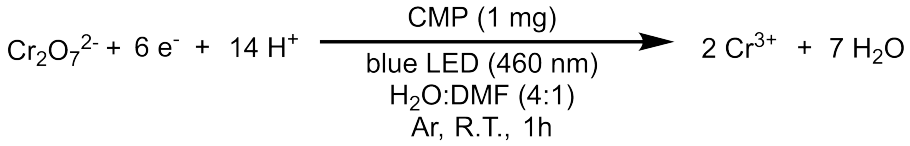

A 4 mL screw cap vial with septum was charged with 1 mg of the corresponding CMP (CMP-NH_2, CMP-Guanidine). The CMP was dispersed in dimethylformamide (0.5 mL) by sonication in a bath sonicator for 15 min. To this dispersion an aqueous solution of potassium dichromate (0.2 mL, 2.5 mg mL^{-1}) was added. After addition of a stir bar to the reaction mixture, the mixture was degassed with argon for 15 min. Afterwards the reaction vessels were placed into the photoreactor and irradiated with blue light (11.9 mW cm^{-2}, 460 nm) under stirring while water-cooled to 18 °C.The reaction was conducted in triplicates for each CMP systems. Samples were taken every 10 min in a range from 0-60 min. The Cr^{III} concentration was determined via UV/Vis absorption spectroscopy. Therefore, 20 µL of the crude reaction mixture was added into 0.96 mL of 0.2 M H_2SO_4, followed by the addition of 20 µL of diphenylcarbazide solution (0.25 wt% in acetone). Each sample was given exactly 15 min after addition for equilibration. The obtained purple solution was characterized by the UV/Vis absorbance at 542 nm (characteristic for Cr^{VI}).

10. Organocatalytic Reaction Procedures

Bromolactonization of 5-Hexenoic Acid

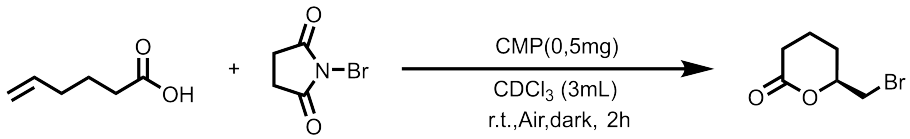

The CMP (0.5 mg) was dispersed in $CHCl_3$ (1 mL) using a bath sonicator for 10 min. Afterwards, a solution of 5-hexenoic acid (1 eq., 11.41 mg, 100 µmol) and NBS (2 eq., 35.6 mg, 200 µmol) in $CHCl_3$ (2 mL) was added to the CMP dispersion. The solution was vortexed for 2 min. The reaction was subsequently conducted at room temperature for 2 h. The crude mixture was submitted to ^{1}H-NMR spectroscopy, enabling the characterization of formed product. The peak change from 5-3.5 ppm was monitored.

Nitro-Reduction of p-Nitrophenol

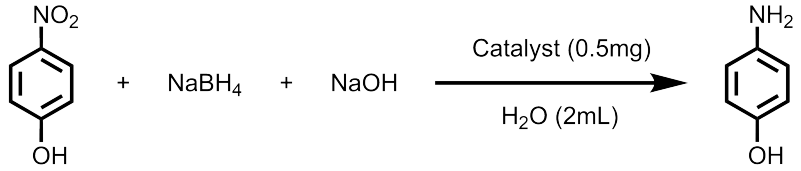

A dispersion of CMP (0.5 mg) in a water:acetonitrile:1M $NaOH_{(aq.)}$ mixture (2.6:1:1.4) was prepared. The mixture was sonicated in a bath sonicator for 10 min. Afterwards, p-nitrophenol (1 eq., 36.77 mg, 264.33 µmol) and sodium borohydride (2 eq., 19.58 mg, 517.58 µmol) were added into the reaction mixture. The reaction was conducted at room temperature under dark conditons for 3 days. The reaction rate was monitored by submission of the crude mixture to ^{1}H-NMR spectroscopy and monitoring of the peak formation at 6.35 and 6.25 ppm.

12. Appendix

For all compound NMR spectra, the reader is referred to the supporting information in section 8.1.2.

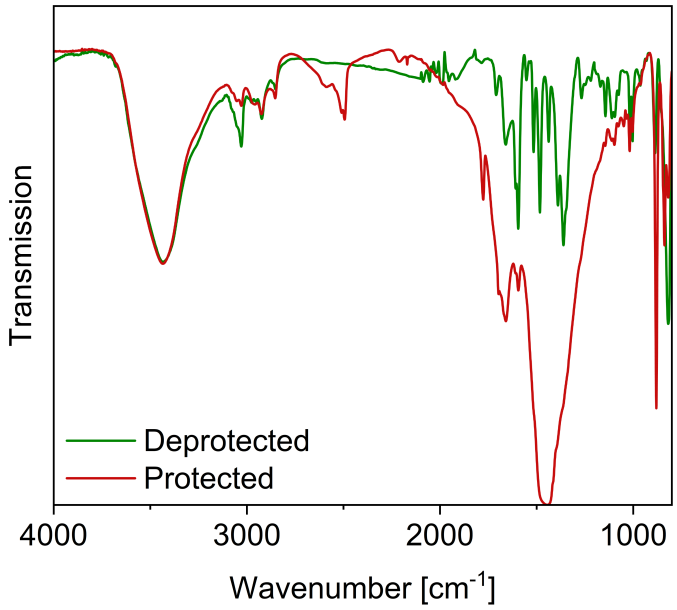

Figure 5.17: Comparison of FT-IR spectra for CMP-Guanidine before and after deprotection.

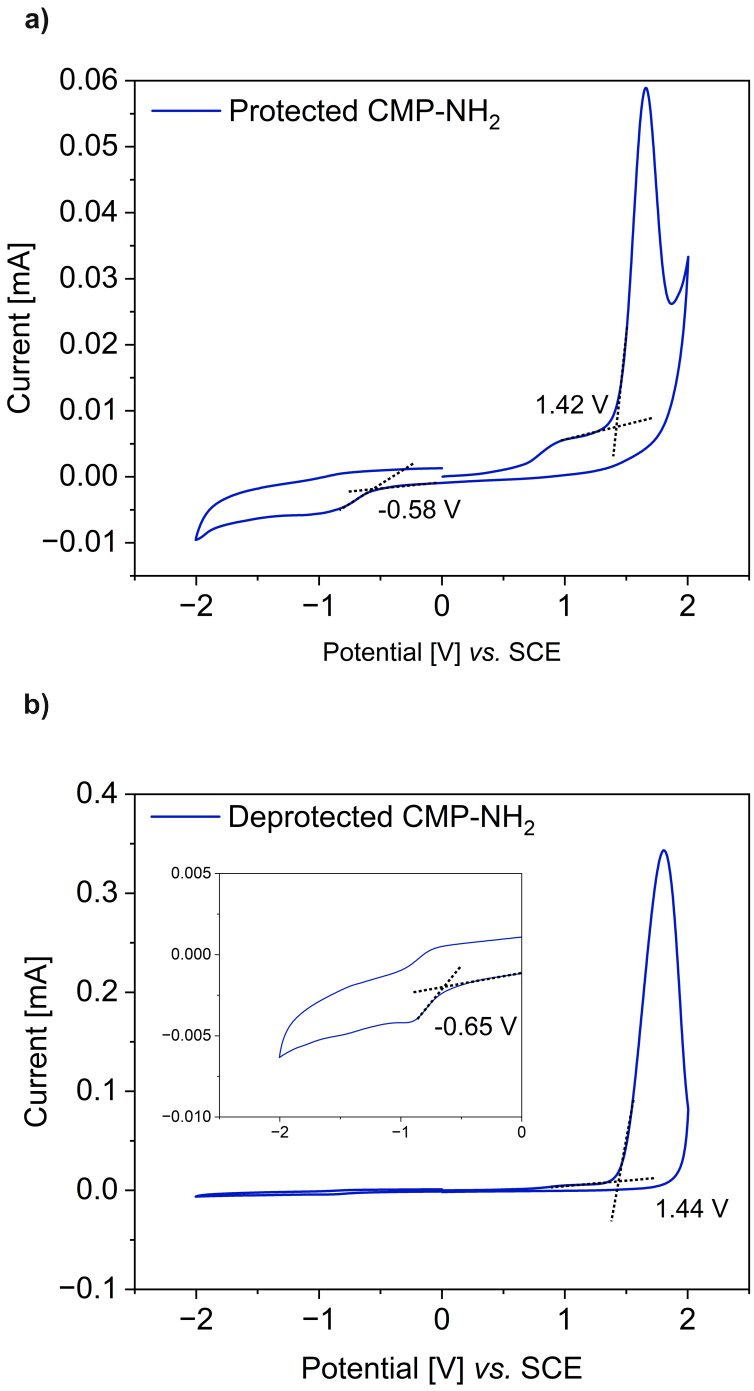

Figure 5.18: Cyclic voltammogram of CMP-NH_2 before (a) and after (b) deprotection.

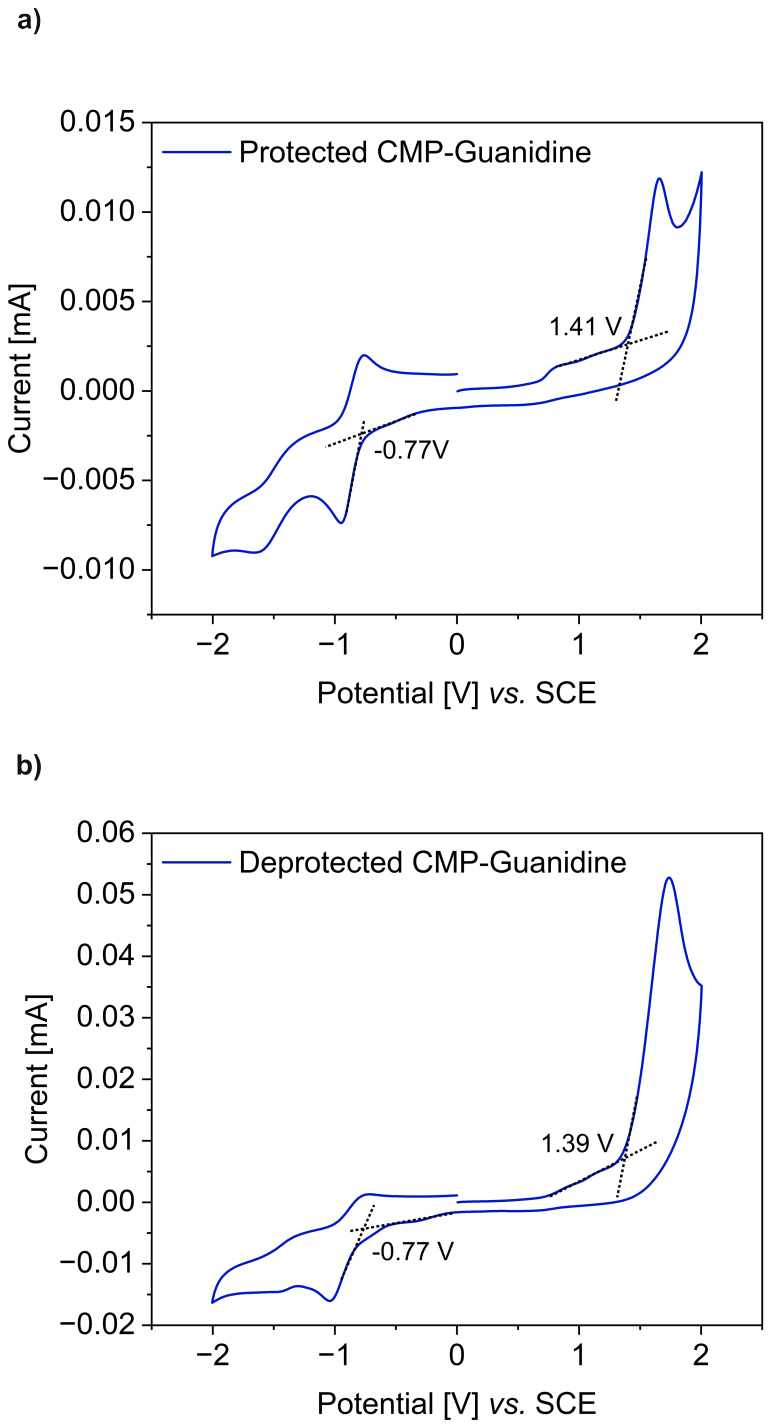

Figure 5.19: Cyclic voltammogram of CMP-Guanidine before (a) and after (b) deprotection.

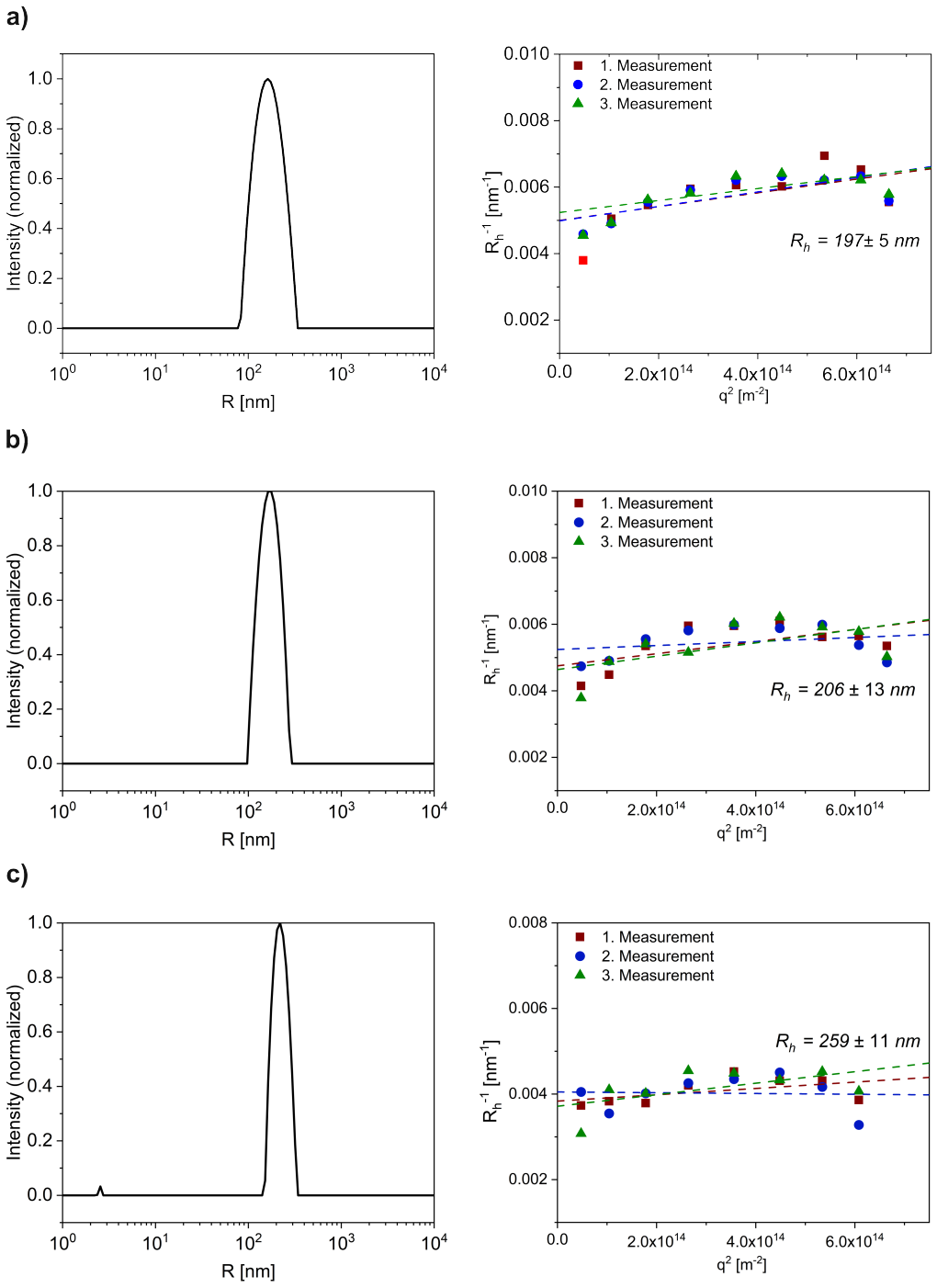

Figure 5.20: Multi-angle dynamic light scattering analysis for (a) CMP-NH_2, (b) CMP-Guanidine and (c) CMP-Guanidine with additional PEG-Phosphate.

Chapter 6

Photocatalysis in Artificial Cell-like Systems

The following Chapter 6 is based on two articles and discusses the potential application of heterogeneous photocatalysts in artificial cell-like systems. Two different approaches will be evaluated. In the first article, presented in section 6.2, the hydrophobicity-driven accumulation of an organic photocatalyst in a dipeptide coacervate and its use as an artificial cell-like organelle will be discussed. The second article, presented in section 6.3, will elaborate on the application of single amino acid coacervates with intrinsic photocatalytic functionality.

The first article, presented in section 6.2, is based on the manuscript "Dipeptide coacervates as artificial membraneless organelles for bioorthogonal catalysis", published in *Nature Communications*, 15, 39 (2024) and is authored by Shoupeng Cao, Tsvetomir Ivanov, Julian Heuer, Calum Ferguson, Lucas Caire da Silva and Katharina Landfester.[255] Shoupeng Cao was responsible for the design, synthesis, and characterization of the presented system. My contribution was the synthesis of the photocatalyst and the design of the photocatalytic model reaction. Paragraphs, sections and sentences that have been adopted from this article are indicated by quotation marks ("").

In this work, the use of dipeptide coacervates as an artificial analogue of cellular compartments is outlined. By exploiting a liquid-liquid phase separation mechanism, dipeptide coacervates form a defined microenvironment in a physiological aqueous medium. Within these colloidally stable droplets, the defined hydrophobic microenvironment is exploited to facilitate bioorthogonal and biomimetic reactions by encapsulating a hydrophobic catalyst system. These artificial, membraneless organelles are then incorporated into biological cells, triggering reactions that are not naturally available, highlighting the great potential of coacervates great within synthetic biology.

The second article, presented in section 6.3, is based on the manuscript "Bio-mimetic minimal peptide coacervates with intrinsic photocatalytic function for biophotocatalysis (TBD)", which is currently under preparation. The manuscript is authored by Tsvetomir Ivanov, Julian Heuer, Huan Dang, Seunghyeon Kim, Lucas Caire da Silva and Katharina

Landfester. In this work, Tsvetomir Ivanov was responsible for the synthesis and characterization of the coacervate droplets. My contribution was the design, synthesis and characterization of the photocatalytic monomer, the conduction of the photocatalytic dye degradation and the conduction of the photocatalytic sulfide oxidation. In section 6.3 exclusively my contributions are presented.

In this project, the use of single amino acid coacervates with in-built photocatalytic functionality for application in phase-separated photocatalysis was evaluated. To maintain similar structural and functional properties of the material, a new synthetic protocol was developed for single amino acid-based coacervates. A functionalizable, hydrophobic photocatalyst was covalently bound to an amino acid, resulting in the reliable formation of phase-separated and colloidally stable coacervates. The incorporation of photocatalytic activity was then investigated for a range of ROS-based photocatalytic reactions. Furthermore, the established hydrophobicity gradient of the phase-separated coacervates in the aqueous medium was found to drive a strong accumulation of hydrophobic substrates, thus facilitating their use as hydrophobic substrate carriers.

6.1 Motivation

The biological cell is the smallest structural and functional unit of life, and it is regarded as the origin of life.[256] Biological cells exhibit a variety of functional modules (organelles), that control and perform processes vital to life. Each of these compartmentalized organelles is defined by a particular structure: either membranized or membraneless with specific internal microenvironment. The microenvironments differ in terms of pH, redox state, concentration of substrates, or ionic composition. It is of great significance that the compartmentalization within cells is highly precise, allowing for the regulation of biological processes through compartment-adjusted enzymes, which are constrained to their specific microenvironment.[257] This enables natural cells to drive highly selective reactions within the complex cellular matrix. Additionally, living cells show various properties, exhibiting self-functioning, self-repairing, self-propagating and also self-optimizing mechanisms.[258] The outstanding performance and significance for life of natural cells, has led to enormous scientific efforts to understand their underlying mechanisms. These marked the rise of cell engineering and biotechnology.[259]

However, due to the inherent complexity of natural cells and their fragility, there is an easy loss of activity and death *in vitro*. Consequently, simplified approaches are desired to simulate, imitate, or investigate isolated characteristics and processes of natural cells.[259] A recently emerging strategy for these purposes is presented by the development of artificial cell systems. A range of strategies for the construction of artificial cell-like systems has been developed. Two distinct approaches were developed: top-down and bottom-up.[256] These utilized biological cell-derived molecules and/or synthetic molecules.[260] Additionally, varying complexities were implemented into these artificial cell systems, ranging from macro compartmentalization (exhibiting just a stable, semi-permeable membrane) to fully organic cells with artificial organelles.[259]

A major challenge in modern artificial cell-like systems is the establishment of multi-compartmentalized microreactors for orthogonal reactions and inter-organelle communication.[261] The controlled localization of molecules or substrates by compartments is thereby of critical importance. This localization can be driven by substrate-tailored microenvironments, facilitating the controlled accumulation of the targeted substrate.[262] By implementation of a catalytic reactivity into these tailored-microenvironments of artificial organelles, biomimetic cellular functions can be established, investigated or manipulated.[263] The regulation of complex chains of chemical reactions would mark an important milestone in the field of synthetic biology.[260]

Recently, the utilization of phase-separated coacervates as artificial organelles with highly customizable microenvironments has shown promising results.[264, 265] Coacervates form spontaneously by liquid-liquid phase separation, resulting in molecularly crowded droplets with tailored microenvironments.[266] These droplets exhibit similar biophysical and functional properties as their cellular analogs.[264, 265] The phase separation-enhanced concentration of substrate builds a powerful foundation for the design of catalytic microreactors. Therefore, several coacervate systems have been developed for the formation of artificial organelles. Among these, peptide-based coacervates represent a popular counterpart to traditional charge-driven coacervation of polyelectrolytes.[267, 268] Peptide-based coacervates undergo self-association through multivalent weak interactions, a process analogous to the formation of biological condensates driven by liquid-liquid phase separation, observed in living cells.[269,–271] This allows for precise adjustment of the supramolecular structure and material properties by exclusively solely natural amino acids, ensuring high biocompatibility.[268] Defined changes in structural composition enable a direct opportunity to introduce structure-function/sequence-function relationships, thereby increasing the tunability of the artificial organelle system.[272] The underlying design principles demonstrate the potential of coacervates as membraneless artificial organelles, particularly as bioorthogonal microreactors with differing microenvironments, facilitating the utilization of solubility-limited or low partition coefficient substrates.[255]

This work presents two distinct methodologies for the incorporation of small molecular photocatalysts within coacervate droplets. The potential of these photocatalytic microreactors as artificial organelles for biophotocatalysis is then outlined. In section 6.2, the phase-seperation of molecular dipeptides into stable coacervates is investigated. By exploiting hydrophobic interactions, a controlled partitioning of molecular photocatalysts into the coacervate droplets is presented, demonstrating high photocatalytic activity as microreactors. Section 6.3 discusses the application of coacervate droplets with in-built photocatalytic activity by covalent incorporation of the photocatalytic moiety. The photocatalytic activity of these microreactors will be evaluated by assessing their performance in organic photocatalytic transformations.

6.2 Dipeptide Coacervates as Artificial Membraneless Organelles for Bioorthogonal Catalysis

In this work, we targeted the utilization of dipeptide coacervates as artificial membraneless organelles and microreactors. Especially the employment of these microreactors for biomimetic and bioorthogonal processes was thereby investigated. Therefore, a library of diphenylalanin-based coacervates was synthesized and designed to exhibit a hydrophobic microenvironment. Previous studies demonstrated a thermodynamically stable nanostructure and nanofibre formation for amphiphilic diphenylalanine-based motifs. The intermolecular aggregation of the diphenylalanin compounds was thereby driven by hydrophobic interactions and subsequent dehydration of the phase-separated aggregates. The interactions mainly involved were found to be aromatic-aromatic interactions (hydrophobic), as well as defined inter- and intramolecular hydrogen-bonding interactions. In contrast to conventional literature studies, we found that diphenylalanin compounds methoxylated-capped at the carboxylate site exhibit a strong aggregation and liquid-liquid phase separation behavior. The less hydrophilic head group (NH_2 instead of COOH) and a less hydrophobic tail group (compared against the carboxybenzyl-derivative) are expected to yield strong phase separation behavior.

The prepared diphenylalanine (FF-OMe) derivative was dissolved completely into aqueous HEPES buffer at a pH of around 6 (Figure 6.1b). After a slight increase of the pH to 7 or higher, the deprotonation of the amino-functionality resulted in the formation of a turbid solution. Analysis via light and confocal microscopy showed the existence of phase separated 1-10 µm droplets with liquid-like properties, like droplet coalescence, fusion and deformation (Figure 6.1c). At low pH (pH 6 or less), no stable droplet formation was observed, possibly reasoned by electrostatic repulsion of the protonated amino functionalities. The observed process of coacervation was reversible. Additionally, a strong concentration dependency of the coacervation of FF-OMe was found. Increasing the concentration from 3 mg mL^{-1} to 20 mg mL^{-1} allowed a coacervaertion at a pH of 6.5. Furthermore, the colloidal stability of the coacervates was evaluated. While conventional complex coacervates show limited stability towards high electrolyte concentrations, our coacervates droplets showed a resistant and stable character in up to 1 M NaCl solutions.

After the colloidal stability and formation of coacervate droplets was thoroughly investigated, the colocalization of guest molecules into the droplets was analyzed. The colocalization of two different enzymes, namely glucose oxidase and horse radish peroxidase and the subsequent demonstration as enzymatic microreactors, showing accelerated activities compared to coacervate-free conditions. To gain a deeper understanding on the colocalization and partitioning of guest molecules, further experiments were conducted, examining the sequestration of hydrophobic and hydrophilic small molecules within the droplets. Therefore, a range of dye molecules like methylene blue, rhodamine or calcein, but also different catalyst systems like Zn-Protoporphyrin or dithiophenebenzothiadiazole (DTB) were successfully accumulated within the coacervate droplets. These results underline the promising application possibilities as microreactors or artificial organelles,

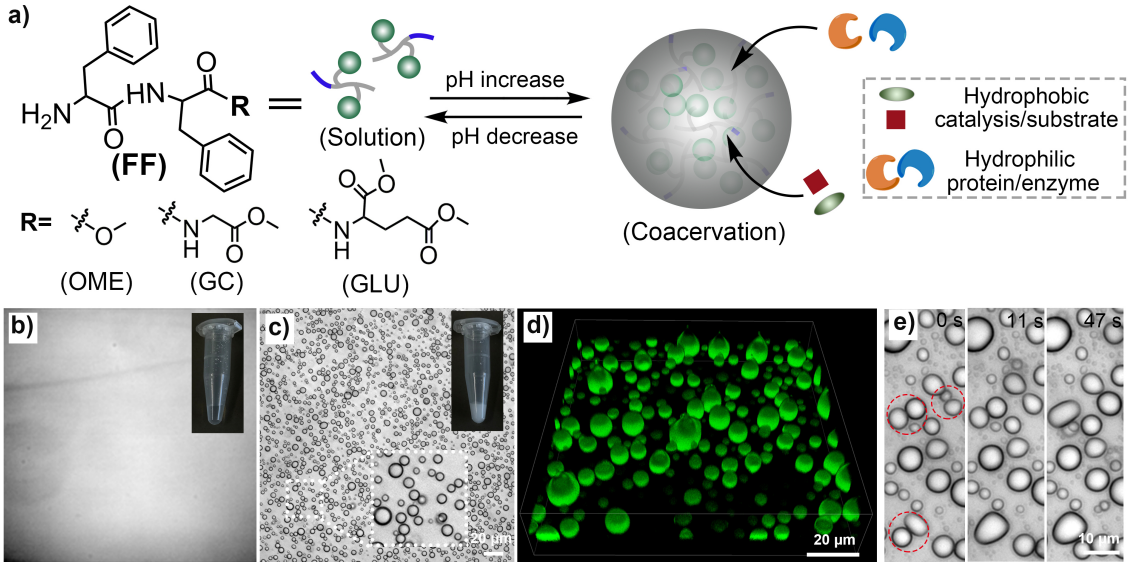

Figure 6.1: Components, formation and properties of dipeptide coacervates (DCs). a) Schematic of pH-triggered self-coacervation with dipeptide components. b) Micrograph of an FF-OMe solution (10 mg mL^{-1}) at pH 6 (5 experiments were repeated independently with similar results). c) Micrograph of an FF-OMe coacervate dispersion (10 mg mL^{-1}) at pH 9, scale bar = 20 µm (5 experiments were repeated independently with similar results). d) 3D confocal image of the dipeptide coacervates (10 mg mL^{-1}) encapsulating hydrophobic photocatalyst (green colored, 4,7-di(2-thienyl)-2,1,3-benzothiadiazole, abbreviated as DTB, 50 µg mL^{-1}), scale bar = 20 µm. e) Time-lapse microscopy of an FF-OMe coacervate dispersion (10 mg mL^{-1}) at pH 9. Dotted circles indicate droplet coalescence events, scale bar = 10 µm. Reproduced with permission from ref[255].

empowered by the sequestration of hydrophilic and hydrophobic compounds with precisely adjustable microenvironments. Special emphasis lies thereby in the stabilization and accumulation of strongly hydrophobic compounds within an aqueous environment.

The utilization of coacervate droplets as microreactors was then investigated. For this, a hydrophobic catalyst was colocalized with the corresponding substrate within the coacervate droplet. The immobilization of a catalyst into the solid phase is an effective way to increase the catalytic activity and enhance the catalyst's application range. As a preliminary illustrative example, the encapsulation of a strongly hydrophobic photocatalyst (DTB) into the phase-separated coacervate droplets was investigated. This was followed by the photocatalytic degradation of a model dye methylene blue (Figure 6.2a). The immobilization of DTB into the coacervate droplets was monitored by UV/Vis spectroscopy (Figure 6.2b). A 5 mg mL^{-1} solution of FF-OMe in HEPES/PBS buffer (1:1 volume ratio, pH 8) was prepared, to which a DTB stock solution (0.05 mg mL^{-1} in DMSO) was added. The UV/Vis spectra of free DTB (in ACN), DTB in PBS, and loaded coacervates were then compared, and significant differences were observed. The strong scattering behavior of the blank coacervates resulted in the absence of a distinct peak. The pure photocatalyst DTB in ACN displayed the characteristic absorption peaks for the DTB compound at 440 nm. In contrast, the highly hydrophobic DTB photocatalyst showed no distinct peak in PBS due to the compound's insolubility in the solvent. Comparative analysis of the results obtained

for the DTB-loaded coacervates revealed successful stabilization and immobilization of the hydrophobic DTB within an aqueous solution, due to accumulation within the coacervate droplets. Similar results were obtained for the emission spectrum, which showed the characteristic DTB emission peaks only for DTB in ACN and the coacervate-stabilized DTB. Following the successful encapsulation, the photocatalytic performance of the DTB-loaded coacervates was evaluated. Methylene blue (0.05 mg mL^{-1}) was incorporated into the DTB-coacervates. The reaction was initiated by irradiating the turbid mixture with blue light (460 nm) at room temperature. At the designated time points, samples were collected and the conversion of the methylene blue dye degradation was evaluated by the decrease in absorption at the characteristic methylene blue peak at 670 nm (Figure 6.2d). The DTB-loaded coacervates exhibited a rapid degradation of the substrate, with 95% degradation already observed after 5 minutes. A comparison of these results to a coacervate-free solution of DTB in HEPES/PBS revealed a conversion of only 20% (Figure 6.2e). Furthermore, lowering the pH to fully dissolve the coacervates resulted in a much lower degradation yield, below 20%. The analysis of the rate constants for the different conditions yielded the following values: 0.004 ± 0.001 min^{-1} (pH 6, free FF-OMe), 0.012 ± 0.001 min^{-1} (no FF-OMe) and 0.458 ± 0.001 min^{-1} (DTB-loaded coacervates). The high reactivity of the DTB-microreactors demonstrated a 38-fold increase in reaction rate compared to coacervate-free conditions. These results therefore demonstrate the potential of coacervates as biocompatible microreactors, which possess a hydrophobic microenvironment. This enables the utilization of hydrophobic catalysts and photocatalysts in aqueous media, the accumulation of hydrophobic substrates, and the acceleration of monitored reaction rates compared to coacervate-free conditions.

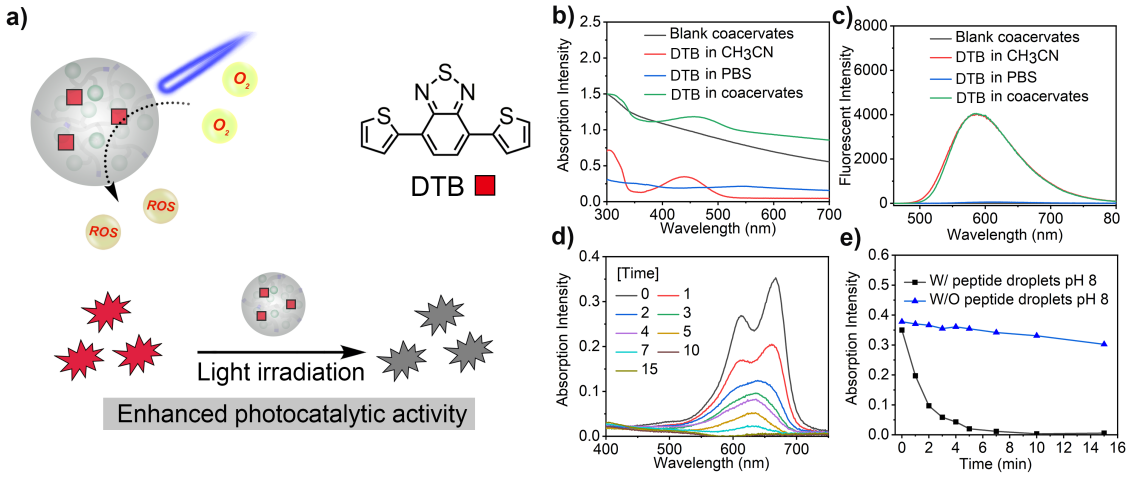

Figure 6.2: Photocatalysis in dipeptide coacervates. a) Schematic diagram of dipeptide-based photocatalytic microreactor for dye degradation. b) UV-Vis absorption curve of pure FF-OMe coacervates, DTB in acetonitrile, DTB in PBS and DTB in coacervates (FF-OMe coacervates: 5 mg mL^{-1}; DTB: 50 µg mL^{-1}). c) Fluorescence emission curves of empty coacervates, DTB in acetonitrile, DTB in PBS and DTB in coacervates. d) Absorption curves of methylene blue during photocatalytic degradation by DTB-microreactor at pH 8. e) Absorption intensity of methylene blue during photocatalytic degradation under different conditions, W/ indicates with and W/O means without. Reproduced with permission from ref[255]

6.3 Bio-Mimetic Minimal Peptide Coacervates with Intrinsic Photocatalytic Function for Biophotocatalysis

To further optimize the concept of peptide coacervates as artificial photocatalytic organelles, a simplification of the previous system was developed. A covalent attachment of the photocatalytic moiety to the peptide structure was targeted, to reduce the synthetic complexity and the number of steps required. Streamlining the synthetic procedure not only increases step economy but also improves coacervate droplet formation. Since the photocatalytic species used is a diphenylbenzothiadiazole derivative, a highly hydrophobic moiety was introduced into the peptide coacervate, facilitating a single amino acid coacervation process. To the best of our knowledge, there are no literature reports of reliable peptide-based coacervate formations using a single amino acid. Single amino acid coacervation is explained by the accelerated aggregation of hydrophobic species and complementary hydrophobic intermolecular interactions between DPBT and phenylalanine. The introduction of a bifunctionality into the molecular structure, namely structural (amino acid) and functional (photocatalyst), is expected to maintain the biocompatibility of the coacervate while exhibiting an intrinsic catalytic functionality. Therefore, the covalent linkage of the photocatalyst to the peptide coacervates proved to be advantageous for the applicability of the coacervates. Due to the covalent attachment of the photocatalytic species, no secondary loading of the coacervate is required as compared to the previously discussed dipeptide coacervates. This not only simplifies the applicability of the coacervate system, but also eliminates the issue of catalyst leakage into other compartments or external media. This allows for highly controlled localization of the catalytic moiety and enhances the possibility of orthogonal microreactors through localization-enhanced multicompartmentalization. In addition, the photocatalytic reactivity of the photocatalyst is expected to increase, as the aggregation (and possible precipitation) of the DPBT species is reduced compared to the dipeptide coacervate, thereby inhibiting aggregation-induced quenching mechanisms.

To realize the outlined concept, a functionalizable diphenylbenzothiadiazole (DPBT) moiety was synthesized. Functionalization targeted a para-substitution at the terminal phenyl-group with a methyleneamine group. The methylene spacer was incorporated to minimize the impact on the DPBT's optoelectronic properties, ensuring the core characteristics of the compound were preserved. This design allows the methyleneamine group to serve as a versatile site for further chemical modifications. The primary amine group in the functionalized DPBT facilitates reliable functionalization through amide bond formation, a well-established protocol in synthetic chemistry. A HBTU-based coupling reaction was employed to attach Boc-protected phenylalanine to the amine-functionalized DPBT, successfully yielding a photocatalyst-functionalized amino acid. Attempts to functionalize a phenylalanine dipeptide with DPBT-NH_2, however, resulted in an insoluble product under the desired experimental conditions, highlighting a solubility challenge for the dipeptide. The phase behavior of the phenylalanine-functionalized DPBT was investigated, focusing on its ability to undergo liquid-liquid phase separation and form coacervate droplets.

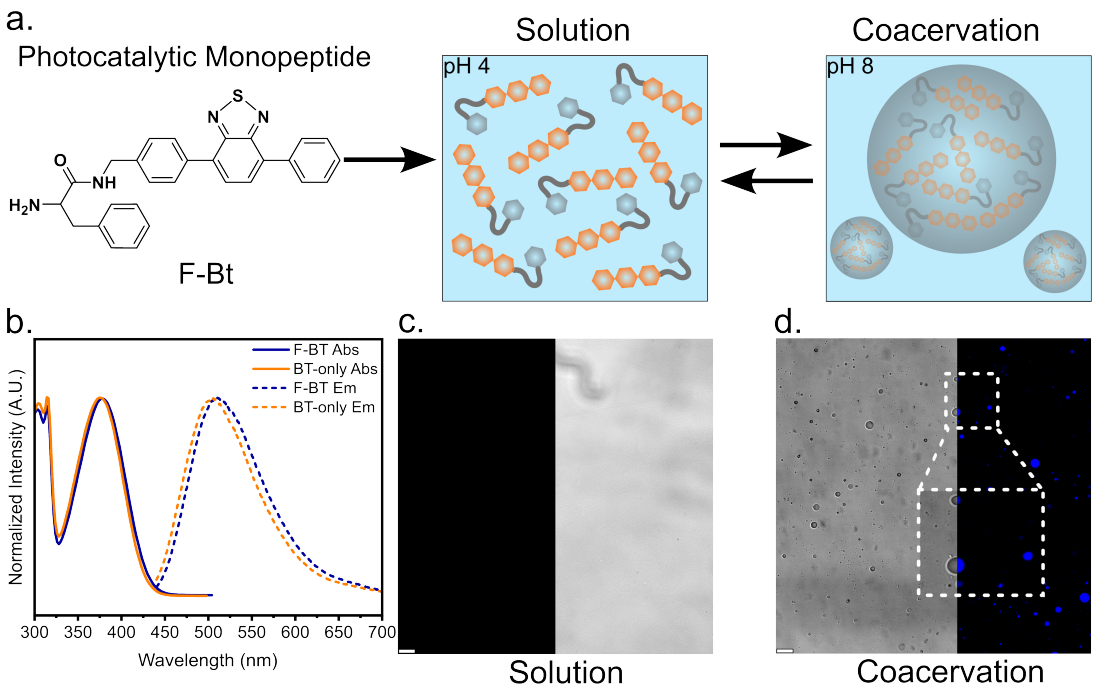

Figure 6.3: Coacervation of DPBT-phenylalanine. a) Schematic diagram of DPBT-coacervate-based coacervate formation. b) Absorption and emission behavior of DPBT-coacervates (F-BT) and the small molecule photocatalyst (BT-only), measured in acetonitrile:water (1:1) at 10^{-6} M. c) Fluorescence and light microscopy images of the DPBT-coacervates at 2.5 mg mL^{-1} in aqueous solution at pH 4 (10 µm scale). d) Fluorescence and light microscopy images of the DPBT-coacervates at 2.5 mg mL^{-1} in aqueous solution at pH 8 (10 µm scale).

The results indicated a reproducible and reversible formation of coacervates at pH levels above 8, which completely dissolved when the pH dropped below 6. This pH-dependent phase separation behavior was confirmed to be fully reversible. A notable advantage of this system is the ability to characterize these coacervates using fluorescence emission microscopy without the need for additional imaging agents or dyes. The intrinsic fluorescence of the covalently attached DPBT moiety enabled the precise localization of the photoactive species within the coacervate droplets, showing a controlled colocalization of the photocatalyst exclusively within the coacervate droplets. This feature is particularly valuable for applications in bioimaging, where precise visualization of dynamic processes is essential.

The photocatalytic activity of the prepared compound was subsequently evaluated. To assess the reactivity differences between DPBT-loaded coacervates and intrinsically photocatalytically active coacervates, a methylene blue dye degradation was conducted. For this experiment, identical conditions to the previously reported dye degradation protocol for used for the DPBT-functionalized coacervates. Figure 6.3 presents the time-dependent UV/Vis spectra for the methylene blue degradation. The analysis focused on the characteristic peak at 660 nm, which exhibited a consistent degradation pattern similar to that observed with DPBT-loaded coacervates. Control studies were performed to further understand the photocatalytic efficacy. These included comparisons of methylene blue

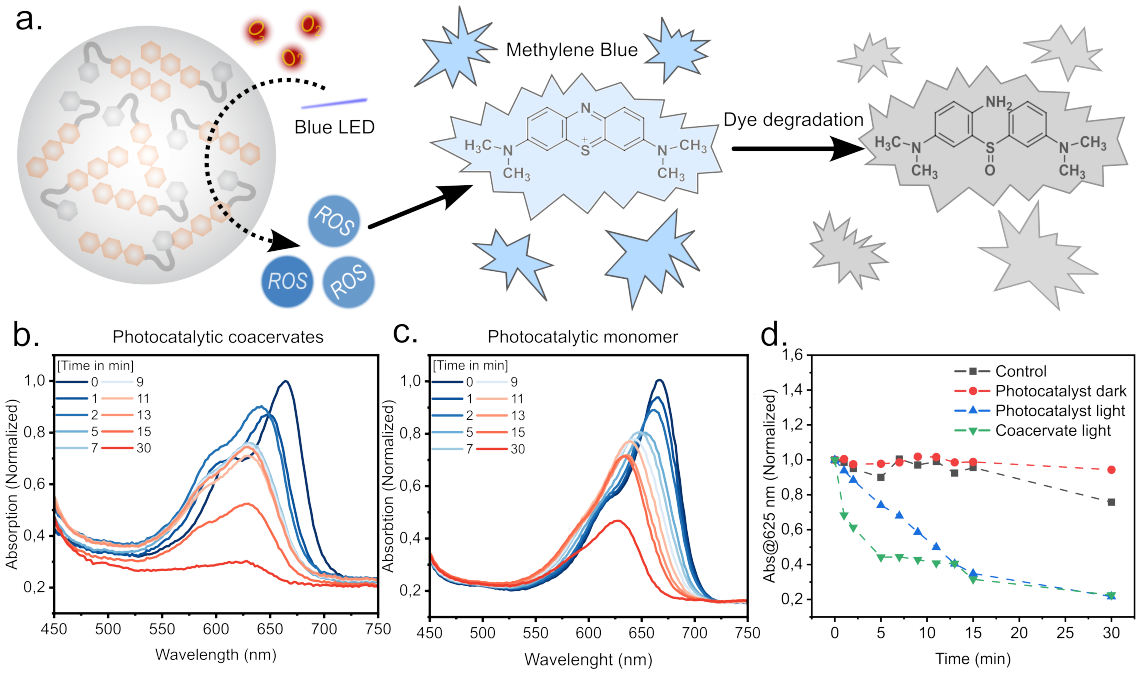

Figure 6.4: Photocatalytic dye degradation with DPBT-coacervates. a) Schematic diagram of DPBT-coacervate-based photocatalytic microreactors for methylene blue dye degradation. b) Absorption curves of methylene blue during photocatalytic degradation by DPBT-coacervates at pH 8 (2.5 mg mL^{-1}). c) Absorption curves of methylene blue during photocatalytic degradation by DPBT monomer at pH 8 (2.5 mg mL^{-1}). d) Absorption intensity of methylene blue during photocatalytic degradation under different conditions.

degradation in four scenarios: a blank sample, DPBT-only under dark conditions, DPBT-only under irradiated conditions, and DPBT-functionalized coacervates under irradiated conditions (Figure 6.4). The results indicated no significant dye degradation for both the blank and DPBT-only under dark conditions. Minor variations observed were attributed to the sensitivity of the UV/Vis absorption analysis. Under irradiated conditions, the DPBT-only sample exhibited a steady, linear degradation of methylene blue, suggesting a diffusion-limited process. After 12 min of reaction time, both the DPBT-only and DPBT-functionalized coacervate samples showed comparable levels of dye degradation. However, a marked acceleration in the degradation rate was observed for the coacervate catalyst. Within 5 minutes, the coacervate system reached a plateau, achieving 56% dye conversion, while the DPBT-only system reached only 25% conversion. Both experiments were conducted with identical catalyst loadings. The pronounced enhancement in the reaction rate with the coacervates can be attributed to the reduction in photocatalyst aggregation, which mitigates aggregation-induced quenching mechanisms. Additionally, the homogeneous distribution of the catalyst within the heterogeneous coacervate phase likely resulted in the accumulation of substrate dye and higher local concentrations of reactive oxygen species (ROS), facilitating more efficient photocatalysis.

For further evaluation of the photocatalytic activity of DPBT-coacervates, the system was employed for a photocatalytic oxidation of sulfides. As a model compound, methyl-p-polysulfide was chosen to be oxidized to the corresponding sulfoxide. This transformation

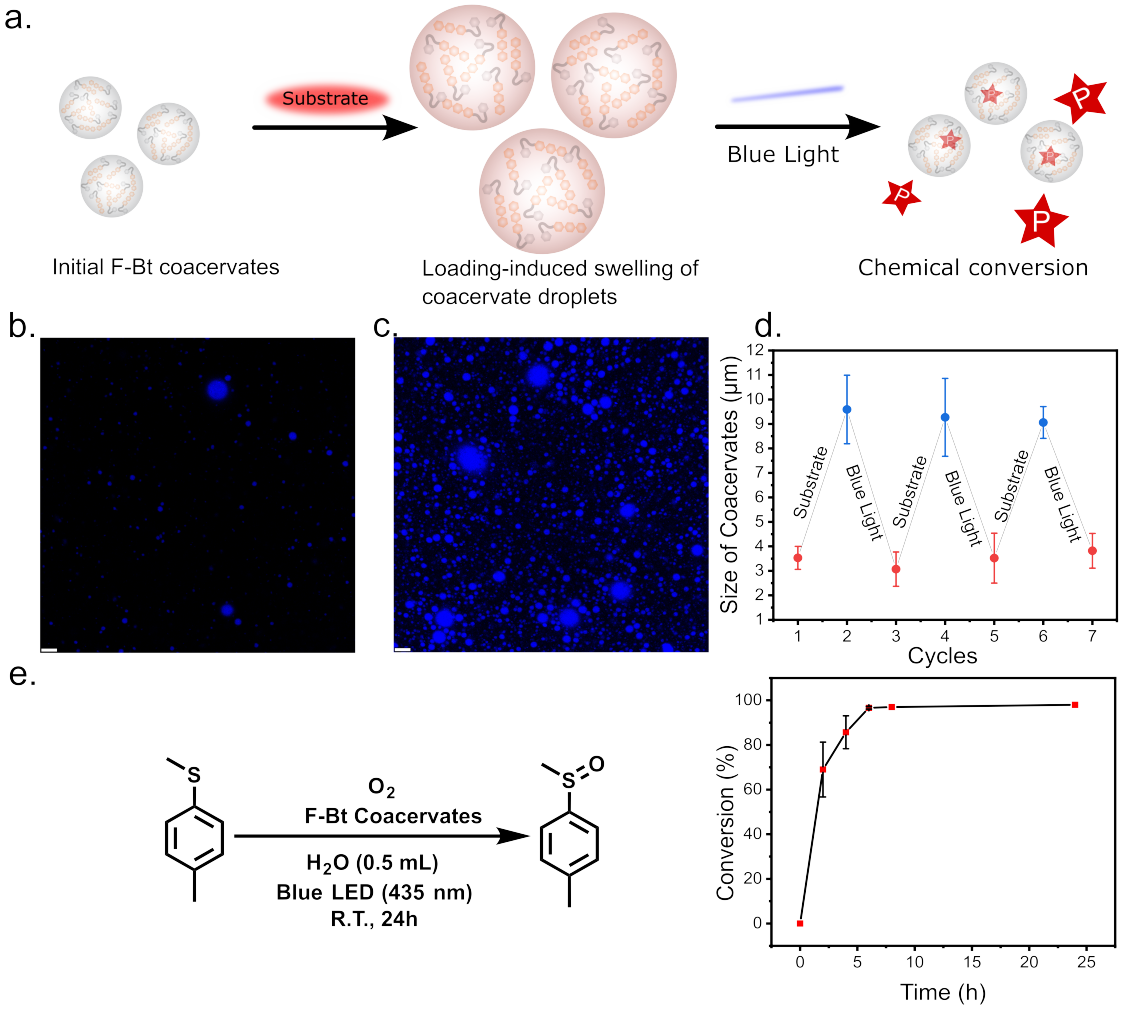

Figure 6.5: Photocatalytic sulfide oxidation in DPBT-coacervates. a) Schematic diagram of substrate-induced swelling of DPBT-coacervates. b) Fluorescence microscopy of DPBT-coacervates in aqueous solution at pH 8 (10 µm scale) before substrate-induced swelling. c) Fluorescence microscopy of DPBT-coacervates in aqueous solution at pH 8 (10 µm scale) after substrate-induced swelling. d) Reversibility screening for the substrate-induced swelling, using methyl-p-tolylsulfide. e) Reaction scheme and conversion diagram for the sulfide oxidation of methyl-p-tolylsulfide to methyl-p-tolylsulfoxide.

represents a well-known reaction for benzothiadiazole-based photocatalysts, following an ROS-based mechanism.[213] Figure 6.5 shows the time-dependent oxidation of methyl-p-tolylsulfide to methyl-p-tolylsulfoxide. The reaction conversion was monitored via GC-MS analysis. The reaction was conducted under air, without additional feeding of oxygen into the solution. The DPBT-coacervate showed a high reactivity, yielding a conversion of 68% already after 2 h of blue light irradiation. Further irradiating the mixture gave 86% and 98% after 4 h and 6 h, respectively. After 6 h reaction time, the system reached a plateau formation, due to full conversion of the substrate. However, as shown in the GC chromatogram in Figure 6.5, the formation of another compound was observed. Peak 1 in the chromatogram represents the sulfoxide, while peak 2 represents the corresponding sulfone product. Typically, the higher oxidation degree is obtained only in trace amounts. The

strong formation of the sulfone could be reasoned by the high hydrophobicity of methyl-p-tolylsulfide. As the DPBT-coacervate droplets represent a hydrophobic microenvironment within the aqueous reaction mixture, a strong accumulation of methyl-p-tolylysulfide within the coacervate droplets was observed (Figure 6.5). The enhanced spatial proximity of photocatalytically active sites and the substrates, paired with an increased concentration of ROS (due to the hydrophobic character of oxygen), represents a possible explanation for the disproportionately high formation of the sulfone product.

6.4 Conclusion

This study presents the design and synthesis of peptide-coacervate droplets functioning as catalytic and photocatalytic microreactors. Initially, colloidally stable dipeptide coacervates were prepared and extensively investigated for their ability to sequester compounds and biocompatibility. These dipeptide coacervates demonstrated exceptional stability and versatility, allowing for the colocalization of a wide range of dye and catalyst molecules. Encapsulation of catalytic and photocatalytic species within the coacervate droplets resulted in the formation of powerful microreactors with a hydrophobic microenvironment. The controlled colocalization of catalytic compounds within these droplets was successfully exploited for their application as artificial organelles in both artificial cell-like systems and biological HeLa cells. To optimize the peptide coacervates for use as artificial, photocatalytic microreactors, a simpler system based on a single amino acids was developed. This involved the covalent attachment of the photocatalytic diphenylbenzothiadiazole (DPBT) species to phenylalanine, which facilitated a more homogeneous dispersion of the photocatalyst and reduced aggregation. A reversible liquid-liquid phase transition was observed for the DPBT-phenylalanine coacervate system. Subsequent evaluation of the photocatalytic activity using methylene blue dye degradation revealed a high level of photocatalytic efficacy. This high activity was further confirmed through a controlled sulfide oxidation reaction to the corresponding sulfoxide. The photocatalytic coacervates outperformed the small molecule photocatalyst, likely due to the hydrophobic microenvironment provided by the coacervates, which facilitated substrate accumulation within the droplets and increased the spatial proximity of the substrate to the photocatalytically active sites. The stability and intrinsic photocatalytic activity of the peptide-coacervates significantly enhances the applicability of these systems. The versatile peptide coacervates developed in this study are poised to contribute significantly to the advancement of innovative biotechnologies.

6.5 Experimental Details

Instrumentation

"Nuclear magnetic resonance (NMR) spectroscopy: Routine proton nuclear magnetic resonance (^{1}H NMR) measurements were performed on a Bruker Avance 300 MHz UltrashieldTM spectrometer equipped with a Bruker SampleCase autosampler, using $CDCl_3$ or DMSO-d_6 as solvent and TMS as internal standard."

"Microplate reader: Catalytic reactions were evaluated using a microplate reader (TECAN, infinite M1000). Reaction progress was monitored by the absorbance or fluorescence signal on the microplate reader (TECAN)."

"UV-Vis spectroscopy: UV-Vis spectra were characterized using UV-Vis spectroscopy (Agilent Cary 60 instrument)."

"Mass spectra: The molecular weights of the peptide compounds were measured using an Advion Express CMS compact mass spectrometer. The resulting spectra were analyzed using Advion CheMS Express software version 5.1.0.2. High-resolution ESI mass spectra were obtained using a Waters SYNAPT G2-Si spectrometer."

"Wide-field fluorescence microscopy imaging: The wide-field fluorescence images were captured using Leica DMi8 inverted microscope. Confocal scanning microscopy imaging: Confocal microscopy was performed using a Leica TCS 264 SP5X system."

Gas chromatography coupled with mass spectrometry: Gas chromatographic analysis was conducted via on an Shimadzu GC-2010 plus GC- system equipped with a 7HG-G010-11 Phenomenex column (0.25 mm x 30 m (diameter:length), film thickness: 0.25 µm) and analysed using QP2010 ultra mass spectrometer.

1) Splitless injection, injection temperature 250 °C, column oven 50 °C. Temperature gradient: 50 °C hold 2 min to 160 °C with a rate of 15 °C min^{-1} hold for 2 min to 280 °C with a rate of 20 °C min^{-1} hold for 8 min. Total flow at 23.1 mL min^{-1}, 42.0 kPa Pressure, 0.86 mL min^{-1} column flow.

2) Splitless injection, injection temperature 280 °C, column oven 100 °C. Temperature gradient: 100 °C to 280 °C with a rate of 10 °C min^{-1} hold for 5 min. Total flow at 19.6 mL min^{-1}, 43.6 kPa Pressure, 0.70 mL min^{-1} column flow.

Preparation of GC-MS samples were performed by addition of 200 µL of crude solution mixture into 2 mL acetonitrile, followed by drying with $MgSO_4$ and then transferred into 2 mL GC vials, washing $MgSO_4$ with 1 mL acetonitrile. GC-MS spectra were analysed with GCMSolution postrun analysis (Version: 4.45 SP1).

Methods

"Preparation of peptide coacervates: As an example of coacervate droplet formation from FF-OMe, the FF-OMe solid was dissolved in 5 mM HEPES buffer (pH 6) at a concentration of 20 mg mL^{-1}. For microscopic imaging of the coacervates, 10 µL of peptide coacervates was added with 0.1 M NaOH solution to reach a pH above 7. The solution immediately turned milky. 0.5 µL Pluronic® F-108 (1% wt) was added to increase the stability of the coacervates. The formation of coacervate droplets was confirmed using a Leica DMi8 inverted microscope. A similar procedure was conducted for the analysis of F-DPBT coacervates. In there, a 5 mg mL^{-1} solution of F-DPBT in 5 mM HEPES was prepared. For microscopic imaging of the coacervates, 10 µL of peptide coacervates was added with 0.1 M NaOH solution to reach a pH above 7."

"Guest molecule partitioning: All experiments were performed at room temperature unless stated otherwise. Briefly, the coacervate droplet solution was first prepared by adding 0.1 M NaOH solution to the peptide solution in HEPES buffer. Then, 10 µL of the prepared coacervate solution (10 mg mL^{-1}) was mixed with the 0.2 µL dye solutions (2 mg mL^{-1} in DMSO or Milli-Q) by pipetting. The mixture was then dropped onto a glass surface with a coverslip using a homemade setup. The droplets were then imaged by confocal microscopy using the Leica TCS 264 SP5X system."

"Photocatalytic dye degradation with peptide coacervates: 2 µL DTB (20 mg mL^{-1}) was first mixed with peptide coacervate solution (5 mg mL^{-1}, 800 µL) by pipetting. Then 10 µL of 2 mg mL^{-1} methylene blue or rhodamine B was added to the mixture and stirred under dark conditions until equilibrium was reached (5 min). The mixture was then exposed to blue LED light (power: 0.36 W cm^{-2}, λ >420 nm) for the desired time. 70 µL samples were taken from the solution and subjected to high centrifugation (12000 rpm, 5 min) to dissolve the coacervates. The change in dye concentration was monitored by UV-vis spectroscopy."

Photocatalytic dye degradation with DPBT functionalized peptide coacervates: 400 µL of a DPBT coacervate stock solution (5 mg mL^{-1}; in water at pH 8) were added to 400 µL H_2O. After homogenization of the mixture, 10 µL of 2 mg mL^{-1} methylene blue was added and stirred under dark conditions until equilibrium was reached (5 min). The mixture was then exposed to blue LED light (power: 0.36 W cm^{-2}, λ >420 nm) for the desired time. 40 µL samples were taken from the solution and subjected to high centrifugation (12000 rpm, 5 min) to dissolve the coacervates. The change in dye concentration was monitored by UV-vis spectroscopy.

Photocatalytic sulfide oxidation with DPBT functionalized peptide coacervates: 400 µL of a DPBT coacervate stock solution (5 mg mL^{-1}; in water at pH 8) were added to 400 µL H_2O. To this mixture, methyl-p-tolylsulfide (11.5 µL) was added and stirred under dark conditions until equilibrium was reached (5 min). The mixture was then exposed to blue LED light (power: 0.36 W cm^{-2}, λ >420 nm) for the desired time. 100 µL samples were taken from the solution and added to 1 mL methanol. The conversion of metly-p-tolylsulfide was monitored via GC-MS.

Synthesis of Dithiophenebenzothiadiazole (DTB) photocatalyst

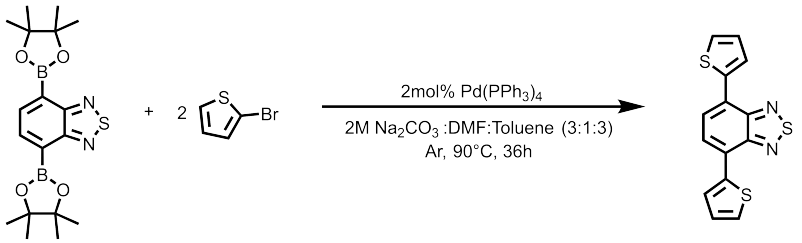

"Into a 150 mL schlenk tube with a stir bar, 25 mL of a 2 M Na_2CO_3 (aq.) solution, 25 mL of toluene and 9 mL of DMF were added. Subsequently, the solution was degassed with an argon stream for 15 min, before 4,7-bis(4,4,5,5-tetramethyl-1,3,2-dioxaborolan-2-yl)-2,1,3-benzothiadiazole (1.0 eq., 1.0 g, 2.58 mmol) and 2-bromothiophene (2.5 eq., 1.05 g, 6.44 mmol) and tetrakis(triphenylphosphane)palladium (0.02 eq., 59.55 mg, 51.53 µmol) were added in an argon counter stream. The reaction mixture was heated to 90 °C for 36 h with an attached reflux condenser under heavy stirring. After cooling down to room temperature, 30 mL of Milli-Q water were added, followed by dichloromethane extraction (4x 25 mL), washing by brine and drying over Na_2SO_4. After evaporation of all volatiles with the rotary evaporator, the crude mixture was purified using SiO_2 column chromatography (gradient from 10% DCM: 90% petrolether to 70% DCM: 30% petrolether). The product was obtained as red powder (310 mg, 40.1% yield)."

^{1}H NMR (400 MHz, DMSO-d_6, δ) :8.23 (dd, J = 3.7, 1.2 Hz, 2H), 8.17 (s, 2H), 7.83 (dd, J = 5.1, 1.1 Hz, 2H), 7.34 (dd, J = 5.1, 3.7 Hz, 2H).
^{13}C NMR (101 MHz, DMSO-d_6, δ) :152.20, 138.87, 128.76, 128.57, 127.91, 126.34, 125.52.

Synthesis of Functionalizable Diphenylbenzothiadiazole (DPBT) Photocatalyst

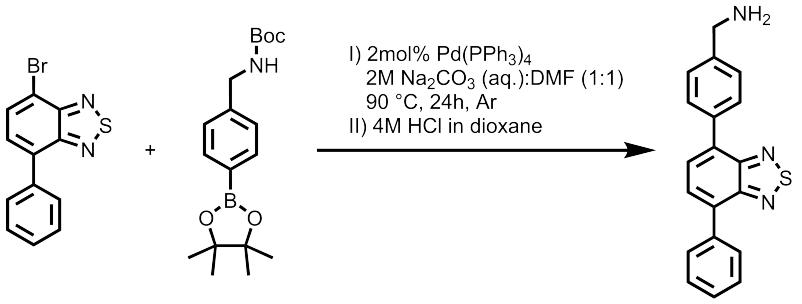

Into a 150ml schlenk tube with a stir bar, 25 mL of a 2 M Na_2CO_3 (aq.) solution and 25 mL of DMF were added. Subsequently, the solution was degassed with an argon stream for 15 min, before 4-bromo-7-phenylbenzo[c] [1,2,5]thiadiazole (1.0 eq., 1.0 g, 3.43 mmol) and tert-butyl (4-(4,4,5,5-tetramethyl-1,3,2-dioxaborolan-2-yl)benzyl)carbamate (1.5 eq., 1.72 g, 5.15 mmol) and tetrakis(triphenylphosphane)palladium (0.02 eq., 79.38 mg, 68.69 µmol) were added in an argon counter stream. The reaction mixture was heated to 90 °C for 24 h with an attached reflux condenser under heavy stirring. After cooling down to room temperature, 30 mL of Milli-Q water were added, followed by dichloromethane extraction (4x 25 mL), washing by brine and drying over Na_2SO_4. After evaporation of all volatiles with the rotary evaporator, the crude mixture was purified using SiO_2

column chromatography (gradient from 10% EtOAc: 90% petrolether to 70% EtOAc: 30% petrolether). The product was obtained as yellow powder (682 mg, 63% yield). Afterwards, the compound was dissolved in 4 M HCl in dioxane, 300 mg in 15 mL HCl, and stirred at room temperautre over night. The resulting precipitate was filtered off and washed 2 times with dioxane.

^{1}H NMR (400 MHz, DMSO-d$_6$, δ): 8.54 (br, 3H, NH_3), 8.07 (m, 2H, Ar H), 8.00 (m, 4H, Ar H), 7.70 (m, 2H, Ar H), 7.58 (m, 2H, Ar H), 7.49 (m, 1H, Ar H), 4.15 (s, 2H, CH_2).
^{13}C NMR (101 MHz, DMSO-d$_6$, δ): 153.8 (2C; Ar C=N), 137.3 (1C, C_q), 134.7 (1C, C_q), 133.1 (1C, C_q), 132.2 (1C, C_q), 129.7 (8C, Ar C-H), 128.8 (5C, Ar C-H), 42.4 (1C, C-NH_2).

Synthesis of DPBT-Functionalized Phenyalanine

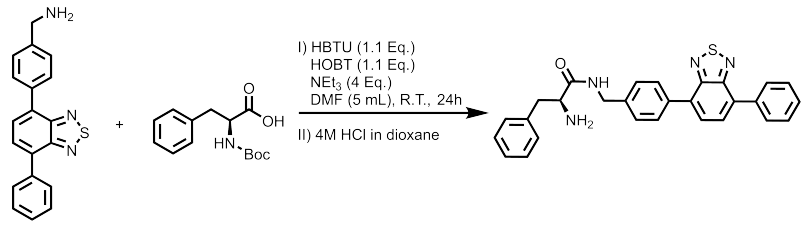

Into a 25 mL round bottom flask equipped with a stir bar, N-Boc phenylalanin (1.1 eq., 291.83 mg, 1.1 mmol), 2-(1H-benzotriazol-1-yl)-1,1,3,3-tetramethyluronium hexafluorophosphate (1.1 eq., 471.75 mg, 1.1 mmol) and N-Hydroxybenzotriazole (1.1 eq., 148.63 mg, 1.1 mmol) were added. To this, DMF (dry, 5 mL) and NEt_3 (4 eq., 0.52 mL, 4 mmol) awere added and the mixture was allowed to homogenize under stirring for 5 min. Next, functionalizable DPBT (1 eq., 317 mg, 1 mmol) were added to the reaction mixture. This mixture was stirred under room temperature for 24 h. After reaction completion, the mixture was added to water (400 mL) and a strong formation of precipitates was observed. The precipitate was filtered off by vacuum filtration. The obtained solid was dissolved in DCM (80 mL), washed with $NaHCO_3$, HCl and NaCl solution. After drying over $MgSO_4$, all volatiles were evaporated and dried at 50 °C over night. The desired product was obtained as yellow powder (502 mg). The obtained product was then dissolved in 4 M HCl in dioxane (355 mg in 5 mL HCl) and stirred at room temperature for 6 h. The resulting precipitate was filtered off and washed 2 times with dioxane, giving the final product as yellow powder (305 mg, 66% yield).

^{1}H NMR (400 MHz, DMSO-d$_6$, δ): 9.07 (t, 1H, NH) 8.41 (br, 3H, NH_3), 8.01 (m, 2H, Ar-H), 7.95 (d, 2H, Ar H), 7.93 (m, 2H, Ar H), 7.57 (m, 2H, Ar H), 7.48 (m, 1H, Ar H), 7.32 (m, 4H, Ar H), 7.27 (m, 4H, Ar H), 4.37 (dd, 2H, CH_2), 4.09 (br, 1H, NH), 3.11 (d, 2H, CH_2).
^{13}C NMR (101 MHz, DMSO-d$_6$, δ): 168.2 (1C; CONH), 153.6 (2C; Ar C=N), 138.8 (1C, C_q), 137.3 (1C, C_q), 136.1 (1C, C_q), 135.5 (1C, C_q), 132.8 (1C, C_q), 132.6 (1C, C_q), 129.9 (8C, Ar C-H), 129.5 (8C, Ar C-H), 129.1 (8C, Ar C-H), 128.8 (8C, Ar C-H), 128.7 (8C, Ar C-H), 128.1 (8C, Ar C-H), 127.7 (8C, Ar C-H), 66.8 (1C, Bz-CH_2), 54.2 (1C, C-NH_2).

Appendix

For all compound NMR spectra, the reader is referred to the supporting information in section 8.1.3.

Chapter 7

Summary and Outlook

Throughout this thesis, we have developed selectivity concepts for heterogeneous photocatalysts by drawing inspiration from the substrate specificity and selectivity processes of natural enzymes. By deciphering and adapting these enzymatic mechanisms, we enhanced the selectivity of photocatalytic reactions, providing a deeper understanding of substrate-dependent effects in heterogeneous photocatalysis.

First, we investigated the impact of hydrophilicity-hydrophobicity gradients on the photocatalytic reactivity of heterogeneous photocatalysts. Therefore, polymeric photocatalytic nanoparticles were functionalized with a diphenylbenzothiadiazole-based photocatalyst, where the incorporation of the photocatalyst was precisely controlled into either the hydrophilic shell or the hydrophobic core of the nanoparticles. Our findings revealed a significant dependency of photocatalytic reactivity on the hydrophilicity of the substrate and the location of the photocatalyst. Hydrophilic substrates were converted more efficiently with the photocatalyst located in the hydrophilic shell, while hydrophobic substrates showed higher reactivity with the photocatalyst in the hydrophobic core. This demonstrated the critical role of the microenvironment in determining photocatalytic efficiency.

Next, inspired by the selective binding mechanisms of natural enzymes, we explored the impact of non-covalent binding interactions between substrates and heterogeneous photocatalysts on the photocatalytic reactivity. We synthesized a conjugated microporous polymer (CMP) photocatalyst and post-functionalized it with guanidyl moieties, leveraging the strong hydrogen-bonding and electrostatic interactions of the guanidine functionality. The guanidine-functionalized CMP exhibited significantly accelerated reaction rates across various photocatalytic reactions compared to the non-functionalized CMP. This enhancement is attributed to the defined binding interactions between the substrate functional groups, like carboxylates or phosphonates, and the guanidine groups near the photocatalytically active surface, facilitating faster substrate diffusion and reaction rates.

Finally, we explored the application of photocatalysts within coacervates as artificial organelles or microreactors. Di- and single amino-acid-based coacervates were developed,

creating hydrophobic microenvironments for the accumulation and colocalization of targeted substrates. A photocatalyst-loaded dipeptide coacervate successfully demonstrated photocatalytic activity as artificial organelles. Further optimization led to the development of phenylalanine-based single amino-acid coacervates with intrinsic photocatalytic activity, by covalent binding of a hydrophobic photocatalyst. This system greatly improved the controlled localization of photocatalytic species and showed enhanced reactivity in a sulfide oxidation compared to the small-molecule photocatalyst.

The results presented in this thesis provide valuable insights into the design of orthogonal selectivity concepts for heterogeneous photocatalysts. By harnessing principles from enzymatic selectivity and integrating them into synthetic systems, we have investigated novel techniques to achieve more precise and efficient photocatalytic processes.

Continued research should aim to design and engineer specific building blocks that enable precise tuning of photocatalytic selectivity. This involves exploiting macromolecular and intermolecular effects to achieve complete control over chemical reactions. Additionally, exploring hybrid systems that combine multiple selectivity concepts could further enhance photocatalytic efficiency. For instance, integrating hydrophilicity gradients with non-covalent binding interactions may provide synergistic effects. The ultimate goal is to develop synthetic catalysts that mimic the high selectivity of natural enzymes. Achieving this could revolutionize selective catalysis, creating highly efficient, custom-designed photocatalytic systems for a wide range of applications in the chemical industry. In addition, future work should also focus on optimizing synthetic processes for industrial-scale production while maintaining high performance. This includes refining the functionalization techniques and ensuring stability and reproducibility of the photocatalytic materials.

In conclusion, this thesis has demonstrated substantial progress in the field of photocatalysis by introducing novel selectivity concepts inspired by natural enzymes. While the results achieved represent an important step towards selective photocatalytic systems, they are only an initial milestone. By continuing to explore and refine these strategies, we can pave the way for the development of highly selective and efficient photocatalytic systems, addressing the growing demands for sustainable catalytic processes.

Chapter 8

Appendix

8.1 Supporting Information

8.1.1 Chapter 4 -Microenvironment Effects on the Photocatalytic Activity of Polymeric Photocatalysts

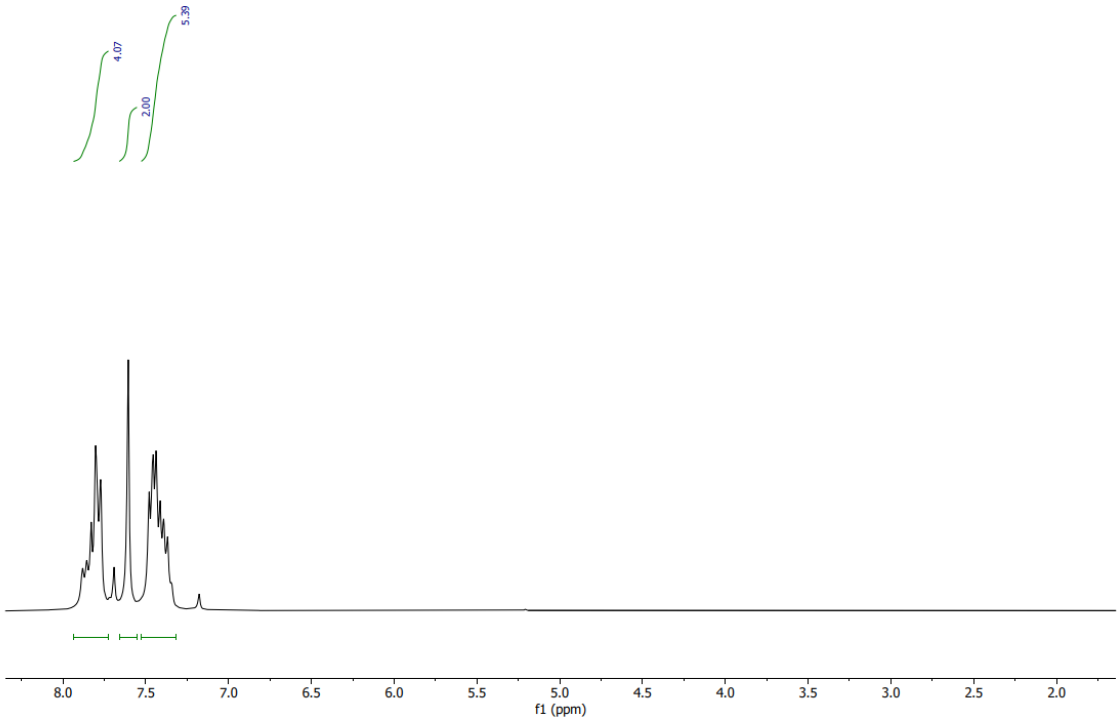

Figure 8.1: ^{1}H-NMR spectrum of the reaction for 4-bromo-7-phenylbenzo[1,2,5]thiadiazole, giving a crude mixture of the above presented structures. Reproduced with permission from ref[165]

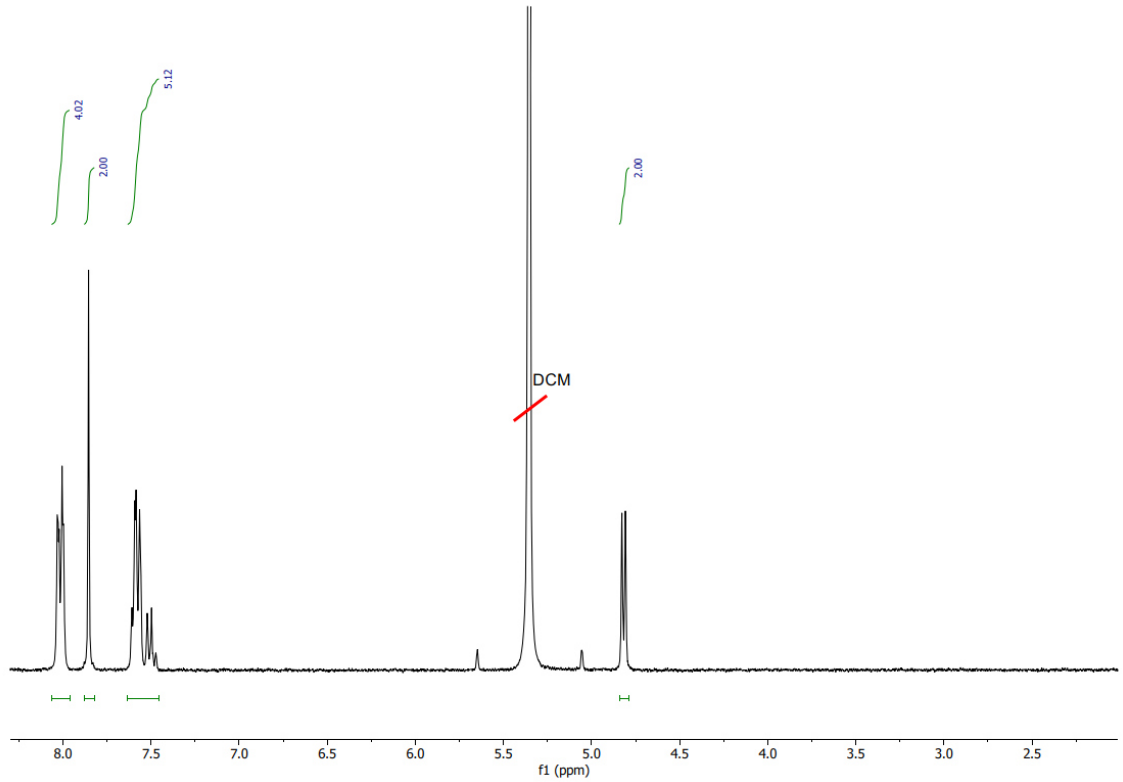

Figure 8.2: ^{1}H-NMR spectrum of (4-(7-phenylbenzo[1,2,5]thiadiazol-4-yl)phenyl)methanol. Reproduced with permission from ref[165].

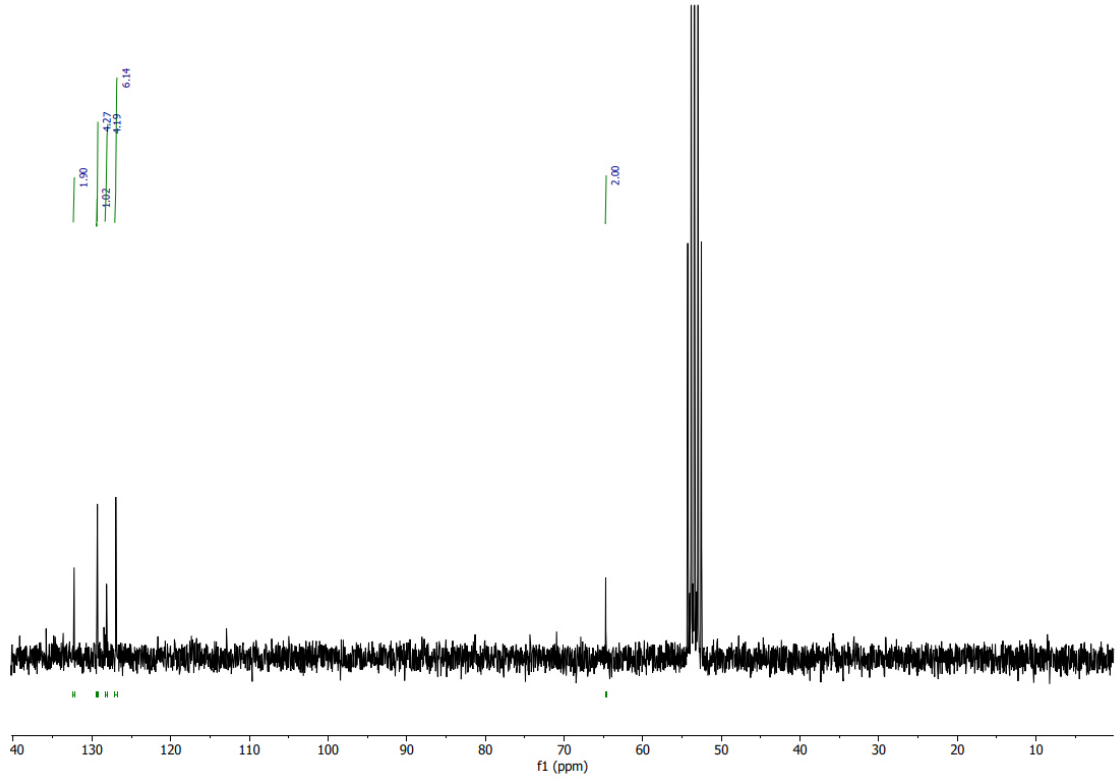

Figure 8.3: ^{13}C-NMR spectrum of (4-(7-phenylbenzo[1,2,5]thiadiazol-4-yl)phenyl)methanol. Reproduced with permission from ref[165].

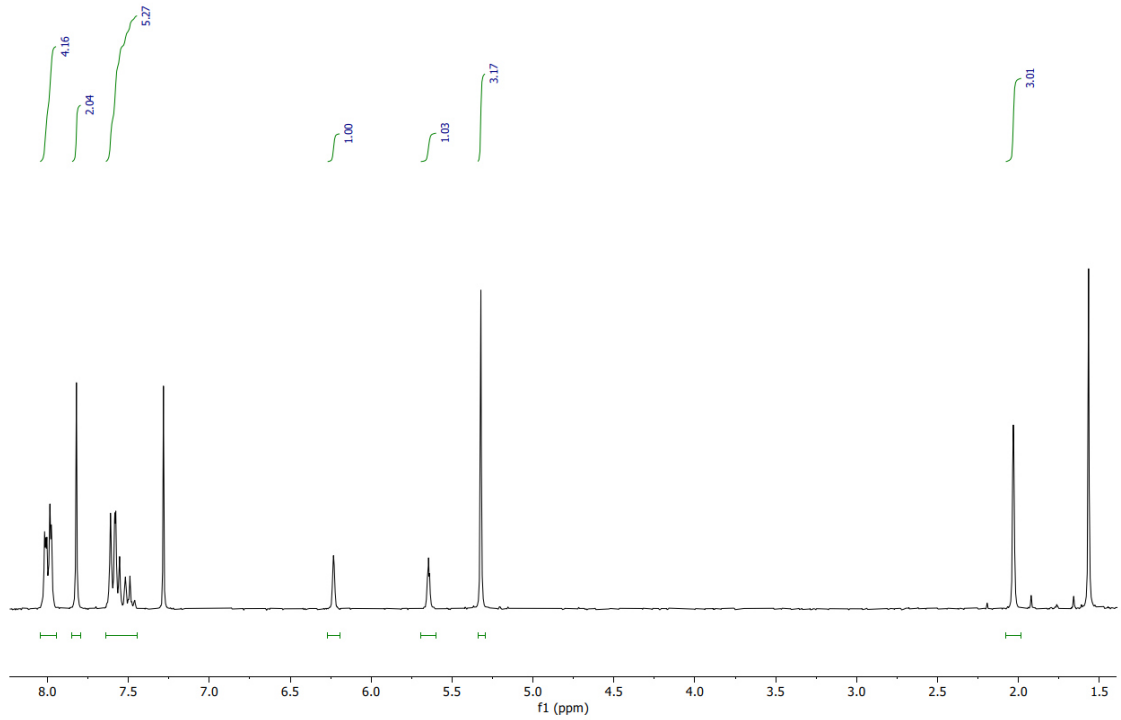

Figure 8.4: ^{1}H-NMR spectrum of 4-(7-phenylbenzo[1,2,5]thiadiazol-4-yl)benzyl methacrylate. Reproduced with permission from ref[165].

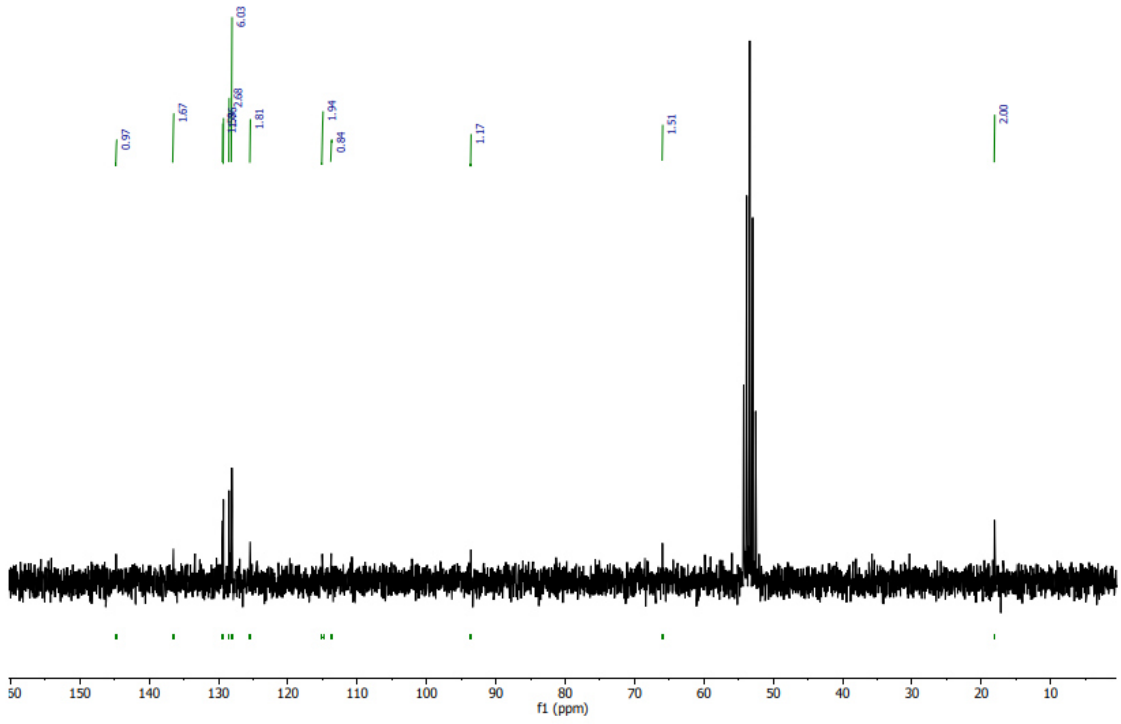

Figure 8.5: ^{13}C-NMR spectrum of 4-(7-phenylbenzo[1,2,5]thiadiazol-4-yl)benzyl methacrylate. Reproduced with permission from ref[165].

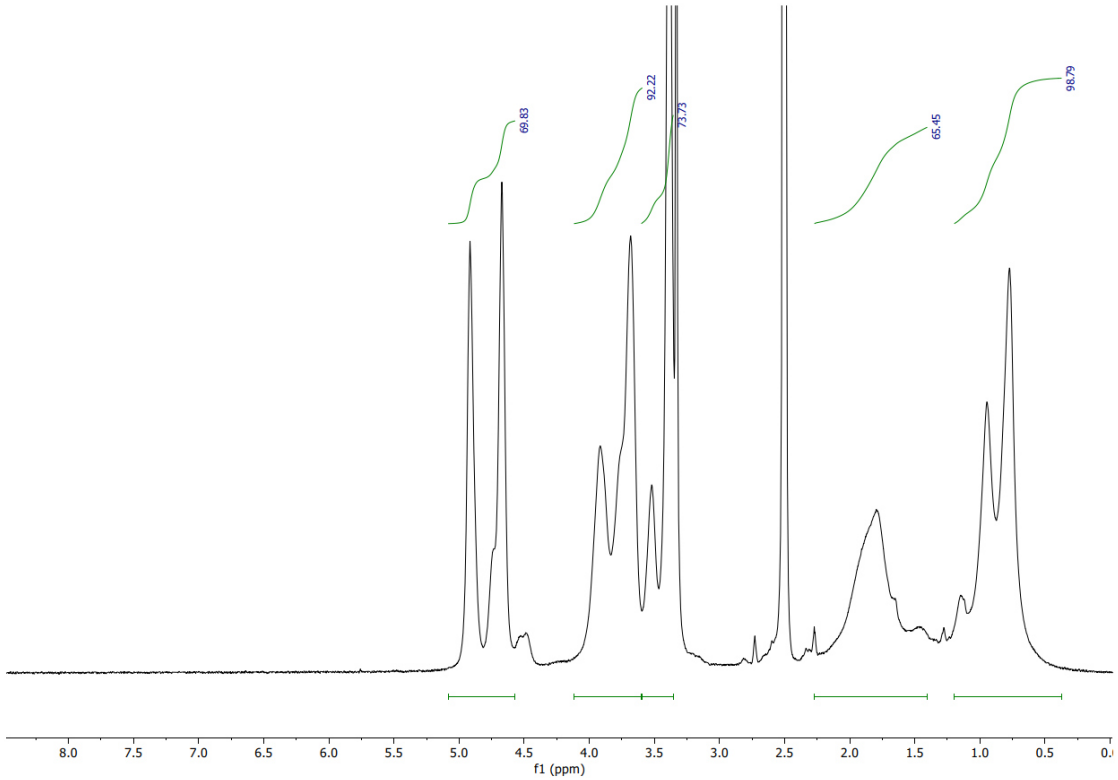

Figure 8.6: ^{1}H-NMR spectrum of the hydrophilic mCTA P(GMA)$_{100}$. Reproduced with permission from ref[165].

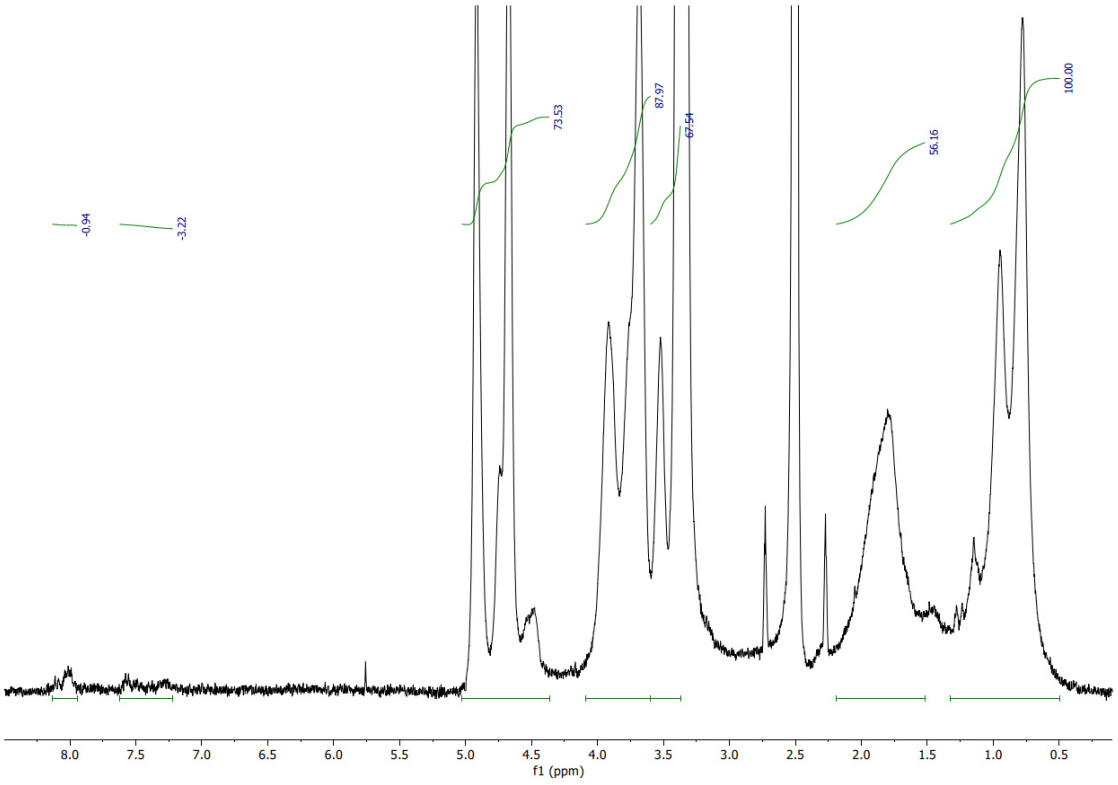

Figure 8.7: ^{1}H-NMR spectrum of the hydrophilic mCTA with photocatalyst P(GMA)$_{100}$-(BTP). Reproduced with permission from ref[165].

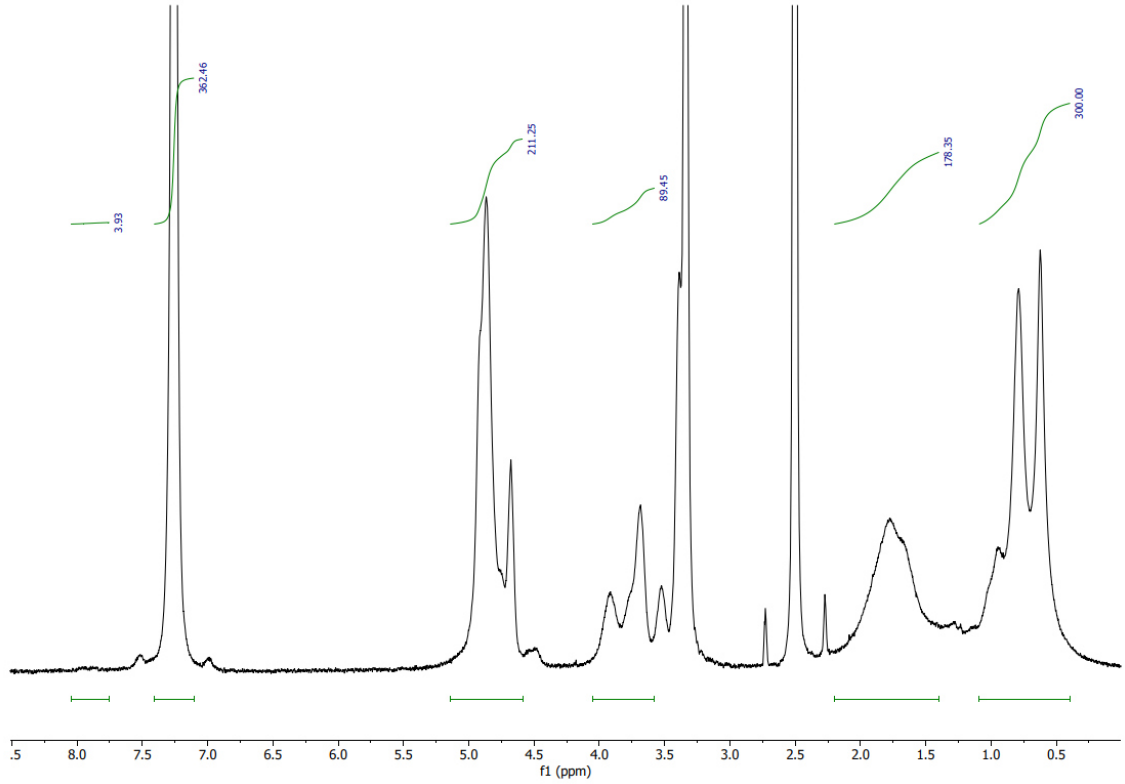

Figure 8.8: ^{1}H-NMR spectrum of the amphiphilic block-copolymer with hydrophilic photocatalyst P(GMA)$_{100}$-(BTP)$_{1}$-P(BzMA)$_{200}$. Reproduced with permission from ref[165].

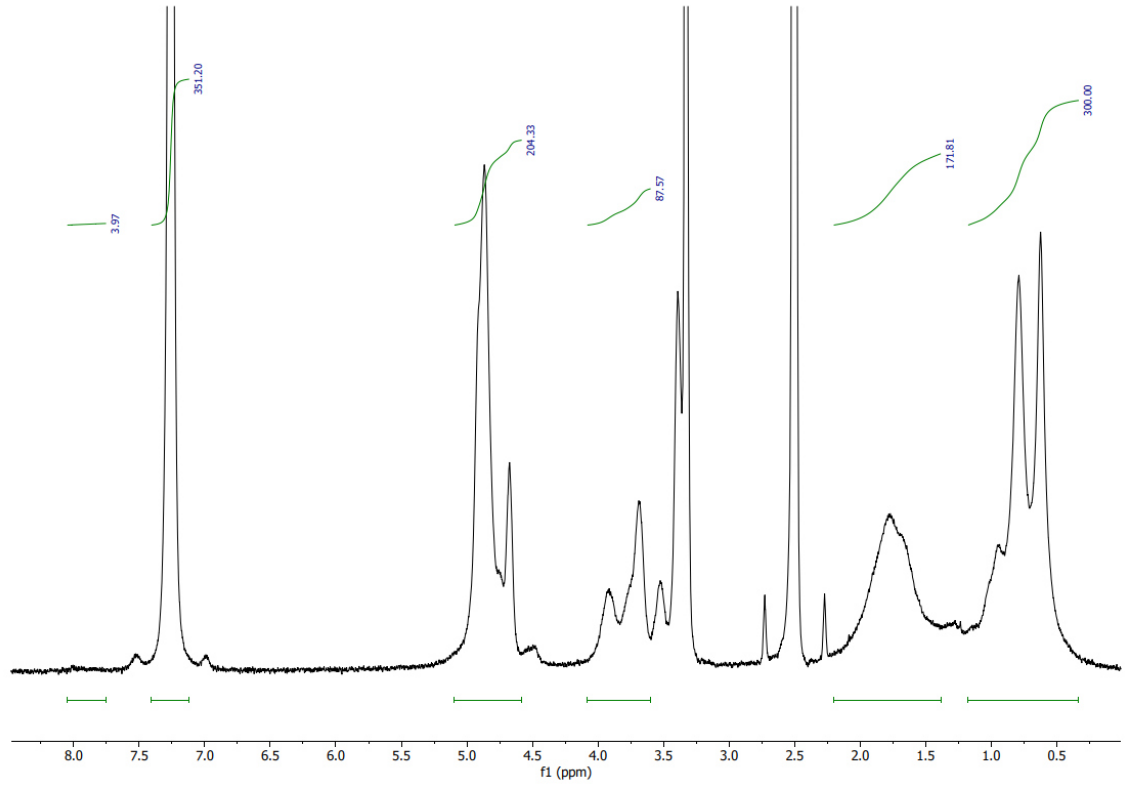

Figure 8.9: ^{1}H-NMR spectrum of the amphiphilic block-copolymer with hydrophobic photocatalyst P(GMA)$_{100}$-(BTP)$_{1}$-P(BzMA)$_{200}$. Reproduced with permission from ref[165].

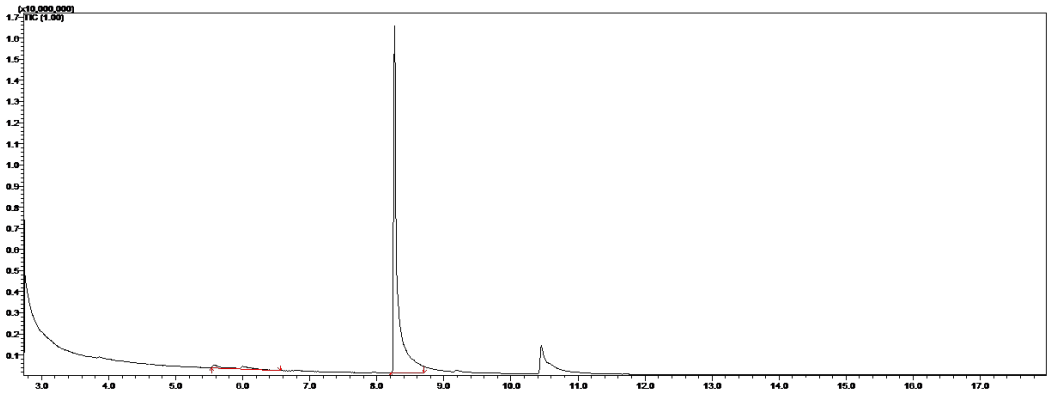

Figure 8.10: GC-MS retention time diagram, showing the formation of tetrahydrothiophene 1-oxide and trace amounts of the starting material tetrahydrothiophene. Reproduced with permission from ref[165].

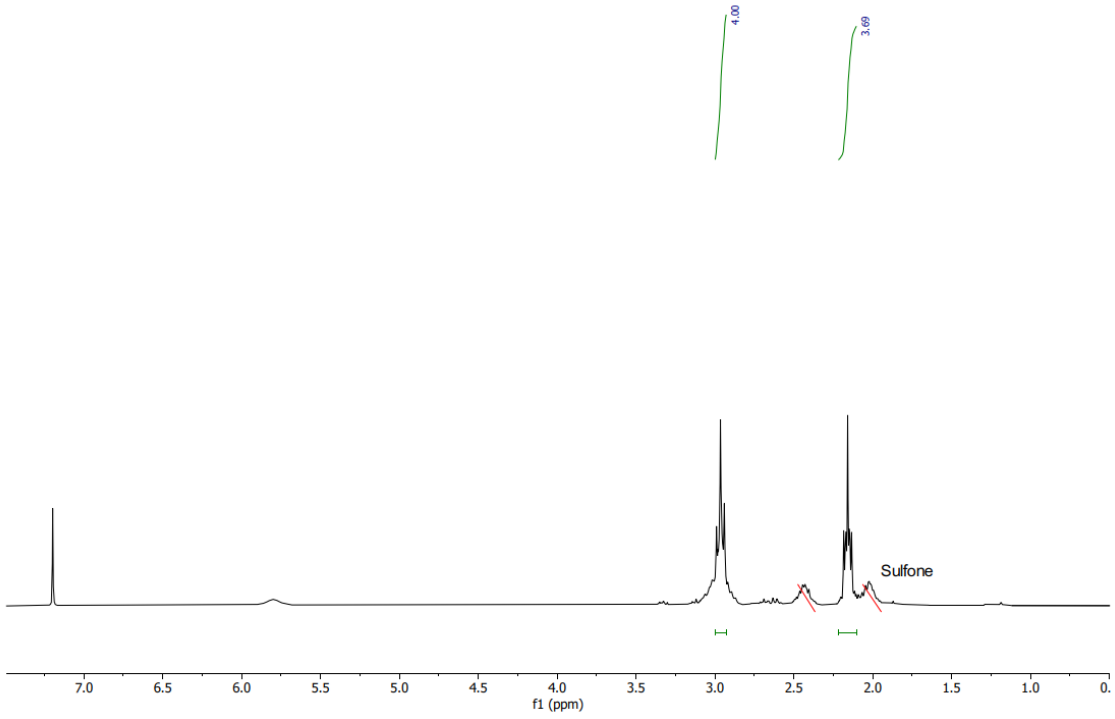

Figure 8.11: ^{1}H-NMR spectrum of tetrahydrothiophene-1-oxide. Reproduced with permission from ref[165].

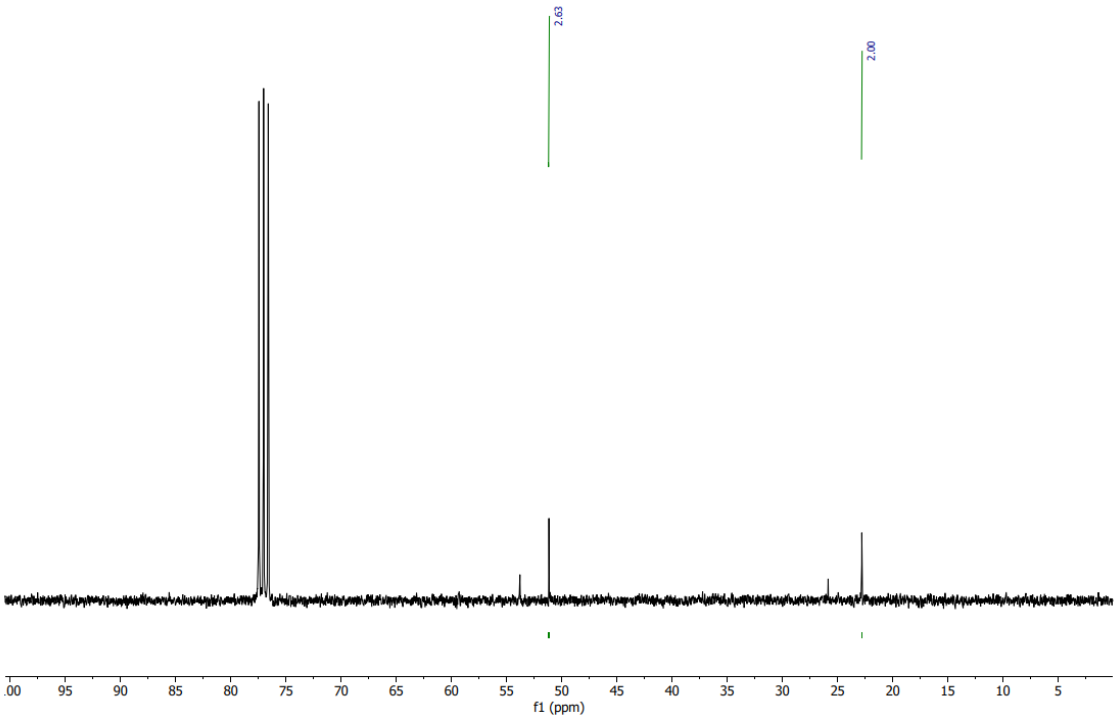

Figure 8.12: ^{13}C-NMR spectrum of tetrahydrothiophene-1-oxide.

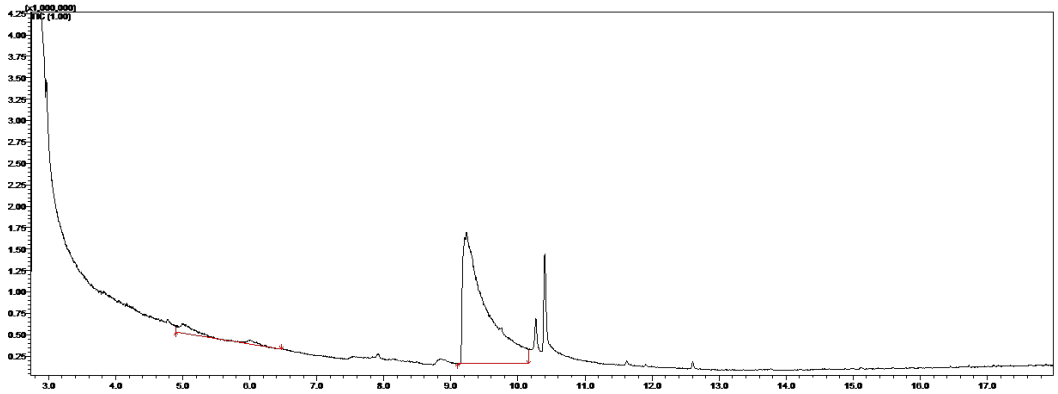

Figure 8.13: GC-MS retention time diagram, showing the formation of 2-(ethylsulfinyl)ethan 1-ol and trace amounts of the starting material 2-(ethylthio)ethan-1-ol. Reproduced with permission from ref[165].

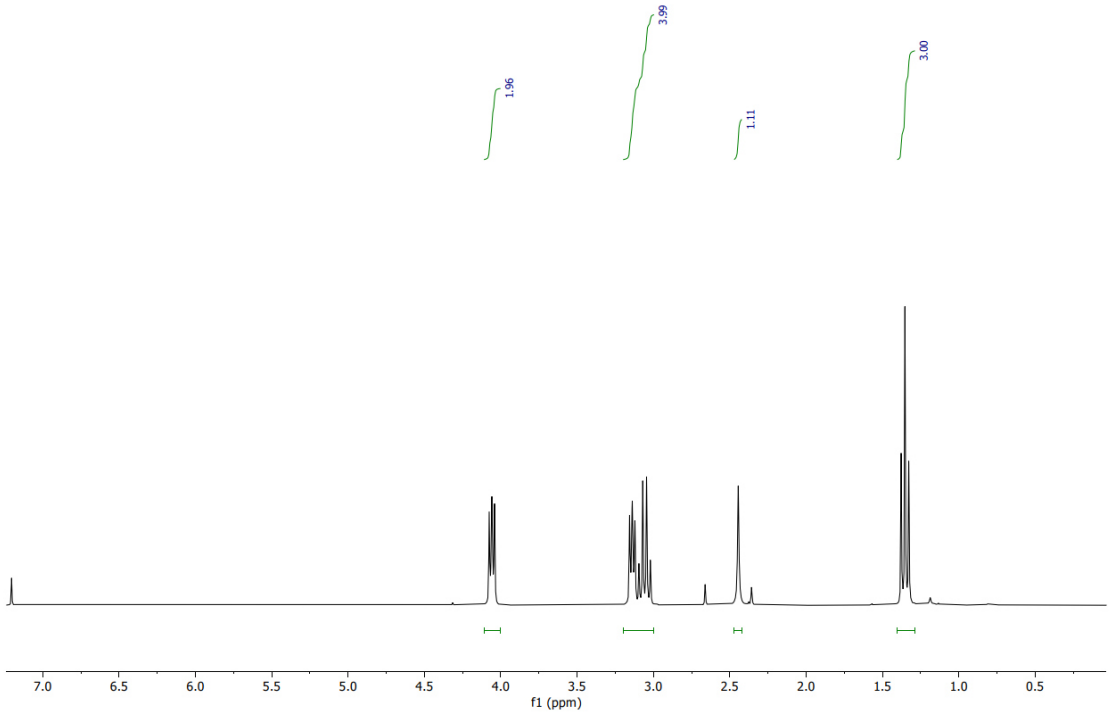

Figure 8.14: ^{1}H-NMR spectrum of 2-(ethylsulfinyl)ethan-1-ol. Reproduced with permission from ref[165].

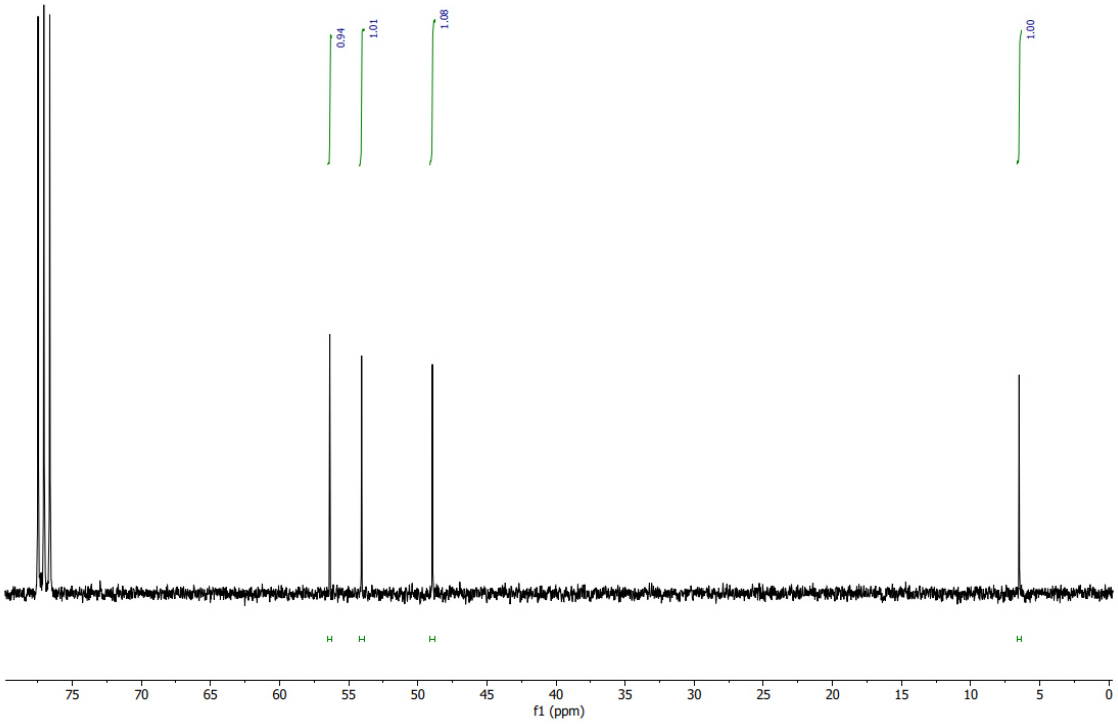

Figure 8.15: ^{13}C-NMR spectrum of 2-(ethylsulfinyl)ethan-1-ol. Reproduced with permission from ref[165].

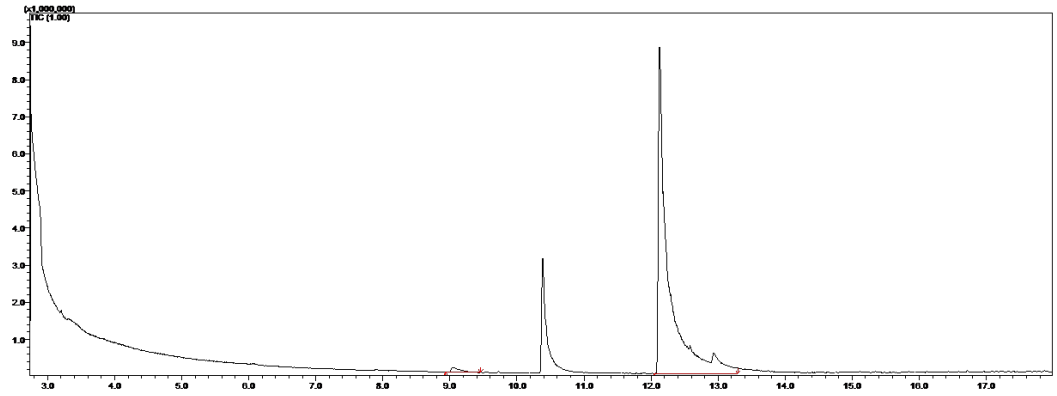

Figure 8.16: GC-MS retention time diagram, showing the formation of 1-methyl-4-(methylsulfinyl)benzene and trace amounts of the starting material methyl(p-tolyl)sulfane. Reproduced with permission from ref[165].

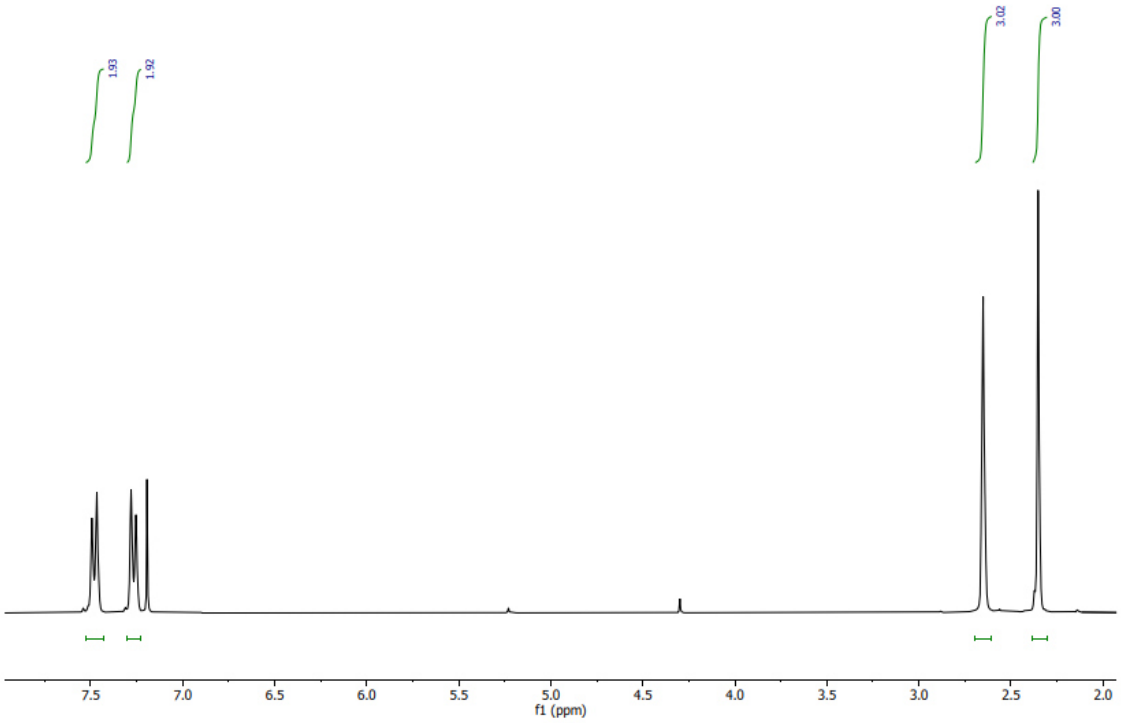

Figure 8.17: ^{1}H-NMR spectrum of 1-methyl-4-(methylsulfinyl)benzene. Reproduced with permission from ref[165].

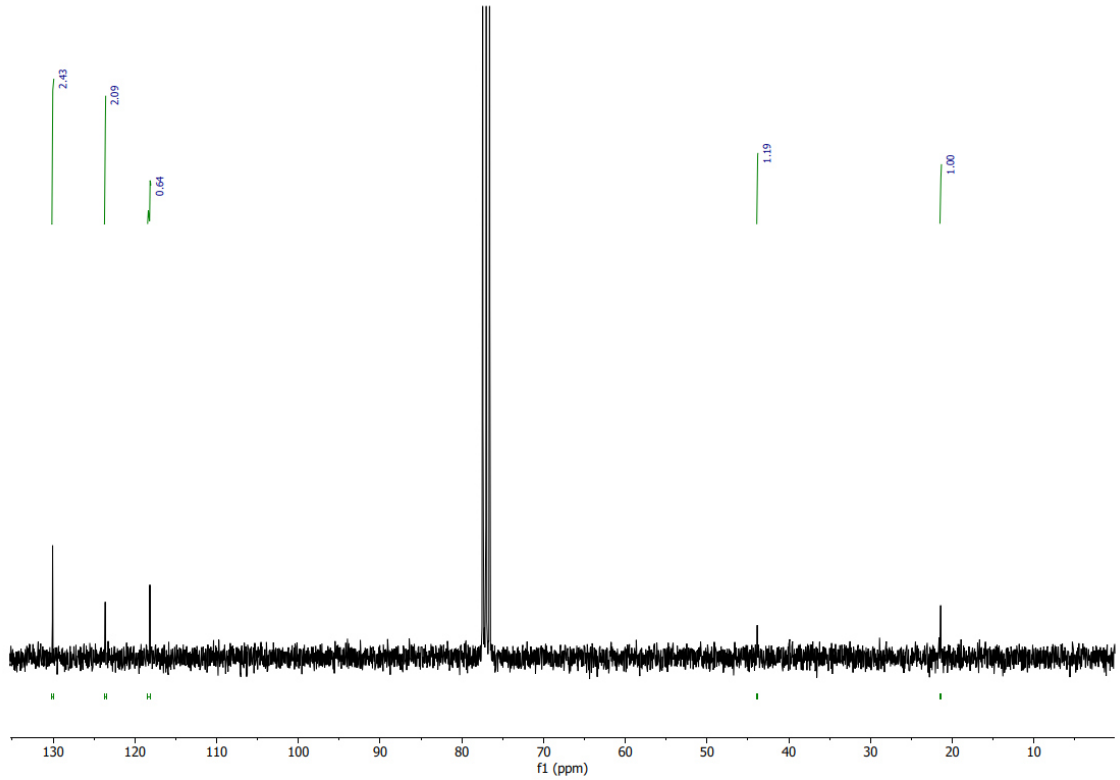

Figure 8.18: ^{13}C-NMR spectrum of 1-methyl-4-(methylsulfinyl)benzene. Reproduced with permission from ref[165].

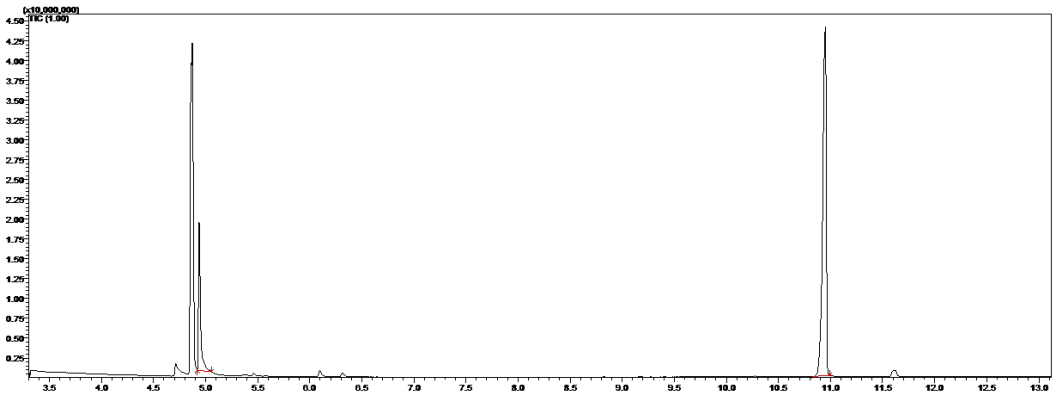

Figure 8.19: GC-MS retention time diagram, showing the formation of N-(4-(tert-butyl)-benzyl)-1-(4-(tert-butyl)phenyl)methanimine and trace amounts of the starting material (4-(tert-butyl)phenyl)methanamine. Reproduced with permission from ref[165].

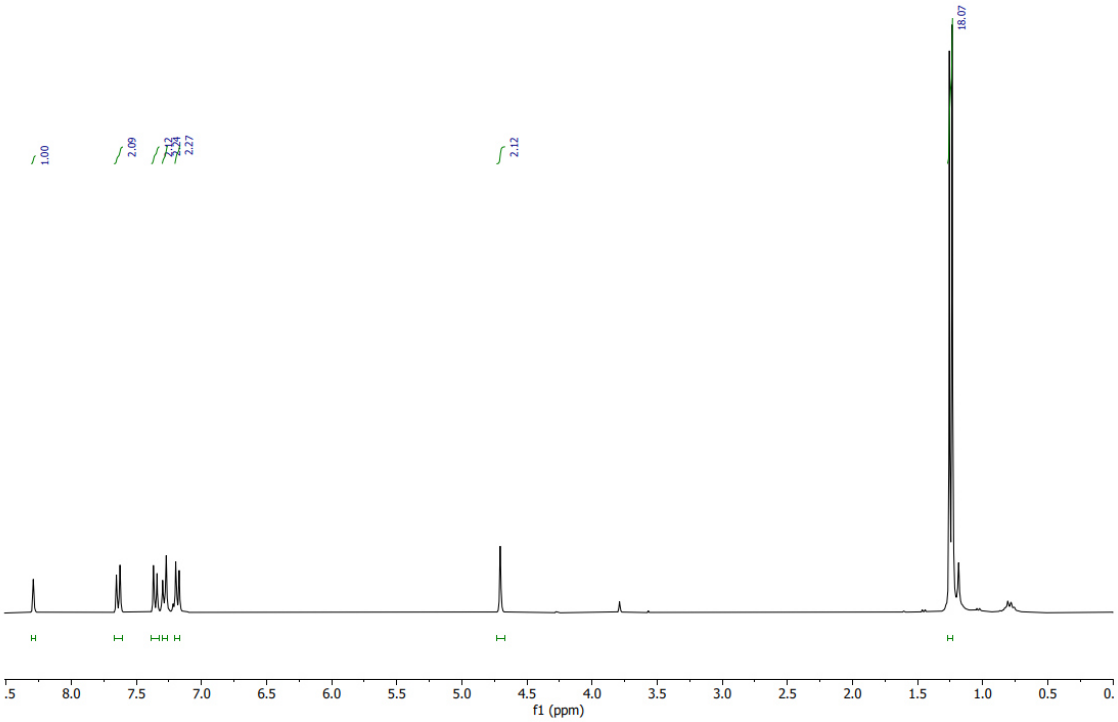

Figure 8.20: ^{1}H-NMR spectrum of N-(4-(tert-butyl)benzyl)-1-(4-(tert-butyl)phenyl)-methanimine. Reproduced with permission from ref[165].

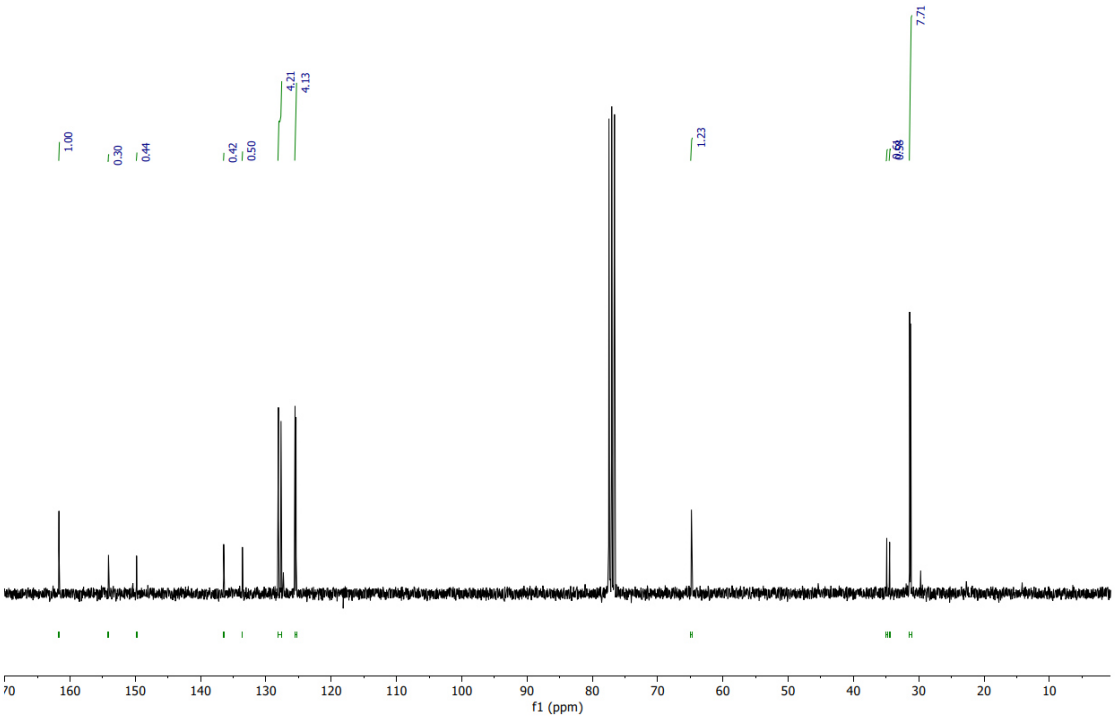

Figure 8.21: ^{13}C-NMR spectrum of N-(4-(tert-butyl)benzyl)-1-(4-(tert-butyl)phenyl)-methanimine. Reproduced with permission from ref[165].

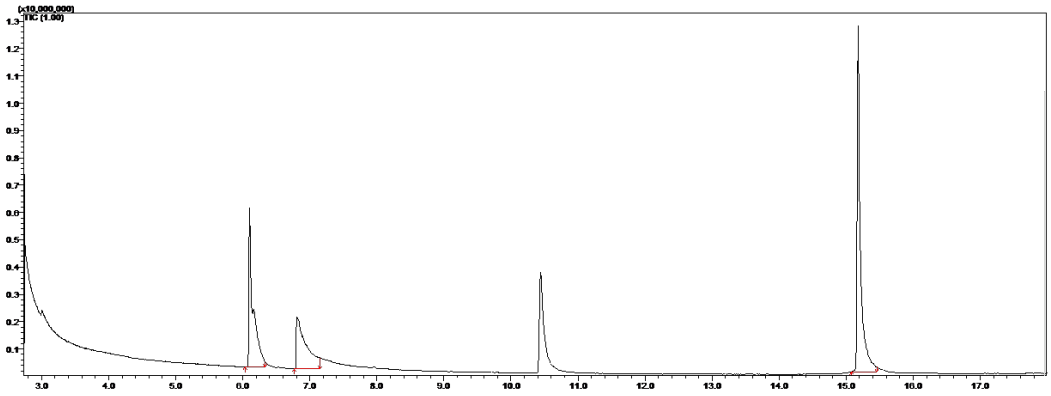

Figure 8.22: GC-MS retention time diagram, showing the formation of N-benzyl-1-phenyl-methanimine and trace amounts of the starting material benzylamine. Reproduced with permission from ref[165].

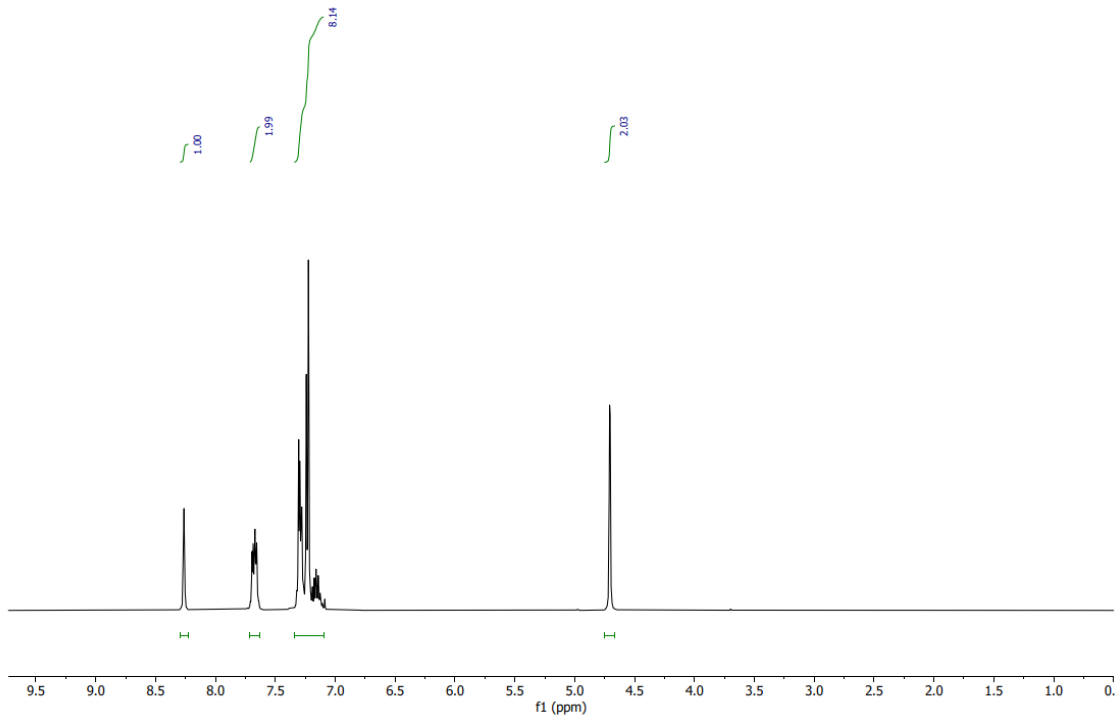

Figure 8.23: ^{1}H-NMR spectrum of N-benzyl-1-phenylmethanimine. Reproduced with permission from ref[165].

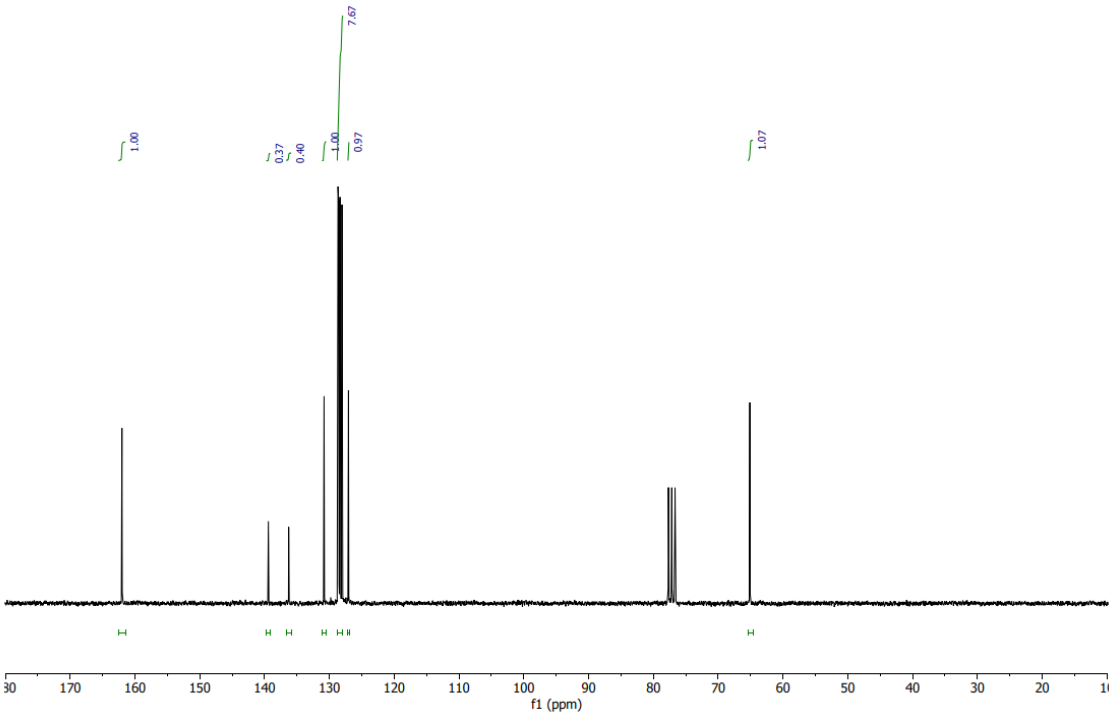

Figure 8.24: ^{13}C-NMR spectrum of N-benzyl-1-phenylmethanimine. Reproduced with permission from ref[165].

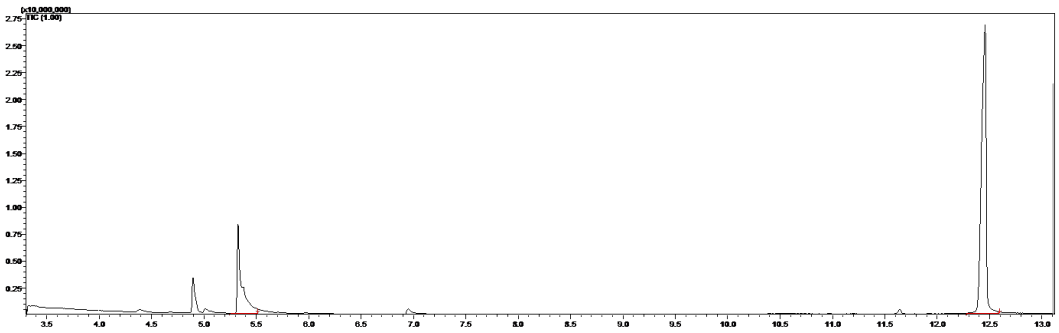

Figure 8.25: GC-MS retention time diagram, showing the formation of (3,4-dimethoxyphenyl)methanamine and trace amounts of the starting material N-(3,4-dimethoxybenzyl)-1-(3,4-dimethoxyphenyl)methanimine. Reproduced with permission from ref[165].

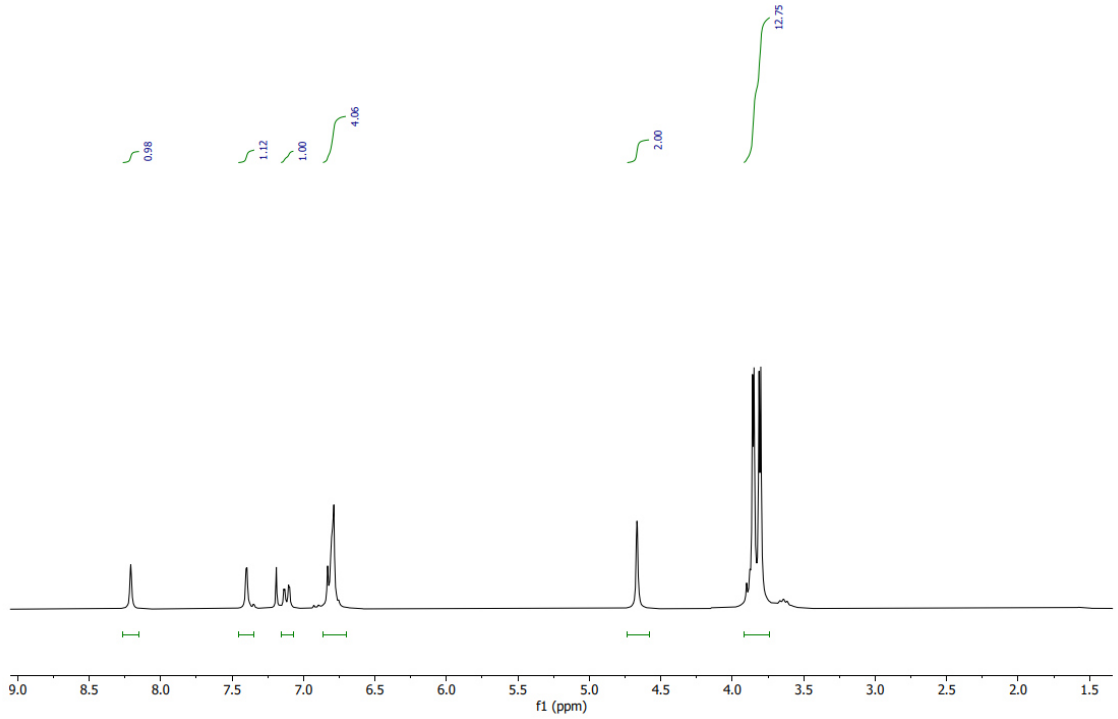

Figure 8.26: ^{1}H-NMR spectrum of (3,4-dimethoxyphenyl)methanimine. Reproduced with permission from ref[165].

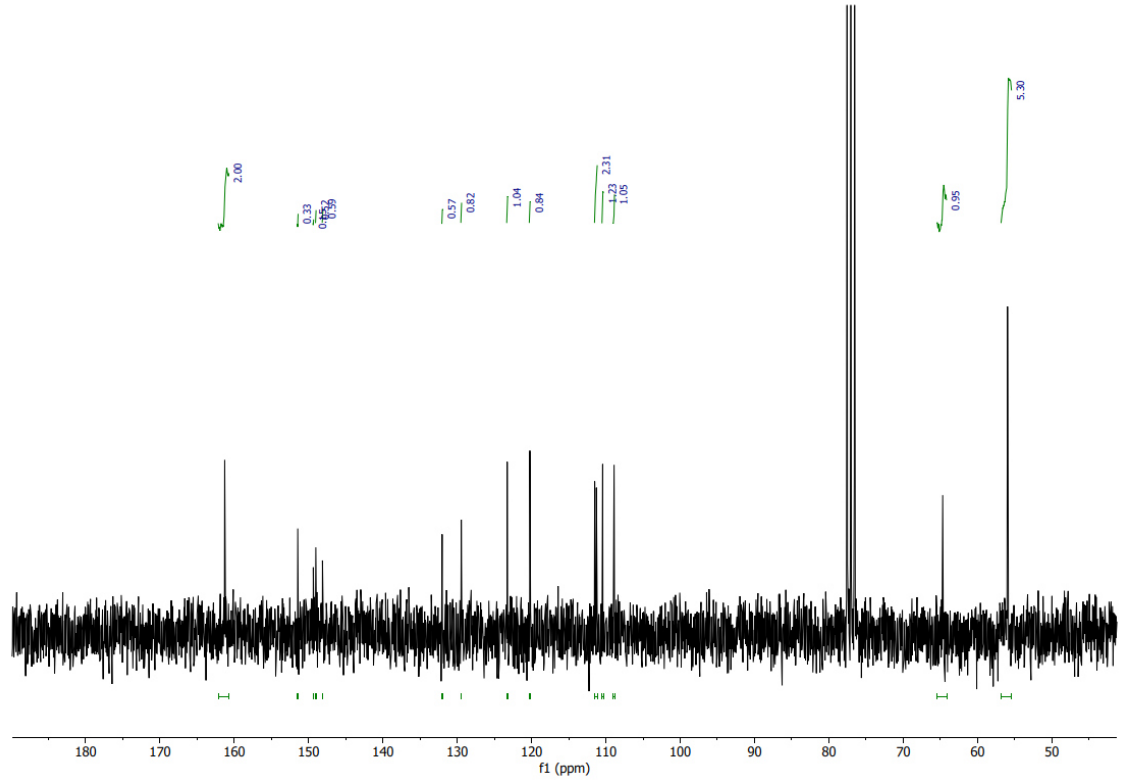

Figure 8.27: ^{13}C-NMR spectrum of (3,4-dimethoxyphenyl)methanimine. Reproduced with permission from ref[165].

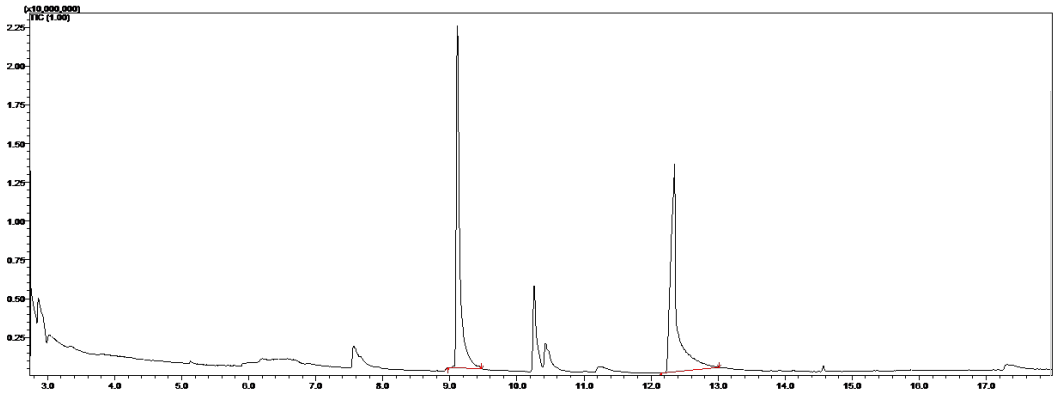

Figure 8.28: GC-MS retention time diagram, showing the formation of [1,1′-biphenyl]-2,2′-dicarbaldehyde and trace amounts of the starting material 2-bromobenzaldehyde. Reproduced with permission from ref[165].

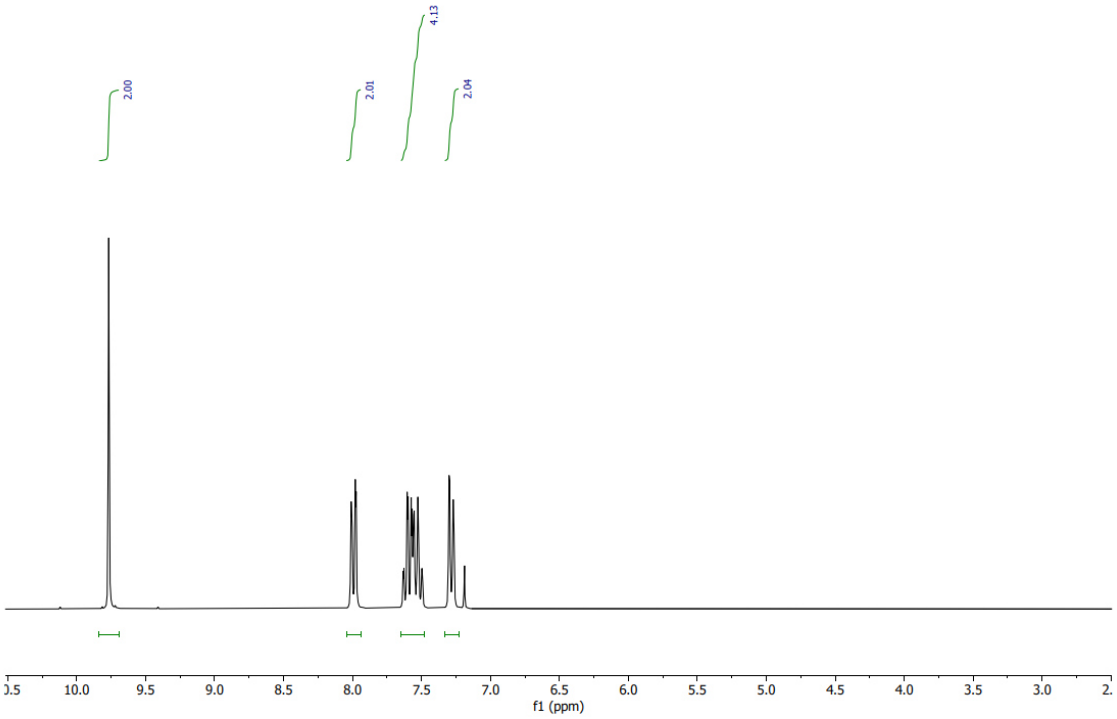

Figure 8.29: ^{1}H-NMR spectrum of [1,1′-biphenyl]-2,2′-dicarbaldehyde. Reproduced with permission from ref[165].

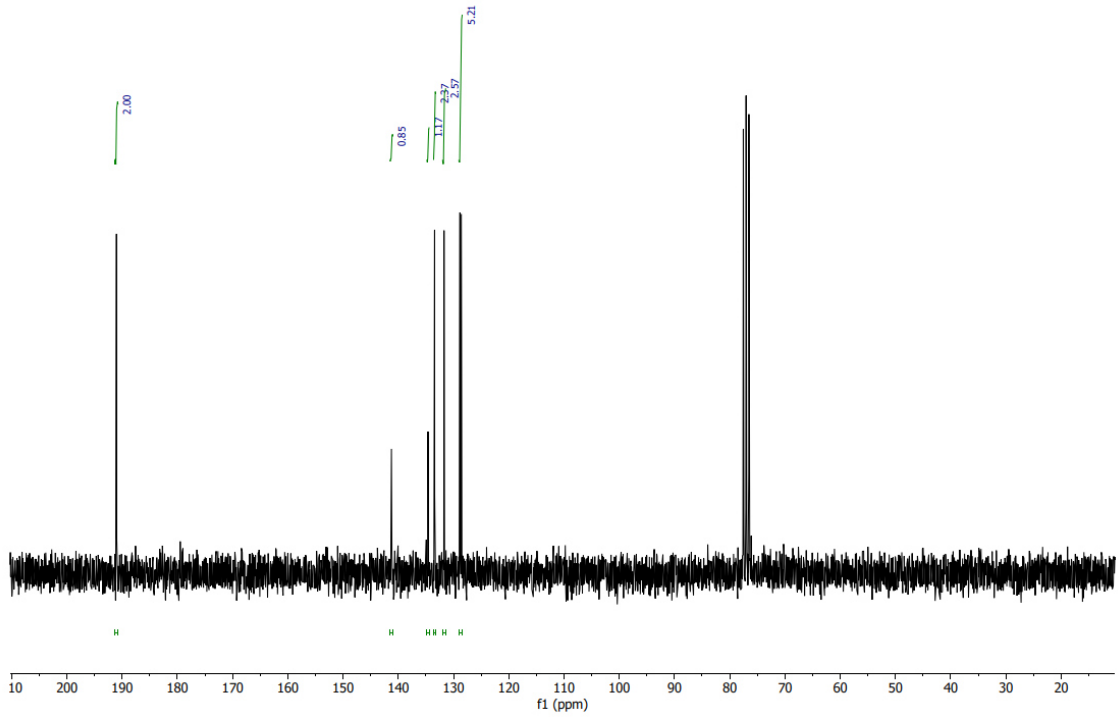

Figure 8.30: ^{13}C-NMR spectrum of [1,1′-biphenyl]-2,2′-dicarbaldehyde. Reproduced with permission from ref[165].

8.1.2 Chapter 5 - Exploiting Binding Interactions to Enhance the Photocatalytic Reactivity

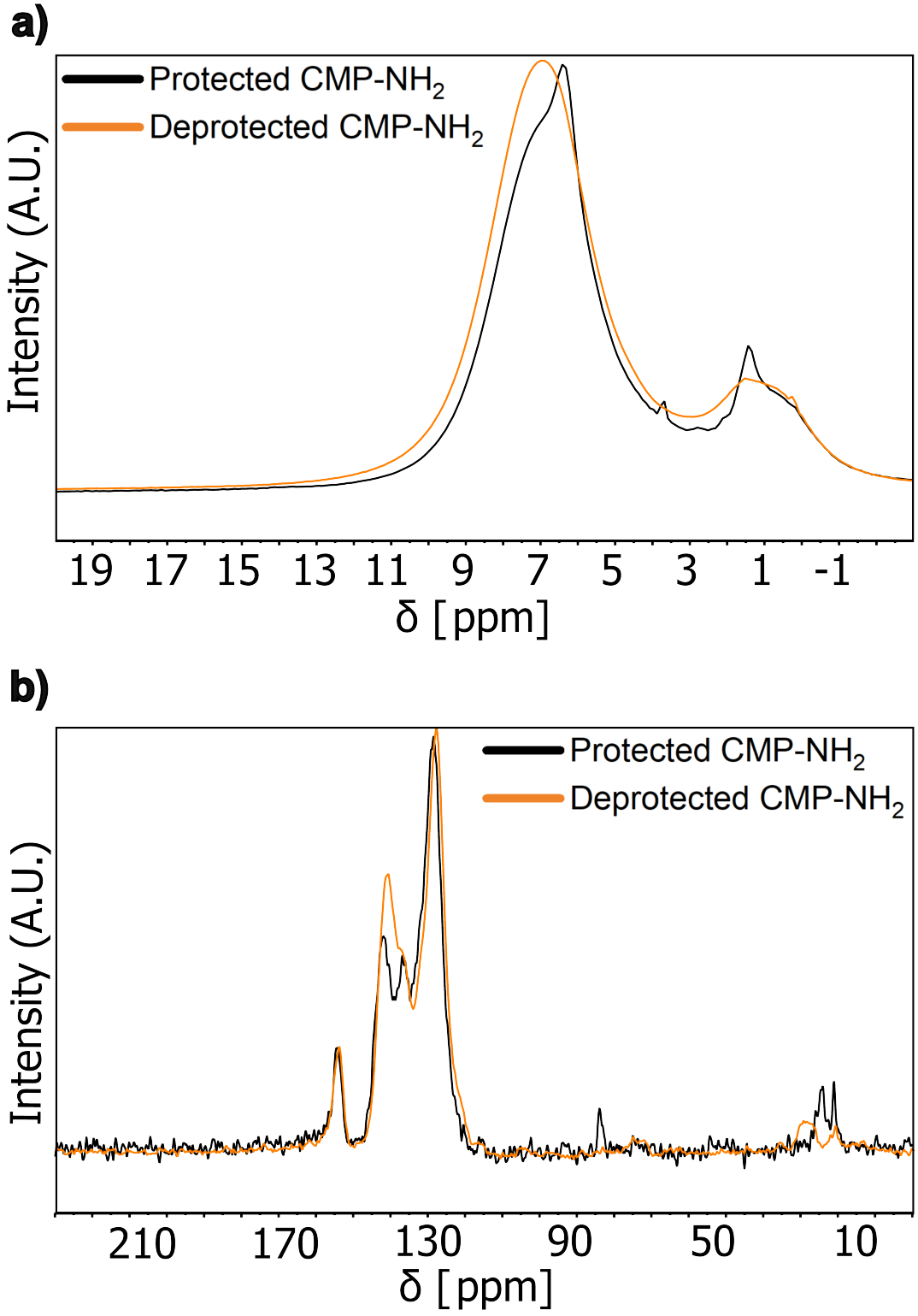

Figure 8.31: Solid-state NMR characterization of CMP-NH_2 before and after Boc-deprotection. (a) ^{1}H-MAS-NMR spectra for both CMP systems. (b) ^{13}C-CP-MAS NMR spectra for both systems.

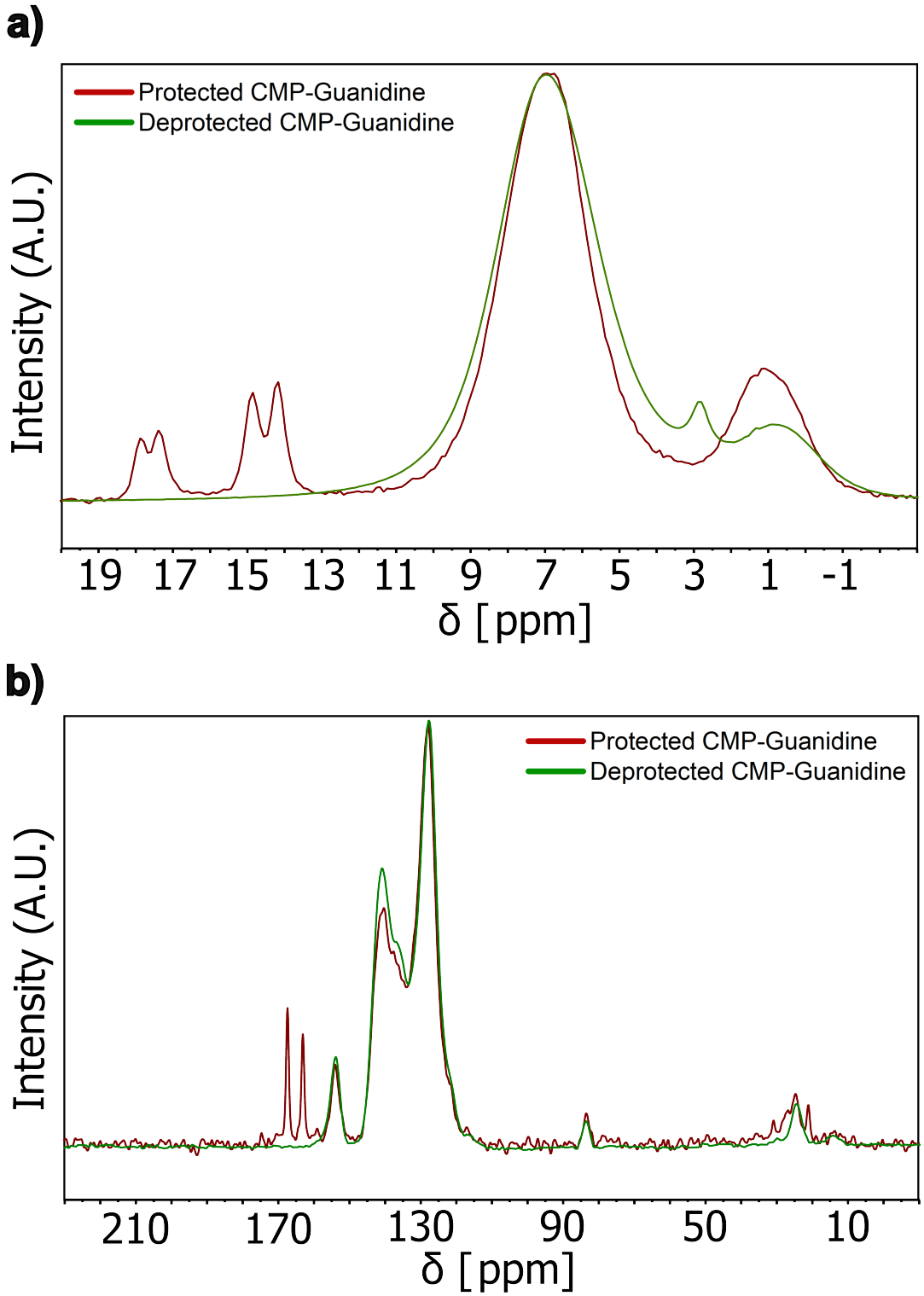

Figure 8.32: Solid-state NMR characterization of CMP-Guanidine before and after Boc-deprotection. (a) ^{1}H-MAS-NMR spectra for both CMP systems. (b) ^{13}C-CP-MAS NMR spectra for both systems.

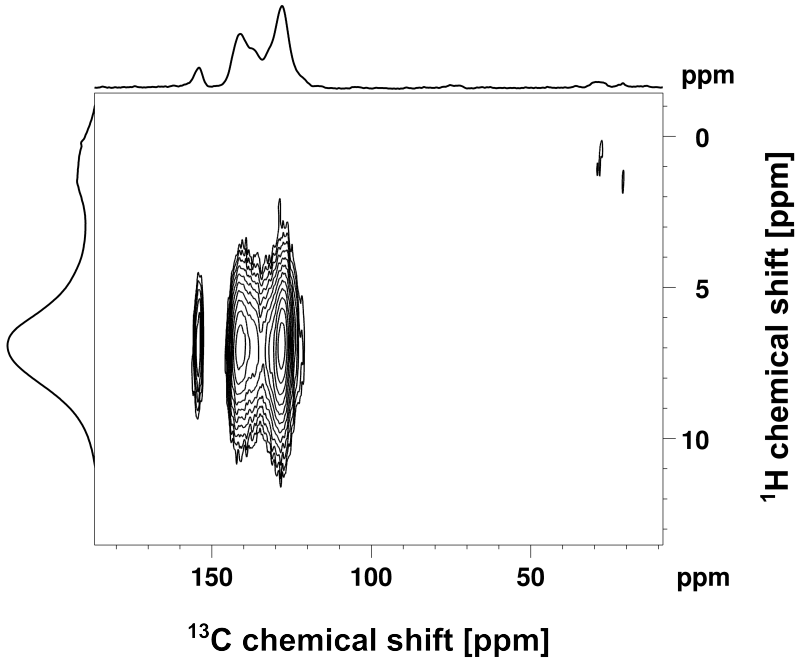

Figure 8.33: 2D-NMR ^{13}C-^{1}H correlation spectroscopy for the deprotected CMP-NH_2.

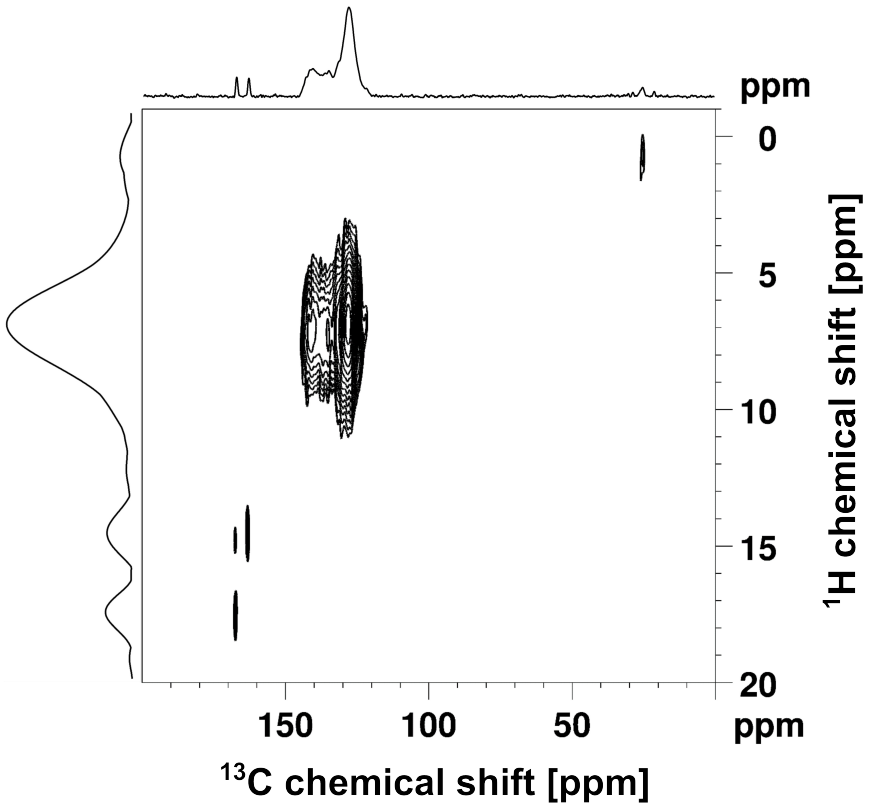

Figure 8.34: 2D-NMR ^{13}C-^{1}H correlation spectroscopy for the protected CMP-Guanidine.

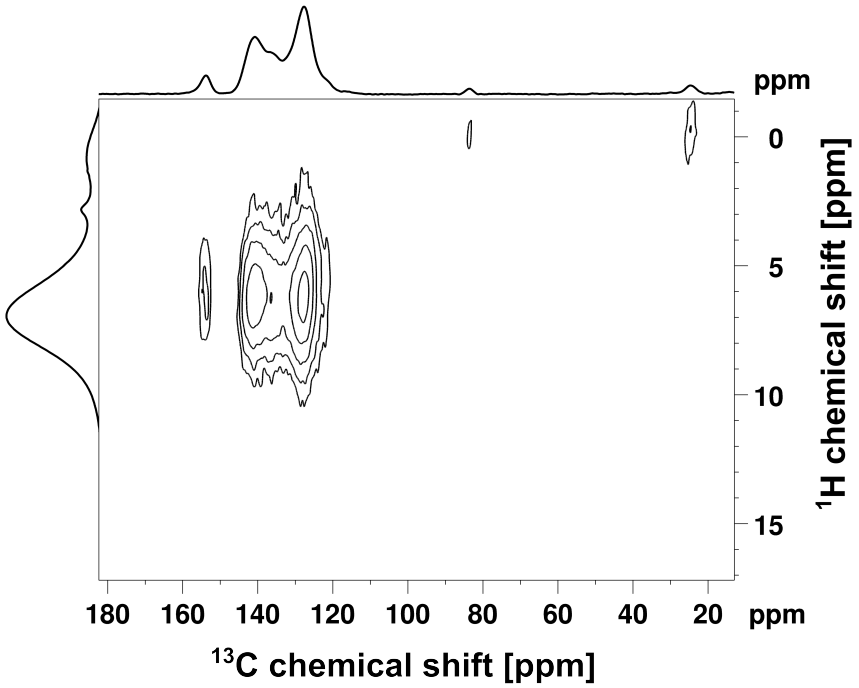

Figure 8.35: 2D-NMR ^{13}C-^{1}H correlation spectroscopy for the deprotected CMP-Guanidine.

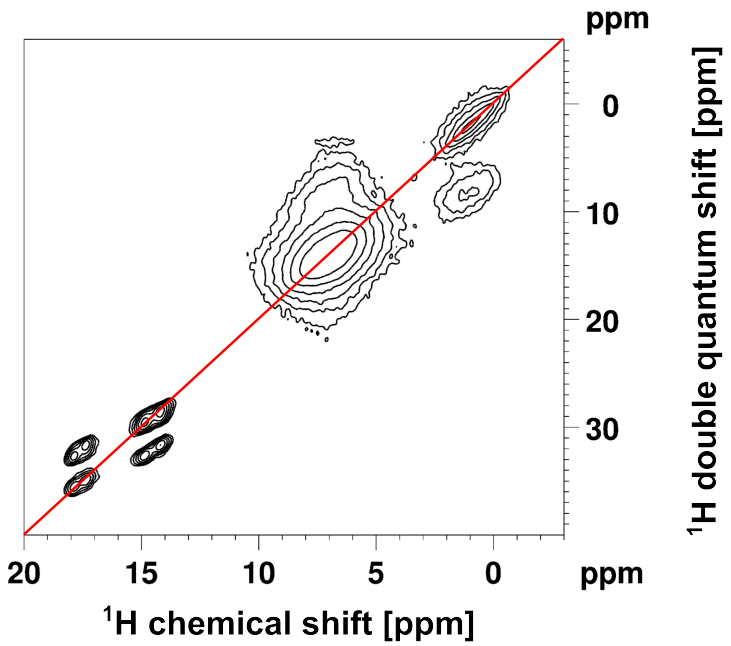

Figure 8.36: 2D-NMR double quantum ^{1}H-^{1}H correlation spectroscopy for the protected CMP-Guanidine.

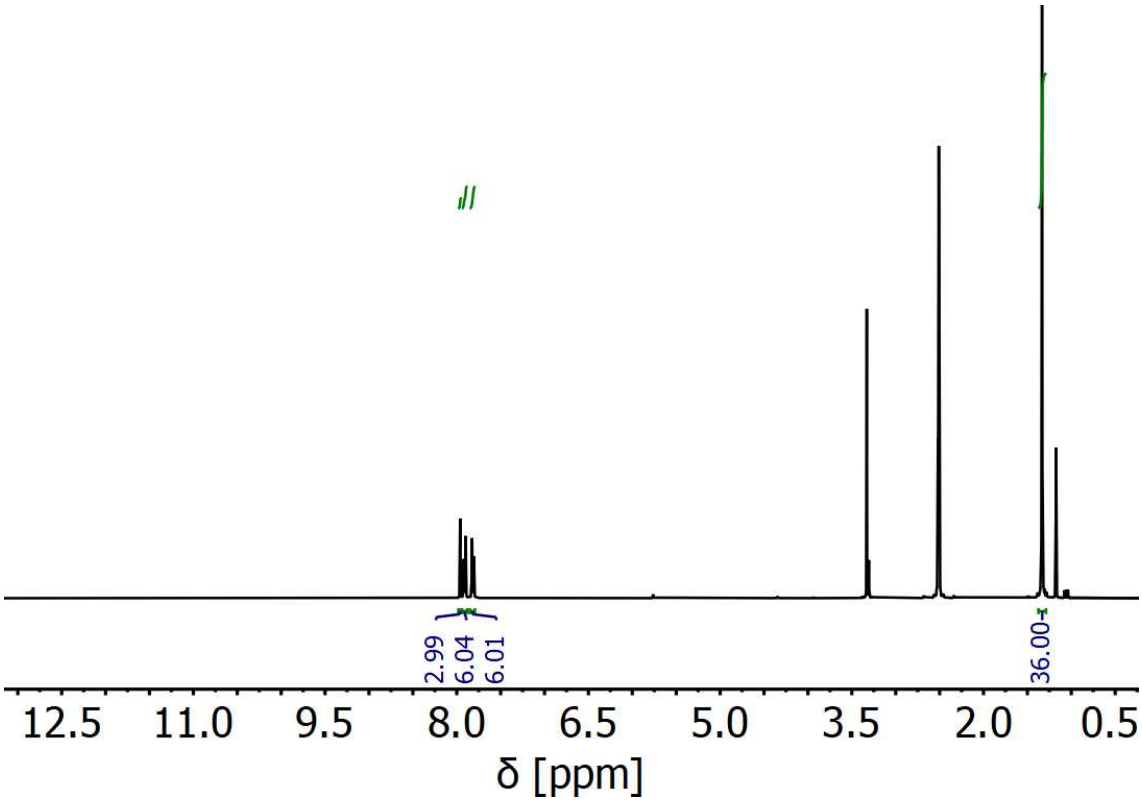

Figure 8.37: ^{1}H spectrum of 2,2′-(5′-(4-(4,4,5,5-tetramethyl-1,3,2-dioxaborolan-2-yl)phenyl)-[1,1′:3′,1″-terphenyl]-4,4″-diyl)bis(4,4,5,5-tetramethyl-1,3,2-dioxaborolane).

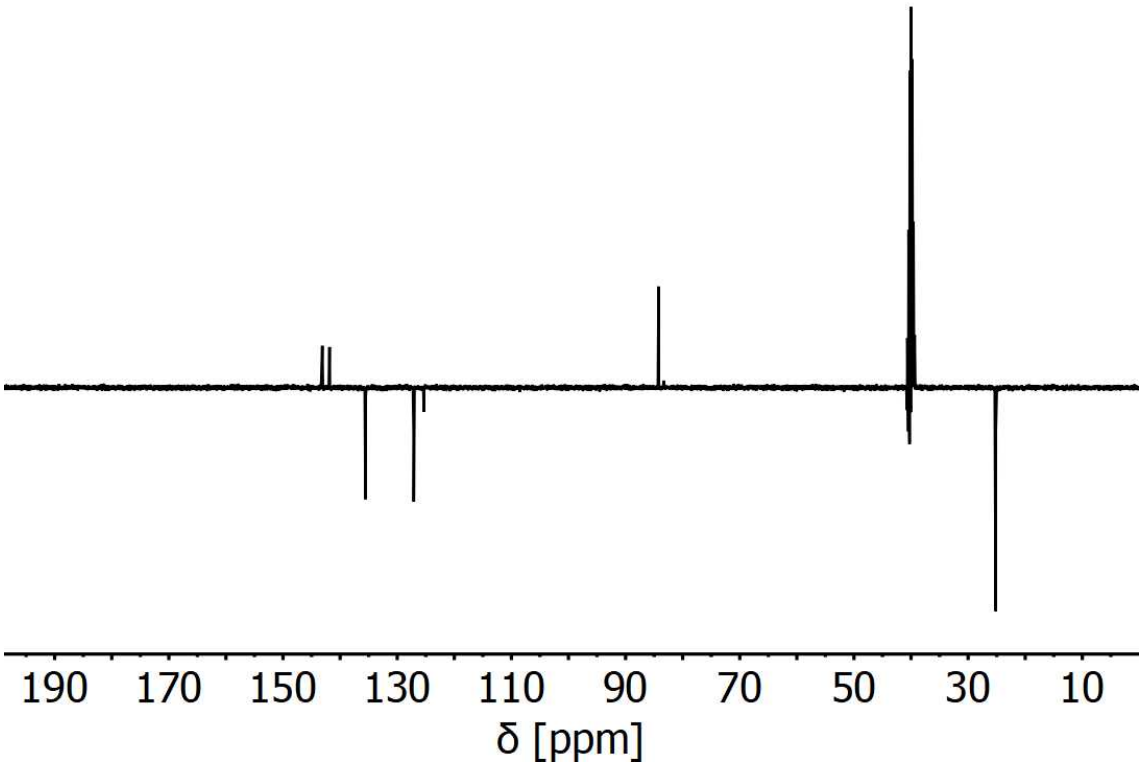

Figure 8.38: ^{13}C spectrum of 2,2′-(5′-(4-(4,4,5,5-tetramethyl-1,3,2-dioxaborolan-2-yl)-phenyl)-[1,1′:3′,1″-terphenyl]-4,4″-diyl)bis(4,4,5,5-tetramethyl-1,3,2-dioxaborolane).

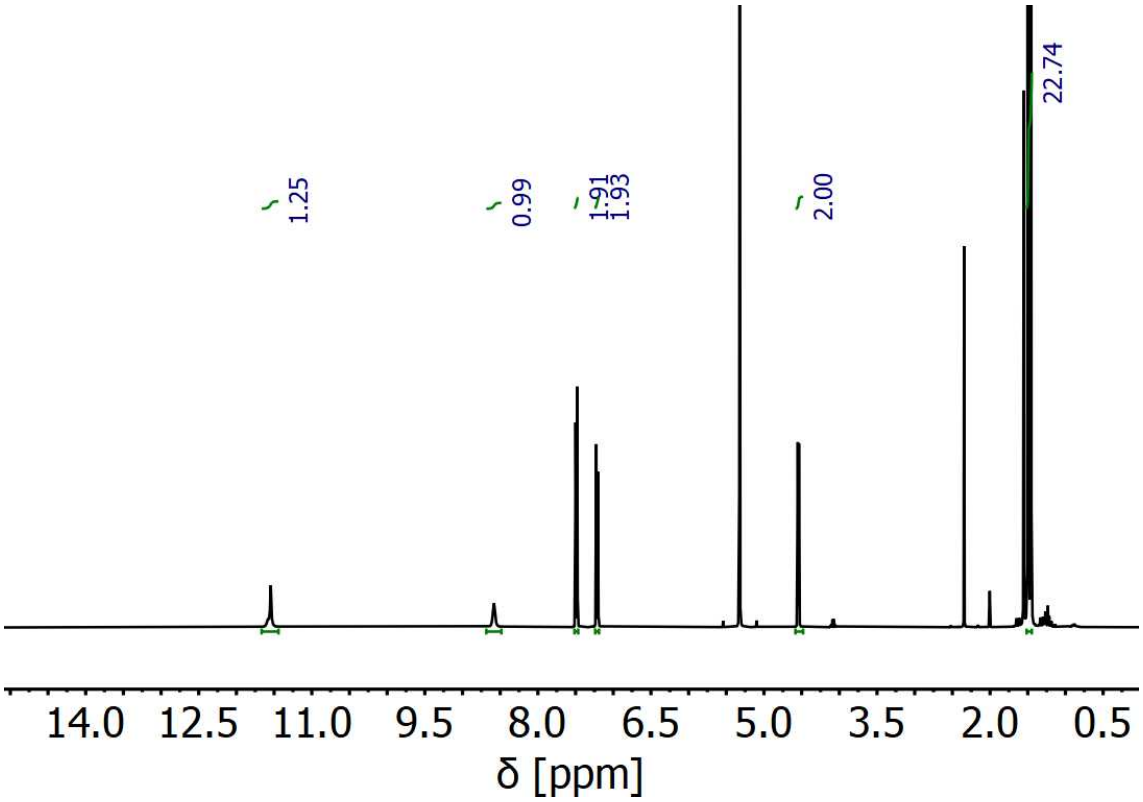

Figure 8.39: ^{1}H spectrum of guanidylated monomeric model compound 4-bromobenzylamine.

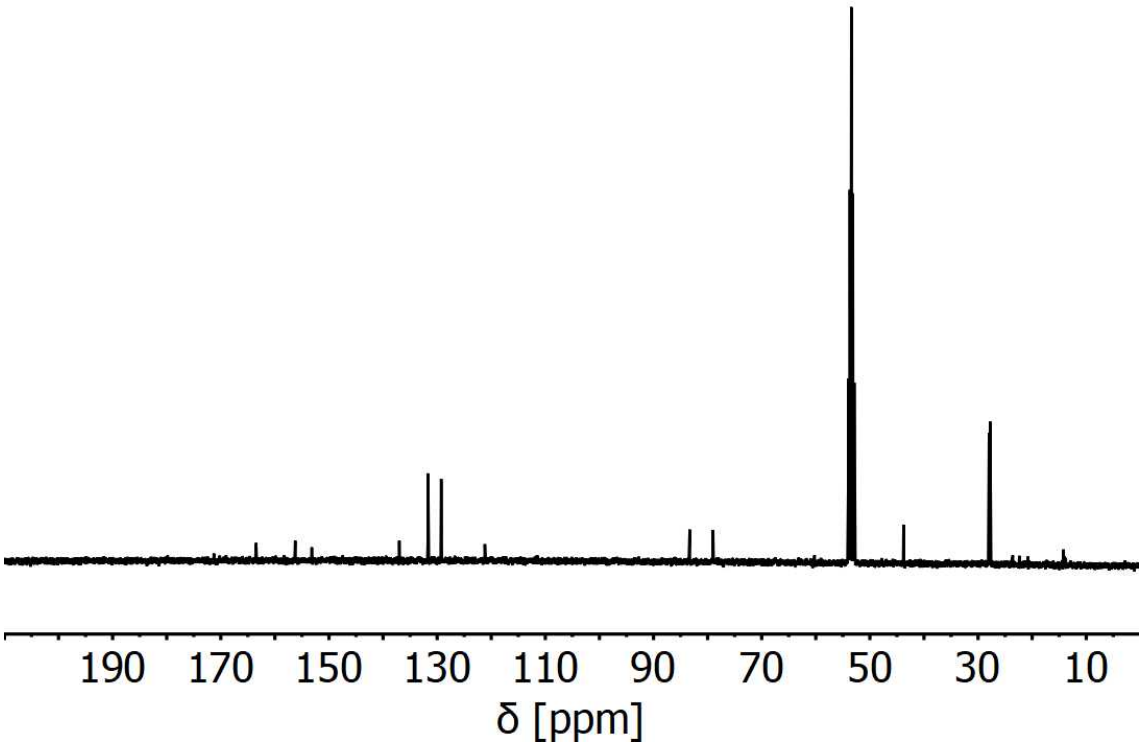

Figure 8.40: ^{13}C spectrum of guanidylated monomeric model compound 4-bromobenzylamine.

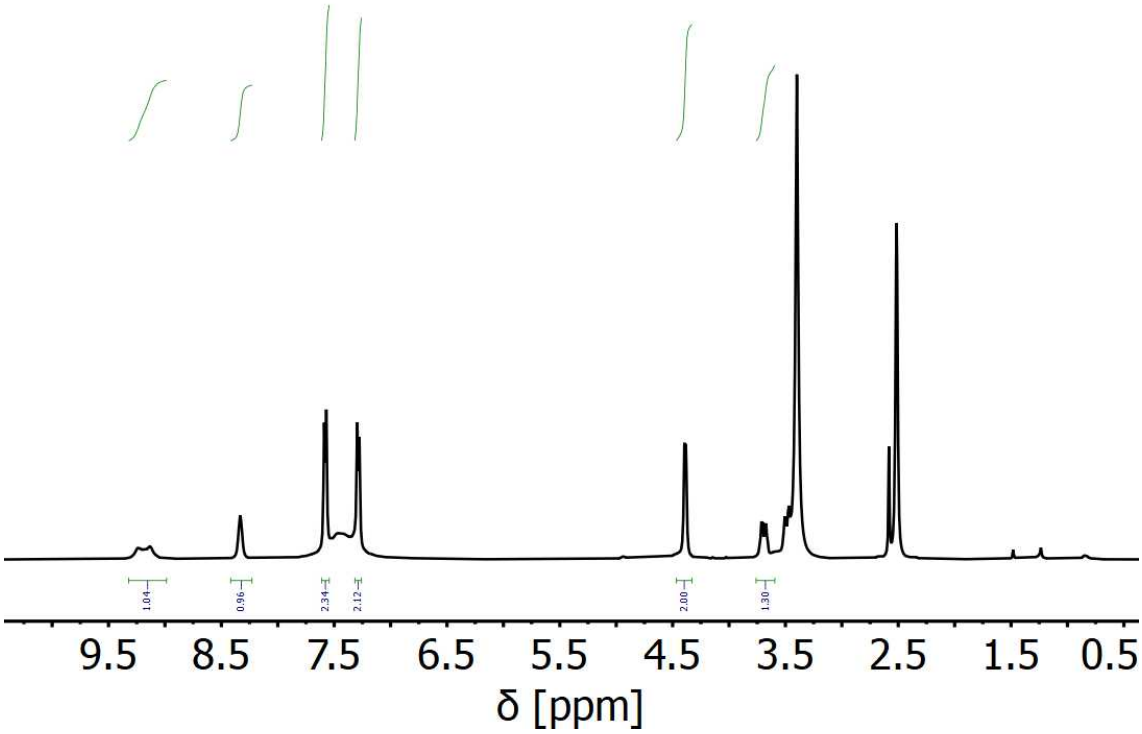

Figure 8.41: ^{1}H spectrum of the deprotected, guanidylated monomeric model compound 4-bromobenzylamine.

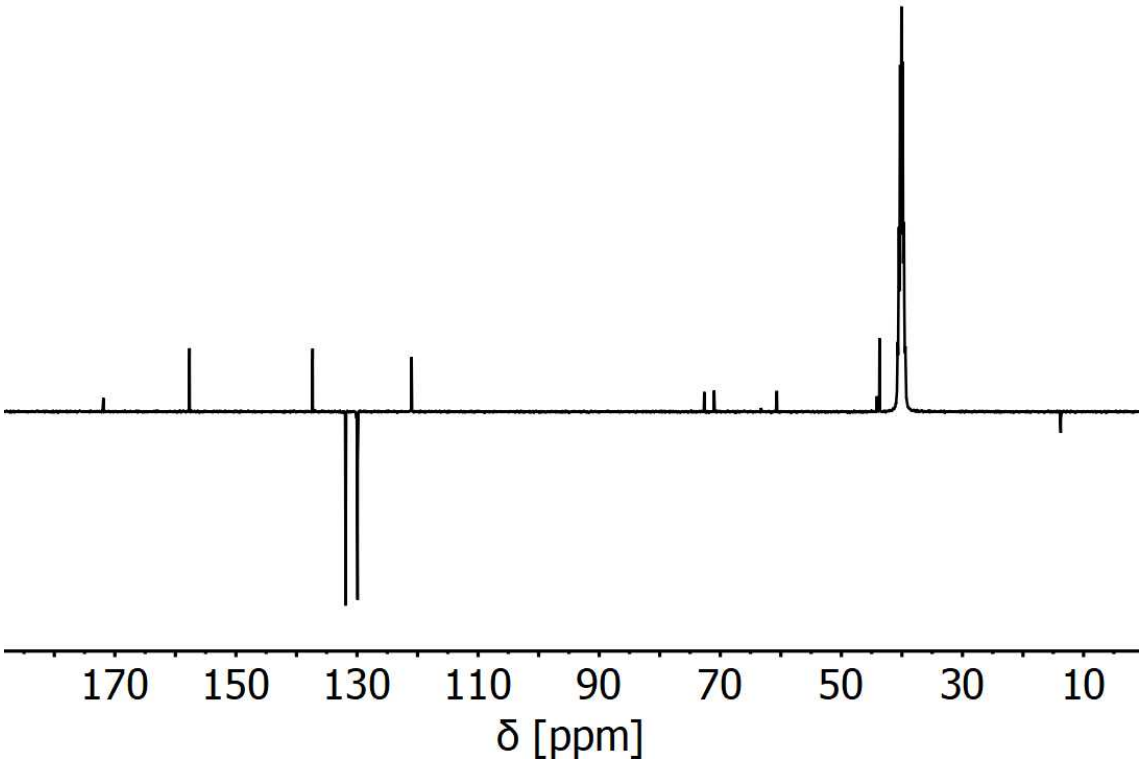

Figure 8.42: ^{13}C spectrum of the deprotected, guanidylated monomeric model compound 4-bromobenzylamine.

8.1.3 Chapter 6 - Photocatalysis in Artificial Cell-like Systems

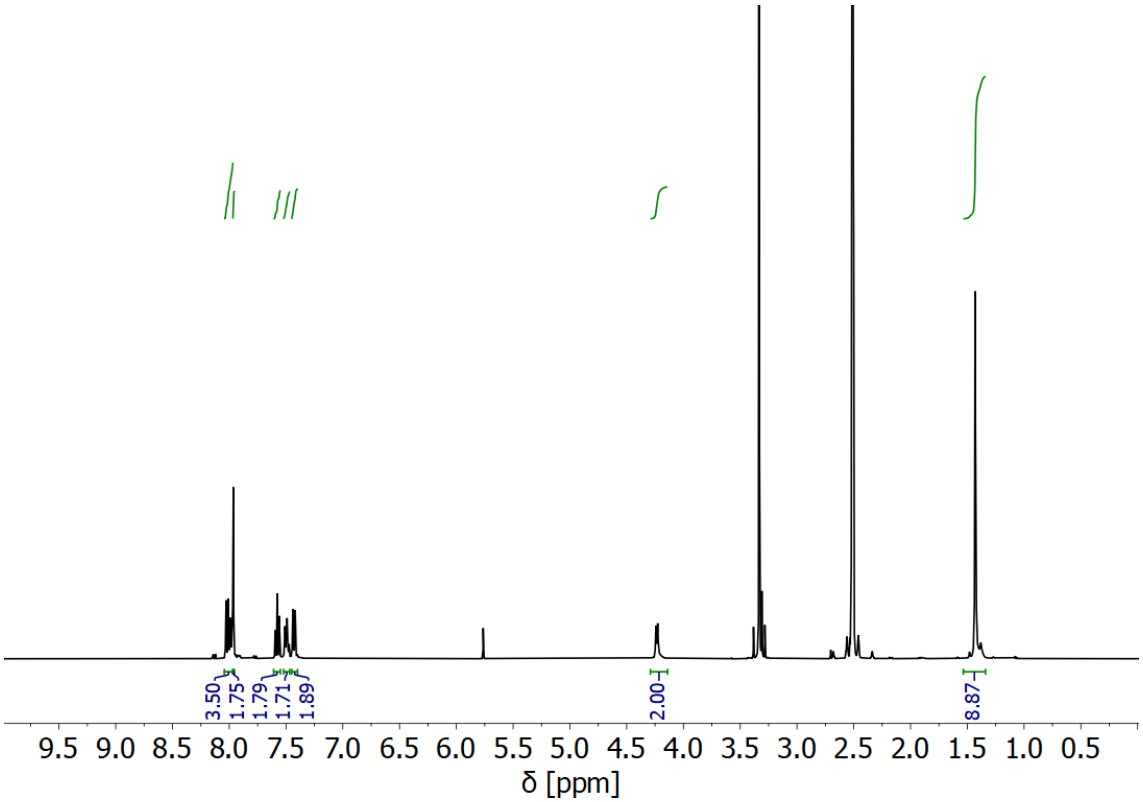

Figure 8.43: ^{1}H spectrum of N-Boc protected DPBT.

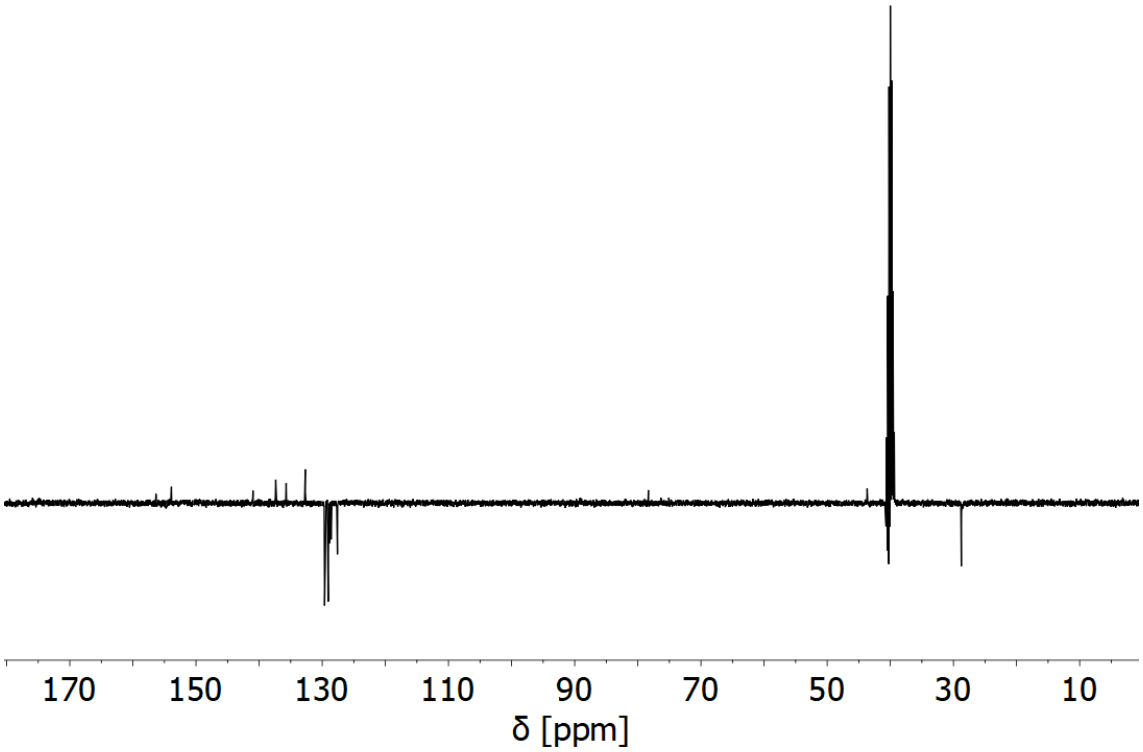

Figure 8.44: ^{13}C spectrum of N-Boc protected DPBT.

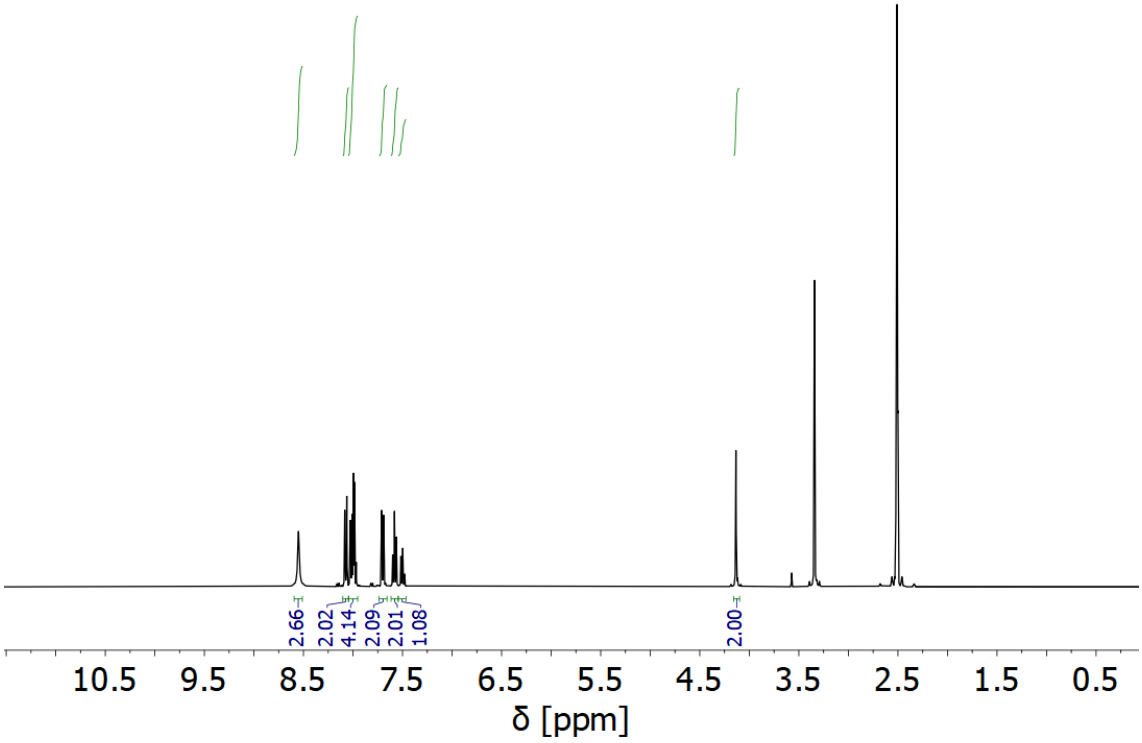

Figure 8.45: ^{1}H spectrum of the deprotected DPBT.

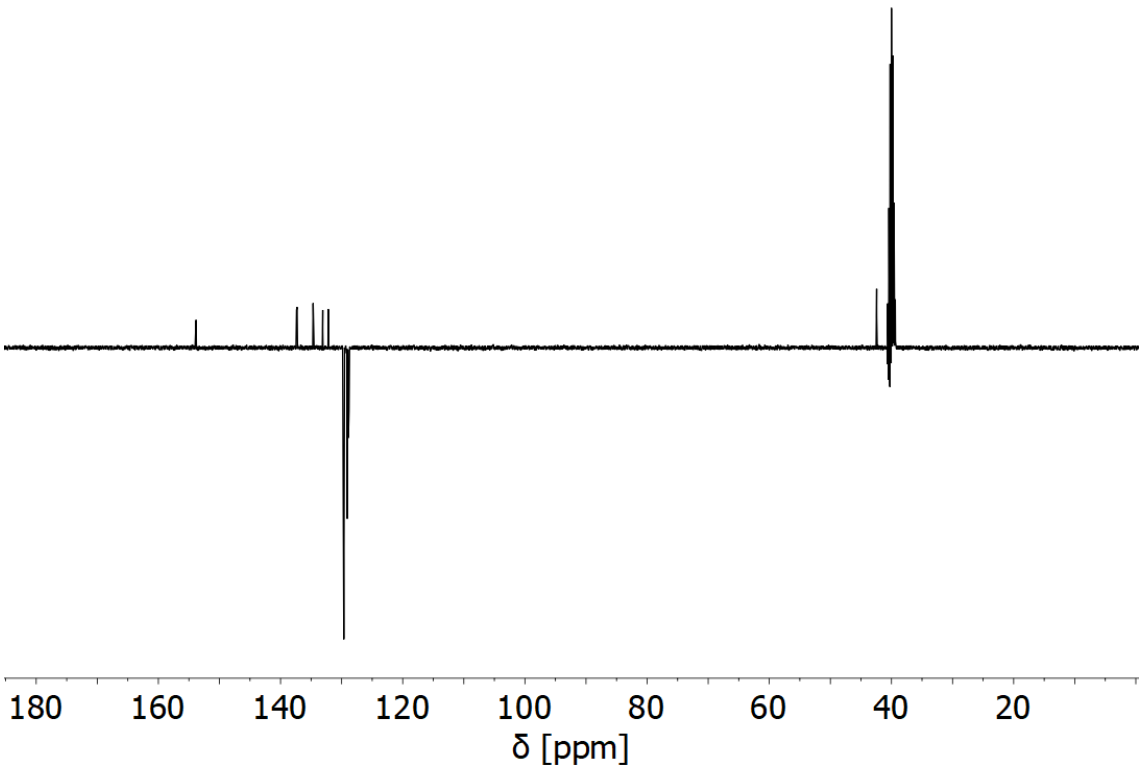

Figure 8.46: ^{13}C spectrum of the deprotected DPBT.

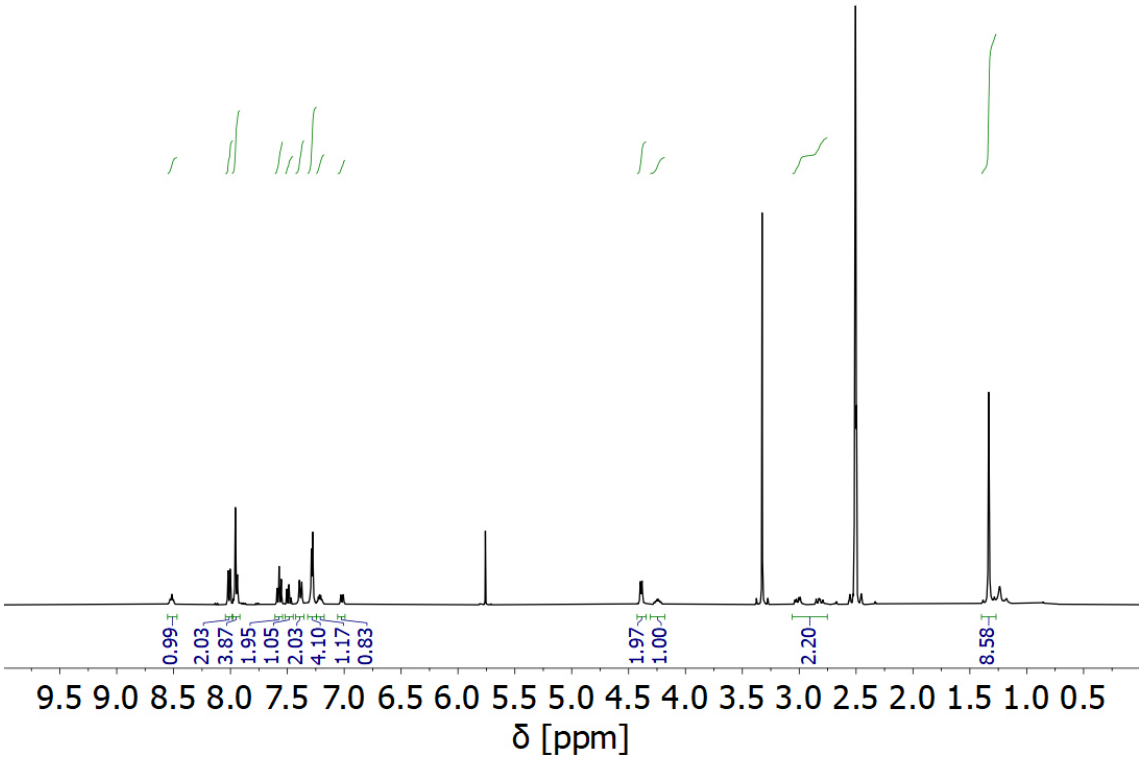

Figure 8.47: ^{1}H spectrum of the N-Boc protected DPBT-functionalized phenyalanine.

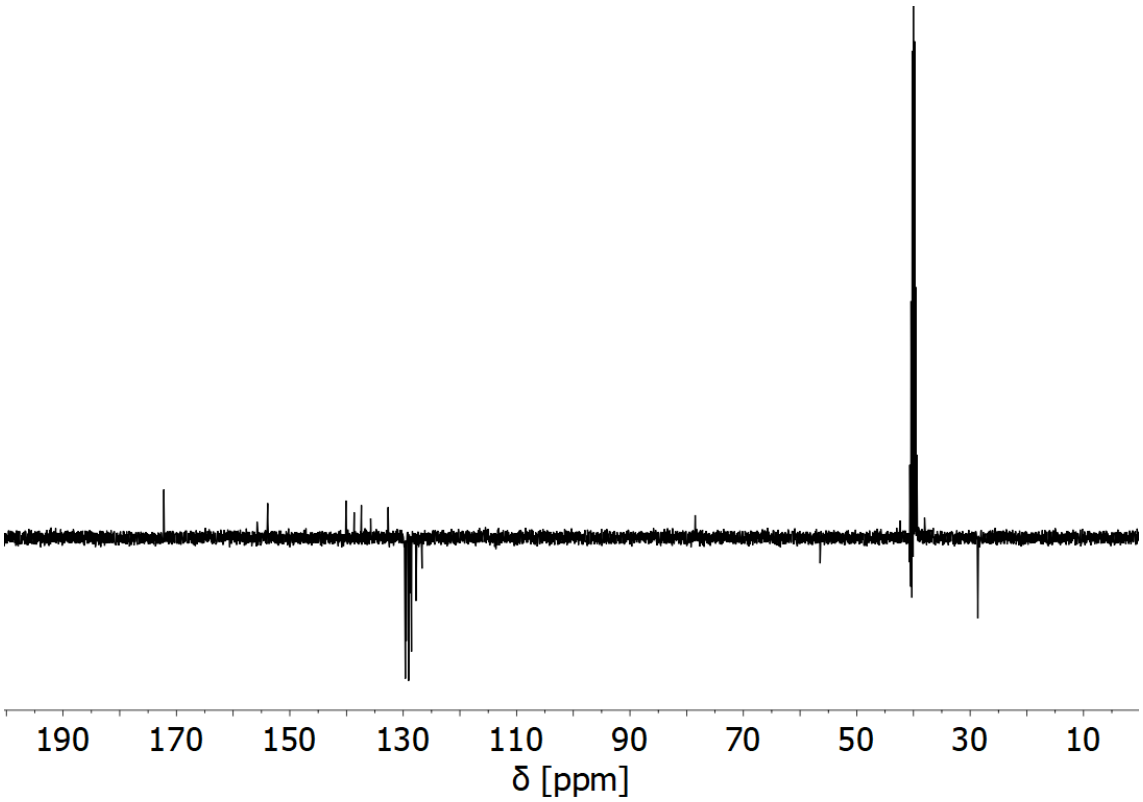

Figure 8.48: ^{13}C spectrum of the N-Boc protected DPBT-functionalized phenyalanine.

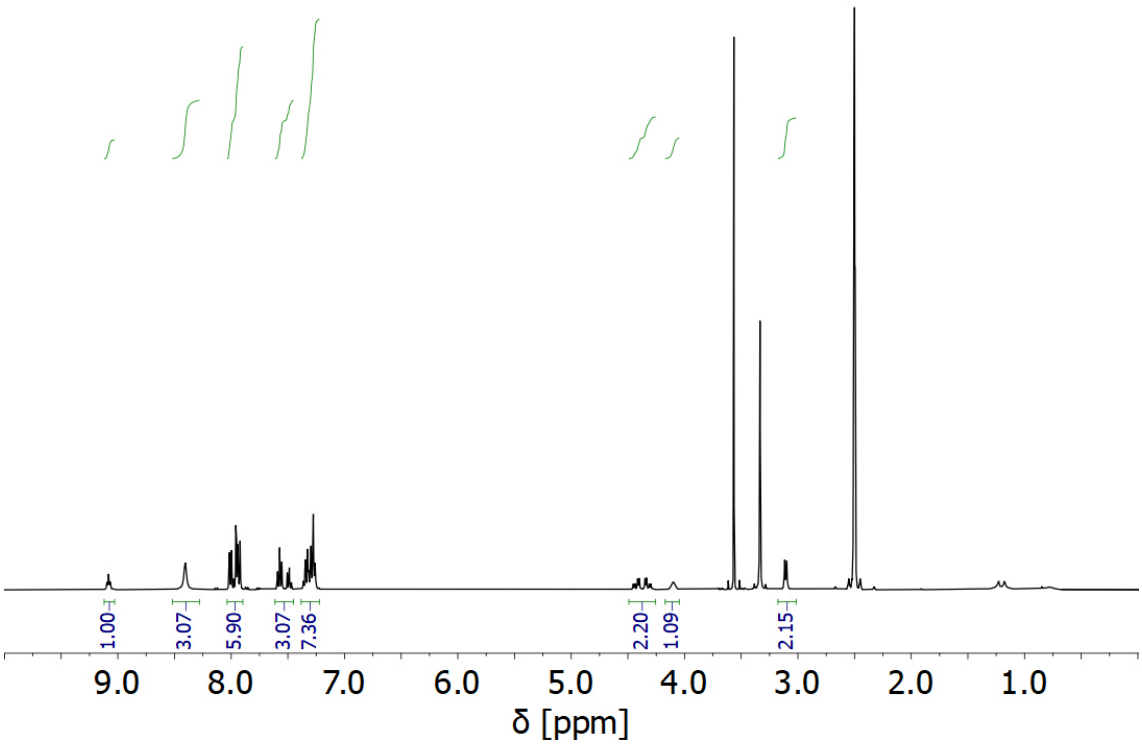

Figure 8.49: ^{1}H spectrum of the deprotected DPBT-functionalized phenyalanine.

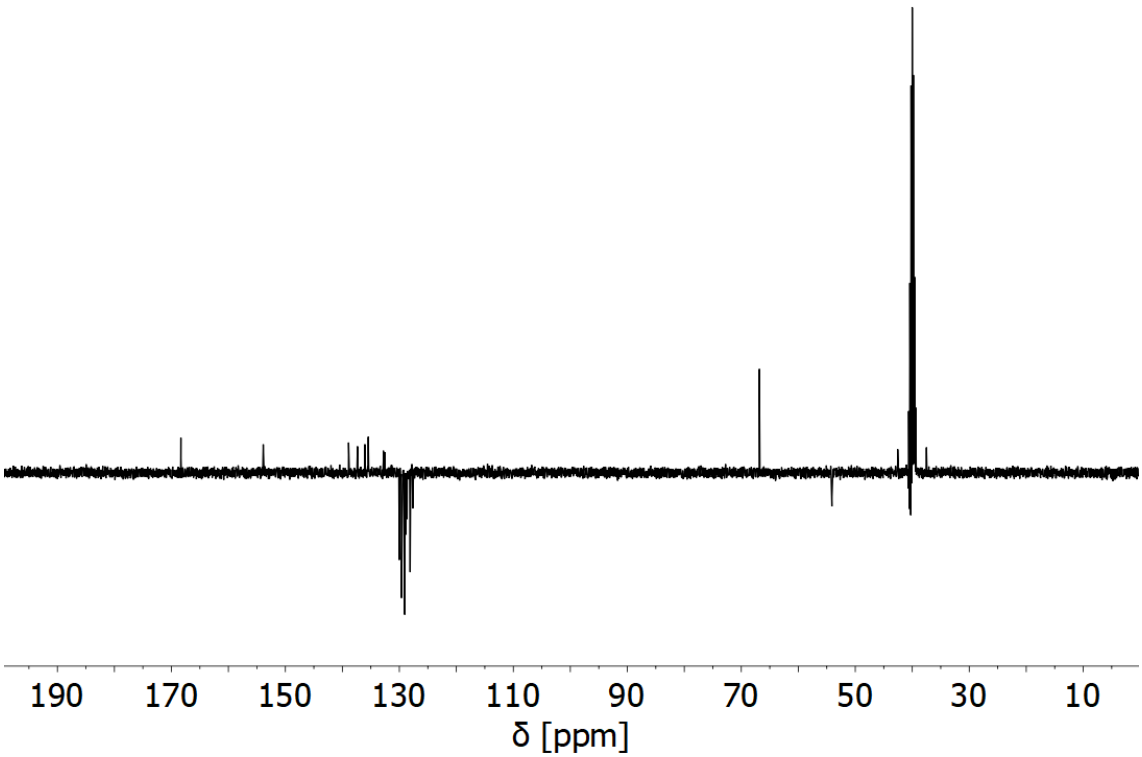

Figure 8.50: ^{13}C spectrum of the deprotected DPBT-functionalized phenyalanine.

Bibliography

[1] M. W. Roberts, *Catal. Lett.* **2000**, *67*, 1–4.

[2] W. Ostwald, *Z. Elektrochem.* **1901**, *7*, 995–1006.

[3] Y. Xia, C. T. Campbell, B. Roldan Cuenya, M. Mavrikakis, *Chem. Rev.* **2021**, *121*, 563–566.

[4] A. Eibner, *Chem. Ztg.* **1911**, *35*, 753–775.

[5] A. Fujishima, K. Honda, *Nature* **1972**, *238*, 37–38.

[6] T. Inoue, A. Fujishima, S. Konishi, K. Honda, *Nature* **1979**, *277*, 637–638.

[7] K. Kalyanasundaram, *Coord. Chem. Rev.* **1982**, *46*, 159–244.

[8] A. Vega-Penaloza, J. Mateos, X. Companyo, M. Escudero-Casao, L. Dell'Amico, *Angew. Chem. Int. Ed.* **2021**, *60*, 1082–1097.

[9] D. A. Nicewicz, T. M. Nguyen, *ACS Catal.* **2013**, *4*, 355–360.

[10] M. Melchionna, P. Fornasiero, *ACS Catal.* **2020**, *10*, 5493–5501.

[11] T. Noël, E. Zysman-Colman, *Chem Catal.* **2022**, *2*, 468–476.

[12] B. König, *Eur. J. Org. Chem.* **2017**, *2017*, 1979–1981.

[13] G. Ciamician, *Science* **1912**, *36*, 385–394.

[14] J. M. Coronado in *Design of Advanced Photocatalytic Materials for Energy and Environmental Applications*, Springer London, London, **2013**, pp. 5–33.

[15] S. Dutta, J. E. Erchinger, F. Strieth-Kalthoff, R. Kleinmans, F. Glorius, *Chem. Soc. Rev.* **2024**, *53*, 1068–1089.

[16] D. Rehm, A. Weller, *Isr. J. Chem.* **1970**, *8*, 259–271.

[17] R. A. Marcus, N. Sutin, *Biochim. Biophys. Acta* **1985**, *811*, 265–322.

[18] C. P. Hsu, *Acc. Chem. Res.* **2009**, *42*, 509–518.

[19] L. Capaldo, D. Ravelli, M. Fagnoni, *Chem. Rev.* **2022**, *122*, 1875–1924.

[20] E. C. Gentry, R. R. Knowles, *Acc. Chem. Res.* **2016**, *49*, 1546–1556.

[21] W. Lai, C. Li, H. Chen, S. Shaik, *Angew. Chem. Int. Ed.* **2012**, *51*, 5556–5578.

[22] B. E. Snyder, P. Vanelderen, M. L. Bols, S. D. Hallaert, L. H. Bottger, L. Ungur, K. Pierloot, R. A. Schoonheydt, B. F. Sels, E. I. Solomon, *Nature* **2016**, *536*, 317–321.

[23] T. S. Teets, Y. Wu, D. Kim, *Synlett* **2021**, *33*, 1154–1179.

[24] D. Nicewicz, H. Roth, N. Romero, *Synlett* **2015**, *27*, 714–723.

[25] N. A. Romero, D. A. Nicewicz, *Chem. Rev.* **2016**, *116*, 10075–10166.

[26] A. Savateev, I. Ghosh, B. Konig, M. Antonietti, *Angew. Chem. Int. Ed.* **2018**, *57*, 15936–15947.

[27] F. Strieth-Kalthoff, F. Glorius, *Chem* **2020**, *6*, 1888–1903.

[28] A. Kirch, M. Gmelch, S. Reineke, *J. Phys. Chem. Lett.* **2019**, *10*, 310–315.

[29] B. Sk, S. Hirata, *Chem. Commun.* **2023**, *59*, 6643–6659.

[30] B. R. Masters, *Eur. Phys. J. H* **2014**, *39*, 87–139.

[31] F. Strieth-Kalthoff, M. J. James, M. Teders, L. Pitzer, F. Glorius, *Chem. Soc. Rev.* **2018**, *47*, 7190–7202.

[32] D. L. Dexter, *J. Chem. Phys.* **1953**, *21*, 836–850.

[33] H. E. Bonfield, T. Knauber, F. Levesque, E. G. Moschetta, F. Susanne, L. J. Edwards, *Nat. Commun.* **2020**, *11*, 804.

[34] D. M. Schultz, T. P. Yoon, *Science* **2014**, *343*, 1239176.

[35] M. H. Shaw, J. Twilton, D. W. MacMillan, *J. Org. Chem.* **2016**, *81*, 6898–6926.

[36] Q. Zhang, W. Hu, H. Sirringhaus, K. Mullen, *Adv. Mater.* **2022**, *34*, 2108701.

[37] Z. Qian, K. A. I. Zhang, *Sol. RRL* **2020**, *5*, 2000489.

[38] J. Byun, K. A. I. Zhang, *Mater. Horiz.* **2020**, *7*, 15–31.

[39] S. Yanagida, A. Kabumoto, K. Mizumoto, C. Pac, K. Yoshino, *J. Chem. Soc., Chem. Commun.* **1985**, 474–475.

[40] R. S. Sprick, B. Bonillo, R. Clowes, P. Guiglion, N. J. Brownbill, B. J. Slater, F. Blanc, M. A. Zwijnenburg, D. J. Adams, A. I. Cooper, *Angew. Chem. Int. Ed.* **2016**, *55*, 1792–1796.

[41] L. Wang, R. Fernández-Terán, L. Zhang, D. L. A. Fernandes, L. Tian, H. Chen, H. Tian, *Angew. Chem. Int. Ed.* **2016**, *55*, 12306–12310.

[42] J. Kosco, M. Bidwell, H. Cha, T. Martin, C. T. Howells, M. Sachs, D. H. Anjum, S. Gonzalez Lopez, L. Zou, A. Wadsworth, W. Zhang, L. Zhang, J. Tellam, R. Sougrat, F. Laquai, D. M. DeLongchamp, J. R. Durrant, I. McCulloch, *Nat. Mater.* **2020**, *19*, 559–565.

[43] J. Kosco, F. Moruzzi, B. Willner, I. McCulloch, *Adv. Energy Mater.* **2020**, *10*, 2001935.

[44] Y. Markushyna, C. A. Smith, A. Savateev, *Eur. J. Org. Chem.* **2019**, *2020*, 1294–1309.

[45] I. Ghosh, J. Khamrai, A. Savateev, N. Shlapakov, M. Antonietti, B. Konig, *Science* **2019**, *365*, 360–366.

[46] S. Bi, Z.-A. Lan, S. Paasch, W. Zhang, Y. He, C. Zhang, F. Liu, D. Wu, X. Zhuang, E. Brunner, X. Wang, F. Zhang, *Adv. Funct. Mater.* **2017**, *27*, 1703146.

[47] K. Schwinghammer, S. Hug, M. B. Mesch, J. Senker, B. V. Lotsch, *Energy Environ. Sci.* **2015**, *8*, 3345–3353.

[48] L. Wang, Y. Wan, Y. Ding, S. Wu, Y. Zhang, X. Zhang, G. Zhang, Y. Xiong, X. Wu, J. Yang, H. Xu, *Adv. Mater.* **2017**, *29*, 1702428.

[49] J. Lin, Z. Pan, X. Wang, *ACS Sustainable Chem. Eng.* **2013**, *2*, 353–358.

[50] K. Wang, Q. Li, B. Liu, B. Cheng, W. Ho, J. Yu, *Appl. Catal. B* **2015**, *176-177*, 44–52.

[51] C. Yang, W. Huang, L. C. da Silva, K. A. I. Zhang, X. Wang, *Chem. Eur. J.* **2018**, *24*, 17454–17458.

[52] G. Zhang, G. Li, T. Heil, S. Zafeiratos, F. Lai, A. Savateev, M. Antonietti, X. Wang, *Angew. Chem. Int. Ed.* **2019**, *58*, 3433–3437.

[53] X. H. Li, M. Baar, S. Blechert, M. Antonietti, *Sci. Rep.* **2013**, *3*, 1743.

[54] A. Mills, C. O'Rourke, *Catal. Today* **2014**, *230*, 256–264.

[55] C. Ayed, L. C. da Silva, D. Wang, K. A. I. Zhang, *J. Mater. Chem. A* **2018**, *6*, 22145–22151.

[56] A. K. Singh, R. Chawla, L. D. S. Yadav, *Tetrahedron Lett.* **2015**, *56*, 653–656.

[57] N. Huber, R. Li, C. T. J. Ferguson, D. W. Gehrig, C. Ramanan, P. W. M. Blom, K. Landfester, K. A. I. Zhang, *Catal. Sci. Technol.* **2020**, *10*, 2092–2099.

[58] C. Yang, R. Li, K. A. I. Zhang, W. Lin, K. Landfester, X. Wang, *Nat. Commun.* **2020**, *11*, 1239.

[59] S. Ghasimi, K. Landfester, K. A. I. Zhang, *ChemCatChem* **2016**, *8*, 694–698.

[60] C. Lu, P. Zhang, S. Jiang, X. Wu, S. Song, M. Zhu, Z. Lou, Z. Li, F. Liu, Y. Liu, Y. Wang, Z. Le, *Appl. Catal. B* **2017**, *200*, 378–385.

[61] S. Lin, S. Sun, K. Wang, K. Shen, B. Ma, Y. Ren, X. Fan, *Nanomaterials* **2018**, *8*, 127.

[62] J. Liu, M. Antonietti, *Energy Environ. Sci.* **2013**, *6*, 1486–1493.

[63] D. A. Nagib, D. W. MacMillan, *Nature* **2011**, *480*, 224–228.

[64] Y. Yasu, T. Koike, M. Akita, *Chem. Commun.* **2012**, *48*, 5355–5357.

[65] Y. Huang, Z. Xin, W. Yao, Q. Hu, Z. Li, L. Xiao, B. Yang, J. Zhang, *Chem. Commun.* **2018**, *54*, 13587–13590.

[66] T. Maji, A. Karmakar, O. Reiser, *J. Org. Chem.* **2011**, *76*, 736–739.

[67] W. X. Wei, R. Li, N. Huber, G. Kizilsavas, C. T. J. Ferguson, K. Landfester, K. A. I. Zhang, *ChemCatChem* **2021**, *13*, 3410–3413.

[68] Z. Li, W. F. Zhang, Q. S. Zhao, H. Y. Gu, Y. Li, G. L. Zhang, F. B. Zhang, X. B. Fan, *ACS Sustainable Chem. Eng.* **2015**, *3*, 468–474.

[69] P. Kuhn, A. Thomas, M. Antonietti, *Macromolecules* **2009**, *42*, 319–326.

[70] W. Huang, N. Huber, S. Jiang, K. Landfester, K. A. I. Zhang, *Angew. Chem. Int. Ed.* **2020**, *59*, 18368–18373.

[71] B. C. Ma, S. Ghasimi, K. Landfester, K. A. I. Zhang, *J. Mater. Chem. B* **2016**, *4*, 5112–5118.

[72] L. Jiao, Y. L. Hu, H. X. Ju, C. D. Wang, M. R. Gao, Q. Yang, J. F. Zhu, S. H. Yu, H. L. Jiang, *J. Mater. Chem. A* **2017**, *5*, 23170–23178.

[73] S. Ghosh, N. A. Kouame, L. Ramos, S. Remita, A. Dazzi, A. Deniset-Besseau, P. Beaunier, F. Goubard, P. H. Aubert, H. Remita, *Nat. Mater.* **2015**, *14*, 505–11.

[74] S. Bhowmik, R. G. Jadhav, A. K. Das, *J. Phys. Chem. C* **2018**, *122*, 274–284.

[75] Y. Xie, T. T. Wang, X. H. Liu, K. Zou, W. Q. Deng, *Nat. Commun.* **2013**, *4*, 1960.

[76] X. Wang, K. Maeda, A. Thomas, K. Takanabe, G. Xin, J. M. Carlsson, K. Domen, M. Antonietti, *Nat. Mater.* **2009**, *8*, 76–80.

[77] L. W. Li, Z. X. Cai, *Polym. Chem.* **2016**, *7*, 4937–4943.

[78] B. C. Ma, S. Ghasimi, K. Landfester, F. Vilela, K. A. I. Zhang, *J. Mater. Chem. A* **2015**, *3*, 16064–16071.

[79] S. Kim, K. Landfester, C. T. J. Ferguson, *ACS Nano* **2022**, *16*, 17041–17048.

[80] B. C. Ma, L. Caire da Silva, S. M. Jo, F. R. Wurm, M. B. Bannwarth, K. A. I. Zhang, K. Sundmacher, K. Landfester, *ChemBioChem* **2019**, *20*, 2593–2596.

[81] H. S. Jena, C. Krishnaraj, G. B. Wang, K. Leus, J. Schmidt, N. Chaoui, P. Van der Voort, *Chem. Mater.* **2018**, *30*, 4102–4111.

[82] M. Y. Liu, L. P. Guo, S. B. Jin, B. E. Tan, *J. Mater. Chem. A* **2019**, *7*, 5153–5172.

[83] T. Banerjee, F. Podjaski, J. Kröger, B. P. Biswal, B. V. Lotsch, *Nat. Rev. Mater.* **2021**, *6*, 168–190.

[84] Y. Wang, A. Vogel, M. Sachs, R. S. Sprick, L. Wilbraham, S. J. A. Moniz, R. Godin, M. A. Zwijnenburg, J. R. Durrant, A. I. Cooper, J. Tang, *Nat. Energy* **2019**, *4*, 746–760.

[85] P. Katekomol, J. Roeser, M. Bojdys, J. Weber, A. Thomas, *Chem. Mater.* **2013**, *25*, 1542–1548.

[86] W. Huang, Z. J. Wang, B. C. Ma, S. Ghasimi, D. Gehrig, F. Laquai, K. Landfester, K. A. I. Zhang, *J. Mater. Chem. A* **2016**, *4*, 7555–7559.

[87] C. T. J. Ferguson, N. Huber, T. Kuckhoff, K. A. I. Zhang, K. Landfester, *J. Mater. Chem. A* **2020**, *8*, 1072–1076.

[88] J. Byun, K. Landfester, K. A. I. Zhang, *Chem. Mat.* **2019**, *31*, 3381–3387.

[89] M. J. Liu, Y. Ishida, Y. Ebina, T. Sasaki, T. Aida, *Nat. Commun.* **2013**, *4*, 1–7.

[90] J. Yang, Z. Li, H. Zhu, *Appl. Catal. B* **2017**, *217*, 603–614.

[91] L. Petrizza, M. Le Bechec, E. Decompte, H. El Hadri, S. Lacombe, M. Save, *Polym. Chem.* **2019**, *10*, 3170–3179.

[92] R. Radjagobalou, J. F. Blanco, L. Petrizza, M. Le Bechec, O. Dechy-Cabaret, S. Lacombe, M. Save, K. Loubiere, *ACS Sustainable Chem. Eng.* **2020**, *8*, 18568–18576.

[93] C. T. J. Ferguson, N. Huber, K. Landfester, K. A. I. Zhang, *Angew. Chem. Int. Ed.* **2019**, *58*, 10567–10571.

[94] C. T. J. Ferguson, K. A. I. Zhang, *ACS Catal.* **2021**, *11*, 9547–9560.

[95] J. J. Lessard, G. M. Scheutz, A. B. Korpusik, R. A. Olson, C. A. Figg, B. S. Sumerlin, *Polym. Chem.* **2021**, *12*, 2205–2209.

[96] A. B. Korpusik, Y. Tan, J. B. Garrison, W. H. Tan, B. S. Sumerlin, *Macromolecules* **2021**, *54*, 7354–7363.

[97] C. Boussiron, M. Le Bechec, L. Petrizza, J. Sabalot, S. Lacombe, M. Save, *Macromol. Rapid Commun.* **2018**, *40*, 1800329.

[98] C. Boussiron, M. Le Bechec, J. Sabalot, S. Lacombe, M. Save, *Polym. Chem.* **2021**, *12*, 134–147.

[99] V. Ibrahimova, S. A. Denisov, K. Vanvarenberg, P. Verwilst, V. Preat, J. M. Guigner, N. D. McClenaghan, S. Lecommandoux, C. A. Fustin, *Nanoscale* **2017**, *9*, 11180–11186.

[100] Y. Wang, F. Silveri, M. K. Bayazit, Q. Ruan, Y. Li, J. Xie, C. R. A. Catlow, J. Tang, *Adv. Energy Mater.* **2018**, *8*, 1801084.

[101] M. L. Tang, Z. Bao, *Chem. Mater.* **2010**, *23*, 446–455.

[102] J. Chen, J. Yang, Y. Guo, Y. Liu, *Adv. Mater.* **2022**, *34*, 2104325.

[103] C.-G. Zhan, J. A. Nichols, D. A. Dixon, *J. Phys. Chem. A* **2003**, *107*, 4184–4195.

[104] K.-K. Niu, T.-X. Luan, J. Cui, H. Liu, L.-B. Xing, P.-Z. Li, *ACS Catal.* **2024**, *14*, 2631–2641.

[105] M. L. Tang, A. D. Reichardt, P. Wei, Z. Bao, *J. Am. Chem. Soc.* **2009**, *131*, 5264–5273.

[106] S. K. Lower, M. A. El-Sayed, *Chem. Rev.* **1966**, *66*, 199–241.

[107] M. Mońka, I. E. Serdiuk, K. Kozakiewicz, E. Hoffman, J. Szumilas, A. Kubicki, S. Y. Park, P. Bojarski, *J. Mater. Chem. C* **2022**, *10*, 7925–7934.

[108] P. She, Y. Yu, Y. Qin, Y. Zhang, F. Li, Y. Ma, S. Liu, W. Huang, Q. Zhao, *Adv. Opt. Mater.* **2020**, *8*, 1901437.

[109] S. P. McGlynn, R. Sunseri, N. Christodouleas, *J. Chem. Phys.* **1962**, *37*, 1818–1824.

[110] T. J. Penfold, E. Gindensperger, C. Daniel, C. M. Marian, *Chem. Rev.* **2018**, *118*, 6975–7025.

[111] Y. Dong, A. A. Sukhanov, J. Zhao, A. Elmali, X. Li, B. Dick, A. Karatay, V. K. Voronkova, *J. Phys. Chem. C* **2019**, *123*, 22793–22811.

[112] Y. Shi, H. Guo, M. Qin, Y. Wang, J. Zhao, H. Sun, H. Wang, Y. Wang, X. Zhou, A. Facchetti, X. Lu, M. Zhou, X. Guo, *Chem. Mater.* **2018**, *30*, 7988–8001.

[113] Y. He, N. A. Kukhta, A. Marks, C. K. Luscombe, *J. Mater. Chem. C* **2022**, *10*, 2314–2332.

[114] M. Li, C. An, W. Pisula, K. Mullen, *Acc. Chem. Res.* **2018**, *51*, 1196–1205.

[115] Z. Ma, H. Geng, D. Wang, Z. Shuai, *J. Mater. Chem. C* **2016**, *4*, 4546–4555.

[116] Y. Yang, Z. Liu, G. Zhang, X. Zhang, D. Zhang, *Adv. Mater.* **2019**, *31*, 1903104.

[117] H. Wang, H. Wang, Z. Wang, L. Tang, G. Zeng, P. Xu, M. Chen, T. Xiong, C. Zhou, X. Li, D. Huang, Y. Zhu, Z. Wang, J. Tang, *Chem. Soc. Rev.* **2020**, *49*, 4135–4165.

[118] H. Park, D. J. Shin, J. Yu, *J. Chem. Educ.* **2021**, *98*, 703–709.

[119] C. Yan, J. Dong, Y. Chen, W. Zhou, Y. Peng, Y. Zhang, L.-n. Wang, *Nano Res.* **2022**, *15*, 3835–3858.

[120] M. Ellis, H. Yang, S. Giannini, O. G. Ziogos, J. Blumberger, *Adv. Mater.* **2021**, *33*, 2104852.

[121] G. Li, B. Wang, D. E. Resasco, *Surf. Sci. Rep.* **2021**, *76*, 100541.

[122] Y. Nosaka, A. Y. Nosaka, *Chem. Rev.* **2017**, *117*, 11302–11336.

[123] M. A. Bryden, F. Millward, O. S. Lee, L. Cork, M. C. Gather, A. Steffen, E. Zysman-Colman, *Chem. Sci.* **2024**, *15*, 3741–3757.

[124] D. J. Durand, N. Fey, *Chem. Rev.* **2019**, *119*, 6561–6594.

[125] L. Brüss, R. Jeyaseelan, J. C. G. Kürschner, M. Utikal, L. Næsborg, *ChemCatChem* **2022**, *15*, e202201146.

[126] M. Giedyk, R. Narobe, S. Weiß, D. Touraud, W. Kunz, B. König, *Nat. Catal.* **2019**, *3*, 40–47.

[127] F. Eisenreich, A. R. A. Palmans, *Chem. Eur. J.* **2022**, *28*, e202201322.

[128] A. Stank, D. B. Kokh, J. C. Fuller, R. C. Wade, *Acc. Chem. Res.* **2016**, *49*, 809–815.

[129] S. Scheiner, *J. Indian Inst. Sci.* **2020**, *100*, 61–76.

[130] T. Kuckhoff, R. C. Brewster, C. T. J. Ferguson, A. G. Jarvis, *Eur. J. Org. Chem.* **2023**, *26*, e202201412.

[131] R. Breslow, N. Greenspoon, T. Guo, R. Zarzycki, *J. Am. Chem. Soc.* **2002**, *111*, 8296–8297.

[132] Y. Zhang, J. Phipps, S. Ma, *Nat. Catal.* **2022**, *5*, 973–974.

[133] S. Ghosh-Mukerji, H. Haick, M. Schvartzman, Y. Paz, *J. Am. Chem. Soc.* **2001**, *123*, 10776–10777.

[134] X. Shen, L. Zhu, J. Li, H. Tang, *Chem. Commun.* **2007**, 1163–1165.

[135] Y. Hao, Y. L. Lu, Z. Jiao, C. Y. Su, *Angew. Chem. Int. Ed.* **2024**, *63*, e202317808.

[136] R. Ham, C. J. Nielsen, S. Pullen, J. N. H. Reek, *Chem. Rev.* **2023**, *123*, 5225–5261.

[137] L. Feng, K. Y. Wang, G. S. Day, H. C. Zhou, *Chem. Soc. Rev.* **2019**, *48*, 4823–4853.

[138] A. B. Grommet, M. Feller, R. Klajn, *Nat. Nanotechnol.* **2020**, *15*, 256–271.

[139] A. Kumar, R. Saha, P. S. Mukherjee, *Chem. Sci.* **2021**, *12*, 5319–5329.

[140] F. Glaser, M. Schmitz, C. Kerzig, *Nanoscale* **2023**, *16*, 123–137.

[141] A. N. Muttathukattil, S. Srinivasan, A. Halder, G. Reddy, *J. Phys. Chem. B* **2019**, *123*, 9302–9311.

[142] S. S. Chavali, C. E. Cavender, D. H. Mathews, J. E. Wedekind, *J. Am. Chem. Soc.* **2020**, *142*, 19835–19839.

[143] G. Halligudra, C. C. Paramesh, R. Mudike, M. Ningegowda, D. Rangappa, P. D. Shivaramu, *ACS Omega* **2021**, *6*, 34416–34428.

[144] J. Yao, Z. Yan, J. Ji, W. Wu, C. Yang, M. Nishijima, G. Fukuhara, T. Mori, Y. Inoue, *J. Am. Chem. Soc.* **2014**, *136*, 6916–6919.

[145] A. Milo, T. Ooi, T. Bach, *J. Org. Chem.* **2023**, *88*, 7615–7618.

[146] B. B. C. Peters, J. Zheng, N. Birke, T. Singh, P. G. Andersson, *Nat. Commun.* **2022**, *13*, 361.

[147] R. Noyori, H. Takaya, *Acc. Chem. Res.* **2002**, *23*, 345–350.

[148] R. Noyori, *Adv. Synth. Catal.* **2003**, *345*, 15–32.

[149] A. Bauer, F. Westkamper, S. Grimme, T. Bach, *Nature* **2005**, *436*, 1139–1140.

[150] F. Pecho, Y. Q. Zou, J. Gramuller, T. Mori, S. M. Huber, A. Bauer, R. M. Gschwind, T. Bach, *Chem. Eur. J.* **2020**, *26*, 5190–5194.

[151] N. Vallavoju, S. Selvakumar, S. Jockusch, M. P. Sibi, J. Sivaguru, *Angew. Chem. Int. Ed.* **2014**, *53*, 5604–5608.

[152] N. Vallavoju, S. Selvakumar, B. C. Pemberton, S. Jockusch, M. P. Sibi, J. Sivaguru, *Angew. Chem. Int. Ed.* **2016**, *55*, 5446–5451.

[153] A. B. Rolka, B. König, *Nat. Synth.* **2023**, *2*, 913–925.

[154] J. Kou, C. Lu, J. Wang, Y. Chen, Z. Xu, R. S. Varma, *Chem. Rev.* **2017**, *117*, 1445–1514.

[155] K. L. Skubi, T. R. Blum, T. P. Yoon, *Chem. Rev.* **2016**, *116*, 10035–10074.

[156] S. Thanneeru, J. K. Nganga, A. S. Amin, B. Liu, L. Jin, A. M. Angeles-Boza, J. He, *ChemCatChem* **2017**, *9*, 1157–1162.

[157] Y. Markushyna, A. Savateev, *Eur. J. Org. Chem.* **2022**, *2022*, e202200026.

[158] A. Galushchinskiy, C. Pulignani, H. Szalad, E. Reisner, J. Albero, N. V. Tarakina, C. M. Pelicano, H. García, O. Savateev, M. Antonietti, *Sol. RRL* **2023**, *7*, 2300077.

[159] C. G. Thomson, A. L. Lee, F. Vilela, *Beilstein J. Org. Chem.* **2020**, *16*, 1495–1549.

[160] T. P. Yoon, M. A. Ischay, J. Du, *Nat. Chem.* **2010**, *2*, 527–532.

[161] G. E. M. Crisenza, P. Melchiorre, *Nat. Commun.* **2020**, *11*, 803.

[162] T. P. Nicholls, D. Leonori, A. C. Bissember, *Nat. Prod. Rep.* **2016**, *33*, 1248–1254.

[163] J. J. Douglas, M. J. Sevrin, C. R. J. Stephenson, *Org. Process Res. Dev.* **2016**, *20*, 1134–1147.

[164] T. P. Yoon, *Acc. Chem. Res.* **2016**, *49*, 2307–2315.

[165] J. Heuer, T. Kuckhoff, R. Li, K. Landfester, C. T. J. Ferguson, *ACS Appl. Mater. Interfaces* **2023**, *15*, 2891–2900.

[166] W. L. Li, T. Head-Gordon, *ACS Cent. Sci.* **2021**, *7*, 72–80.

[167] R. Cao, X. Liu, Y. Liu, X. Zhai, T. Cao, A. Wang, J. Qiu, *Food Chem.* **2021**, *342*, 128258.

[168] V. Mirceski, S. Skrzypek, L. Stojanov, *ChemTexts* **2018**, *4*, 17.

[169] I.-Y. Kim, S.-H. Suh, I.-K. Lee, R. R. Wolfe, *Exp. Mol. Med.* **2016**, *48*, e203–e203.

[170] T. Kuckhoff, J. Heuer, R. Li, K. A. I. Zhang, K. Landfester, C. T. J. Ferguson, *RSC Appl. Polym.* **2024**, *2*, 155–162.

[171] B. List, *Chem. Rev.* **2007**, *107*, 5413–5415.

[172] T. Ooi, C. Crudden, *ACS Catal.* **2021**, *11*, 15234–15234.

[173] Y. Gao, J. M. Klunder, R. M. Hanson, H. Masamune, S. Y. Ko, K. B. Sharpless, *J. Am. Chem. Soc.* **2002**, *109*, 5765–5780.

[174] R. Noyori, T. Ohkuma, M. Kitamura, H. Takaya, N. Sayo, H. Kumobayashi, S. Akutagawa, *J. Am. Chem. Soc.* **1987**, *109*, 5856–5858.

[175] K. A. Ahrendt, C. J. Borths, D. W. C. MacMillan, *J. Am. Chem. Soc.* **2000**, *122*, 4243–4244.

[176] M. S. Taylor, E. N. Jacobsen, *Angew. Chem. Int. Ed.* **2006**, *45*, 1520–1543.

[177] Y. Hayashi, *Chem. Sci.* **2016**, *7*, 866–880.

[178] W. Watson, *Org. Process Res. Dev.* **2012**, *16*, 1877–1877.

[179] Z. H. Weng, F. Zaera, *J. Phys. Chem. C* **2014**, *118*, 3672–3679.

[180] M. T. Reetz, *Angew. Chem. Int. Ed.* **2011**, *50*, 138–74.

[181] Z. Sun, R. Lonsdale, X. D. Kong, J. H. Xu, J. Zhou, M. T. Reetz, *Angew. Chem. Int. Ed.* **2015**, *54*, 12410–12415.

[182] R. Breslow in *Artificial Enzymes*, John Wiley & Sons, Ltd, **2005**, Chapter 1, pp. 1–35.

[183] I. M. Klotz, J. Suh in *Artificial Enzymes*, John Wiley & Sons, Ltd, **2005**, Chapter 3, pp. 63–88.

[184] M. Morimoto, S. M. Bierschenk, K. T. Xia, R. G. Bergman, K. N. Raymond, F. D. Toste, *Nat. Catal.* **2020**, *3*, 969–984.

[185] Y. Yamamoto, M. Komiyama in *Artificial Enzymes*, John Wiley & Sons, Ltd, **2005**, Chapter 7, pp. 159–175.

[186] H. Zhang, S. Li, A. Qu, C. Hao, M. Sun, L. Xu, C. Xu, H. Kuang, *Chem. Sci.* **2020**, *11*, 12937–12954.

[187] V. Balzani, G. Bergamini, P. Ceroni, *Angew. Chem. Int. Ed.* **2015**, *54*, 11320–11337.

[188] L. Marzo, S. K. Pagire, O. Reiser, B. Konig, *Angew. Chem. Int. Ed.* **2018**, *57*, 10034–10072.

[189] D. A. Nicewicz, D. W. MacMillan, *Science* **2008**, *322*, 77–80.

[190] J. W. Tucker, C. R. Stephenson, *J. Org. Chem.* **2012**, *77*, 1617–1622.

[191] J. Heuer, C. T. J. Ferguson, *Nanoscale* **2022**, *14*, 1646–1652.

[192] M. Ballestri, E. Caruso, A. Guerrini, C. Ferroni, S. Banfi, M. Gariboldi, E. Monti, G. Sotgiu, G. Varchi, *J. Photochem. Photobiol. B* **2018**, *186*, 169–177.

[193] W. Li, L. Li, G. Cui, Y. Bai, X. Xiao, Y. Li, L. Yan, *Chem. Asian J.* **2017**, *12*, 392–396.

[194] T. Takata, J. Jiang, Y. Sakata, M. Nakabayashi, N. Shibata, V. Nandal, K. Seki, T. Hisatomi, K. Domen, *Nature* **2020**, *581*, 411–414.

[195] F. M. Wisser, M. Duguet, Q. Perrinet, A. C. Ghosh, M. Alves-Favaro, Y. Mohr, C. Lorentz, E. A. Quadrelli, R. Palkovits, D. Farrusseng, C. Mellot-Draznieks, V. de Waele, J. Canivet, *Angew. Chem. Int. Ed.* **2020**, *59*, 5116–5122.

[196] T. Kuckhoff, K. Landfester, K. A. I. Zhang, C. T. J. Ferguson, *Chem. Mat.* **2021**, *33*, 9131–9138.

[197] M. Cybularczyk-Cecotka, J. Szczepanik, M. Giedyk, *Nat. Catal.* **2020**, *3*, 872–886.

[198] H. Yi, L. Niu, C. Song, Y. Li, B. Dou, A. K. Singh, A. Lei, *Angew. Chem. Int. Ed.* **2017**, *56*, 1120–1124.

[199] S. Ghasimi, S. Prescher, Z. J. Wang, K. Landfester, J. Yuan, K. A. Zhang, *Angew. Chem. Int. Ed.* **2015**, *54*, 14549–14553.

[200] A. J. Gormley, J. Yeow, G. Ng, O. Conway, C. Boyer, R. Chapman, *Angew. Chem. Int. Ed.* **2018**, *57*, 1557–1562.

[201] C. Kutahya, P. Wang, S. Li, S. Liu, J. Li, Z. Chen, B. Strehmel, *Angew. Chem. Int. Ed.* **2020**, *59*, 3166–3171.

[202] M. Rubens, J. H. Vrijsen, J. Laun, T. Junkers, *Angew. Chem. Int. Ed.* **2019**, *58*, 3183–3187.

[203] H. Huang, S. Banerjee, K. Qiu, P. Zhang, O. Blacque, T. Malcomson, M. J. Paterson, G. J. Clarkson, M. Staniforth, V. G. Stavros, G. Gasser, H. Chao, P. J. Sadler, *Nat. Chem.* **2019**, *11*, 1041–1048.

[204] K. Yang, H. Xu, L. Cheng, C. Sun, J. Wang, Z. Liu, *Adv. Mater.* **2012**, *24*, 5586–5592.

[205] C. Xing, Q. Xu, H. Tang, L. Liu, S. Wang, *J. Am. Chem. Soc.* **2009**, *131*, 13117–13124.

[206] R. Brimioulle, D. Lenhart, M. M. Maturi, T. Bach, *Angew. Chem. Int. Ed.* **2015**, *54*, 3872–3890.

[207] A. Blanazs, A. J. Ryan, S. P. Armes, *Macromolecules* **2012**, *45*, 5099–5107.

[208] A. Blanazs, R. Verber, O. O. Mykhaylyk, A. J. Ryan, J. Z. Heath, C. W. Douglas, S. P. Armes, *J. Am. Chem. Soc.* **2012**, *134*, 9741–9748.

[209] V. J. Cunningham, A. M. Alswieleh, K. L. Thompson, M. Williams, G. J. Leggett, S. P. Armes, O. M. Musa, *Macromolecules* **2014**, *47*, 5613–5623.

[210] A. K. Ghose, G. M. Crippen, *J. Chem. Inf. Comput. Sci.* **1987**, *27*, 21–35.

[211] C. Ye, Y. Zhang, A. Ding, Y. Hu, H. Guo, *Sci. Rep.* **2018**, *8*, 2205.

[212] A. Jimenez-Almarza, A. Lopez-Magano, R. Mas-Balleste, J. Aleman, *ACS Appl. Mater. Interfaces.* **2022**, *14*, 16258–16268.

[213] F. Jensen, A. Greer, E. L. Clennan, *J. Am. Chem. Soc.* **1998**, *120*, 4439–4449.

[214] L. Furst, B. S. Matsuura, J. M. Narayanam, J. W. Tucker, C. R. Stephenson, *Org. Lett.* **2010**, *12*, 3104–3107.

[215] L. Wang, W. Huang, R. Li, D. Gehrig, P. W. Blom, K. Landfester, K. A. Zhang, *Angew. Chem. Int. Ed.* **2016**, *55*, 9783–9787.

[216] M. Bregnhoj, M. Westberg, F. Jensen, P. R. Ogilby, *Phys. Chem. Chem. Phys.* **2016**, *18*, 22946–22961.

[217] P. R. Ogilby, C. S. Foote, *J. Am. Chem. Soc.* **1983**, *105*, 3423–3430.

[218] Z. Kuspanov, B. Bakbolat, A. Baimenov, A. Issadykov, M. Yeleuov, C. Daulbayev, *Sci. Total Environ.* **2023**, *885*, 163914.

[219] A. I. Cooper, *Adv. Mater.* **2009**, *21*, 1291–1295.

[220] M. Barawi, L. Collado, M. Gomez-Mendoza, F. E. Oropeza, M. Liras, V. A. de la Peña O'Shea, *Adv. Energy Mater.* **2021**, *11*, 2101530.

[221] Y. Xu, S. Jin, H. Xu, A. Nagai, D. Jiang, *Chem. Soc. Rev.* **2013**, *42*, 8012–8031.

[222] C. Han, S. Xiang, S. Jin, C. Zhang, J.-X. Jiang, *ACS Catal.* **2022**, *13*, 204–212.

[223] S. Barman, A. Singh, F. A. Rahimi, T. K. Maji, *J. Am. Chem. Soc.* **2021**, *143*, 16284–16292.

[224] S. Wang, X. Hai, X. Ding, S. Jin, Y. Xiang, P. Wang, B. Jiang, F. Ichihara, M. Oshikiri, X. Meng, Y. Li, W. Matsuda, J. Ma, S. Seki, X. Wang, H. Huang, Y. Wada, H. Chen, J. Ye, *Nat. Commun.* **2020**, *11*, 1149.

[225] R. Li, J. Byun, W. Huang, C. Ayed, L. Wang, K. A. I. Zhang, *ACS Catal.* **2018**, *8*, 4735–4750.

[226] W. Huang, B. C. Ma, D. Wang, Z. J. Wang, R. Li, L. Wang, K. Landfester, K. A. I. Zhang, *J. Mater. Chem. A* **2017**, *5*, 3792–3797.

[227] T. Repenko, A. Rix, S. Ludwanowski, D. Go, F. Kiessling, W. Lederle, A. J. C. Kuehne, *Nat. Commun.* **2017**, *8*, 470.

[228] S. Dadashi-Silab, F. Lorandi, M. J. DiTucci, M. Sun, G. Szczepaniak, T. Liu, K. Matyjaszewski, *J. Am. Chem. Soc.* **2021**, *143*, 9630–9638.

[229] W. Zhang, H. Zuo, Z. Cheng, Y. Shi, Z. Guo, N. Meng, A. Thomas, Y. Liao, *Adv. Mater.* **2022**, *34*, 2104952.

[230] J. X. Jiang, F. Su, A. Trewin, C. D. Wood, H. Niu, J. T. Jones, Y. Z. Khimyak, A. I. Cooper, *J. Am. Chem. Soc.* **2008**, *130*, 7710–7720.

[231] J. Z. Bloh, *Catal. Lett.* **2021**, *151*, 3105–3113.

[232] S. Mosleh, M. Ghaedi in *Interface Science and Technology*, Elsevier, **2021**, pp. 761–790.

[233] S. Ghosh-Mukerji, H. Haick, Y. Paz, *J. Photochem. Photobiol. A* **2003**, *160*, 77–85.

[234] M. A. Fox, M. T. Dulay, *Chem. Rev.* **2002**, *93*, 341–357.

[235] K. Inumaru, M. Yasui, T. Kasahara, K. Yamaguchi, A. Yasuda, S. Yamanaka, *J. Mater. Chem.* **2011**, *21*, 12117–12125.

[236] Y. Shiraishi, N. Saito, T. Hirai, *J. Am. Chem. Soc.* **2005**, *127*, 12820–12822.

[237] Y. Ide, Y. Nakasato, M. Ogawa, *J. Am. Chem. Soc.* **2010**, *132*, 3601–3604.

[238] J. Svoboda, B. Konig, *Chem. Rev.* **2006**, *106*, 5413–5430.

[239] B. Bibal, C. Mongin, D. M. Bassani, *Chem. Soc. Rev.* **2014**, *43*, 4179–4198.

[240] X. Shen, L. Zhu, N. Wang, L. Ye, H. Tang, *Chem. Commun.* **2012**, *48*, 788–798.

[241] M. L. Williams, J. E. Gready, *J. Comput. Chem.* **2004**, *10*, 35–54.

[242] B. J. Smith, L. R. Parent, A. C. Overholts, P. A. Beaucage, R. P. Bisbey, A. D. Chavez, N. Hwang, C. Park, A. M. Evans, N. C. Gianneschi, W. R. Dichtel, *ACS Cent. Sci.* **2017**, *3*, 58–65.

[243] Q. Liu, Z. Tang, M. Wu, Z. Zhou, *Polym. Int.* **2014**, *63*, 381–392.

[244] X. Wu, E. Boz, A. M. Sirkis, A. Y. Chang, T. J. Williams, *J. Fluor. Chem.* **2012**, *135*, 292–302.

[245] H. Zhan, Y. Feng, X. Fan, S. Chen, *Appl. Microbiol. Biotechnol.* **2018**, *102*, 5033–5043.

[246] M. Kudzin, R. Żyłła, Z. Mrozińska, P. Urbaniak, *Water* **2019**, *11*, 331.

[247] M. Obara-Michlewska, *Neurochem. Int.* **2022**, *158*, 105363.

[248] R. Li, K. Landfester, C. T. J. Ferguson, *Angew. Chem. Int. Ed.* **2022**, *61*, e202211132.

[249] A. W. Jacobitz, Q. Liu, S. Suravajjala, N. J. Agrawal, *J. Pharm. Sci.* **2021**, *110*, 719–726.

[250] C. Lopez-Alarcon, A. Arenas, E. Lissi, E. Silva, *Biomol. Concepts* **2014**, *5*, 119–130.

[251] R. Li, J. Heuer, T. Kuckhoff, K. Landfester, C. T. J. Ferguson, *Angew. Chem. Int. Ed.* **2023**, *62*, e202217652.

[252] X. Zhuang, J. Hao, X. Zheng, D. Fu, P. Mo, Y. Jin, P. Chen, H. Liu, G. Liu, W. Lv, *Sep. Purif. Technol.* **2021**, *274*, 118993.

[253] P. Selig, *Synthesis* **2013**, *45*, 703–718.

[254] Q. Wang, C. Yu, H. Long, Y. Du, Y. Jin, W. Zhang, *Angew. Chem. Int. Ed.* **2015**, *54*, 7550–7554.

[255] S. Cao, T. Ivanov, J. Heuer, C. T. J. Ferguson, K. Landfester, L. Caire da Silva, *Nat. Commun.* **2024**, *15*, 39.

[256] W. Jiang, Z. Wu, Z. Gao, M. Wan, M. Zhou, C. Mao, J. Shen, *ACS Nano* **2022**, *16*, 15705–15733.

[257] A. A. Ganguin, S. Aleandri, P. Luciani in *Microfluidics for Cellular Applications*, **2023**, pp. 5–26.

[258] B. Ghosh, *Emerg. Top. Life Sci.* **2022**, *6*, 619–627.

[259] C. Xu, S. Hu, X. Chen, *Mater. Today* **2016**, *19*, 516–532.

[260] B. C. Buddingh, J. C. M. van Hest, *Acc. Chem. Res.* **2017**, *50*, 769–777.

[261] L. Schoonen, J. C. van Hest, *Adv. Mater.* **2016**, *28*, 1109–1128.

[262] C. Guindani, L. C. da Silva, S. Cao, T. Ivanov, K. Landfester, *Angew. Chem. Int. Ed.* **2022**, *61*, e202110855.

[263] Y. Tu, F. Peng, A. Adawy, Y. Men, L. K. Abdelmohsen, D. A. Wilson, *Chem. Rev.* **2016**, *116*, 2023–2078.

[264] N. Gao, S. Mann, *Acc. Chem. Res.* **2023**, *56*, 297–307.

[265] A. B. Cook, S. Novosedlik, J. C. M. van Hest, *Acc. Mater. Res.* **2023**, *4*, 287–298.

[266] J. Aumiller, W. M., C. D. Keating, *Nat. Chem.* **2016**, *8*, 129–137.

[267] Y. Dai, L. You, A. Chilkoti, *Nat. Rev. Bioeng.* **2023**, *1*, 466–480.

[268] J. Liu, E. Spruijt, A. Miserez, R. Langer, *Nat. Rev. Mater.* **2023**, *8*, 139–141.

[269] G. L. Dignon, R. B. Best, J. Mittal, *Annu. Rev. Phys. Chem.* **2020**, *71*, 53–75.

[270] M. Abbas, W. P. Lipinski, J. Wang, E. Spruijt, *Chem. Soc. Rev.* **2021**, *50*, 3690–3705.

[271] Y. Sun, S. Y. Lau, Z. W. Lim, S. C. Chang, F. Ghadessy, A. Partridge, A. Miserez, *Nat. Chem.* **2022**, *14*, 274–283.

[272] A. Baruch Leshem, S. Sloan-Dennison, T. Massarano, S. Ben-David, D. Graham, K. Faulds, H. E. Gottlieb, J. H. Chill, A. Lampel, *Nat. Commun.* **2023**, *14*, 421.

List of Figures

List of Tables